GEOLOGICA ULTRAIECTINA

Mededelingen van de
Faculteit Geowetenschappen
Universiteit Utrecht

no. 255

Effects of Pressure Solution and Phyllosilicates on the Slip and Compaction Behaviour of Crustal Faults

André Niemeijer

The research described in this thesis has been carried out at:

Department of Earth Sciences
Experimental Rock Deformation Laboratory
Budapestlaan 4
3584 CD Utrecht
The Netherlands

Printed by Gadella repro, Utrecht

ISBN-10: 90-5744-118-7
ISBN-13: 978-90-5744-118-9

Effects of Pressure Solution and Phyllosilicates on the Slip and Compaction Behaviour of Crustal Faults

Effecten van Drukoplossing en Phyllosilicaten op het Glij en Compactie gedrag van Breuken in de Korst

(met een samenvatting in het Nederlands)

PROEFSCHRIFT

ter verkrijging van de graad van doctor aan de Universiteit Utrecht op gezag van de Rector Magnificus, Prof. Dr. W.H. Gispen, ingevolge het besluit van het College voor Promoties in het openbaar te verdedigen op maandag 20 februari 2006 te 12:45 uur

door

André Rik Niemeijer

geboren op 27 maart 1977, te Tiel

Promotor: Prof Dr. C.J. Spiers
Faculteit Geowetenschappen
Universiteit Utrecht

The most exciting phrase to hear in science,
the one that heralds new discoveries,
is not 'Eureka!' (I found it!) but 'That's funny ...'

Isaac Asimov

Members of the dissertation committee:

Prof. Dr. F.M. Chester
Department of geology and geophysics
Texas A&M University

Prof. Dr. R.E. Holdsworth
Department of Earth Sciences
Durham University

Prof. Dr. C.J. Marone
Faculty of Geosciences
Pennsylvania State University

Prof. Dr. T. Shimamoto
Department of Geology and Mineralogy
Kyoto University

Prof. Dr. M.J.R. Wortel
Department of Earth Sciences
Utrecht University

TABLE OF CONTENTS

Summary

Deformation of the Earth's crust and crust-lithosphere system is for a large part concentrated in localised faults or fault zones. The mechanical behaviour and evolution of these faults are important in controlling a wide range of geological and geodynamical processes, ranging from rifting and seismogenesis to basin evolution and hydrocarbon trapping, and to orogenesis and ore emplacement. Modelling such processes relies heavily on descriptions of the rheology of fault rocks i.e. of the brittle/frictional, compaction and creep behaviour of fault rocks as derived from laboratory experiments. Laboratory experiments on bulk rock rheology have led to the construction of so-called crustal strength profiles in which upper crustal behaviour is described by laboratory-based fault friction laws with plastic flow dominating the lower crust. Assuming a direct relation between frictional behaviour and seismogenesis, these profiles seem to explain the depth distribution of crustal seismicity. However, fault localisation implies internal weakening and a considerable body of geological and geophysical evidence suggests that classical strength profiles significantly overestimate the long-term steady state strength of fault zones. Moreover, strength profiles describe only the steady state strength of fault rock, whereas for processes such as seismogenesis, transient effects such as fault healing and sealing are much more important.

Several explanations have been offered for the inferred weakness of major fault zones. First, it has been suggested that high internal pore fluid pressures are somehow maintained, thus reducing fault friction, but a mechanism allowing this is not clearly established. Another possible explanation is the development, through reaction, of weak phyllosilicates that align to form a pervasive foliation in many fault zones. Finally, it has been proposed that fluid-rock interactions, such as stress-induced dissolution and precipitation or pressure solution creep, can significantly weaken fault rocks. However, these processes can also lead to fault healing and sealing through compaction and cementation. Thus pressure solution effects seem to be able to both weaken and strengthen fault rocks through competing effects of shear versus compaction. Progress in understanding the effects of fluid-rock interaction on steady state and transient fault strength depends on understanding this competition and the role played by phyllosilicate foliation development.

This thesis aims to elucidate the effects of pressure solution and phyllosilicates on the compaction and shear behaviour of granular materials chosen to resemble or simulate granular fault gouge deforming under hydrothermal, brittle-ductile transitional conditions. To achieve my aims, I implemented three different experimental programs. The first experimental program consists of isostatic compaction experiments on both pure quartz sand and phyllosilicate-bearing quartz sand at temperatures of 400-600 ºC, a confining pressure of 300 MPa and fluid pressures of 150-250 MPa. These experiments were designed to quantify rates of compaction by intergranular pressure solution (IPS) and to determine the effects of phyllosilicates on the process. The results of these experiments are reported in Chapters 2 and 3. Clear evidence was found for compaction by IPS. The main conclusion is that IPS compaction under the conditions studied, is probably controlled by the rate of

dissolution of quartz within the grain contacts, at least down to porosities of 15%. The presence of muscovite hinders compaction, probably through a chemical retardation effect, on the dissolution rate, of aluminium ions dissolved in the pore fluid from the muscovite.

The second experimental program consists of high strain rotary shear experiments performed on simulated fault gouges consisting of brine-flooded, halite-muscovite mixtures. This mixture was chosen as a gouge analogue, since the processes of cataclasis, pressure solution and foliation development are known to occur in this material in room temperature experiments of a few days duration. The effects of these processes on gouge strength could therefore be easily investigated. Normal stresses explored were 1-9 MPa and sliding velocities ranged from 0.001 to 13 μm/s. A series of normal stress-stepping, velocity-stepping, constant sliding velocity and slide-hold-slide experiments were performed at room temperature, reaching shear strains in excess of 50. The results are reported in Chapters 4 and 5.

As described in Chapter 4, I observed velocity-strengthening behaviour up to a sliding velocity of ~0.3-1 μm/s, along with the development of an apparently mylonitic microstructure consisting of an anastomosing muscovite foliation enveloping elongate halite clasts. The deformation mechanism was one of frictional slip on the phyllosilicate foliation with accommodation by pressure solution of the intervening halite. I refine a previous microphysical model for this type of deformation mechanism in halite-kaolinite mixtures and extend it to include the possibility of plastic flow in the phyllosilicates. The model predictions compare well with the experimental results, and extrapolations of the model to natural quartz-phyllosilicate fault rocks under crustal conditions predict significant weakening (factor 2-5) with respect to classical crustal strength profiles. At higher sliding velocities, I observed a strong velocity weakening effect in the mixtures of halite and muscovite. This was accompanied by a cataclastic microstructure with no foliation but with significant porosity development. The porosity increased with increasing sliding velocity. I explain this behaviour in terms of a granular flow mechanism involving competition between shear-induced dilatation and pressure solution controlled compaction. The time-dependence of pressure solution compaction leads to higher porosities at higher sliding velocities. Higher porosity implies smaller grain contact areas, a lower dilatancy angle for granular flow and hence lower grain boundary shear resistance. Thus faster shear produces a lower macroscopic shear strength and velocity-weakening. Since velocity weakening is a prerequisite for an instability (i.e. an earthquake) to initiate, the marked, phyllosilicate-related velocity weakening effect observed in these experiments (one order of magnitude higher than previously observed) is potentially important in developing our understanding of the seismic cycle.

The marked difference in behaviour between the two velocity regimes seen in the salt-muscovite experiments is also associated with completely different healing and restrengthening behaviour as evidenced from the results of the slide-hold-slide experiments which are reported in Chapter 5. These experiments show that samples deformed in the low-velocity regime do not heal or restrengthen significantly on re-shear, while those deformed

in the high velocity regime regain high strength. Static healing rates, recorded for the latter samples, increase with increasing pre-hold sliding velocity. This is explained by a higher steady state porosity being maintained during rapid steady state sliding, so that compaction is increased during hold periods. The increased compaction leads to an increased granular dilatancy angle and to higher intergranular friction, hence higher healing rates following rapid slip. If a similar mechanism operates under natural conditions, this implies that the velocity history of fault gouges will have a strong effect on the restrengthening potential of these gouges with unstable, seismogenic fault segments being prone to effective healing and recurrent failure.

The third experimental program consists of high strain rotary shear experiments on simulated quartz gouges under hydrothermal conditions. The experiments were performed in a purpose-built apparatus at temperatures of 400-600 ºC, effective normal stresses of 20-100 MPa, a fluid pressure of 200 MPa and sliding velocities of 0.01-1 μm/s and reached shear strain γ up to 50. I report the results of these experiments in Chapter 6. They show strain hardening up to a shear strain γ of 0.6-1.8, followed by strain weakening of up to 30% towards a steady state value at a strain γ of ~8-12. This strain weakening effect is much higher than previously reported for quartz gouge. The steady state shear strength increases with decreasing grain size, increasing sliding velocity, and decreasing temperature. The microstructure of the deformed quartz gouge is characterised by the presence of a through-going boundary-parallel Y-shear. Some samples also show Riedel shears oriented oblique to the shear zone boundary. Deformation in these tests was largely by cataclastic, with most displacement being accommodated along the boundary-parallel Y-shear, causing the strong weakening observed. Intergranular pressure solution did not contribute significantly to shear strain accommodation, but appears to play a role in smoothening and weakening the localised slip surface and in controlling gouge compaction.

Finally, I turn back to our rock-analogue experiments in Chapter 7, where I present a microphysical model predicting the steady state velocity-weakening behaviour reported in Chapter 4 for analogue samples deformed at high sliding velocities. The model is based on a quantitative description of the competition between shear-induced dilatation and IPS-controlled compaction processes. The aim was to assess whether the dramatic velocity weakening effect seen in the analogue system (Chapter 4) can be expected to occur in quartz-phyllosilicate fault rocks under upper to mid crustal conditions, where they might be important for seismogenesis. The model results agree favourably with the experimental results. Extrapolation of the model to natural conditions shows a velocity weakening effect which is an order of magnitude larger than previously seen in low strain experiments on quartz/granite gouges. Combining the model with that derived for the velocity strengthening regime in Chapter 4, yields curves describing the maximum static stress drop accompanying earthquakes, as a function of depth. The predicted stress drops agree favourably with static stress drop estimates inferred from seismological observations. This implies that if similar deformation mechanisms operate in quartz-phyllosilicate fault rocks, we will be able to provide a microphysical basis for extrapolating laboratory-derived rate and state dependent

fault friction parameters to natural conditions for numerical modelling of faulting and seismogenesis.

Chapter 1

GENERAL INTRODUCTION

1.1. Motivation and scope of this study

Deformation of the Earth's crust and lithosphere is generally heterogeneous, with most displacement being concentrated in zones of inter-linked faults and shear zones. These localised zones of deformation play an important role in determining the location, geometry and evolution of numerous geological features, ranging from fault-bounded basins and rift zones to continental margins, subduction zones and orogenic belts (Govers and Wortel, 1995; Cloetingh and Burov, 1996; Ter Voorde et al., 1998; Cattin et al., 2005). In addition, fault systems often act as conduits for or barriers to fluid flow, thus influencing emplacement of economically important hydrocarbon accumulations and mineral deposits (Knopf, 1929; Newhouse, 1942; Sibson, 2001). Moreover, most active seismicity occurs on crustal fault systems and an understanding of the mechanical process of fault displacement is therefore of central importance for understanding the seismic cycle (Sibson, 1983; Marone, 1998b; Scholz, 2002). This in turn has direct bearing on assessing seismic hazards in active continental regions as well as tsunami risk in the case of active submarine faults (Kanamori, 1972; Abe, 1973; Bilek and Lay, 2002).

The study of faults and shear zones and their mechanical behaviour thus forms a subject of significant scientific, industrial and societal interest. An important question in this field concerns the effects of fluid-assisted compaction and healing (i.e. strengthening) processes versus fluid-assisted slip or creep processes (i.e. weakening) in the seismogenic zone of the crust (3-15 km depth). In this thesis, I report and discuss the results of an experimental program, set-up to explore the effects of fluid-rock interaction on deformation of crustal rocks in this upper to middle crustal depth range. Fluid-assisted compaction processes are investigated in relation to compaction of both sedimentary rocks and fault rocks, while the shear-behaviour of gouge-bearing faults is studied by means of rotary shear experiments on simulated fault gouge.

1.2. Strength properties of long-lived fault zones: Evidence for effects of fluids

The existence of localized faults and shear zones in deformed regions of the crust generally implies that these zones are weaker than the surrounding country rocks (Rutter et al., 2001). In addition, repeated reactivation of such structures over very long time scales, as evidenced by exhumed fault zones, suggests that their weakness is persistent (e.g. White et al., 1986; Butler et al., 1997; Imber et al., 1997; Holdsworth et al., 2001; Jefferies et al., 2006, in press).

Laboratory and field studies have shown that deformation in the upper, seismogenic part of the crust (upper 10-15 km) occurs predominantly by frictional processes, involving brittle fracture or faulting and frictional sliding (Byerlee, 1978; Goetze and Evans, 1979; Sibson, 1983; Scholz, 2002). The strength of rocks and pre-existing faults in this zone accordingly increases with increasing effective normal stress and thus increasing depth. Microstructural studies on naturally and experimentally deformed fault rocks have shown that as the depth of burial increases into the range 5-15 km, with concomitant temperature increase, chemically active fluids start to play a larger role in the deformation of fault gouges (Rutter and Mainprice, 1979; Rutter et al., 1986; Chester et al., 1993; Caine et al., 1996). Compaction/healing and cementation processes may be enhanced, maintaining brittle shearing strength (Karner et al., 1997; Marone, 1997; Olsen et al., 1998; Bos et al., 2000b; Bos and Spiers, 2002a; Nakatani and Scholz, 2004; Yasuhara et al., 2005). On the other hand, shear strength may be reduced, either directly by switching the internal deformation mechanism from cataclasis to one controlled by solution-transfer creep (Rutter and Mainprice, 1978, 1979; Lehner and Bataille, 1984/85; Chester and Higgs, 1992; Kanagawa et al., 2000; Wintsch and Yi, 2002; Nakatani and Scholz, 2004), or indirectly by enhancing fluid-rock reactions that form a weak reaction product (clays and phyllosilicates, Rutter et al., 1986; Wintsch et al., 1995; Imber et al., 1997; Vrolijk and van der Pluijm, 1999; Warr and Cox, 2001; Yan et al., 2001). At still greater depths and temperatures (>15 km), we know from experimental and field studies (Goetze and Evans, 1979; Hirth and Tullis, 1992; Luan and Paterson, 1992; Gleason and Tullis, 1995; Kohlstedt et al., 1995; Sleep, 1995; Küster and Stöckhert, 1999; Hirth et al., 2001; McKenzie and Jackson, 2002) that thermally activated plastic/viscous deformation processes such as dislocation creep and diffusion creep become increasingly important, and shear zones are formed that widen with depth as the stress required for deformation decreases (Sibson, 1977; Tullis and Yund, 1977; Goetze and Evans, 1979; Schmid and Handy, 1991; Luan and Paterson, 1992; Kohlstedt et al., 1995).

Steady state strength profiles such as that shown in Figure 1.1 have been widely constructed for the crust on the basis of brittle/frictional and fully plastic rock rheologies, assuming deformation at a fixed rate. These steady state strength profiles show a brittle, rate-independent upper part, where strength increases with depth, and a viscous (plastic) rate-dependent lower part, where strength decreases with depth. The brittle/friction portion is generally constructed assuming a hydrostatic increase of pore fluid pressure with depth. “Classical” strength profiles of this type have long been accepted, since they seem to account for the depth distribution of seismic activity in the apparently brittle upper 15 km of the crust (Sibson, 1983; Scholz, 2002). Also, stress levels measured in bore holes to depths of several kilometres in intraplate regions are consistent with these strength profiles (Zoback and Healy, 1992; Zoback et al., 1993; Brudy et al., 1997; Hickman et al., 1997; Townend and Zoback, 2000). This has led to widespread use of these laboratory-based strength profiles in numerical modelling studies of crustal tectonics (Govers and Wortel, 1995; Beaumont et al., 1996; Beaumont et al., 2000; Wang et al., 2005)

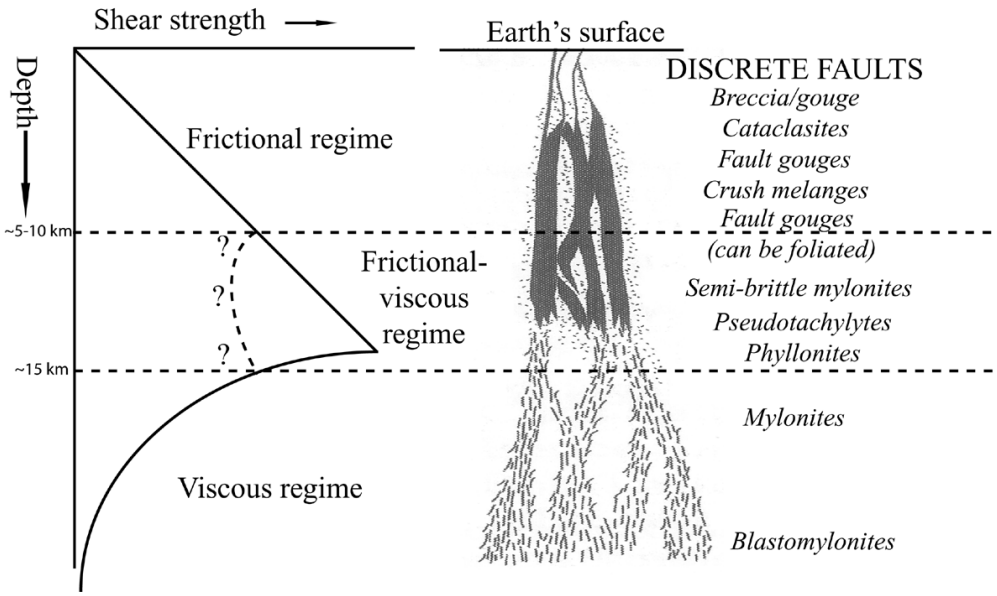

Figure 1.1.: Schematic of a classical crustal strength profile involving frictional behaviour in the upper part of the crust (Byerlee's law) and viscous flow by crystal plasticity in the lower part. Such profiles are typically drawn assuming constant strain rate and a hydrostatic gradient in fluid pressure.Also shown is a conceptual model for the way the character of fault zones vary with depth along with their associated fault rocks(after Rutter et al. 2001, see also Sibson, 1977 and Scholz, 2002). At mid-crustal depths, the classical profile is likely truncated due to the operation of fluid-rock interaction processes (dashed line).

However, it has long been speculated that classical strength profiles overestimate the strength of fault zones, especially at upper to mid-crustal (hydrothermal) depths, since they are generally based on experiments on single phase rock materials, without considering the above-mentioned effects of a chemically active fluid, i.e. effects such as solution transfer or pressure solution creep and phyllosilicate production (e.g. Rutter and Mainprice, 1979; Angevine et al., 1982; Sibson, 1983; Rutter and Brodie, 1991; Paterson, 1995; Wintsch et al., 1995; Wintsch and Yi, 2002). Moreover, the shear strains and durations achieved in most previous experiments on simulated fault rocks under hydrothermal conditions are too low to produce mature, steady state microstructures and mineral assemblages with a pervasive foliation, so that anomalously high strengths are probably obtained. These expectations regarding classical strength profiles are supported by observations that the steady state strength of the crust, as predicted using laboratory data for brittle/frictional slip, is higher than usually inferred from geophysical observations for long-lived crustal fault zones, such as the San Andreas. The strength of the San Andreas Fault forms a subject of long-standing debate (Zoback et al., 1987; Rice, 1992; Evans and Chester, 1994; Scholz, 2000; Zoback, 2000; Hardebeck and Michael, 2004). Nonetheless, there are two lines of evidence indicating that the shear strength of the San Andreas is low. First, heat flow data reveal that the fault zone is not marked by a positive thermal anomaly of the type expected if

the average fault shear stress were of the magnitude predicted using classical strength profiles (Lachenbruch and Sass, 1980; Lachenbruch and Sass, 1992). Second, measurements of principal stress directions along the San Andreas faults suggest that the angle between the greatest compressive stress direction and the fault plane far exceeds the angle expected for a high shear strength(Zoback et al., 1987; Zoback, 2000; Townend and Zoback, 2001; Townend and Zoback, 2004). Explanations offered for the inferred long-term weakness of the San Andreas fault include a) high pore fluid pressures, which would reduce the effective normal stress, b) the presence of interconnected, weak phyllosilicates, and c) fluid-rock interaction effects leading to phyllosilicate production and/or enhanced deformation by solution-transfer processes (see Sibson et al., 1975; Wu et al., 1975; Rice, 1992; Chester et al., 1993; Byerlee, 1994; Blanpied et al., 1995; Chester, 1995; Hickman et al., 1995; Kanagawa et al., 2000; Jefferies et al., 2006, in press). However, the issue is not resolved and further work is clearly needed on the effects of fluid-rock interaction to clarify its role. An effort which will help greatly is the drilling of an active part of the San Andreas fault zone in the SAFOD drilling project (Hickman and Langbein, 2002). In this project, gouge from a seismically active fault will shortly be sampled, and in situ stresses and pore fluid pressures will be measured for the first time.

1.3. Transient strength of fault zones

The steady state or long-term strength properties of faults, as expressed in terms of strength profiles, determine their resistance to large displacements accumulated over geological time scales. However, it is the short term, transient behaviour of faults that is important with respect to earthquake generation and the seismic cycle. The effects of sliding velocity on the transient behaviour of faults and fault gouges have been extensively studied in laboratory friction experiments, since these effects might be directly related to the processes operating in the seismic cycle. In order to describe these effects, Dieterich (1978) proposed the so-called rate-and-state friction or RSF law, which is written

$$\mu = \mu_0 + a \ln\left(\frac{V}{V_0}\right) + b \ln\left(\frac{V_0 \theta}{D_c}\right) \tag{1.1}$$

With reference to Figure 1.2, μ is the instantaneous friction coefficient on the fault (shear stress divided by the effective normal stress), μ_0 is a reference friction coefficient at a reference sliding velocity V_0, V is the instantaneous sliding velocity, a is a parameter that reflects the magnitude of the so-called ”direct effect”, (which is the instantaneous change in shear stress upon a change in sliding velocity), b reflects the magnitude of the “evolution effect” (which is the gradual change of shear stress after a change in velocity), θ is a (micro)physical state variable that represents the evolving internal state of the sliding surface zone, and D_c is the characteristic sliding distance over which the evolution effect takes place. Stable slip occurs when $(a-b) \geq 0$ and unstable slip will occur when $(a-b) < 0$.

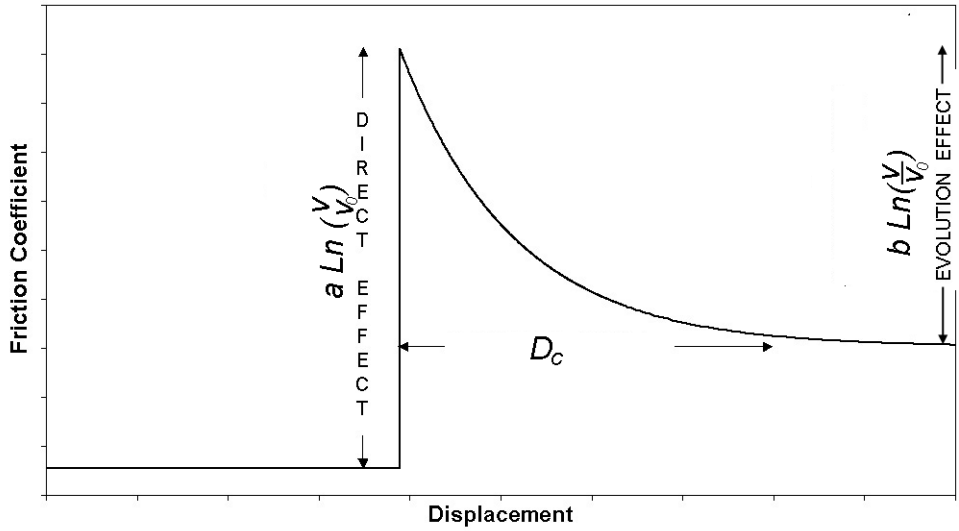

Figure 1.2: Plot showing the effect of a step in sliding velocity on the friction coefficient for a hypothetical velocity-strengthening material. D_c is the critical sliding displacement

Experiments on different geological materials have established a suite of values for the parameters appearing in the RSF equations (e.g. Dieterich, 1978, 1979; Marone et al., 1990; Kilgore et al., 1993; Beeler et al., 1994; Beeler et al., 1996; Mair and Marone, 1999), which have subsequently been used to analyse earthquake mechanics as well as other faulting phenomena such as localisation (e.g. Cao and Aki, 1986; Dieterich, 1994; Ben-Zion and Rice, 1995; Marone et al., 1995; Ben-Zion and Rice, 1997; Sleep, 1997; Marone, 1998b; Beeler et al., 2001; Scholz, 2002). In experiments, a typically has values of 0.01, b takes values of 0.01-0.05 and D_c is of the order of 10 μm.

However, in order to produce realistic RSF-based numerical models, capable of reproducing seismological data such as earthquake energy release, rupture time, displacement (area) and stress drop, the critical displacement must often be taken to be in the order of 1 m. Notably, most RSF experiments have been done under room temperature conditions and/or dry conditions. Scaling of laboratory-based RSF parameters to natural seismogenic (upper to mid-crustal) conditions is therefore done generally without much consideration of the deformation processes involved in natural fault zones or of the effects these processes may have on the values of the RSF parameters. Indeed, an experimentally verified, mechanism-based description of the role of fluid-rock interactions in determining transient behaviour is still lacking. This is despite the long-standing recognition that fluid-rock interactions, such as pressure solution, may strongly influence D_c and might be key to this aspect of modelling the seismic cycle (e.g. Sleep and Blanpied, 1994; Segall and Rice, 1995; Miller et al., 1999). As in the case of steady state fault strength, then, progress in quantifying the transient slip behaviour of faults also requires a better understanding of the role of fluid-rock interactions.

1.4. Mechanisms of fluid-rock interaction in the upper to mid crust

Fluid-rock interaction may have strong effects on both steady state and transient behaviour of fault zones, since it can lead to low stress creep and compaction, it can affect fluid pressures and it facilitates mineral reactions. Here, we summarize the main fluid-rock interaction processes known to affect rock strength via these routes.

Microstructural observations in quartzose reservoir rocks and upper to mid crustal fault rocks (see Figure 1.3) have long been interpreted to show that fluids strongly enhance compaction of such rocks by a process known as intergranular pressure solution (IPS, Rutter, 1976, 1983; Gratier and Guiguet, 1986; Tada and Siever, 1989; Stöckhert et al., 1999; Oelkers et al., 2000; Renard et al., 2000; Imber et al., 2001; Wintsch and Yi, 2002; Collettini and Holdsworth, 2004; Kenis et al., 2005). In a buried rock material, IPS compaction is a result of enhanced normal stress at grain-to-grain contacts leading to dissolution of material, diffusion of the dissolved material along the grain contacts and precipitation in the pore areas (or removal by an advecting pore fluid), thereby reducing the porosity and permeability. Under steady state conditions, any of the serial processes of dissolution, diffusion and precipitation (or advective mass removal) may control the overall compaction rate.

However, despite the fact that IPS has long been recognized and studied in laboratory compaction experiments performed on sands and other granular aggregates (Renton et al., 1969; De Boer et al., 1977; Gratier and Guiguet, 1986; Dewers and Hajash, 1995; Chester et al., 2004; Gratier et al., 2005), the reaction/diffusion kinetics and rate-controlling process of IPS in quartz rocks are still poorly known.

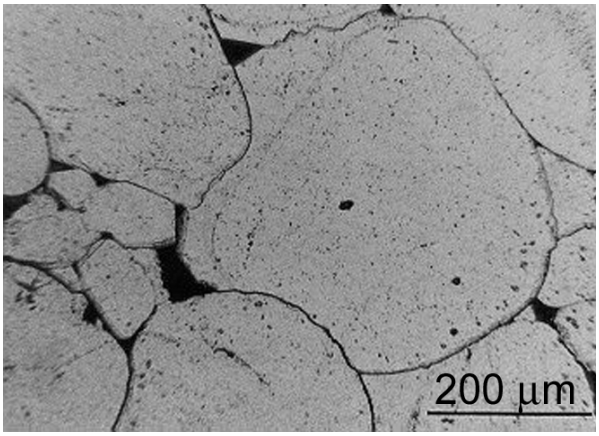

Figure 1.3: Plane polarized light image of an intergranular pressure solution microstructure in a sandstone (Bromide Sandstone Oklahoma, Barker and Kopp, 1991). Note the well-developed grain-to-grain indentation, overgrowths and newly developed crystals in the pores.

Such data are essential for modelling compaction of sedimentary reservoirs and seals, but also for modelling compaction and healing processes in fault gouges. IPS compaction has been put forward as an important fault strength recovery (fault healing) process during interseismic periods, as well as a fault sealing process whereby high pore fluid pressure may be developed, reducing effective normal stress and hence shear strength (Angevine et al., 1982; Sleep and Blanpied, 1992; Sleep, 1995; Karner et al., 1997; Olsen et al., 1998; Bos and Spiers, 2000, 2002a; Nakatani and Scholz, 2004; Yasuhara et al., 2005). Aside from IPS, strengthening of fault gouge by solution transfer may also occur through intergranular "sintering" or neck growth, without porosity reduction. This growth in grain-to-grain contact area, and hence strength, is driven by a reduction in interfacial area rather than by mechanical forces (Hickman and Evans, 1992).

Besides the effects IPS may have on compaction and the transient strength of faults, it has also been suggested as a fault creep mechanism operating at low shear stress levels (Rutter and Mainprice, 1979; Lehner and Bataille, 1984/85; Sleep and Blanpied, 1992; Paterson, 1995). The creep mechanism is envisaged as active grain boundary sliding, accommodated by diffusion of solute material through an intergranular fluid phase and precipitation of the material at low stress sites. Theoretical considerations have yielded predictions of shear stresses which are commensurate with those observed for active natural faults (Rutter and Mainprice, 1979; Paterson, 1995). However, though stress relaxation experiments show some evidence for IPS effects (Rutter and Mainprice, 1978), fault slip experiments point to IPS controlled compaction and have not demonstrated pressure solution controlled shear creep (Chester, 1994; Bos et al., 2000b; Kanagawa et al., 2000).
In addition to the above effects of IPS, microstructural observations (Bjørkum, 1996) and rock-analogue compaction experiments (NaCl + clay, Renard et al., 2001) indicate that the presence of phyllosilicates strongly enhances IPS compaction rates, whereas geochemical considerations suggest that phyllosilicates may decrease IPS compaction rates (Iler, 1973, 1979; Mullis, 1993; Dove and Rimstidt, 1994). Such effects may be important in fault rocks, which often contain high concentrations of phyllosilicates, but they are poorly understood to date.

Lastly, fluids are known to accelerate chemical reactions, especially the breakdown reaction of K-feldspar. The replacement of strong minerals by weak phyllosilicates or clays may be an important weakening mechanism in controlling long term fault strength (Wintsch et al., 1994; Wintsch et al., 1995; Warr and Cox, 2001; Yan et al., 2001). This may be particularly effective when the reaction products form a connected phyllosilicate foliation, providing a persistent weak site of localisation (Wintsch et al., 1995; Warr and Cox, 2001). At the same time, the presence of a phyllosilicate or clay foliation may act as an inhibitor for healing effects by solution transfer, as the presence of phyllosilicates and clays on grain boundaries inhibits neck growth (e.g. Hickman and Evans, 1995; Bos and Spiers, 2000). Thus phyllosilicate production and content can be expected to significantly influence transient fault strength and healing behaviour too.

1.5. Recent experiments on simulated faults: progress and outstanding problems

Over the last three decades, numerous experimental studies have addressed the effects of fluids on the steady state and transient sliding behaviour of simulated quartz and granitic fault gouges, and bare fault surfaces, with the aim of better understanding the effects of fluid-rock interaction on mechanical behaviour in the seismogenic zone (e.g. Blanpied et al., 1991; Chester and Higgs, 1992; Chester, 1994; Cox, 1994; Tullis, 1994; Blanpied et al., 1995; Karner et al., 1997; Kanagawa et al., 2000; Nakatani and Scholz, 2004; Yasuhara et al., 2005). All of these studies have demonstrated important effects of fluids on sliding behaviour and a considerable body of evidence exists indicating that the steady state frictional strength of simulated fault gouges and fault surfaces tends to decrease with increasing temperature and decreasing strain rate, when fluids are present (Chester, 1994; Cox, 1994; Kanagawa et al., 2000).

Chemically active fluids have also been shown to influence transient effects (Chester and Higgs, 1992; Karner et al., 1997; Olsen et al., 1998; Nakatani and Scholz, 2004). Slide-hold-slide experiments have demonstrated a strong increase in compaction/healing rates of quartz and granitic fault gouge in the presence of fluids. More specifically, healing rates in quartz and granitic fault gouges under hydrothermal conditions have been demonstrated to be at least one order of magnitude higher than under dry conditions (Karner et al., 1997; Olsen et al., 1998; Nakatani and Scholz, 2004; Yasuhara et al., 2005).

The above effects of fluids have all been loosely attributed to fluid-rock interaction effects such as IPS and secondary mineral production (Olsen et al., 1998; Yasuhara et al., 2005). However, systematic data have proven hard to obtain. In particular, the effects of sliding velocity, grain size, fault gouge thickness and shear strain on the sliding and compaction/dilatation behaviour of fault gouges under hydrothermal conditions (i.e. in the presence of a chemically active fluid) lack systematic study. This is mainly because of the long time scales and technical limitations associated with performing high strain fault shear experiments under high temperatures and pressures and in the presence of a fluid. Notably the total amount of shear strain (γ) achieved in previous experimental studies is relatively low ($\gamma < 5$), so that a true steady state or mature fault rock microstructure, and hence mechanical behaviour, are probably not achieved. Especially the effects of phyllosilicate foliation development and cataclastic grain size reduction, in combination with solution-transfer effects, are still unknown.

The principal experimental techniques used for simulated fault experiments are saw-cut, double-direct shear and rotary shear experiments (e.g. Marone et al., 1990; Marone, 1998a; Bos et al., 2000a; Bos et al., 2000b; Kanagawa et al., 2000; Karner and Marone, 2001). The conventional saw-cut and double-direct shear experimental set-ups allow only rather low shear strains to be reached ($\gamma < 10$). In contrast, the rotary shear set-up is suitable for reaching very high shear strains (shear strains of >1000 have been reached, see Bos and

Spiers, 2001), but it is difficult to implement in high pressure and temperature experiments. For this reason, several authors (e.g. Chester and Logan, 1990; Bauer et al., 2000a; Bauer et al., 2000b; Bos et al., 2000a, b; Bos and Spiers, 2000, 2001, 2002a) have performed experiments on rock-analogue materials which exhibit, at room conditions, the microphysical processes occurring in real rock materials at hydrothermal conditions. Halite plus phyllosilicate mixtures offer a useful fault rock analogue, because cataclasis, IPS and foliation development occur at measurable rates at room temperature. Moreover, from previous work on the compaction behaviour of halite we know the kinetics of the IPS process relatively well (Spiers and Schutjens, 1990; Spiers et al., 1990).

Recently, Bos and coworkers (2000a; 2000; 2001; 2002b) showed that the addition of phyllosilicates exerts a strong influence on the sliding behaviour of brine-flooded halite fault gouges deformed, in a rotary shear apparatus, to strains of typically 30-100. In their initial experiments, Bos and coworkers studied the effect of solution-transfer processes on steady state fault strength in simulated fault gouges of pure halite. They found that the operation of solution transfer processes did not significantly weaken their samples in comparison to "normal" dry friction (i.e. friction coefficients of ~0.8). Indeed, pure halite samples were found to exhibit pure frictional/brittle behaviour, which strengthened slightly with increasing displacement as a result of ongoing compaction by IPS. By contrast, mixtures of halite and kaolinite were found to significantly weaken with increasing shear displacement and decreasing sliding velocity. The microstructures of the mixed gouges closely resembled natural mylonitic microstructures, with the kaolinite grains forming an anastomosing foliation separating elongated halite porphyroclasts. Bos and coworkers provided convincing evidence that deformation occurred by a process of frictional sliding of the halite grains over the kaolinite foliation, with viscous accommodation by pressure solution and they accordingly termed this deformation process "frictional-viscous flow". A microphysical model was developed for this process (Bos and Spiers, 2002b). Application of this model to quartz/mica gouge under natural crustal conditions predicts significant weakening with respect to the classical strength profile, with a reduction of mid-crustal strengths of a factor of 2-4.5.

In addition, Bos and coworkers performed a number of so-called slide-hold-slide tests in the rotary shear configuration to study fault healing (Bos and Spiers, 2000, 2002a). In slide-hold-slide tests, a simulated fault gouge is sheared through a certain amount of displacement, after which sliding is stopped for a pre-defined period of time, and then started again to determine the extent of time-dependent strength recovery. Bos and coworkers found that foliated gouges of halite-kaolinite mixtures do not significantly heal, whereas pure halite and non-foliated halite-kaolinite gouges heal rapidly. This large difference in healing was explained by the coating of halite grains by the kaolinite foliation, inhibiting contact cementation. Clearly, if similar processes operate in crustal fault gouges under hydrothermal conditions, they will lead to a distinctly different sliding and healing behaviour of fault gouges than observed in low strain shear experiments with low or no phyllosilicate content.

While experiments on halite/kaolinite gouge have demonstrated important effects of foliation development and IPS, a number of aspects of the behaviour of such systems, and their relevance to real fault gouges, remain unclear. Several aspects of the microphysical model of Bos and Spiers (2002b) have not been tested or are physically unrealistic. For example, the grain size of the kaolinite used in their experiment was much finer than the halite phase, which is not comparable to the microstructure of natural quartz/phyllosilicate fault rocks (Imber et al., 1997). Also, the range of sliding velocities that Bos and coworkers explored, does not cover the full range of sliding behaviour predicted by their model. Finally, the microphysical model does not account for the possibility of viscous/plastic (internal) deformation of the phyllosilicates. Last but not least, their model has not been tested against experiments on realistic fault gouge materials (e.g. quartz-phyllosilicate mixtures) under hydrothermal conditions

In summary of previous experimental work on simulated faults and analogue systems, it is evident that fluids and phyllosilicates do have significant effects on the steady state and transient sliding behaviour of fault rocks under brittle-ductile transitional conditions where fluid-rock interaction is important. However, the effects of foliation development, grain size reduction and solution-transfer processes have not yet been fully quantified in analogue systems, nor have they been systematically studied in real rock materials under hydrothermal conditions. Moreover, the kinetics and rate-controlling process of IPS, as well as the effects of phyllosilicates on IPS rates and compaction/healing in real rock and fault gouge materials, are still relatively unknown. In short, it remains to be studied what the kinetics and rate-controlling process of IPS in quartz aggregates are, what the effect of phyllosilicates on IPS is, to what extent the Bos and Spiers model works for analogue systems tested using a wider range of velocities and phyllosilicate grain size, and whether the processes occurring in analogue fault gouge materials (IPS, cataclasis, foliation development and healing) also occur in real rock materials.

1.6. Present aims

In view of the above-mentioned research question, I now define the following aims for the present research:

1. Experimental determination and characterization of the rate-controlling mechanism of compaction creep by intergranular pressure solution in granular quartz sands under hydrothermal conditions, through comparison with appropriate microphysical models for compaction by IPS. This aim is relevant to studies of both sedimentary diagenesis and fault gouge compaction.
2. Experimental investigation of the effect of muscovite on compaction creep rates by intergranular pressure solution in quartz sands.
3. Determination of the steady state shearing and healing behaviour of halite-muscovite fault gouge analogue materials, under brittle-ductile transitional

conditions favouring pressure solution and foliation development, and using coarser phyllosilicate grain size and a wider range of sliding velocities then employed previously.

4. Application of the results to test, refine and renew microphysical models for steady state deformation of phyllosilicate-bearing fault/rock, and to the assess the implications for the behaviour of natural faults.
5. Experimental investigation of the sliding behaviour of simulated faults containing quartz gouge material, at high shear strains under hydrothermal conditions.

To adress aim 5, a new hydrothermal rotary shear apparatus was designed and built by the HPT laboratory team at Utrecht.

Chapter 2

COMPACTION CREEP OF QUARTZ SAND AT 400-600 ºC: EXPERIMENTAL EVIDENCE FOR DISSOLUTION-CONTROLLED PRESSURE SOLUTION

This chapter was published as: Niemeijer, A.R., Spiers, C.J. and Bos, B., 2002. Compaction creep of quartz sand at 400-600 °C: experimental evidence for dissolution-controlled pressure solution. Earth and Planetary Science Letters, 195(3-4): 261-275. Reprinted with permission from Elsevier.

Abstract

Intergranular pressure solution (IPS) is an important compaction and deformation mechanism in quartzose rocks, but the kinetics and rate-controlling process remain unclear. The aim of the present study is to test microphysical model for compaction creep by IPS against isostatic hot pressing experiments performed on quartz sand under conditions expected to favour pressure solution (confining pressure 300 MPA, pore water pressure 150-250 MPa, temperatures 400-600 ºC). Microstructural observations revealed widespread intergranular indentation features and confirmed that intergranular pressure solution was indeed the dominant deformation mechanism under the chosen conditions. For porosities down to 15%, the mechanical data agree satisfactorily with a microphysical model incorporating a previously determined kinetic law for dissolution of loose granular quartz, suggesting that the rate-limiting mechanism of IPS was dissolution. The model also predicts IPS rates within one order of magnitude of those measured in previous experiments at 150-300 ºC, and thus seems robust enough to model sandstone compaction in nature. Such applications may not be straightforward, however, as the present evidence for dissolution control implies that compositional variability of natural pore fluids may strongly influence IPS rates in sandstones.

2.1. Introduction

Despite its importance as a compaction, deformation and fault healing mechanism in the upper crust (Angevine et al., 1982; Rutter, 1983; Tada and Siever, 1989; Hickman and Evans, 1992), the rate-controlling mechanism and kinetics of intergranular pressure solution (IPS) in quartz are poorly constrained, mainly because of the extreme slowness of the process under laboratory conditions (Rutter, 1976, 1983). Nonetheless, microstructural evidence for the operation of IPS has been obtained in a number of experimental studies, as have crude rate data. The earliest such studies involved uniaxial (one-dimensional) compaction experiments on wet quartz sand at temperatures of 270-550 ºC, conducted by Renton et al. (1969) and de Boer et al. (1977). These authors demonstrated slow compaction creep that accelerated towards higher temperature, higher effective pressure and finer grain size, though they did not systematically investigate these effects. From intergranular indentations they inferred that IPS was the dominant compaction mechanism, accompanied by grain cataclasis at the lower temperatures.

In densification experiments performed at 360 ºC, using an effective pressure of ~50 MPa and a variety of pore fluid compositions (pure water vs. 0.1-1.0 molar NaOH solution), Gratier and Guiguet (1986) obtained convincing microstructural evidence for deformation by IPS. By inserting dissolution kinetics estimates for quartz into a theoretical model for IPS, they inferred that diffusion must have been rate controlling in their experiments. Schutjens (1991) performed more systematic 1-D compaction creep experiments on wet quartz sand (40-100 μm) at temperatures of 250-350 ºC, using confining pressure of 20-30 MPa and an alkaline pore fluid ($Na_2SiO_3 \cdot 5H20$ added to achieve silica saturation) at a pressure of ~15 MPa. He too found grain indentations and contact truncations evidencing IPS, with grain cracking at lower temperatures. However, on the basis of the apparent activation energy for creep ($\Delta H \approx 60$-75 kJ/mol), Schutjens suggested that the rate-limiting IPS process was dissolution at grain contacts. In a single isostatic compaction experiment on fine-grained (4 μm) granular quartz, performed at a confining pressure of 300 MPa and a pore pressure of 200 MPa, but at much higher temperatures (927 ºC), Cox and Paterson (1991) obtained compaction creep strain rates as high as 10^{-5}-10^{-6} s^{-1}. From grain contact microstructures, they concluded that this occurred by IPS, but did not investigate the effects of varying stress, temperature and grain size and did not consider the rate-controlling process. More recently, Dewers and Hajash (1995) reported long-term isostatic compaction experiments performed on aeolian quartz sand (grain size 90-350 μm) at 150-200 ºC at a confining pressure of ~ 70 MPa and pore fluid (pure water) pressure of ~ 35 MPa (effective pressure of ~ 35 MPa). Though the strains achieved were small (< 10%), on the basis of mechanical, microstructural and chemical data, they inferred that pressure solution was again the dominant compaction mechanism, accompanied by time-dependent cataclasis, particularly at lower temperatures. From the apparent activation energy for creep ($\Delta H \approx 73$ kJ/mol), and their finding that the pore fluid silica concentration increased with applied stress, Dewers and Hajash suggested that interface kinetics may have controlled IPS.

From these studies, it is clear that while IPS occurs at detectable rates in experiments on quartz at temperatures above ~ 150 ºC, systematic data on the effects of temperature, effective pressure and grain size on the rate of the process are sparse and the kinetics and rate-controlling mechanisms remain poorly understood. In this paper, we report isostatic compaction experiments performed on quartz sand at 400-600 ºC, a confining pressure of 300 MPa, pore fluid pressures of 150-250 MPa and using grain sizes of 30-100 μm, in an attempt to assess better the effect of these variables on volumetric strain rate by IPS. Our choice of stress and temperature conditions was expected to yield IPS strain rates which would be measurable on a time scale of 1-5 days and was based on extrapolations of previous data. Our study extends the previous 1-D compaction experiments of Schutjens (1991) to higher temperatures and effective pressures, and to higher volumetric strains or lower porosities (down to ~10%). We chose the isostatic configuration rather than 1-D, because this rules out any effects of vessel wall friction or shear stress. The results obtained are compared with non-linear theoretical models for both reaction- and diffusion-controlled

IPS in an attempt to identify the rate-controlling process and constrain better what this may be in nature.

2.2. Theoretical background

In a chemically closed system (no addition or removal of solid mass via long range transport in the pore fluid phase), compaction of fluid-saturated granular aggregate by intergranular pressure solution (IPS) involves dissolution of solid material at stressed grain-to-grain contacts, diffusion of this material through the intergranular fluid into the open pores, followed by precipitation on free pore walls. The process is driven by differences in effective normal stress, hence normal component of solid chemical potential, between grain contacts and pore walls (Rutter, 1983; Lehner, 1990; Lehner, 1995). If the pore fluid pressure acting on the free pore walls is P_f, the thermodynamic driving force (chemical potential difference) for transport between source (grain boundary) and sink (pore wall) sites is given:

$$\Delta\mu = \mu_{gb} - \mu_{pore} = (\sigma_n - P_f)\,\Omega_s \tag{2.1}$$

where μ_{gb} is the average chemical potential of the solid within a representative element of the grain contact, μ_{pore} is the chemical potential of the solid at pore wall sites, σ_n is the normal stress acting across the grain boundary element, P_f is the pore fluid pressure and Ω_s is the molar volume of the solid (Rutter, 1976, 1983; Tada and Siever, 1989). Under steady state conditions, this thermodynamic driving force drives the three serial processes of dissolution, diffusion and precipitation, such that the slowest kinetic step controls the overall deformation rate of the aggregate.

Making use of the relation between the chemical potential (μ) of a dissolved solid and its concentration (C) in an ideal solution ($\mu = \mu_0 + RT \ln C/C_0$), it is easily shown that the potential drop ($\Delta\mu_n$) between source and sink sites corresponds to a difference in solubility of the solid (ΔC) such that:

$$\Delta\mu_n = RT \ln\left(\frac{C_p + \Delta C}{C_p}\right) \approx RT\frac{\Delta C}{C_0} \tag{2.2}$$

Here R is the gas constant, T is absolute temperature, ΔC is the enhancement of the solubility of the solid within a stressed grain contact element relative to free pore wall sites, and C_p is the solubility of the solid at free pore wall sits. Neglecting minor deformation at the free grain surfaces, C_p will be approximately equal to the solubility (C_0) of the solid grain under purely hydrostatic reference conditions (pressure in solid and fluid = P_f).

Grain boundary diffusional IPS requires a grain boundary structure that allows fluid access despite high intergranular normal stresses. Two grain boundary models are well known in the literature, namely the adsorbed fluid film model (Rutter, 1976; Renard et al., 1997) and the island-channel model (Raj, 1982; Spiers and Schutjens, 1990). For the

development of a rate theory of IPS it is not important which grain boundary structure exists during the process, provided that the amplitude of any roughness and associated fluctuations in the Helmholtz free energy of the solid are small compared with grain contact length. Numerous authors (Rutter, 1976; Raj, 1982; Lehner, 1990; Spiers and Schutjens, 1990; Lehner, 1995; Shimizu, 1995) have published theoretically derived rate equations for IPS. Assuming that all of the driving force, $\Delta\mu_n$, is taken up in driving the rate-controlling processes of either dissolution at grain boundaries, diffusion within the grain boundary or precipitation on the pore walls, all of these models lead to essentially identical results. For compaction creep of a regular pack of spherical grains, this can be written (De Meer and Spiers, 1997):

$$\dot{\varepsilon}_x = A_x \cdot Z_x(T) \cdot \left[B(\phi,\phi_0) \cdot P_e \cdot \Omega/(R \cdot T) \right]^n f_x(\phi,\phi_0)/d^p \qquad (2.3)$$

Here $\dot{\varepsilon}$ is the volumetric strain rate (s^{-1}), x denotes dissolution, diffusion or precipitation control (x= s, d, p), the A_x are geometric constants, $Z_x(T)$ is a temperature-dependent kinetic coefficient for the relevant rate-controlling process, P_c is the applied effective pressure, B (ϕ/ϕ_0) is a measure of the stress concentration at grain contacts due to aggregate structure, d is grain diameter and the $f_x(\phi/\phi_0)$ represent mechanism-specific functions of the ratio of instantaneous aggregate porosity (ϕ, %) to starting porosity (ϕ_0, %). The powers p and n take values of 3 and 1 respectively, when grain boundary diffusion is the rate-controlling process of IPS. When dissolution or precipitation is rate controlling, p is 1 and n reflects the order of the interface velocity vs. driving force relation (typically n=1 for a rough interface, or 2 for spiral growth/dissolution; Nielsen, 1986). Note that the functions $B(\phi/\phi_0)$ and $f_x(\phi/\phi_0)$ respectively describe the progressive changes in grain contact area, and in transport path length and pore surface area, during ongoing compaction. For an assumed starting configuration of equi-dimensional spherical grains in a simple cubic (SC), a face centered cubic (FCC) or a body centered cubic (BCC) packing, B, f_x and thence the strain rate can be expressed as exact functions of ϕ and ϕ_0 as indicated in equation 2.3. However, computations of compaction by IPS, assuming an SC, FCC, BCC or random packing, predict B, f_x and strain rate vs. ϕ/ϕ_0 curves that approach single master curves at $\phi > 5\%$. For the purpose of comparing experimental trends with IPS theory, the quantity ϕ/ϕ_0 thus offers a useful way of measuring porosity reduction, since it, in theory, reduces the effect of varying initial porosity and packing on strain rate under otherwise fixed conditions.

In deriving equation 2.2. and hence 2.3, the approximation is made that $\ln(1+\Delta C/C_p) \approx \Delta C/C_p$, following the now almost standard assumption made by Rutter (1976) that $\Delta C/C_p \ll 1$, i.e. assuming that the solubility enhancement at stressed grain boundaries is small. It is this approximation which leads to the linear relation between stress and strain rate widely considered characteristic of IPS. However, several workers have recently argued that the approximation is not valid for high grain contact stresses (small contact area, high B-values) and materials with large molar volume (Dewers and Hajash, 1995, Rutter,

personal communication). Indeed, order of magnitude estimates of the term ($B\sigma_e\Omega/RT$), for a SC pack, taking $B \geq 5$, show that the approximation is significantly in error for the conditions encountered in compaction tests on granular quartz. Following the analysis employed by previous workers (Rutter, 1976; Raj, 1982; Lehner, 1990; Spiers and Schutjens, 1990; Lehner, 1995; Shimizu, 1995) to obtain equation 2.3, but omitting the approximation $\Delta C/C_p \ll 1$, produces the result:

$$\dot{\varepsilon}_x = A_x \cdot Z_x(T)(\exp(\frac{B(\phi,\phi_0)\cdot P_e \cdot \Omega}{R \cdot T}) - 1) \cdot f_x(\phi,\phi_0)/d^p \qquad (2.4)$$

for the case that n is 1, i.e. for the case of diffusion-controlled IPS or of linear reaction-controlled IPS. A similar exponential form for the strain rate vs stress relation for compaction is also given by Dewers and Hajash (1995).

2.3. Experimental method

Our experiments consisted of isostatic compaction or hot pressing (HIPing) experiments carried out on wet quartz sand. The aim was to test the applicability of the above exponential models for IPS (equation 2.4) by systematically varying effective pressure, temperature and grain size. The temperature range used was 400-600 ºC, the effective pressure 50-150 MPa, the confining pressure 300 MPa and the pore fluid pressure 150-250 MPa. The experiments were carried out using the same starting material as that used by Schutjens (1991), namely milled and HF-rinsed quartz sand from the Miocene 'Bolderiaan' formation, Belgium. We sieved this material into grain size fractions with initial grain sizes (d_i) of 28-37 μm, 45-75 μm and 100-125 μm.

2.3.1. Apparatus and Procedure

Figure 2.1 shows a schematic diagram of the apparatus used. It consists of a cold seal 'Tuttle bomb' pressurized with argon, plus an internal sample/capsule assembly linked to a pore fluid system, consisting of a vacuum pump, a reservoir and a volumetric pump. The pore fluid pressure was measured with a Bourdon-type pressure gauge (resolution ~ 1 MPa) in our earlier tests and later using a pressure transducer (resolution ~ 0.2 MPa). The argon confining pressure was measured using a Bourdon gauge. The temperature of the sample was measured indirectly using a K-type thermocouple embedded in the bomb wall, with an error of ~ 2 ºC estimated from calibration runs.

In initiating each experiment, ~ 2 g. of sand was loaded into the annealed copper capsule assembly via the initial open 'top cup' end (see enlargement Figure 2.1). The capsule was then sealed by pressing and welding in the copper 'top cup' (Figure 2.1), producing a sample porosity of 45-50 %. The sample assembly was subsequently loaded into the Tuttle bomb and evacuated and flooded with water from the pore fluid reservoir. Each sample was the cold isostatically pressed (CIPed) at a confining pressure 300 MPa under drained conditions for 30 minutes. This was done with the aim of producing a reproducible starting porosity and microstructure for the hot pressing stage (cf. Spiers and Brzesowsky, 1993; De Meer and Spiers, 1997), and to minimize strain by grain rearrangement and contact cataclasis during HIPing (conducted at only 50-150 MPa). The confining pressure was subsequently reduced to ~ 140 MPa (depending on the desired test temperature) and the pore fluid pressure raised to ~ 135 MPa using the manually operated volumometer pump. The sample was then heated at ~ 15 ºC per minute. During heating, the effective pressure was maintained as low as possibly and was always < 10 MPa. Note that any surface damage introduced into the grains by CIPing would be more or less entirely removed during heating, since significant surface dissolution is required to saturate the pore fluid with silica under the chosen test conditions. After attaining thermal equilibrium at the desired test temperature and confining pressure (300 MPa), the required effective pressure was applied and maintained by extracting fluid from the sample using the volumometer. The confining and pore fluid pressures were subsequently kept within ± 5 MPa of the desired values. The minimum measurable fluid volume increment was ~ 2 μl. This corresponds to an absolute resolution in volumetric strain at room temperature of ~ 0.02 %.

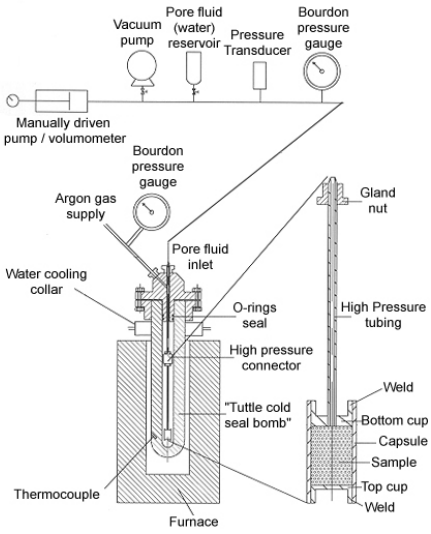

Figure 2.1. Schematic diagram of the experimental apparatus with an enlargement showing the capsule/sample set-up.

Experiments were terminated when the pore volume loss was no longer detectable via changes in pore fluid pressure. At this stage, the bomb was quenched using compressed air, at an average cooling rate of ~ 30 ºC per minute. The indurated sample was then removed from the apparatus and capsule, and dried in an oven at 60 ºC for 24 hours. The final porosity (ϕ_f) was measured by wrapping it in ultra-thin plastic film and determining its volume (V_f) using the Archimedes method. The samples were finally impregnated with epoxy resin and sections were cut for optical and SEM study.

2.3.2. Data acquisition and processing

As indicated above, pore volume loss during the experiments was determined incrementally by measuring the volume of fluid extracted from the sample to maintain constant pore pressure. The measurements were accurately corrected for density changes associated with the cooling of the pore fluid during extraction, using appropriate P-V-T equations for water (Burnham et al., 1969). The 'starting porosity' (ϕ_0) of the sample, i.e. before HIPing at the test temperature, was calculated by adding the total amount of fluid expelled from the sample during HIPing to the final pore volume (ϕ_f, V_f) of the sample. The error introduced here, through the difference in the pore and sample volumes measured at room temperature and pressure compared to the post-HIPing volumes at test condition, can be estimated using bulk modulus values for sandstone (~ 2.5-7.5 × 10^{11} Pa, Birch, 1966) and the volumetric thermal expansion coefficient of quartz (~ 4-5 × 10^{-5} K^{-1}, Skinner, 1966), and was found to be negligible. However, measurement of final porosities was problematic, since it was difficult to wrap the plastic film precisely around the sometimes irregular samples. Final porosity measurements were therefore repeated 10 times to obtain an average value. The resulting absolute standard error was around 0.5 %. Taking all errors sources into account, we estimate that the overall relative standard error in volume measurements was approximately 5%, implying an absolute standard error in the porosity measurements of less than 0.5 %. Volumetric strain rates were calculated from our volume/porosity vs time data using the two-point central difference method. Because considerable grain breakage was demonstrated during the CIPing stage of each test, the arithmetic mean grain size (d_f) of all samples was determined after testing by applying the linear intercept method to both reflected light and SEM backscatter images (Han and Kim, 1998). We have used this final mean grain size d_f in the analysis of our results.

2.3.3. Dry control runs

Control HIPing experiments on 'dry' sand fractions were performed in the same apparatus as the wet tests, but using fully sealed capsules with no added water (pore fluid system not connected). The 'dry' samples were first CIPed at 300 MPa for 30 minutes and their porosity determined at atmospheric pressure using the Archimedes method. The samples were then HIPed at 500 ºC and pore volume loss was measured periodically by removing the capsule from the bomb and re-determining its total (current) volume.

2.4. Results

2.4.1. Mechanical data

The complete set of experiments along with our data on the pre-HIPing or 'starting porosities' (ϕ_0), final porosities (ϕ_f), final grain sizes and total strains achieved are listed in Table 2.1. CIPing of the wet samples led to compaction from the initial porosity of 45-50% to ~30% (see CIPed only sample D9, Table 2.1). The HIPing curves obtained for all dry and wet samples are presented in Figures 2.2a-d, in the form of ϕ/ϕ_0 vs time plots. Normalized porosity, ϕ/ϕ_0 is used following the reasoning, given in our explanation of equations 2.3 and 2.4, that it forms a useful single measure of porosity when ϕ_0 is not constant. Figure 2.2a demonstrates time-dependent compaction in the 'dry' HIPed samples plus increased compaction with increasing confining pressure. However, the rates of dry compaction are very slow.

The starting porosity ϕ_0 of the wet samples (i.e. porosity before HIPing) varied from 24 to 31 % (Table 2.1). These variations are probably the result of different heating times, effective pressure differences during heating and different sieved grain size (CPf8 and CPf9). HIPing of the wet samples led to much more rapid compaction than seen in the 'dry' samples, producing volumetric strains up to 24% and porosities as low as ~ 10% after only 1-2 days (Table 2.1 and Figures 2.2b-d). Figure 2.2b shows the compaction curves for wet samples HIPed at different effective pressures. Porosity reduction clearly increases with increasing effective pressure. Figures 2.2c and 2.2d demonstrate that porosity reduction also accelerates with increasing temperature and with decreasing final grain size (at least for the early stage of compaction). Figure 2.3 shows typical strain rate vs. ϕ/ϕ_0 data for wet HIPed samples CPf3, 4 and 5. Note the near linear trends in the region $\phi/\phi_0 > 0.5$-0.6 ($\phi > 15\%$). Data for the dry HIPed sample D17 are added for comparison and demonstrate much slower creep rates (~ 10 times). Such plots were used (by interpolation/extrapolation of the best fits) to construct graphs showing the dependence of strain rate ($\dot{\varepsilon}$) in the wet HIPed samples on effective pressure (P_e), temperature (T) and grain size (d_f) at constant normalized porosity (ϕ/ϕ_0) – see Figures 2.4a-c. The slopes of the best-fit trends (dashed lines) seen in the log-log plot of Figure 2.4a (3.35-3.58) imply that the strain rate during HIPing is roughly proportional to the effective pressure raised to the power 3.5. Similarly, the Arrhenius fits of Figure 2.4b yield slopes in the range –65 to –85, implying an apparent activation energy for creep of 75 ± 10 kJ/ml. The best fits seen in Figure 2.4c show the strain rate is relatively insensitive to grain size, decreasing with d_f raised to powers in the range -0.9 ± 0.5.

The complete data set for the region $\phi/\phi_0 > \sim 0.55$ has been analyzed using multiple linear regression, assuming a power law dependence of strain rate on P_e and d_f and an exponential dependence on 1/RT and ϕ/ϕ_0. The results are shown in Table 2.2., along with the mean fit

parameters obtained for the individual fits shown in Figures 2.4a-c. Note that the two sets of fit parameter are mostly very similar.

Table 2.1 List of experiments performed showing initial (pre-HIPing) porosities (ϕ_0), final porosities (ϕ_f), sieved grain sizes (d_i) final grain sizes (d_f) as determined by image analysis (linear intercept method) after the

Sample number	T (°C)	d_i (μm)	d_f (μm)	P_c (MPa)	P_f (MPa)	P_e (MPa)	ϕ_0 (%)	ϕ_f (%)	Total strain (%)
D9	20	45–75	27.9 ± 19.3	300	~0.1	~300	30.31[a]	30.31	–
D15	500	45–75	10.2 ± 9.5	300	'dry'	300	29.96[a]	15.24	16.64
D17	500	45–75	14.9 ± 12.8	60	'dry'	60	27.17[a]	19.65	9.06
CPf3	500	45–75	47.1 ± 23.3	300	200	100	27.31[b]	12.71	16.70
CPf4	500	45–75	42.9 ± 24.9	300	150	150	29.39[b]	10.51	20.78
CPf5	500	45–75	40.5 ± 23.3	300	250	50	26.12[b]	16.60	11.35
CPf6	400	45–75	40.9 ± 25.0	300	200	100	25.14[b]	15.36	10.99
CPf7	600	45–75	43.2 ± 22.4	300	200	100	31.38[b]	9.70	23.86
CPf8[c]	500	28–35	11.7 ± 7.2	300	200	100	31.08[b]	14.65	19.21
CPf9	500	100–125	85.9 ± 43.9	300	200	100	24.51[b]	10.32	15.72

T denotes test temperature, P_c confining pressure, P_f pore fluid pressure and P_e the applied effective pressure. `Dry' means no water added.
a Starting or pre-HIPing porosity measured under atmospheric conditions, i.e. after CIPing.
b Starting or pre-HIPing porosity calculated for loaded conditions from the final porosity and porosity change determined during HIPing.
c Fluid pressure measured with high pressure transducer.

Table 2.2. Coefficient and intercept parameter values determined by multiple linear regression fitting to the data shown in Figure 4 and by averaging the individual linear regression fits shown in Figure 4.

	Multiple Linear Regression		*Individual LinearRegression*	
Term	**Coefficient**	**Standard error**	**Coefficient**	**Standard error**
ln(ε)	-	0.4432	-	0.5399
intercept	-70.3994	3.4753	-79.1387	-
ln(σ)	3.0910	0.1792	3.3532	-
ln(grain size)	-0.5849	0.0814	0.9948	-
1000/RT	-77.5655	4.3330	-81.4287	-
ln(10^ϕ/ϕ$_0$)	5.0650	0.1717	5.2596	-

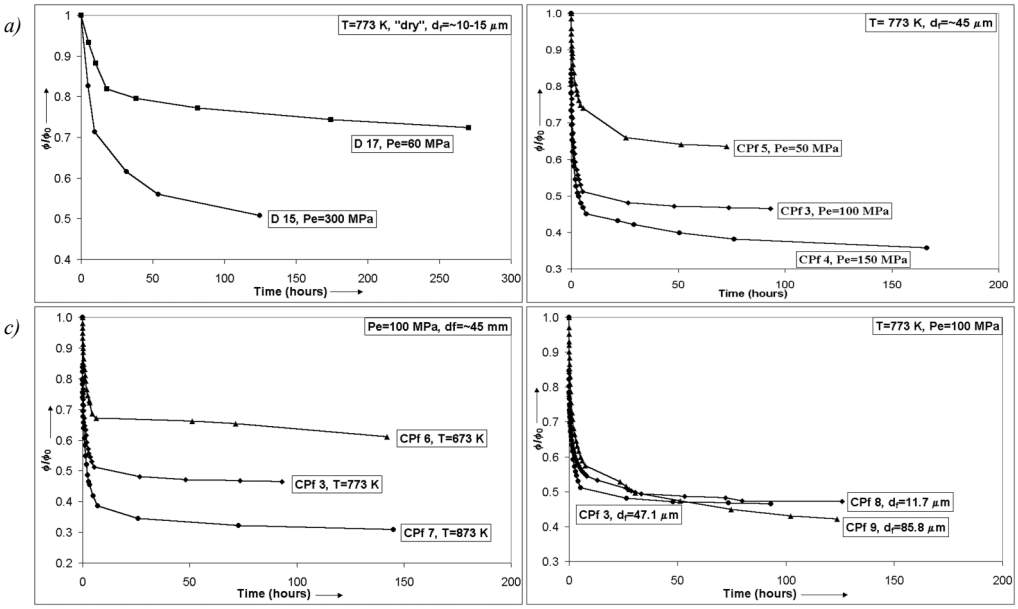

Figure 2.2. Compaction creep curve in the form of ϕ/ϕ_0 vs. time plots of (a) Dry compacted samples.(b), (c) and (d) Wet compacted samples showing the influence of effective pressure, temperature and grain size, respectively.

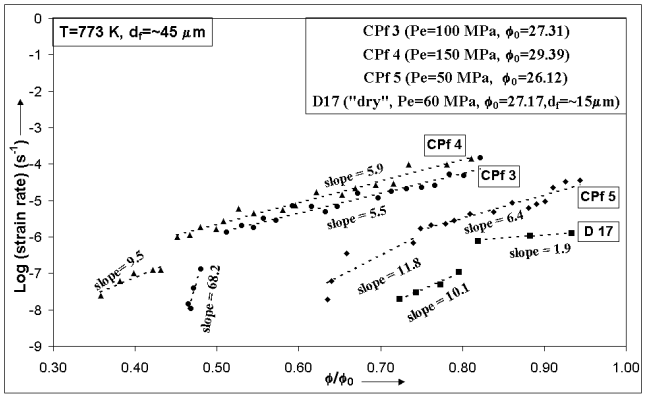

Figure 2.3: Log (strain rate) vs. ϕ/ϕ_0 plots with linear best fits for "dry" sample D17 and wet samples CPf 3, CPf 4, and CPf 5 (varying effective pressures).

a)

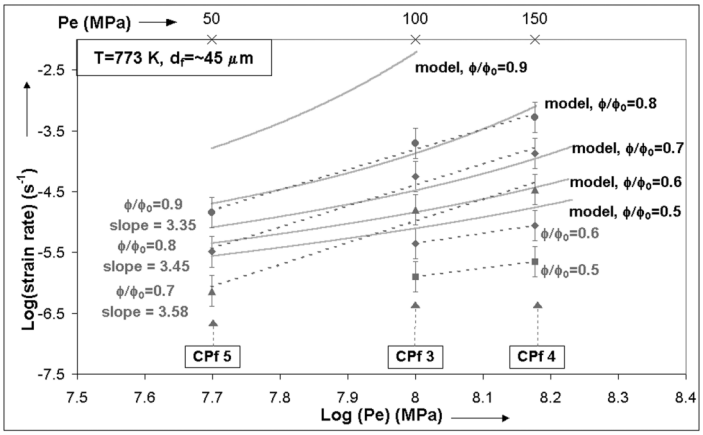

b)

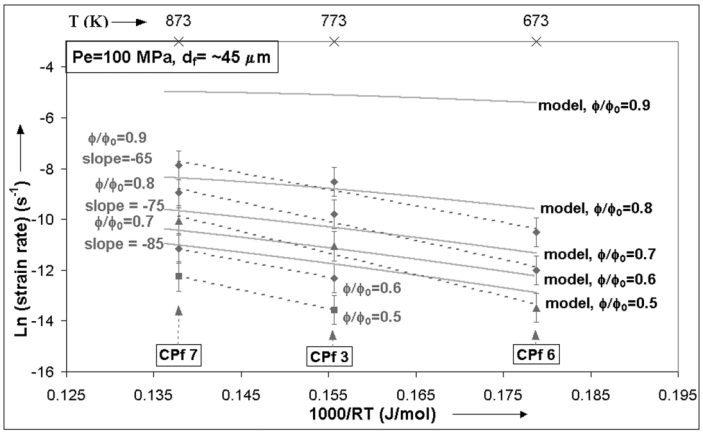

c)

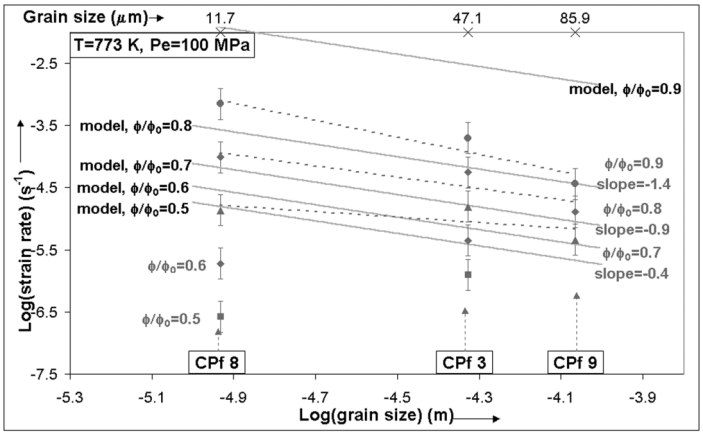

Figure 2.4: Plots showing effects of (a) effective pressure, (b) temperature and (c) grain size on experimentally determined compaction strain rates. Data sets represent experimental values obtained for fixed ϕ/ϕ_0. Dotted lines are best fits. Gray lines are the model predictions for the dissolution controlled case.

2.4.2. Microstructural observations

Starting fraction of the Bolderiaan sand (>99% quartz) were described by Schutjens (1991). Our optical and SEM observations confirmed the quartz grains to be subangular to angular with surfaces characterized by triangular, pyramidal and sickel-shaped etch pits (0.1-0.5 μm). In about 5% of the grains, subparallel planar arrays of fluid inclusions were present, resembling healed intragranular microcracks.

Optical microscopy and SEM performed on CIPed only material (sample D9, which underwent identical treatment to all wet HIPed samples prior to their wet HIPing stage) and on 'dry' HIPed samples (D15, D17) revealed qualitatively indistinguishable microstructures characterized by widespread transgranular and intragranular cracks, strongly reduced final grain size and sharp grain contact points (Figure 2.5a). Quantitatively, however, the 'dry' HIPed samples were significantly finer grained as well as denser than the CIPed only sample (see Table 2.1.) We found no microstructural evidence that dissolution/precipitation processes were active in these samples.

The final mean grain size of the wet HIPed samples was reduced compared to the starting sand fractions, but much less than in the case cold compacted or 'dry' HIPed samples (Table 2.1.). In the wet HIPed samples (Figures 2.5b,c) fewer fines and fewer cracks were observed than in CIPed only material, suggesting that many of the finest cataclastic fragments seen in the cold-pressed material dissolved during pre-HIP heating and/or HIPing itself, and that some cracks may have healed. All wet HIPed samples show a relatively dense microstructure (Figure 2.5c). Minor undulatory extinction is visible optically, but the total fraction of grains showing this is less than 5%. All wet samples show tightly fitting, often micro-sutured grain boundaries and concave-convex grain to grain contacts (indentations and truncations, Figures 2.5b,c). We observed only a few intragranular fractures associated with well-fitting or indented grain contacts, suggesting that interaction between fracturing and pressure solution (Gratier et al., 1999) did not play an important role in our experiments.

a)

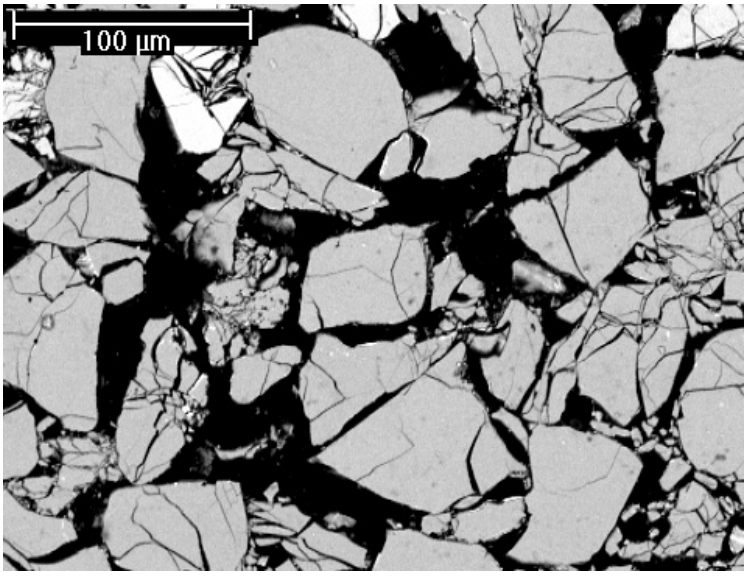

b)

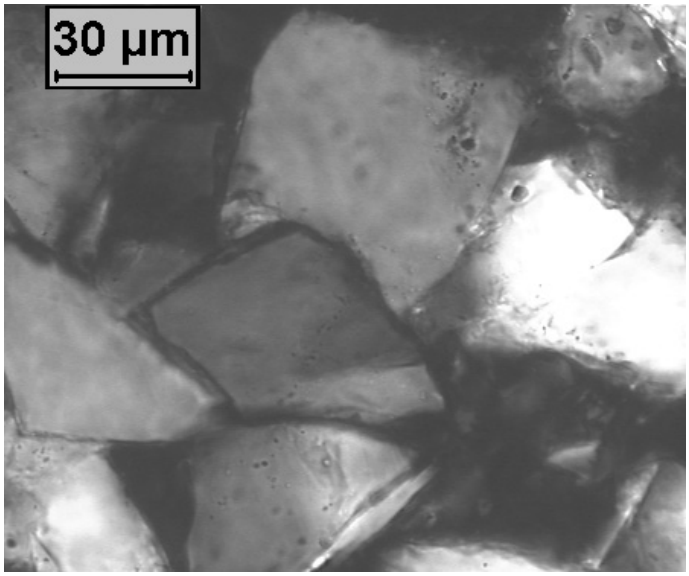

c)

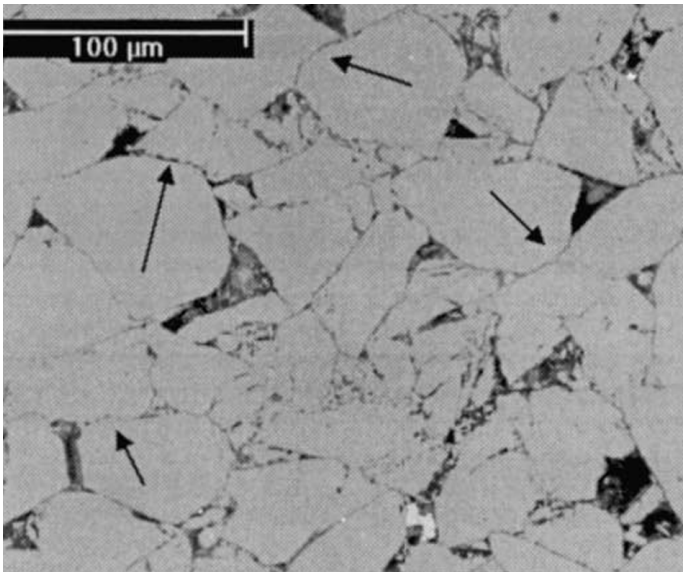

Figure 2.5: (a) SEM backscatter image of sample D 9 (cold, wet compacted sample, P_c=300 MPa for 0.5 hour, P_f=0.1 MPa, d_f=27.9 µm and Φ=30.53 %). (b) Transmission optical micrograph of sample CPf 4 with crossed polarizers (P_e=150 MPa, T=773 K (500 °C) , d_f=~45 µm and Φ_f=10.51). (c) SEM backscatter image of sample CPf 5 (P_e=50 MPa, T=773 K (500 °C), d_f=~45 µm and Φ_f=16.60). Note the widespread indentation features (indicated by the arrows).

2.5. Discussion

2.5.1. Deformation mechanisms in the 'dry' compacted samples

Our microstructural observations on the 'dry' HIPed samples (D15,D D17, Table 2.1) suggest that the recorded compaction (Figure 2.2a) involved mainly grain fracturing. Intergranular rearrangements must also have taken place. The slow but significant time-dependent component of compaction in the 'dry' HIPed samples (Figures 2.2.a and 2.3) suggests that dislocation creep, diffusion creep or subcritical cracking mechanisms contributed. However, no evidence was found from microstructural observations for significant dislocation or diffusion creep. We conclude that some form of subcritical cracking mechanism was responsible for most of the strain and porosity reduction measured.

2.5.2. Deformation mechanisms in the wet compacted samples

Like the dry HIPed samples, the microstructures of wet material CIPed at room temperature shows microcracking and strong grain size reduction ($d_f \approx 28$ μm) compared with the starting fractions (60 ± 15 μm). By contrast, the wet HIPed samples show only modest grain size reduction ($d_f \approx 45$ μm, Table 2.1). In addition, these samples exhibit numerous truncated and concave-convex grain to grain contacts (indentations) as well as sutured and tightly fitting grain boundaries, providing evidence for the operation of intergranular pressure solution (Tada and Siever, 1989; Spiers and Schutjens, 1990). However, the mechanical data for the wet HIPed samples indicate a power law stress dependence of creep rate, with a power (n) much larger than the value of 1 predicted by conventional models for pressure solution (equation 2.3). The observed n-values (~ 3.5) are closed to the stress exponent inferred for dislocation creep in quartzite ($2 \leq n \leq 4$, Luan and Paterson, 1992; Hirth and Tullis, 1992; Gleason and Tullis, 1995). On the other hand, we found an apparent activation energy of ~ 75 ± 10 kJ/mol in our experiments, whereas dislocation creep in wet quartz is characterized by values of 120-167 kJ/mol (Koch et al., 1989; Hirth and Tullis, 1992; Luan and Paterson, 1992). Moreover, we found an inverse grain size dependence of strain rate, whereas dislocation creep is grain size insensitive (Luan and Paterson, 1992). These considerations rule out dislocation creep as the dominant deformation mechanism in our wet HIPing experiments.

Another time-dependent mechanism that could have operated in our wet HIPed samples is stress corrosion cracking accompanied by intergranular sliding/rearrangement. As already discussed, however, grain size reduction was less pronounced than in the CIPed only and 'dry' HIPed samples. Moreover, stress corrosion crack growth velocity depends on stress in a highly non-linear way, with power law stress exponent values > 8 (Atkinson and Meredith, 1989). Stress corrosion cracking plus intergranular sliding is therefore unlikely to have been an important mechanism in our wet HIPing experiments. We found no evidence

for micro-scale cracking/crushing and subsequent dissolution within grain contacts, though such a process cannot be ruled out, particularly in the early part of the experiments.

From the above, we conclude that compaction in our wet HIPed samples was most likely dominated by IPS, presumably with intergranular sliding accommodation. The fact that the dependence of compaction rate on final grain size (d_f) can be described by a power law with an exponent of –0.9 ± 0.5 (Figure 2.4c, Table 2.2.), rather than the of -3 expected for diffusion-controlled IPS, renders it unlikely that diffusion was rate limiting. Moreover, the apparent activation energy found in this study is much higher than typical values for diffusion (15-25 kJ/mol, Nakashima, 1995), whereas it falls exactly in the range characterizing quartz dissolution/precipitation kinetics (Rimstidt and Barnes, 1980), suggesting that pressure solution was interface controlled in the present experiments. The fact that the stress sensitivity of strain rate (n-value) observed in our wet HIPing tests is significantly larger than 1 can potentially be explained by the exponential (rather than linear) stress dependence predicted by equation 2.4 for IPS under conditions of high grain contact stress. Several previous experimental studies of IPS in quartz (Schutjens, 1991; Dewers and Hajash, 1995) also show stress exponents larger than 1. We address this further below.

2.5.3. Comparison with theoretical model

To gain further insight into the rate-controlling mechanism of IPS in our wet HIPing experiments, we now compare our results with the non-linear microphysical models for compaction by IPS represented in equation 2.4. To this end, we inserted the kinetic 'law' for quartz dissolution given by Rimstidt and Barnes (1980) into the creep model for the dissolution-controlled case (x=s in equation 2.4). We focus on the dissolution-controlled case because, for the small grain contact vs. pore wall areas relevant for the present experiments, insertion of precipitation kinetics laws (Rimstidt and Barnes, 1980) or reasonable values of the grain boundary diffusive transport coefficient Z_d (e.g. from Raj, 1982; Gratier and Guiguet, 1986; Farver and Yund, 1991) into equation 2.4 predicts much faster creep, so that dissolution control is predicted. Note that $Z_d=DC\delta$, where D is the diffusivity of dissolved solid in the grain boundary fluid phase, C is it solubility and δ is the average thickness of the grain boundary fluid (Rutter, 1983; Hickman and Evans, 1992; Shimizu, 1995). In incorporating the dissolution law of Rimstidt and Barnes into equation 2.4, we used their value for the dissolution rate constant k^+ (given by them in mol/m^{2}s) times the molar volume as the velocity of dissolution of grain surface in (m/s) for a driving force of 1 RT ($Z_s=k^+\Omega$ in equation 2.4). For an SC grain packing this yields:

$$\dot{\varepsilon} = 6\cdot\Omega\cdot 10^{\left(1.174-0.002028\cdot T-4158/T\right)}\cdot\left[\exp\left(B\cdot\frac{P_e\cdot\Omega}{R\cdot T}\right)-1\right]\cdot\frac{f_s(\phi,\phi_0)}{d} \qquad (2.5a)$$

with

$$f_s = \left(\frac{100 - \phi_0}{100 - \phi} \right) \text{ and } B = \frac{d^2}{\pi} \cdot f_s \cdot \left[R_i^2 - \frac{d^2}{4} (f_s)^{2/3} \right]^{-1} \quad (2.5b,c)$$

where d is the grain diameter (m), P_e is the applied effective pressure (Pa), porosities are in % and R_i is the instantaneous grain (pore wall) radius. This is given by the root of the equation:

$$\left(\frac{d}{2} \right)^3 - 2R_i^3 + \left(\frac{3}{2} R_i \right)^2 \cdot \left[\frac{f_s}{4} \right]^{4/3} - \frac{3}{128} \cdot (f_s)^4 = 0 \quad (2.6)$$

which is easily solved numerically. Note that in inserting the rate law of Rimstidt and Barnes (1980) into equation 2.4, we assume that their dissolution law for free quartz surfaces also applies to a wetted grain boundary zone. Provided that dissolution is the dominant dissipative process operating within grain contacts (as opposed to plastic, frictional or acoustic dissipation), the non-equilibrium thermodynamic theory of Lehner (1990) implies that this assumption is reasonable. Figures 2.6a,b compare the compaction creep rate vs. normalized porosity curves predicted by equations 2.5a,b,c and 2.6, for conditions of typical experiments (CPf3 and CPf7) with the corresponding experimental data. The model yields reasonable agreement with the experimental data at normalized porosities $\phi/\phi_0 > 0.5$ ($\phi \approx 15\%$), though it tends to overestimate the strain rate notably at lower porosity. If IPS is indeed the dominant deformation mechanism at high porosities, there could be several explanations for the sharp decrease in measured strain rates at $\phi/\phi_0 \approx 0.5$. First, there could be a change in rate-controlling mechanism from say dissolution to grain boundary diffusion-controlled IPS, as the grain contact structure evolves to a tighter 'fit' and larger area with increasing strain, or perhaps to precipitation control as pore wall area decreases. A second possibility is that there is a completely different evolution of mean grain contact geometry than embodied by the model. However, this should lead to a more gradual change in strain rate than observed. The abrupt change might otherwise be due to internal healing of the grain boundary structure, reducing the mean grain boundary fluid thickness or connectivity, or to contact overgrowth by neck growth (Lehner, 1995). Yet another explanation might lie in dissolution of copper from the capsule. The fact that the abrupt change in strain rate occurred in all experiments after ~ 12 hours might correlate with a critical concentration of copper being reached after this period. The presence of dissolved copper strongly hinders dissolution rates of quartz (Iler, 1979; Dove and Rimstidt, 1994; Dove, 1999) and thus may cause a strong decrease in IPS rate.

Focusing now on the main body of our experimental data, i.e. that obtained in the higher porosity regime ($\phi > \sim 15\%$ or $\phi/\phi_0 > \sim 0.5$), we have superposed our model predictions for dissolution-controlled IPS (equations 2.5a,b,c and 2.6) onto these results (see Figure 2.4a-c). Comparing behaviour for individual values of ϕ/ϕ_0, the predictions of the model show similar trends and mostly fall within a half to one order of magnitude of the

experimental data in absolute terms. Best agreement is seen regarding the stress sensitivity of the compaction rate (see trends at fixed ϕ/ϕ_0 in Figure 2.4a plus best fit slopes in Table 2.2.). With reference to Table 2.2., the grain size sensitivity of strain rate averaged over the individual fits of Figure 2.4c also agrees favourably with the model, though the multiple regression fit agrees less well and we cannot eliminate the possibility that dissolution of fines produced in the CIPing stage may have influenced the observed grain size dependence. The model does tend to overestimate strain rate towards lower temperatures, lower effective pressures and higher porosities. Moreover, the temperature sensitivity of strain rate predicted by the model is lower than observed in the experiments. Note, however, that the dissolution kinetics data of Rimstidt and Barnes (1980) were determined for the range 20-300 ºC, so that extrapolation to our conditions might lead to significant error in absolute rate and temperature sensitivity. Viewed overall, we feel that the model yields reasonable agreement with our measured creep rates and general trends, suggesting that compaction in our experiments was due to dissolution-controlled IPS, at least for porosities down to ~ 15%.

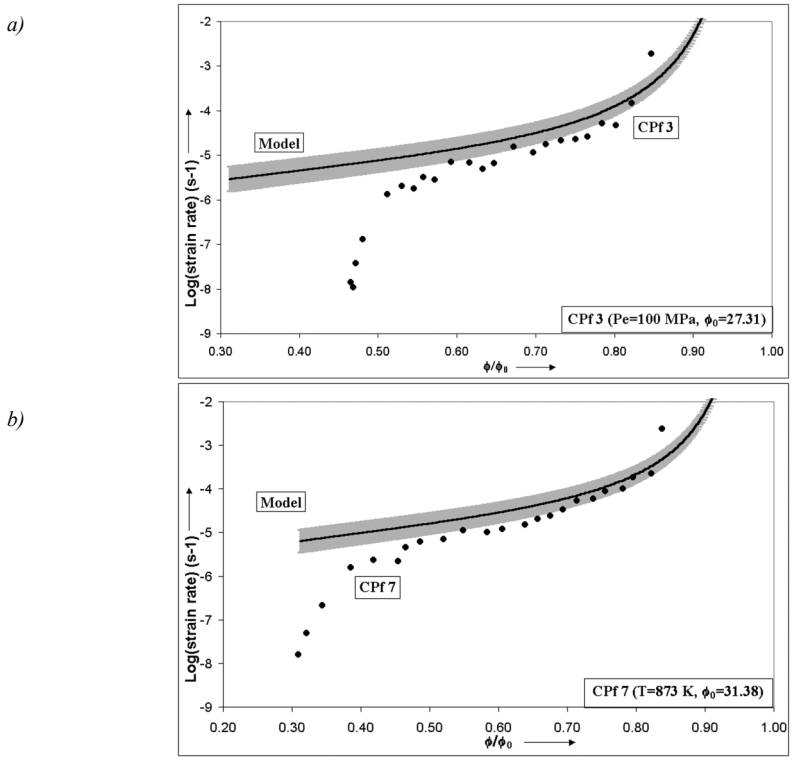

Figure 2.6: Log (strain rate) vs. (Φ/Φ_0) curves comparing the experimental data of (a) sample CPf3 and (b) sample CPf 7 with our microphysical model. The width of the band reflects a relative range in log (strain rate) of ± 5%.

2.5.4. Comparison with previous work

We now compare our experimental results and model predictions with previous data on IPS in pure quartz sands. We justify consideration of data obtained in both 1-D and isostatic compaction experiments on the grounds that our IPS model takes identical forms for both configurations, differing only by a numerical factor of 2-3. The strong effect of compaction mode seen in soil mechanics (Rutter and Wanten, 2000) is therefore not expected when IPS dominates. We begin by recalling that Schutjens (1991) inferred dissolution to be the rate-controlling mechanism of IPS in his 1-D tests done at 250-350 ºC and 15 MPa effective pressure using alkaline pore fluids. Both the temperature and stress sensitivity of compaction rate found (ΔH=67 kJ/mol and $2 \leq n \leq 4$) were similar to those seen in our experiments, though Schutjens found no systematic grain size effect. The activation energy for creep (73 kJ/mol) found by Dewers and Hajash (1995) in their isostatic tests likewise resembles our value and suggests that interface kinetics controlled compaction by IPS. The non-linear dependence of strain rate on stress which they observed also resembles our result but the sensitivity to grain size that they report was higher ($\dot{\varepsilon} \propto d^{-p}$ with p=2.3). This may reflect differences in starting porosity ϕ_0 between the different grain size fractions used by Dewers and Hajash (hence the effect of their fitting parameter, ε_0), since in contrast to our approach they did not pre-press their samples to obtain a reproducible starting state. Figure 2.7 shows a quantitative comparison of our dissolution-controlled model (equations 2.5a,b,c and 2.6) with empirical fits takes from Schutjens (1991) and from Dewers and Hajash (1995) for the range 150-350 ºC. Dewers and Hajash quote only an initial porosity of 35 % in their micrograph captions, so we have assumed that this was the starting porosity in their experiments. Our model predicts creep rates which are about ~10 times faster than obtained in the previous 1-D and isostatic experiments, compared with 3-10 times faster than obtained in our isostatic tests. Similar agreement is obtained with two isostatic experiments on pure quartz sand at 400 ºC and 70 MPa effective pressure (P4, P7) recently reported by Rutter and Wanter (2000). We therefore infer that compaction of quartz by IPS is probably dissolution controlled across the entire range of 150-600 ºC.

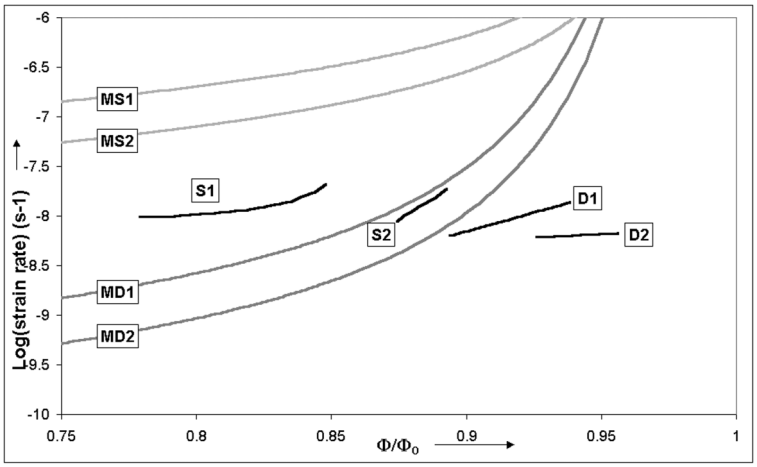

Figure 2.7: Log (strain rate) vs. (ϕ/ϕ_0) curve comparing the experimental data of Schutjens (1991), Dewers and Hajash (1995) with our microphysical model.
S1: Schutjens (1991), T=623 K (350°C), Pe=15 MPa, d=90 μm, data reproduced from strain-time plot. MS1: Microphysical model corresponding to conditions of S1.
S2: Schutjens (1991), T=523 K (250°C), Pe=15 MPa, d=25 μm, data reproduced from strain-time plot. MS2: Microphysical model corresponding to conditions of S2.
D1: Dewers and Hajash (1995), T=423 K (150°C), Pe=35 MPa, d=105 μm, data reproduced from empirical strain-time equation. MD1: Microphysical model corresponding to conditions of D1.
D2: Dewers and Hajash (1995), T=423 K (150°C), Pe=35 MPa, d=215 μm, data reproduced from empirical strain-time equation. MD2: Microphysical model corresponding to conditions of D2.

2.5.5. Implications

Our findings suggest that IPS rates in granular quartz are controlled by the dissolution reaction down to a porosity of ~15 % at 400-600 ºC and effective pressures of 50-150 MPa. Since the activation energy for quartz dissolution (~ 70 kJ/mol, Rimstidt and Barnes, 1980) is expected to be higher than that for diffusion in wetted grain boundaries (15-25 kJ/mol, Nakashima, 1995), then, unless diffusion at lower temperatures is much slower than currently thought (Raj, 1982; Gratier and Guiguet, 1986; Farver and Yund, 1991), pressure solution rates in quartz rocks at temperatures below 600 ºC and porosities above ~ 15% should be controlled by the rate of dissolution. This implies that our model should be crudely applicable to predict IPS rates in natural sandstone formations with porosities > 15 %. Note, however, that since pore fluid chemistry strongly influences dissolution/ precipitation rates in quartz (Iler, 1979; Rimstidt and Barnes, 1980; Schutjens, 1991; Dove and Rimstidt, 1994; Dove, 1999), the composition of the pore fluid in sandstones may turn out to play a key role in determining IPS compaction rates, either slowing them down (e.g. Al^{3+}, Fe^{3+}, Zn^{2+}, Cu^{2+}, Dove and Rimstidt, 1994) or speeding them up (e.g.. Na^{+}, K^{+}, Li^{+}, Mg^{2+}, Dove and Rimstidt, 1994).

Further work on such effects is clearly needed, preferably using finer grain sizes and lower effective pressures than in the present study to further reduce any effects of cataclasis. For typical upper crustal conditions (depth 2 km, lithostatic pressure 50 MPa, fluid pressure 20 MPa, temperature 60-70 ºC, starting porosity 30-35%), the present dissolution-controlled IPS model predicts that sandstones with a grain size of 300 μm and a porosity of 20% will compact at strain rates of 10^{-13} to 10^{-12} s^{-1}. Our multiple regression fit predicts rates about one order lower.

2.6. Conclusions

1. From our mechanical data and microstructural observations we infer that the dominant compaction mechanism in our wet, hot-pressed samples at temperatures of 400-600 ºC and effective pressures of 50-150 MPa was intergranular pressure solution, though we cannot eliminate a minor contribution of cataclasis process in the early stages of our tests.
2. A microphysical model incorporating an independently determined dissolution rate law with a non-linear (non-simplified) strain rate vs. driving force (stress) relationship was compared with our data, as well as previous experimental data for the temperature range 150-600 ºC and the effective pressure range 15-150 MPa. The fit of our model to our own experimental data was good for porosities higher than 15%, indicating that the rate-controlling mechanism of IPS was quartz dissolution at grain contacts. The fit was poor for lower porosities where measured rates slowed dramatically, possibly because of a change in rate-controlling mechanism, grain boundary healing or copper ions entering the pore fluid from the sample capsules. Predicted rates were 3-10 times faster than the compaction rates we measured and ~ 10 times faster than previous data.
3. The stress sensitivity of strain rate (n-values) of 3-4, which we found in our experiments, matched our non-linear IPS model prediction well and supports the notion that pressure solution in quartz needs not be linear viscous, when grain contact stresses are high.
4. Our dissolution-controlled model thus seems to give a robust order of magnitude description of quartz sand compaction by IPS, down to porosities of ~15 %, and offers a basis to model compaction rates of quartz sandstones down to such porosity values. It is important to note, however, that pore fluid contamination might drastically slow down or accelerate the IPS process in nature depending on the ions present. More experimental work is needed on such effects, preferably using sufficiently fine grain sizes and low effective pressure to eliminate completely any effect of cataclasis.

Chapter 3

COMPACTION CREEP OF QUARTZ-MUSCOVITE MIXTURES AT 500 ºC: PRELIMINARY RESULTS ON THE INFLUENCE OF MUSCOVITE ON PRESSURE SOLUTION

This chapter was published as: Niemeijer, A.R. and Spiers, C.J., 2002. Compaction creep of quartz-muscovite mixtures at 500 °C: Preliminary results on the influence of muscovite on pressure solution. In: S. De Meer, M.R. Drury, J.H.P. De Bresser and G.M. Pennock (Editors), Deformation Mechanisms, Rheology and Tectonics. Special Publication. Geological Society of London, Noordwijk, pp. 61-71.

Abstract

It is widely claimed that the presence of phyllosilicates in sandstones increases intergranular pressure solution (IPS) rates in these rocks. However, this has not been experimentally confirmed. This study reports the results of isostatic hot-pressing compaction experiments at a temperature of 500 ºC and an effective pressure of 100 MPa on mixtures of quartz and muscovite. Previous work has shown that under these conditions dissolution is rate controlling in pure quartz. No acceleration of compaction of quartz by the addition of muscovite was observed. Instead, a modest decrease in IPS rates was observed (factor 3-10), which we infer was due to a decrease in IPS rate. The effect of muscovite in slowing IPS may be due to the influence of dissolved aluminium (Al^{3+}) dominating over any accelerating effects of alkali-metal cations. From the geochemical literature, Al^{3+} in solution is expected to decrease the solubility, dissolution rates and precipitation rates of quartz. However, the effect of the addition of muscovite on IPS rates in quartz when controlled by diffusion or precipitation may be different. Experiments should be conducted on quartz sand under conditions where diffusion or precipitation is rate controlling to investigate these effects.

3.1. Introduction

From microstructural evidence, it is widely accepted that intergranular pressure solution (IPS) is an important compaction, lithification and deformation mechanism in clastic sediments under diagenetic and low-grade metamorphic conditions (Rutter, 1983; Tada and Siever, 1989). IPS exerts a strong influence on porosity and permeability reduction in sandstones and mudstones, and hence on reservoir and top-seal evolution in sedimentary basins (Addis and Jones, 1985; Houseknecht, 1987; Rutter and Wanten, 2000). It is also likely to play an important role in controlling strength recovery and seismic vs. frictional-viscous slip on gouge-bearing crustal faults ((Bos et al., 2000a, b; Bos and Spiers, 2000, 2001).

Despite the importance of IPS in siliciclastic sediments and quartz-phyllosilicate fault gouges, the rate controlling mechanism and kinetics of IPS in quartz are still poorly constrained, principally because of the slowness of the process under lab conditions. Recent experimental work has suggested that when there is no long range advective or diffusive transport, IPS in pure quartz sand is probably controlled by the kinetics of quartz dissolution, at least at porosities down to ~15% (see Chapter 2). Regarding the effects of

phyllosilicates, numerous field and petrographic associations between phyllosilicate content and enhanced IPS or pressure solution seams (e.g.. Heald, 1959; Rutter, 1983; Engelder and Marshak, 1985; Tada and Siever, 1989; Renard et al., 1997) have led to the view that phyllosilicates dramatically increase IPS rates in quartz, presumably via enhanced grain boundary diffusion or enhanced reaction kinetics. However, the influence of phyllosilicates on IPS rates in quartz has remained largely unexplored from the experimental and theoretical points of view.

Though few experiments have been done on the influence of phyllosilicates on IPS, two recent studies indicate strong enhancement effects. Hickman & Evans (1995) studied pressure solution rates at halite-silica contacts by pressing a convex halite lens against a fused silica plate under brine. One experiment was conducted in which the silica plate was coated with a 0.8-μm-thick film of Na-montmorillonite. The presence of the clay film produced an approximately fivefold increase in pressure solution convergence rate over clay-free experiments conducted under otherwise identical conditions. Assuming diffusion to be rate-limiting, as observed in their halite-silica experiments, Hickman & Evans (1995) calculated an effective grain boundary (clay layer) diffusivity about 30 times greater than for the halite-silica interfaces. Montmorillonite was used as the phyllosilicate phase because of its propensity for extreme swelling through incorporation of interlayer water. The observed increase in effective grain boundary diffusivity per unit clay layer thickness is therefore likely to represent the maximum effect of phyllosilicates on pressure solution rate enhancement, when diffusion is rate controlling. However, in other materials such as quartz, where interface reactions may be rate controlling, where different surface forces may come into play at contacts with phyllosilicates, and where surface reactions may be influenced by chemical effects of phyllosilicates present, the influence of phyllosilicates on IPS may be quite different.

In the second recent study, Rutter & Wanten (2000) investigated IPS rates by hot isostatic pressing of samples consisting of granular quartz embedded in a matrix of fine-grained illite and muscovite, with a small adjacent volume of porous quartz sand to provide a sink for precipitation of silica dissolved from the phyllosilicate-quartz mixture. The presence of phyllosilicates in the matrix strongly enhanced compaction rates compared to pure quartz samples. Rutter & Wanten argue that this was caused by enhancement of pressure solution of the quartz at quartz/phyllosilicate contacts and by a strain contribution due to intracrystalline plasticity plus frictional flow in the phyllosilicates. However, they give no suggestions about the rate-limiting process controlling IPS. Their experiments are indeed difficult to interpret since, compared with the pure quartz sand samples, the introduction of the phyllosilicate matrix leads to changes in the stresses transmitted across quartz grain surfaces (hence in the driving force for IPS), in the source-sink diffusion path, in the areas available for quartz dissolution and precipitation, in the chemistry and pH of the pore fluid and probably in the state of the intergranular fluid. As all of these factors can potentially influence the rate and/or rate controlling mechanism of IPS, the exact effect of

the phyllosilicates on IPS in quartz is hard to deduce from the experiments of Rutter & Wanten (2000).

It is thus evident that while there are ample indications in nature for an influence of phyllosilicates on IPS rates in quartz rich rocks, the effect has yet to be confirmed, mechanistically identified, or systematically characterized in laboratory experiments. This preliminary study consists of compaction experiments on quartz-muscovite mixtures at a confining pressure of 300 MPa, a pore fluid pressure of 200 MPa and a temperature of 500 ºC, and extends our previous study of IPS in pure quartz sand under similar conditions (Chapter 2). In that study, we found that IPS dominated over both cataclasis and dislocation creep, and we concluded that IPS rates were controlled by the quartz dissolution reaction at grain contacts. Here, we attempt to systematically examine the effect of adding sufficient muscovite to coat grain contacts, without filling all the intergranular pore space.

3.2. Background Considerations

In a chemically closed system (no removal or addition of solid mass by long range diffusive or advective transport in the pore fluid), compaction of a fluid-saturated granular aggregate, by intergranular pressure solution (IPS), involves dissolution of solid material at stressed grain-to-grain contacts, diffusion of this material through the intergranular fluid into the open pores, followed by precipitation on the free pore walls. The process is driven by differences in effective normal stress, hence the normal component of the solid chemical potential, between grain contacts and free pore walls (e.g.. Lehner, 1990). Under steady state conditions, any of the three mechanisms of dissolution, diffusion and precipitation may be rate controlling (De Meer and Spiers, 1995). When we wish, as in the present study, to investigate the influence of phyllosilicates on IPS rates in quartz, it is therefore useful to first consider what, in theory, their influence on the three serial processes of IPS can be. These considerations form the basis for our choice of experimental method.

We begin by briefly considering the physical and chemical properties of phyllosilicates, especially the surface properties in the presence of water. Phyllosilicates are characterised by $[SiO_4]^{4-}$ tetrahedra linked together to form flat sheets with the composition $[Si_4O_{10}]_n$. This group of minerals includes muscovite, biotite, phlogopite, chlorite, clays, talc and serpentine, all of which are soft, plastically deformable minerals of variable but generally low density, and which always contain a specific amount of structurally bound water.

Muscovite, the mineral used in this study, belongs to the *mica* sub-group and is characterised by a 2:1 layering, i.e. a periodic structure consisting of 2 tetrahedral sheets $[Si_4O_{10}]_n$ and one octahedral $[Al_2(OH)_6]_n$ sheet repeated throughout the mineral structure (Deer et al., 1977). Muscovite (and mica in general) always contains a variable amount of structurally bound water, in the form of hydroxyl ions in the octahedral sheets (Deer et al., 1977). Cation substitution in the tetrahedral sheets (i.e. Al^{3+} for Si^{4+}), results in an overall negative charge on the tetrahedral layers. The charge is compensated, and the layers bonded

together by large, positively charged interlayer cations, most commonly K^+, Na^+ or Ca^{2+}. However, as a result of substitution of Si^{4+} by Al^{3+} in the tetrahedral sheets, freshly cleaved muscovite (and mica in general) has a negative surface charge under vacuum. In aqueous solution protons will sorb to the surface of the muscovite to balance the negative charge. The pH at the point of zero charge (pH_{pzc}, i.e. the pH of the solution at which the surface is electrically neutral) of muscovite in an aqueous solution has been calculated to be 6.6 (Sverjensky, 1994).

When diffusion is the rate controlling process of IPS, the effect of phyllosilicates on IPS rates in quartz is expected to be one of accelerating pressure solution (Hickman & Evans 1995; Renard et al. 1997; Rutter & Wanten 2000). This expectation is mainly based on measurements of the disjoining pressure acting between quartz-quartz and quartz-mica surfaces (Figure 3.1). For a flat, interfacial fluid film, the disjoining pressure equals the amount by which the fluid pressure acting on the fluid-solid interface exceeds the hydrostatic pressure in the bulk fluid. In general, it is believed to be caused mainly by hydration forces (i.e. forces which result from the short range ordering of water molecules along the solid/liquid interface) and not by van de Waals interactions or electrical double-layer repulsion, since these can not explain the observed forces (Heidug, 1995; Hickman and Evans, 1995). In the case of stressed granular solids, the disjoining pressure in an interfacial fluid film balances the effective compressive stress to maintain an open, wetted grain boundary with a stress-dependent thickness. The various measurements imply that quartz/mica interfaces can support a thicker layer of water in the grain boundary than quartz/quartz interfaces at a given normal stress. At a film thickness of 1 nm a mica/mica interface can support ~10 times more stress than a quartz/quartz interface, see Figure 3.1. (Pashley and Israelachvili, 1984; Heidug, 1995; Renard et al., 1997). At a quartz/quartz interface van der Waals forces are attractive and the surface charge is low, resulting in only weak ordering of water molecules and thus in weak hydration forces. At a quartz/mica interface however, van der Waals forces are repulsive and the surface charge (of the mica) is high, resulting in strong ordering of water molecules and thus in strong hydration forces, ultimately leading to a higher fluid film thickness than at a quartz/quartz interface at similar stresses. Nonetheless, at sufficiently high intergranular stresses, water will be squeezed out, even from a quartz-mica interface (Israelachvili, 1992; Heidug, 1995). When dissolution or precipitation is the rate controlling process, the influence of muscovite on pressure solution rate can be chemical

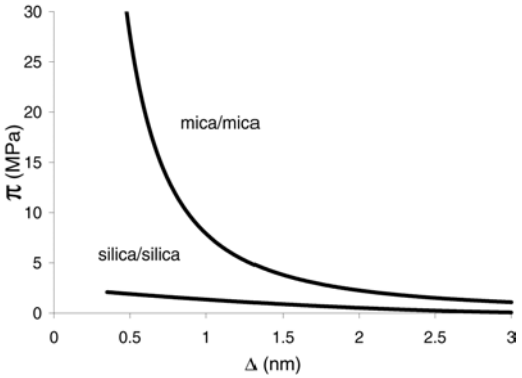

Figure 3.1. Disjoining pressure π for a water film of thickness Δ confined between parallel silica and mica surfaces. The disjoining pressure is the difference between the pressure acting on the solid and the fluid pressure; it is similar to an effective stress (after Heidug 1995).

or physical. First, the presence of muscovite in quartzitic rocks changes the chemistry of the pore fluid by (in)congruent dissolution of the muscovite (typical dissolution rate at 70 ºC and a pH of 6.2 is ~10^{-16} mol/cm^2·s; (Knauss and Wolery, 1989). This releases cations (e.g.. K^+, Al^{3+}) into the solution, and/or modifies the pH of the pore fluid. When the pore fluid contains alkali-metal or alkali-earth ions, or has a non-neutral pH, the solubility and interfacial reaction rates of quartz are increased by approximately one order of magnitude, depending on the concentrations of the cations (Dove and Rimstidt, 1994; Dove and Nix, 1997; Renard et al., 1997; Dove, 1999). This will increase the IPS dissolution rate, the diffusive transport rate and the precipitation rate, so that IPS rates will increase. However, the presence of a minute amount of aluminium in the pore fluid (as low as 0.15 ppm equivalent of Al_2O_3) can strongly decrease the apparent solubility of quartz as well as dissolution and precipitation rates (Iler, 1973, 1979; Mullis, 1993; Dove and Rimstidt, 1994) presumably by adsorption of Al^{3+} onto quartz surfaces. The amount of decrease in dissolution/precipitation rates, however, remains unclear. Estimates vary from 3 to as much as 8 orders of magnitude, but the effect may be much smaller (~1 order of magnitude, Dove, *pers. comm.*). Moreover, the presence of muscovite in pore spaces, and on pore walls, decreases the area available for precipitation on the quartz surface (Tada and Siever, 1989; Dewers and Ortoleva, 1991; Mullis, 1993), resulting in a decrease in overall precipitation rate. Thus, the presence of phyllosilicates in general, and muscovite in particular, can increase or decrease IPS rates in quartz. In addition, the reaction mechanism at a quartz-muscovite interface may be completely different from that at a quartz-quartz interface, due to a different surface charge, a different pH and the presence of cations such as Al^{3+} and K^+.

Finally, it is important to note that the presence of phyllosilicates may cause a change in rate controlling mechanism of IPS, compared with a pure quartz rock, through any of the above-mentioned effects on dissolution, diffusion and precipitation rates.

3.3. Experimental method

Our experiments consisted of isostatic compaction or hot-pressing (HIPing) experiments carried out on wet quartz sand with 0-20 wt% added muscovite. The temperature used was 500 °C, the confining pressure was 300 MPa, the pore fluid pressure 200 MPa and the effective pressure thus 100 MPa. The experiments were carried out using the same starting material as used by Niemeijer et al. (2002, Chapter 2) in their study of IPS in quartz, namely quartz sand from the Miocene "Bolderiaan" formation, Belgium. The material had previously been refined in a ball-mill, ultrasonically cleaned in distilled water and etched in HF solution to remove surface damage. We sieved the product to obtain a starting grain size fraction of 45-75 μm. Muscovite additive was prepared using natural muscovite from Norway. This was crushed in a ball mill and the resulting powder sieved to obtain fractions of 45-90 and < 28 μm. This was in turn mixed with the sieved quartz sand, in different ratios, to obtain 5, 10 wt% and 20 wt% muscovite-quartz samples, in addition to several pure quartz samples.

3.3.1. Apparatus and Procedure

The apparatus used is described in Chapter 2. It consists of a cold seal "Tuttle bomb" pressurized with Argon, plus an internal sample/capsule assembly linked to an independent pore fluid system (Figure 3.2.). The pore fluid and Argon pressures were measured with a Bourdon-type pressure gauge (resolution ~ 1 MPa) and/or a pressure transducer (resolution ~ 0.2 MPa). The temperature of the sample was measured using a pre-calibrated K-type thermocouple embedded in the bomb wall (error of ~2 °C).

In each experiment, ~2 grams of quartz-muscovite mixture were loaded into the annealed copper capsule assembly via the "top cup" end (enlargement Figure 3.2.). The capsule was then sealed by pressing- and welding-in the copper "top cup" (Figure 3.2.), producing a sample porosity of ~45-50%. The sample assembly was subsequently loaded into the Tuttle bomb, evacuated and flooded with water from the pore fluid reservoir. Each sample was then Cold Isostatically Pressed (CIPed) at a confining pressure of 300 MPa for 30 minutes, with the pore pressure maintained close to 0.1 MPa (1 atm.). This was done to produce a reproducible starting porosity and microstructure for the hot pressing stage (cf. Spiers and Brzesowsky, 1993; De Meer and Spiers, 1995) and to minimize strain due to grain rearrangement and cataclasis during HIPing at 100 MPa. The confining pressure was subsequently reduced to ~140 MPa and the pore fluid pressure raised to ~135 MPa using the volumometer pump. The sample was then heated at ~15 °C per minute. During heating, the effective pressure was maintained as low as possible and was always <10 MPa. After

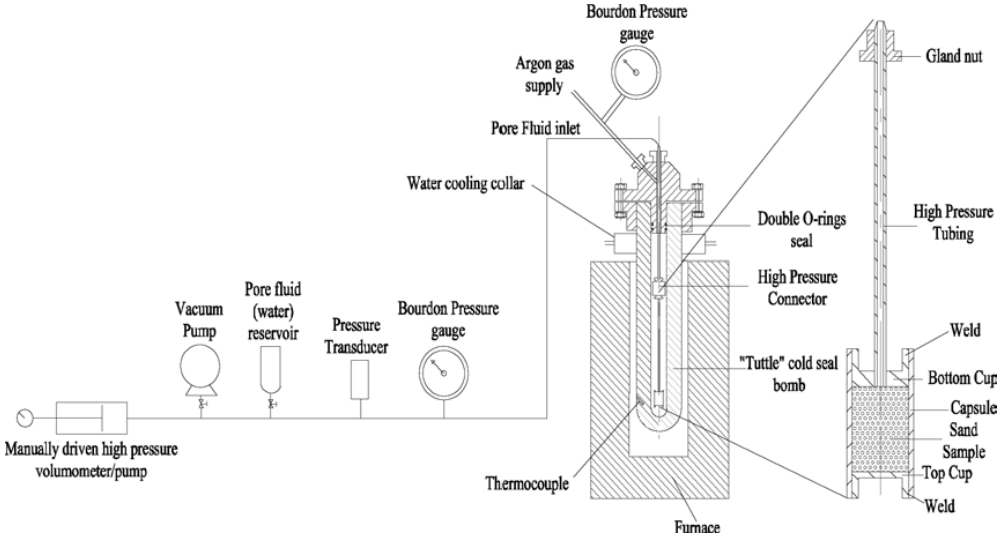

Figure 3.2.: Schematic diagram of the experimental apparatus with an enlargement showing the capsule/sample set-up.

attaining thermal equilibrium at the desired test temperature (500 °C) and confining pressure (300 MPa), the required effective pressure was applied by extracting fluid from the sample using the volumometer. The confining and pore fluid pressures were subsequently kept within ± 5 MPa of the desired values. The minimum measurable fluid volume increment was ~2 μl, yielding an absolute resolution in volumetric strain at room temperature of ~0.02 %.

Experiments were terminated when the pore volume loss was no longer detectable via changes in pore fluid pressure. At this stage, the bomb was quenched, using compressed air, at an average cooling rate of ~30 °C per minute. The indurated sample was then removed from the apparatus and capsule and dried in an oven at 60 ºC for 24 hours. The final porosity (ϕ_f) of the sample was measured by wrapping it in ultra-thin plastic film and determining its volume (Vf) using the Archimedes method and density data on quartz and muscovite (Deer et al. 1977). The samples were finally impregnated with epoxy resin and sectioned for optical and SEM study.

3.3.2. Data Acquisition and Processing

As indicated above, pore volume loss during the experiments was determined incrementally by measuring the volume of fluid extracted from the sample to maintain constant pore pressure. The volume of muscovite was assumed to be constant and thus of no direct influence on porosity reduction. The measurements were accurately corrected for density changes associated with the cooling of the pore fluid during extraction, using appropriate P-V-T equations for water (Burnham et al., 1969). The "starting porosity" (ϕ_0) of the sample, i.e. before HIPing at the test temperature, was calculated by adding the total amount of fluid expelled from the sample during HIPing to the final pore volume (ϕ_f, V_f) of the sample. The difference in the pore and sample volumes, measured at room temperature and pressure compared to the post-HIPing volumes at test conditions, can be estimated using the bulk modulus of sandstone (~$2.5\text{-}7.5\cdot10^{11}$ Pa, Birch 1966) and the volumetric thermal expansion coefficient of quartz (~$4\text{-}5\cdot10^{-5}$ K^{-1}, Skinner 1966) and was found to be negligible. The overall relative standard error in volume measurements was approximately 5 %, implying an absolute standard error in the porosity measurements of less than 0.2 %. The volumetric strain rate associated with individual data was calculated using the 2 point central difference method.

3.3.3. Dry Control Runs

Control HIPing experiments on "dry" sand fractions were performed in the same apparatus as the wet tests, but using fully sealed capsules with no added water. The "dry" samples were first CIPed at 300 MPa for 30 minutes and their porosities determined at atmospheric pressure using the Archimedes method. The samples were then HIPed at 500

°C and pore volume loss was measured periodically by removing the capsule from the bomb and re-determining its total (current) volume.

3.4. Results

3.4.1. Mechanical Data

The complete set of experiments reported here is listed in Table 3.1., along with data on the starting and final porosities of the samples and the total volumetric strains achieved. The CIPed-only quartz sand sample (D9) showed compaction from ~45% porosity to ~30% (Table 3.1.). Compaction creep data obtained during HIPing of the wet quartz-muscovite samples (CPf 10, 11, 12, 13), the wet quartz only sample (CPf 3) and the "dry" sand sample (D17) are presented in Figure 3.3a. in the form of ϕ/ϕ_0 *vs.* time curves. These demonstrate time-dependent compaction in all samples. The "dry" control sample (D17) shows relatively slow compaction and modest final strain (Table 3.1.). By contrast, the wet, quartz-only sample (CPf 3) compacted very rapidly in the first ~12 hours of the experiment, halving its porosity in that time. The wet muscovite-quartz samples (CPf 10, 11,12 and 13) compacted more slowly initially, but attained similar final porosities and porosity reduction rates after 3-4 days. Note that the curves of samples CPf 10, 11 and 12 are closely similar, although sample CPf 12 seems to maintain a higher strain rate to lower values of ϕ/ϕ_0. Sample CPf 13 (5wt% muscovite) compacted slightly faster than CPF 10, 11 and 12, but still more slowly than the quartz-only sample (CPf 3). Figures 3b and 3c show compaction rate data computed for the dry and wet samples (0 wt%, 5 wt%, 10 wt%, 45-75 μm and <28 μm and 20 wt% muscovite) versus normalized porosity ϕ/ϕ_0. Normalized porosity was used rather than volumetric strain or absolute porosity since this quantity reduces the influence of variations in starting porosity upon strain rate as discussed by Niemeijer et al (2002 and Chapter 2). Figure 3.3b shows compaction rate data computed for the dry and wet samples (0 wt%, 10 wt% and 20 wt% muscovite) versus normalized porosity ϕ/ϕ_0. It demonstrates that the dry sample (D17) compacted at rates 1-3 orders of magnitude slower than the wet samples at given strain (ϕ/ϕ_0). The fits shown in Figures 3.3b and c were used to construct plots of compaction strain rate versus muscovite content for the wet samples (CPf 3, 10, 11 and 13) at constant ϕ/ϕ_0 values (Figure 3.3c.). Both Figures 3.3b. and 3.3c. show a decrease in strain rate of 0.5-1 order of magnitude, caused by addition of muscovite, with no further reduction in the range 10-20 wt% muscovite.

Table 3.1: List of experiments performed showing initial (pre-HIPing) porosities (ϕ_0), final porosities (ϕ_0), wt% muscovite and isostatic pressing conditions. T denotes test temperature, Pc confining pressure, Pf pore fluid pressure and Pe the applied effective pressure. "Dry" means no water added.
* Starting or pre-HIPing porosity measured under atmospheric conditions, i.e. after CIPing, $^{+}$ Starting or pre-HIPing porosity calculated for loaded conditions from the final porosity and porosity change determined during HIPing, , $^{\Psi}$ Fraction of <28 μm muscovite used, $^{++}$ Fluid pressure measured with High Pressure transducer.

Sample number	T (K)	wt% muscovite	Pc (MPa)	Pf (MPa)	Pe (MPa)	ϕ_0 (%)	ϕ_f (%)	Total volumetric strain(%)
D 9	298	0	300	~0.1	~300	30.31*	30.31	-
D 17	773	0	60	"dry"	60	27.17*	19.65	9.06
CPf 3	773	0	300	200	100	27.31^{+}	12.71	16.70
CPf 10^{++}	773	10	300	200	100	24.46^{+}	10.52	15.56
CPf 11^{++}	773	20	300	200	100	24.53^{+}	10.30	15.84
CPf 12$^{++,\Psi}$	773	10	300	200	100	22.17^{+}	8.31	15.07
CPf 13^{++}	773	5	300	200	100	24.15^{+}	9.51	16.00

a)

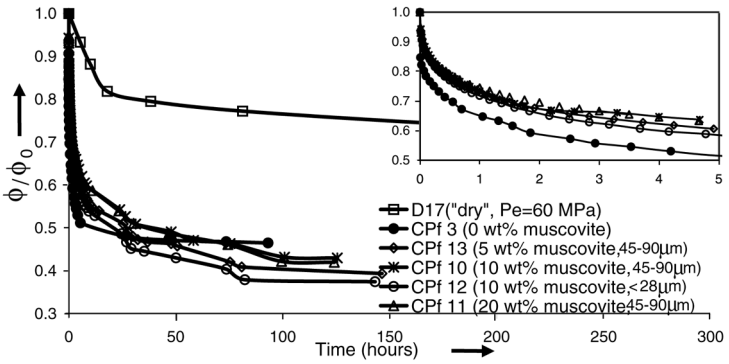

b)

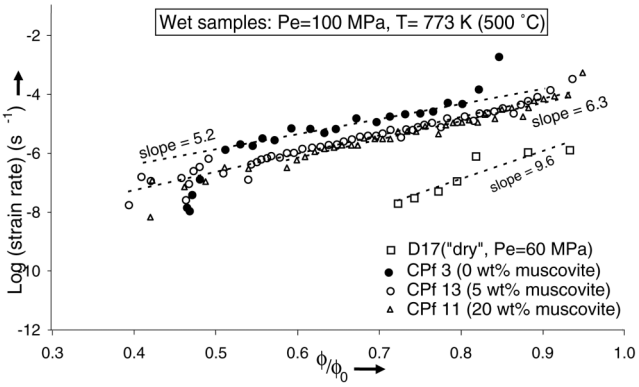

c)

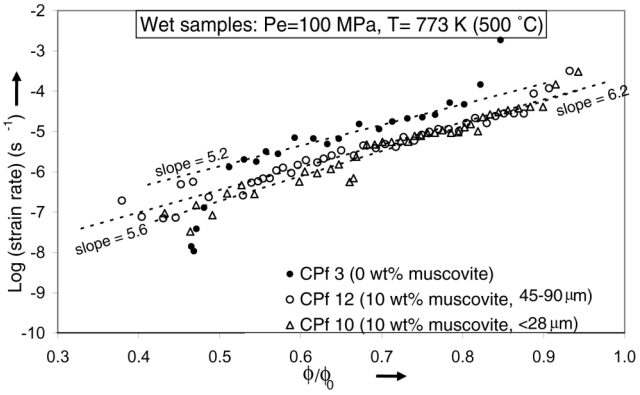

d)

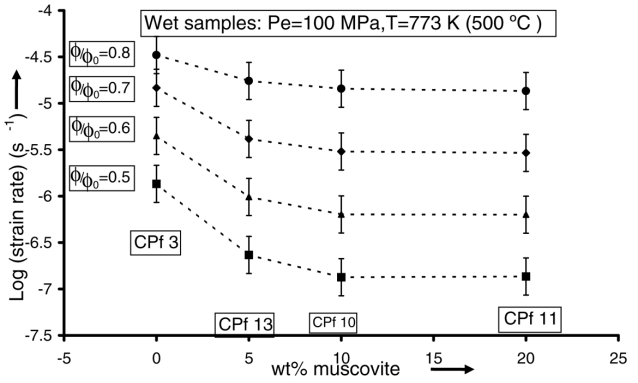

Figure 3.3: Compaction creep data showing influence of muscovite.
(a): Compaction creep curves in the form of ϕ/ϕ_0 vs. time plots for the samples D17, CPf 3, CPf 10 and CPf 11. Inset shows compaction creep curves in the first 5 hours.
(b): Log (strain rate) vs. ϕ/ϕ_0 plots with linear best fits for samples D17, CPf 3, CPf 11, and CPf 13.
(c): Log (strain rate) vs. ϕ/ϕ_0 plots with linear best fits for samples CPf 3, CPf 10 and CPf 12
(d): Log (strain rate) vs. wt% muscovite curves showing the influence of muscovite on compaction rates in wet samples CPf 3, CPf 10, CPf 11 and CPf 13.

3.4.2. Microstructural Observations and Compositional Data

The starting fraction of Bolderiaan Sand consisted of > 99% quartz (Chapter 2). Our optical and SEM observations showed the quartz grains to be subangular to angular with surfaces characterized by triangular, pyramidal and sickel-shaped etch pits. The sieved fraction of the natural muscovite was analysed using x-ray diffraction (XRD), inductively coupled plasma mass spectrometry (ICP-MS) and thermogravimetric analysis (TGA). The material consists of > 99% muscovite, with the chemical composition given in Table 3.2.

Table 3.2.:Chemical composition of natural muscovite (fraction 45-90 μm) determined by ICP-MS analyses. Other elements are less than 0.1 wt%. H_2O-content was determined by TGA.

Composition	wt%
SiO_2	43.35
Al_2O_3	34.53
K_2O	10.93
Fe_2O_3	4.40
MgO	1.21
Na_2O	0.53
CaO	0.10
BaO	0.14
TiO_2	0.15
H_2O	4.61
Total	**99.85**

Optical microscopy and SEM observations made on both CIPed-only material (D9- equivalent to the "starting material" for the HIPing samples) and "dry" HIPed sample (D17) show closely similar microstructures characterized by widespread intragranular and transgranular cracks, grain size reduction and sharp grain contact points (Figure 3.4a.). We found no microstructural evidence that dissolution/precipitation processes were active in these samples. The final grain size of all wet-HIPed samples (CPf 3, 10 and 11) was reduced compared to the starting sand fractions, but much less than in the cold compacted sample (compare Figures 3.4a-d, see also Chapter 2). In all wet-HIPed samples (Figures 3.4b-d) fewer fine grain fragments and fewer cracks were observed than in the CIPed only material (Figure 3.4a), suggesting that many of the finest cataclastic fragments seen in the cold-pressed material dissolved during HIPing and that some cracks may have healed. All wet samples show tightly fitting, often micro-sutured grain boundaries and concave-convex grain-to grain contacts (indentations and truncations), indicative of IPS (Figures 3.4b-d). We observed only a few intragranular fractures associated with well-fitting or indented grain contact, suggesting that interaction between fracturing and pressure solution (Gratier et al., 1999) did not play an important role in our experiments. Minor undulatory extinction is visible optically in the quartz grains, but the total fraction of quartz grains showing this is less than 5%. Muscovite sheets in the muscovite-bearing wet-tested samples almost always show some undulatory extinction (Figures 3.4c-d). They are often sharply "bent" around the quartz grains with no clear indication of fracturing. Muscovite sheets are present in ~50-75% of quartz grain contacts that show indications of IPS. About ~25% of the pore spaces have also been filled with muscovite with the muscovite coating the free pore wall area (Figure 4c and d). No sheets were observed that penetrated quartz grains "end on" (cf. Bjørkum, 1996). The muscovite sheets have not developed a preferred orientation, nor do they form a continuous network in 2-D section.

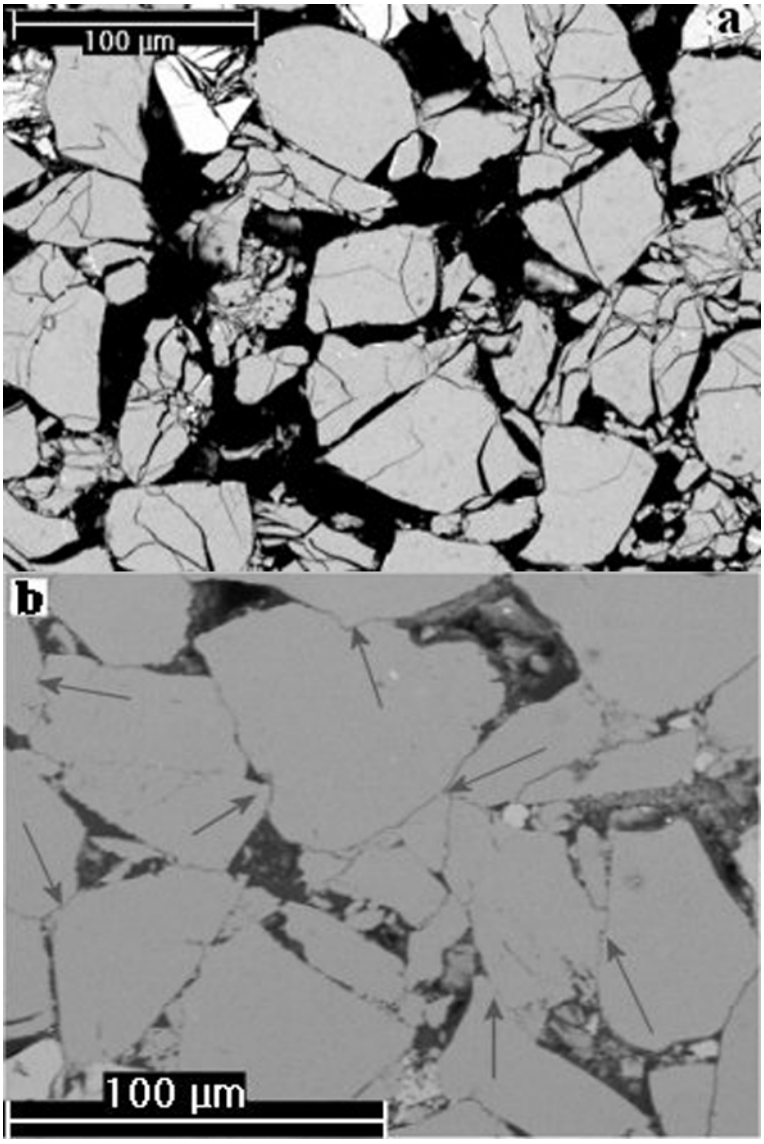
100 µm
a
b
100 µm

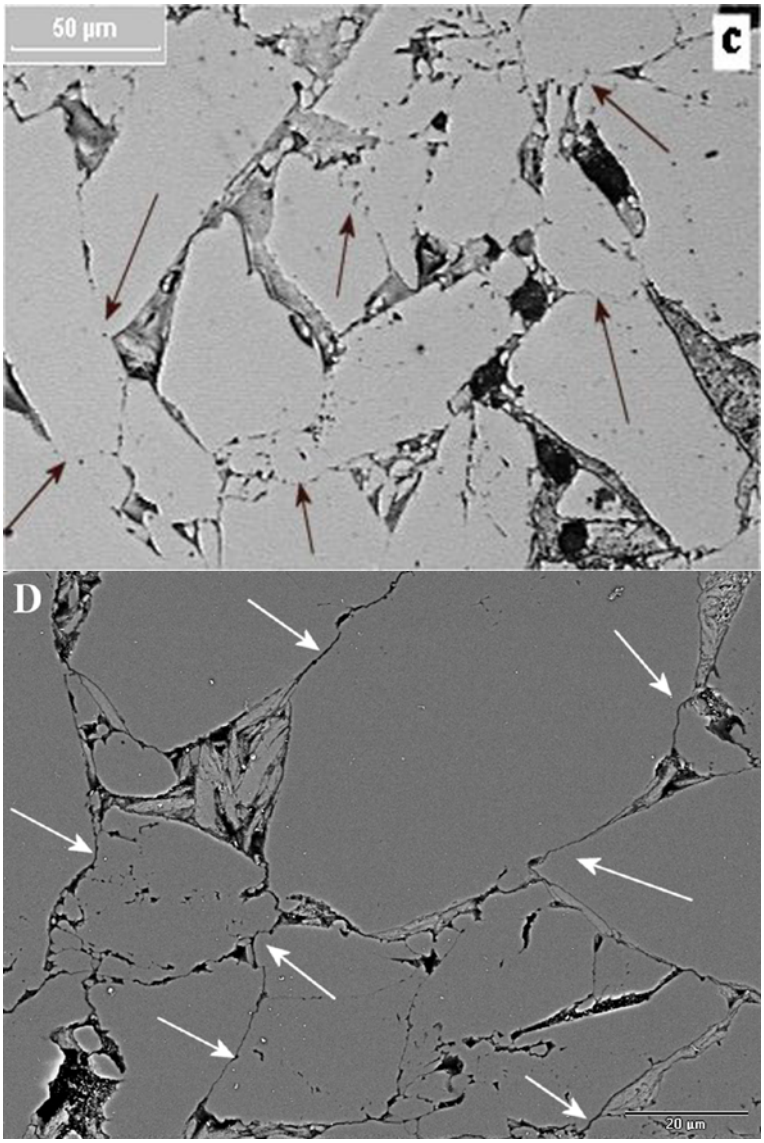

Figure 3. 4: Microstructures characterizing the various experiments.
(a): SEM backscatter image of sample D 9 (CIPed-only sample, Pc=300 MPa, Pf=0.1 MPa, ϕ_f=30.31%)
(b): SEM backscatter image of sample CPf 3 (wet compacted sample, P_c=300 MPa, P_f=200 MPa, 0 wt% muscovite, ϕ_f=12.71 %), showing grain-to-grain indentations and truncations (black arrows) indicative of IPS.
(c): Reflected light micrograph of sample CPf 10 (wet compacted sample, P_c=300 MPa, P_f=200 MPa, 10 wt% muscovite, ϕ_f=10.52 %), showing grain-to-grain indentations and truncations (black arrows) indicative of IPS.
(d): SEM backscatter image of sample CPf 12 (wet compacted sample, P_c=300 MPa, P_f=200 MPa, 10 wt% muscovite <28 µm, ϕ_f=8.31 %), showing grain-to-grain indentations and truncations (white arrows) indicative of IPS.

3.5. Discussion

Using identical methods and identical quartz sand, Niemeijer et al. (2002 and Chapter 2) demonstrated that IPS dominates the compaction of quartz sand at 400-600 ºC and effective pressures of 50-150 MPa, and is probably controlled by the quartz dissolution reaction rate. Our present microstructural results show evidence for IPS in both quartz-only and quartz-muscovite samples under the same conditions. The mechanical data demonstrate that the presence of muscovite hinders rather than enhances compaction. The amount of muscovite in the samples was too low to form a continuous network or to completely fill the pore space, suggesting that the muscovite did not form a load supporting matrix, so that the quartz grain framework must have supported almost as much of the applied effective pressure as in the pure quartz sand samples. Plastic deformation of intergranular micas could have modestly hindered compaction or enhanced it by promoting grain boundary sliding between quartz grains. However, since IPS was clearly important in all wet samples, we infer that the presence of muscovite did not enhance IPS rates dramatically, but may even have decreased IPS rates.

Recalling the possible effects of phyllosilicates on IPS rates which we have already identified, a decrease in IPS rate due to the addition of muscovite could potentially be explained by dissolution of aluminium from the muscovite in the pore fluid, the dissolved Al^{3+} then lowering the solubility of quartz and slowing the dissolution and precipitation kinetics of quartz (Iler, 1973, 1979; Dove and Rimstidt, 1994) . The amount of Al_2O_3 equivalent in solution after heating (~ 1 hour) was calculated using the only data we know of on the dissolution kinetics of muscovite (Knauss and Wolery, 1989). We extrapolated Knaus and Wolery's dissolution rate data obtained at 70 ºC to the temperature conditions of our experiments using their activation energy of 59 kJ/mol. The results obtained was of the order of ~0.8 ppm Al_2O_3 equivalent for sample CPf 10, which is sufficient to lower dissolution rates of quartz by a measurable amount according to previous work on the effects of Al^{3+} (Iler, 1973, 1979).

However, muscovite can also hinder the precipitation of quartz by decreasing the number of precipitation sites on pore walls (Tada and Siever, 1989; Dewers and Ortoleva, 1991; Mullis, 1993). This could cause a shift in rate controlling mechanism from dissolution towards precipitation, decreasing IPS rate accordingly. If in a pure quartz aggregate the grain boundary fluid occupies an open island-channel structure, rather than an ultra thin film maintained by surface forces, the presence of muscovite in the quartz grain boundaries could possibly retard diffusion of quartz out of the boundaries by supporting a thin fluid film which replaces the more open island-channel structure. This would cause a shift in rate controlling mechanism from dissolution to diffusion, again decreasing IPS rates. It is even possible that in our experiments contact stresses may have been high enough to squeeze water out of some mica-quartz contacts (Israelachvili 1992).

Our microstructural observations do not exclude any of the above explanations for a possible reduction in IPS rates due to the addition of muscovite, since it was present in

quartz grain contacts actively undergoing IPS and at the pore walls. However, our mechanical data show that the decrease in compaction rates caused by adding muscovite does not seem to depend strongly on the amount of muscovite added (5 wt% *vs.* 10 wt% and 20 wt%). This suggests that the observed decrease in IPS rate was caused by a chemical effect, such as a decrease in dissolution rate due to saturation of the pore fluid with Al^{3+}, rather than an effect of muscovite coating grain boundaries or pore walls, or filling the pore space and thus supporting the load. Due to lack of experimental data on the combined influence of alkali-metal cations (notably K^+ in the case of muscovite) and Al^{3+} on dissolution rates in quartz, we can not estimate the amount of decrease or increase in IPS rate the presence of both would cause.

Our results do not confirm the inference of Rutter & Wanten (2000) regarding the accelerating influence of phyllosilicates on pressure solution rate in quartz, nor the work of Hickman & Evans (1995) on the accelerating influence of clay films on pressure solution at halite/silica contacts. However, the pressure solution process at clay-free halite/silica and halite/halite contacts is diffusion controlled (Spiers et al., 1990), rather than interface controlled so that clay in grain boundaries can potentially increase pressure solution rates if it supports a thicker fluid film than in a clay-free boundary. Rutter & Wanten (2000) used an experimental set-up which included a separate reservoir of pure quartz sand as a (easy) sink for dissolved quartz. Precipitation is accordingly unlikely to become rate controlling in their experiments, and any decrease in precipitation rate caused by the presence of phyllosilicates would not be measured as a decrease in compaction rate. The increase of compaction rate that Rutter & Wanten (2000) reported, could perhaps have been caused by an increase in dissolution rate by the presence of alkali-metal cations (e.g.. K^+, Na^+), released from the clay minerals and/or the muscovite. This is purely speculative, however, since doubt remains whether the increase in dissolution kinetics by alkali-metal cations is larger than the decrease caused by cations such as Al^{3+} or Fe^{3+}. Alternatively, the enhancement of IPS reported by Rutter & Wanten (2000) could have been caused by a switch from precipitation or dissolution control in pure quartz sand to the parallel process of source-sink diffusion control in the sand-phyllosilicate samples with pure sand sink. Finally, Rutter & Wanten (2000) argue that the increase in IPS rates they observed may have been caused, in part, by the smaller total amount of quartz compared to the pure quartz samples and by additional compaction of the clay matrix by frictional and intracrystalline plastic processes, but these processes may have played a role in our experiments as well.

Clearly further systematic research is necessary to resolve the question of the effects of phyllosilicates on IPS in quartz. Nonetheless, our results have shown that muscovite causes no dramatic enhancement of IPS under condition favouring dissolution controlled IPS. IPS in nature may be diffusion controlled, especially since predictions of dissolution controlled IPS are too fast for low porosity sandstones. To asses if phyllosilicates have an accelerating effect in the diffusion-controlled field, experiments need to be conducted on coarse-grained samples and/or low porosity samples.

3.6. Conclusions

1. We have conducted 1-D compaction experiments on quartz-muscovite mixtures at a confining pressure of 300 MPa, a fluid pressure of 200 MPa, an effective pressure of 100 MPa and a temperature of 500 °C, in order to investigate the effect of muscovite on IPS rates in quartz sand. Under the chosen conditions dissolution controls the rate of IPS in pure quartz sand.
2. The presence of muscovite does not accelerate IPS rates in quartz sand under these conditions, but decreases compaction rates slightly, possibly due to a decrease in IPS rate.
3. If real, the effect of muscovite in slowing IPS may be due to the net effect of dissolved aluminium (Al^{3+}) decreasing the solubility, dissolution rate and precipitation rate of quartz.
4. The possibility that muscovite (and other phyllosilicates) strongly enhances grain boundary diffusion and hence IPS in quartz under laboratory or natural conditions favouring grain boundary diffusion control in pure quartz can not be eliminated on the basis of our experiments. To test if this occurs, experiments need to be performed on coarse quartz sand, lower porosities or using different pore fluid(s) (e.g. acidic fluids).
5. Enhanced IPS in nature and experiments could also be due to chemical effects on the precipitation and/or dissolution reactions, depending on the composition of the phyllosilicate and competing effects of alkali-metals vs. Al^{3+} or Fe^{3+}. Experiments should be conducted on pure quartz sand with phyllosilicates of systematically varied influence on the composition of the pore fluid but not mixed with the sand.

Chapter 4

INFLUENCE OF PHYLLOSILICATES ON FAULT STRENGTH IN THE BRITTLE-DUCTILE TRANSITION: INSIGHTS FROM ROCK ANALOGUE EXPERIMENTS

This chapter was published as: Niemeijer, A.R. and Spiers, C.J., 2005, Influence of phyllosilicates on fault strength in the brittle-ductile transition: Insights from rock analogue experiments In: High Strain Zones: Structure and Physical Properties, D. Bruhn and L. Burlini (eds) Special Publication. Geological Society of London, pp.303-327

Abstract

Despite the fact that phyllosilicates are ubiquitous in mature fault and shear zones, little is known about the strength of phyllosilicate-bearing fault rocks under brittle-ductile transitional conditions where cataclasis and solution transfer processes are active. In this study, we explored steady state strength behaviour of a simulated fault rock, consisting of muscovite and halite, using brine as a pore fluid. Samples were deformed in a rotary shear apparatus under conditions where cataclasis and solution transfer are known to dominate the deformation behaviour of the halite. It was found that the steady state strength of these mixtures is dependent on normal stress and sliding velocity. At low velocities (<0.5 μm/s), the strength increases with velocity and normal stress, and a strong foliation develops. Comparison with previous microphysical models shows that this is a result of the serial operation of pressure solution in the halite grains accommodating frictional sliding over the phyllosilicate foliation. At high velocities (>1 μm/s), velocity-weakening frictional behaviour occurs along with the development of a structureless cataclastic microstructure. Revision of previous models for the low velocity behaviour results in a physically realistic description that fits our data well. This is extended to include the possibility of plastic flow in the phyllosilicates and applied to predict steady state strength profiles for continental fault zones containing foliated quartz-mica fault rocks. The results predict a significant reduction of strength at mid-crustal depths and may have important implications for crustal dynamics and seismogenesis.

4.1. Introduction

Classical models for the steady state strength of the crust consist of a two-mechanism brittle-ductile strength profile, based on Byerlee's Law plus a dislocation creep law for quartz (e.g. Sibson, 1977; Schmid and Handy, 1991; Scholz, 2002). However, grain size sensitive processes, such as pressure solution, and the production of weak phyllosilicates known to be important under mid-crustal, brittle-ductile transitional conditions (e.g. Rutter and Mainprice, 1979; Passchier and Trouw, 1996; Imber et al., 1997; Holdsworth et al., 2001) are neglected, as are the effects of phyllosilicate foliation development. Such processes have long been anticipated to lead to some form of hybrid frictional-viscous rheological behaviour in the brittle-ductile transition (Sibson, 1977; Rutter and Mainprice, 1979; Lehner and Bataille, 1984/85; Schmid and Handy, 1991; Wintsch et al., 1995; Handy et al., 1999). The steady-state stress levels at which mid-crustal fault rocks deform may, therefore, be much lower than those predicted using a classical two-mechanism

strength profile (see Figure 1 and Sibson, 1977; Byerlee, 1978; Schmid and Handy, 1991; Scholz, 2002). Moreover, phyllosilicate foliation development and processes such as pressure solution can be expected to play an important role in controlling transient healing, cementation and strength recovery of fault rocks, thus influencing the rate and state dependent frictional and seismogenic behaviour (Fredrich and Evans, 1992; Beeler et al., 1994; Karner et al., 1997; Bos and Spiers, 2000; Beeler et al., 2001; Bos and Spiers, 2002a; Saffer and Marone, 2003).

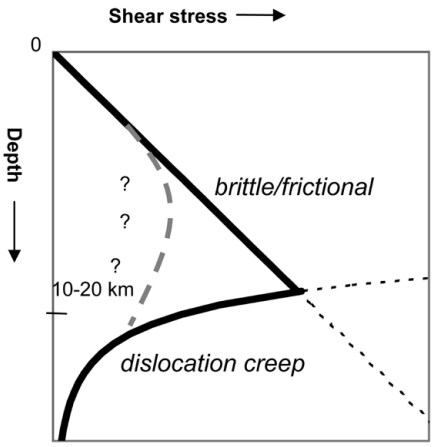

Figure 4.1: Schematic of classical crustal strength profile, showing brittle-frictional behaviour dominating at upper crustal levels, and dislocation creep determining crustal strength at deeper levels (solid lines). The dashed line represents the widely accepted effects of fluid-assisted deformation mechanisms on crustal strength (Figure after Bos et al. 2000b)

Numerous authors have considered the possible weakening effects of phyllosilicates, foliation development, pressure solution and cataclasis within faults and shear zones in the brittle-ductile transition, using both theoretical and experimental approaches (Rutter and Mainprice, 1979; Lehner and Bataille, 1984/85; Logan and Rauenzahn, 1987; Kronenberg et al., 1990; Shea and Kronenberg, 1992; Mares and Kronenberg, 1993; Shea and Kronenberg, 1993; Chester, 1995; Blanpied et al., 1998; Gueydan et al., 2001; Gueydan et al., 2003; Jefferies et al., 2006, in press). Such studies have produced a consensus that fault rocks containing a contiguous and well-developed phyllosilicate (mica) foliation can potentially be as weak as the frictional strength of the phyllosilicate, at high crustal levels (Logan and Rauenzahn, 1987; Shea and Kronenberg, 1992), or as weak as the crystal plastic flow strength of the phyllosilicate basal plane, at deeper levels (Hickman et al., 1995; Wintsch et al., 1995). However, the time and technical limitations of experiments on silicate fault rocks (e.g. Blanpied et al., 1991; Chester and Higgs, 1992; Chester, 1994; Blanpied et al., 1995; Kanagawa et al., 2000) have precluded systematic studies of large strain sliding behaviour, with associated foliation development, under hydrothermal, brittle-ductile conditions where the relevant processes are active. Large strain, steady state rheological laws for faults incorporating the effects of cataclasis, pressure solution and foliation development in the brittle-ductile transition are therefore not available.

Recently, Bos and co workers (Bos et al., 2000a, b; Bos and Spiers, 2001) performed ultra high strain rotary shear experiments on simulated fault gouges consisting of mixtures of halite (rock salt) and kaolinite. The experiments were done under room temperature conditions where pressure solution and cataclasis are known to dominate over dislocation creep in the halite, thus modelling the brittle-ductile transition. In wet samples with >10 wt% clay brittle failure was followed by strain weakening towards a steady state

shear strength that was dependent on both sliding rate and normal stress (frictional-viscous flow). Strongly foliated microstructures were produced in these experiments, closely resembling natural mylonite or phyllonite microstructures, without the operation of dislocation creep. Bos and Spiers (2002b) developed a microphysical model to explain the observed steady state behaviour, based on the steady-state microstructure and corresponding mechanical analogue diagram of Figure 4.2. In this model, the shear strength of the gouge is determined by the combined resistance to shear offered by frictional sliding on the phyllosilicate foliae, pressure solution in the halite and dilatation on the foliation (work against the normal stress). The model accordingly predicts three velocity regimes, namely 1) a low-velocity regime, where pressure solution is so easy that the strength of the gouge is determined by sliding friction on the foliation, 2) an intermediate velocity regime, where the strength of the gouge is determined by accommodation through pressure solution, and 3) a high velocity regime, where pressure solution is too slow to accommodate geometric incompatibilities, so that dilatation occurs. Bos and Spiers (2002b) reported good agreement between their experimental data and model and went on to apply the model to predict crustal strength profiles for quartz-mica fault rocks. These showed a major weakening (2-5 times) of crustal fault zones around the brittle-ductile transition (5-15 km, see Bos and Spiers, 2002b), in qualitative agreement with inferences drawn from numerous geological and geophysical studies (Lachenbruch and Sass, 1980; Schwarz and Stöckhert, 1996; Imber et al., 1997; Stewart et al., 2000; Zoback, 2000; Townend and Zoback, 2001).

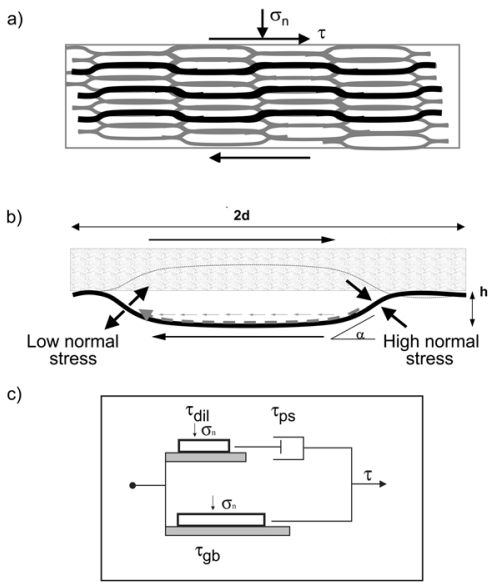

Figure 4.2:
a) Schematic diagram of the model microstructure proposed by Bos and Spiers (2002b), showing contiguous, anastomosing network of phyllosilicates surrounding elongate grains of a soluble solid. The shear strength of the gouge is determined by the combined resistance to shear offered by frictional sliding on the phyllosilicate foliae, pressure solution in the halite and dilatation on the foliation (work done against the normal stress).
b) Schematic drawing of representative grain element of matrix, showing an active sliding surface in black. Shear sense is right-lateral. The diffusive mass flux from source to sink regions is indicated by a dashed arrow. The foliation waves have amplitude h, the grains have long axis d. The leading edge of the grain is inclined at angle α to the horizontal (Figure from Bos and Spiers, 2002b).
c) Mechanical analogue diagram for shear deformation of the model microstructure, assuming zero porosity. τ_{gb} is the shear stress contribution offered by frictional sliding on the phyllosilicate foliae (regime 1), τ_{ps} is the shear stress contribution offered by pressure solution of the soluble solid (regime 2), τ_{dil} is the shear contribution offered by dilatation on the foliation (work against the normal stress, regime 3) and σ_n is the normal stress on the gouge.

However, there are several aspects of the Bos-Spiers model that have not been tested or are not physically realistic. First, the model is based on experiments in which the phyllosilicate phase (ultrafine kaolinite) was unrealistically fine in relation to the halite grains and to natural fault rock microstructures (e.g Imber et al., 1997; Jefferies et al., 2006, in press). Second, the model has not been tested in the low velocity regime (Regime 1), nor adequately at high velocities (Regime 3) where it must eventually break down due to fault rock failure. Third, the model employs an unnecessary and physically unrealistic approximation to couple the mechanical effects of pressure solution and dilatation, and deals only with a single-valued grain size. Finally, the model is restricted to frictional behaviour of the phyllosilicate foliae, whereas under the conditions of the brittle-ductile transition, phyllosilicates may more easily deform by dislocation creep processes (see Kronenberg et al., 1990; Shea and Kronenberg, 1992; Mares and Kronenberg, 1993; Shea and Kronenberg, 1993).

In this chapter, we present experimental results on synthetic halite-muscovite mixtures, obtained using a more realistic phyllosilicate grain size (d_{med}= ~13 μm). We explore a wider range of sliding velocities (0.001 μm/s-13 μm/s) than Bos and Spiers (2002b) accessing both low and high velocity regimes and thus testing their model across regimes 1-3. In addition, we re-formulate the Bos-Spiers model to incorporate proper mechanical coupling of viscous (pressure solution) and frictional (dilatation) processes and to allow for crystal plastic flow in the phyllosilicates. We also consider the effects of a distributed grain size. Finally, we extrapolate our improved model to natural conditions to construct crustal strength profiles and we consider their implications for mature crustal fault zones.

4.2. Experimental method

4.2.1. Apparatus

The present experiments were conducted at room temperature on simulated (NaCl-Muscovite) fault gouge using the rotary shear apparatus, previously described in detail by Bos et al (2000a, 2000b) with the annular sample assembly shown in Figure 4.3a. This assembly consists of two, toothed, stainless steel rings (teeth height is ~0.1 mm) , sandwiching a layer of synthetic halite-muscovite gouge. When located in the shear apparatus the rings are rigidly gripped between two cylindrical forcing blocks. The lower forcing block is rotated at controlled angular velocity by a servo-controlled drive motor plus gearbox, while the upper block is maintained stationary, thus leading to shear on the synthetic fault. Sliding velocity is controlled to within 0.001 μm/s. Normal stress is applied and servo-controlled to within 0.01 MPa using an Instron 1362 loading frame and measured using a 100 kN Instron load cell. Shear stress on the fault is measured with a resolution of ~ 10 kPa, using a torque gauge which provides the couple necessary to hold the upper forcing block stationary. Displacement normal to the fault surface (i.e. gouge compaction/dilatation)

is measured using a Linear Variable Differential Transformer (LVDT, 1 mm full scale, 0.01 % resolution) located inside the upper forcing block. Rotary displacement is measured using a potentiometer geared to the rotation of the lower forcing block. The synthetic fault assembly is sealed using a plastic inner ring and a stainless steel outer ring, both fitted with O-rings (see Figure 4.3b). Pore fluid is introduced through the outer sealing ring. All experiments were conducted at room temperature and atmospheric pore fluid pressure (drained conditions).

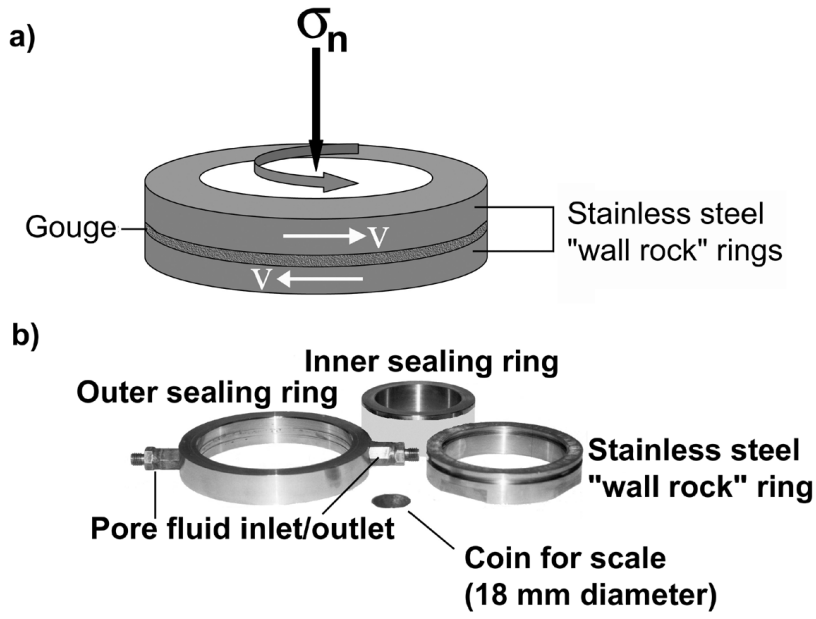

Figure 4.3:
a) Schematic diagram of the ring-shear configuration used in this study. Granular fault gouge is sheared between annular stainless steel wall rock rings at controlled velocity v and normal stress σ_n.
b) Photograph of the wall-rock rings and the sealing rings that constitute the sample assembly.

4.2.2. Sample Material

Synthetic fault gouge material was prepared by mixing analytical grade granular halite with fine-grained muscovite in the appropriate proportions (0 wt%, 10 wt%, 20 wt%, 30wt%, 50 wt%, 80 wt% and 100 wt% muscovite, see Table 4.1). Particle size analysis, performed using a Malvern particle sizer showed that the halite had a median grain size of 104 μm, with 90% of the grains in the range 60-110 μm. The muscovite was a commercially available natural muscovite mined in Aspang, Austria, and was supplied by Internatio B.V. The median grain size of this material was 13 μm (equivalent spherical diameter), with 90% of the grains in the range 3-50 μm. Sodium chloride solution (brine), saturated with respect to the halite, was used as the pore fluid, except for one control experiment in which silicone oil was used.

Table 4.1:
List of experiments performed plus corresponding experimental conditions. Note that σ_n is the normal stress on the fault and v is the applied sliding velocity.
n.d. : not determined
** : total shear displacement after the dry run-in stage*

Sample Code	Composition Muscovite : Halite	Dry run-in displacement(mm)	Fluid	σ_n stepping sequence (MPa)	Velocity-stepping sequence (μm/s)	Total shear displacement *	Final Gouge thickness (μm)
Hal1	0% : 100%	0	brine	1, 0.5, 2, 3, 1	1	29.38	n.d.
Mus1	100% : 0%	69	brine	5, 7, 9, 5, 3, 1	1, 10, 0.1, 1, 0.03, 1	40.01	1028
Mus2	10% : 90%	59	brine	5, 9, 1, 5	1, 10, 0.1, 1, 0.03, 1	44.18	1470
Mus3	20% : 80%	49	brine	5	1, 0.8, 0.5, 1, 0.1, 0.03, 0.3, 1, 0.01, 0.003, 0.008, 0.3, 1	44.96	1318
Mus4	20% : 80%	61	brine	5	1, 3, 5, 7, 9, 11, 13, 11, 9, 7, 5, 3, 1, 5, 10	171.04	975
Mus5	20% : 80%	50	brine	5	0.03	35.35	967
Mus6	20% : 80%	50	brine	5	1	30.10	1142
Mus7	20% : 80%	50	brine	5	5	30.11	1135
Mus8	20% : 80%	53	brine	5	13	30.05	1295
Mus9	20% : 80%	0	brine	5, 4, 3, 2, 1	1	32.43	1212
Mus10	20% : 80%	0	brine	5, 4, 3, 2, 1	5	38.87	1361
Mus11	20% : 80%	0	brine	5, 4, 3, 2, 1, 2, 3, 4, 5	10	60.14	1376
Mus12	20% : 80%	0	silicone oil	5	1, 10, 0.1, 1, 0.03, 1, 3, 5, 1, 0.1	44.62	1007
Mus13	20% : 80%	0	none	5	1, 10, 0.1	38.05	n.d.
Mus14	30% : 70%	45	brine	5	1, 10, 0.1, 1, 0.03, 1, 3, 5, 10, 1	33.72	n.d.
Mus15	30% : 70%	66	brine	5	1, 10, 0.1, 1, 0.03, 1, 10, 1, 3, 1, 0.01	50.53	997
Mus16	20% : 80%	0	none	5	1, 10, 0.1, 1, 0.03, 1, 10, 1, 0.1	38.46	1555
Mus17	20% : 80%	0	brine	5	1, 0.001	8.27	880
Mus20	0% : 100%	54.8	brine	5	1, 10, 0.1, 1, 0.03, 1, 3, 5, 7, 9, 11, 13, 11, 1, 0.01, 0.003	106.51	1100
Mus21	80% : 20%	50.3	brine	5	1, 10, 0.1, 1, 0.03, 1, 0.00	30.91	793
Mus22	50% : 50%	55.5	brine	5	1, 10, 0.1, 1, 0.03, 1, 0.01	47.05	955
Mus23	20% : 80%	49.5	brine	5	0.1	30.3	1026
Mus24	20% : 80%	51.8	none	5	1	-	1568
Mus25	20% : 80%	0	brine	5, 4, 3, 2, 1	0.03	30	1300

4.2.3. Testing Procedure

Samples were prepared for testing by sandwiching a quantity of uniformly distributed gouge (usually ~ 8 g) between the two stainless steel wall rock rings shown in Figure 4.3, with the two sealing rings in place. This yielded a starting gouge thickness of ~1.5-2.0 mm. The sample assembly was then located in the rotary shear machine and subjected to a fixed normal stress of 1 MPa under "room dry" conditions for 10 minutes, by which point all compaction had ceased. Most samples were dry-sheared to a displacement of ~50 mm at a sliding velocity of 1 μm/s and a normal stress of 5 MPa, to produce a well-controlled microstructure for the wet stage of the experiments. The samples were then unloaded and the thickness of the gouge was determined. The assemblies were then connected to the pore fluid system, evacuated and saturated with the appropriate pore fluid. They were then reloaded to the prescribed normal stress (σ_n) and sheared at a chosen constant sliding velocity (v). Both normal stress and velocity stepping techniques were used to obtain the shear stress as a function of σ_n and v for individual samples (i.e. fixed mica-content), after achieving steady state sliding behaviour. The experiments were terminated by halting the rotary drive motor and unloading the sample. The pore fluid system was then disconnected from the sample assembly and residual brine was flushed out using dry hexane. Finally, the thickness of the sample assembly was re-measured, the sealing rings were removed and the gouge was carefully detached from the stainless steel rings. After macroscopic inspection, the samples were dried, impregnated with blue-stained epoxy resin and sections were cut for optical microscopy study.

In this way, the sliding behaviour of the synthetic halite-muscovite gouge was systematically investigated, varying normal stresses in the range 1-9 MPa, sliding velocities in the range 0.001-13 μm/s and muscovite-content in the range 0-100 wt%. We also performed a number of experiments at constant sliding velocity and constant normal stress to isolate the influence of displacement on sliding behaviour. Note that the dry shearing stage was omitted from a total of eight experiments to be able to directly compare the results with data obtained by Bos et al (2000a); this has little influence on the results for steady state strengths. All experiments and corresponding experimental conditions are listed in Table 4.1.

4.3. Results

4.3.1. Dry run-in stage

Shear stress and compaction versus displacement curves for the dry run-in stage of samples spanning the full range of muscovite content investigated (0-100 wt%, Mus1, 2, 4, 15, 20, 21 and 22) are presented in Figures 4.4a and 4.4b. Recall that all dry shearing was performed at a sliding velocity of 1 μm/s and a normal stress of 5 MPa. The pure muscovite sample and the 80 wt% muscovite sample (Mus1 and 21) showed initial quasi-elastic loading followed by "yield" and then stable sliding with gradual slip hardening. At ~60 mm of displacement the strength of the pure muscovite gouge reached a steady value of ~2.3 MPa. The sample with 80 wt% muscovite (Mus21) is slightly stronger, reaching a steady value of ~2.6 MPa at ~50 mm of displacement.

Salt-mica samples with less than 80 wt% muscovite showed an initial quasi-elastic stress increase, followed at ~2-3 mm displacement by a peak strength and then marked slip weakening up to 15-35 mm displacement (see Mus2, 4, 15 and 22, Figure 4.4a). Beyond ~15–35 mm of displacement a transition from stable sliding to stick-slip behaviour occurred. No systematic correlation was found between the amount of muscovite and the displacement at which the transition to stick-slip behaviour occurred, although the sample with 50 wt% muscovite (Mus22) showed stable sliding up to 35 mm of displacement. Beyond ~35 mm displacement, the peak strength of salt-mica samples with less than 80 wt% muscovite lay in the range 2-2.6 MPa. In contrast to these halite-mica samples, the single pure salt sample tested (Mus20), showed only a minor stress drop after initial loading, followed by slip hardening beyond ~3 mm displacement to result in a final shear stress of ~ 4.6 MPa at 50 mm displacement. All samples showed strong initial compaction normal to the fault in the first 5-10 mm of dry displacement, except for some minor dilatation just before the peak stress was reached. Beyond ~5-10 mm of displacement, compaction proceeded at a lower but still significant rate. The muscovite-rich samples exhibited particularly large compaction up to ~ 50 mm of displacement. The pure salt control sample showed continuous compaction, except for a strong dilatation event at ~ 3 mm displacement, just prior to the peak shear strength.

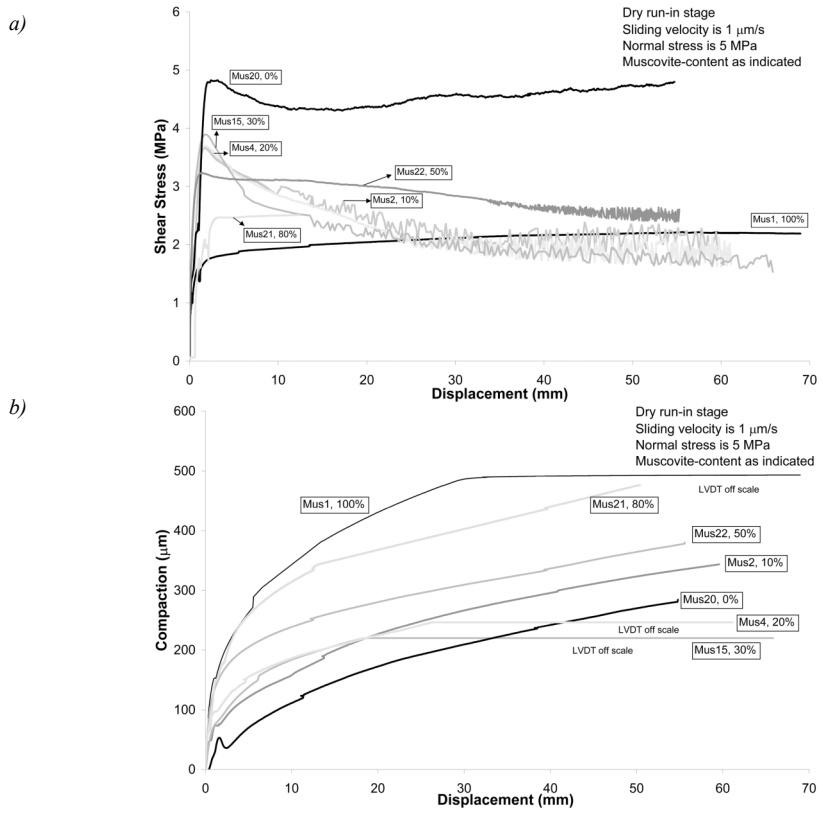

Figure 4.4: Shear stress and volume change versus displacement data for the dry run-in stage for samples Mus1, Mus4, Mus15, Mus20, Mus21 and Mus22.
a) Shear stress versus displacement curves
b) Compaction versus displacement curves

4.3.2. Wet stage: Stress-displacement behaviour

In Figures 4.5a and 4.5b, typical shear stress and compaction versus displacement curves are presented for halite-muscovite samples deformed wet at fixed sliding velocity and normal stress. The samples depicted all contained 20 wt% muscovite (Mus5, 6, 7, 8 and 23). Samples deformed at low velocities (< 1 μm/s) show smooth yielding behaviour followed by stable steady state sliding. Samples deformed at sliding velocities of 1 μm/s and above consistently show an initial stress peak followed by rapid weakening. After displacements of ~10 mm steady state sliding was achieved, except at the highest sliding velocity investigated (13 μm/s), where stick-slip behaviour was obtained beyond ~4 mm of displacement. The peak stress of such stick-slip events remained roughly constant, but the amplitude of the cycles increased (i.e. the minimum stress decreased). All samples

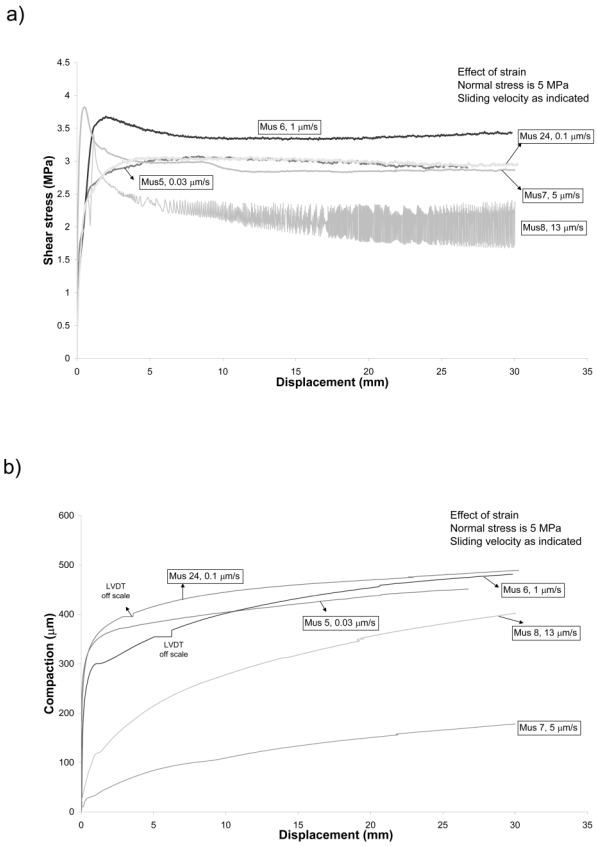

Figure 4.5: Shear stress and volume change versus displacement data for samples containing 20 wt% muscovite deformed at fixed sliding velocity and normal stress (Mus5, Mus6, Mus7, Mus8, Mus24).
a) Shear stress versus displacement curves
b) Compaction versus displacement curves

compacted rapidly during loading to the peak stress or smooth yield point (Figure 4.5b), beyond which compaction continued in a steady fashion. Samples showing a peak stress followed by slip weakening generally displayed minor dilatation just prior to the stress peak. Total compaction was highest in the slowest experiments.

4.3.3. Wet stage: Effect of normal stress

In Figure 4.6a, we show representative mechanical data obtained from one of the four normal stress stepping experiments (Mus10) performed under wet conditions on samples with fixed mica-content (20 wt%). All such experiments showed significant slip weakening in the first 5-10 mm of displacement after the initial peak stress, then reaching a

steady state strength. Subsequent downward (or upward) normal stress stepping led to an immediate decrease (or increase) in shear stress and to transient dilatation (or increased compaction) of the samples. Typical shear stress vs. normal stress data obtained for samples containing 20 wt% muscovite, at fixed sliding velocities of 0.03, 1, 5 and 10 μm/s (Mus9, 10, 11 and 25) are presented in Figure 4.6b. For comparison, similar data are added for pure halite and pure muscovite samples sheared at 1 μm/s (Hal1 and Mus1, respectively). We plot only data obtained for stable, steady state sliding. Note that each sample shows a linear relation between shear stress and normal stress, which can be accurately described by a Coulomb-type criterion written

$$\tau = \mu^{ss} \cdot \sigma_n + C \qquad (4.1)$$

where μ^{ss} is a steady state friction coefficient and C is the cohesion (in MPa). The friction coefficient and cohesion values obtained are given in Table 2. Note from Figure 4.6b that the pure halite sample (Hal1) shows the highest strength with a coefficient of friction of ~0.8 (Table 4.2), while the pure muscovite sample is the weakest, with a coefficient of friction of ~0.3 (Table 4.2). The samples containing 20 wt% muscovite show intermediate strength. Note also that the friction coefficient of the 20% muscovite-halite mixture decreases with increasing sliding velocity for velocities from 1 μm/s (refer Figure 4.6b and Table 4.2).

Table 4.2:
Strength parameters determined for samples Hal1, Mus1, Mus9, Mus10, Mus11 and Mus25

Sample Code	Composition Muscovite : Halite	Sliding Velocity (μm/s)	Friction Coefficient	Cohesion (MPa)
Mus25	20% : 80%	0.03	0.394	0.127
Mus9	20% : 80%	1	0.619	0.149
Mus10	20% : 80%	5	0.486	0.261
Mus11	20% : 80%	10	0.496	0.111
Hal1	0% : 100%	1	0.802	0.137
Mus1	100% : 0%	1	0.312	0.160

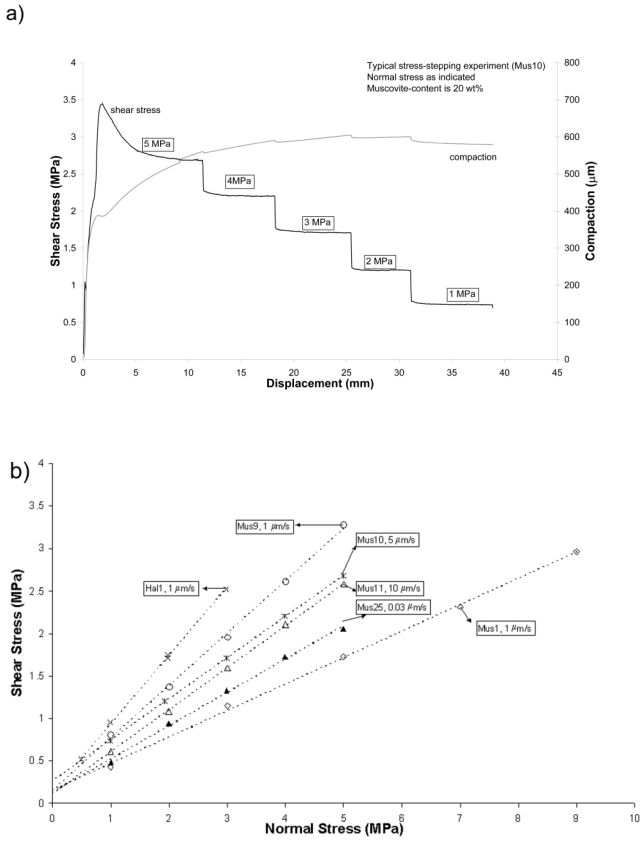

Figure 4.6: Typical data obtained in normal stress stepping experiments.
a) Shear stress and compaction strain versus sliding displacement for a 20 wt% muscovite sample (Mus10), subjected to normal stress stepping at 5 μm/s.
b) Steady state shear stress versus normal stress data which can be described by a Coulomb-type criterion with a friction coefficient and cohesion.

4.3.4. Wet stage: Effect of sliding velocity

We present data from a typical velocity-stepping experiment (Mus2) in Figure 4.7a. Upon a change in sliding velocity, an instantaneous effect on the strength was observed, in all such experiments, followed by a gradual approach to a new steady state strength (cf. conventional rate-and state-dependent friction experiments -(Dieterich, 1979; Ruina, 1983; Marone, 1998; Scholz, 1998). A representative set of data on steady state shear strength versus sliding velocity obtained in our experiments is presented in Figure 4.7b. These data again show that the pure halite and pure muscovite gouges are the strongest and weakest materials tested, with mixed compositions being intermediate in strength. Moreover, the steady state shear strengths of pure halite and pure muscovite gouge are more or less velocity independent. However, mixed muscovite-halite gouges show clear rate effects. For

samples containing 10-80 wt% muscovite, two types of behaviour can tentatively be identified. At sliding velocities below ~ 1 µm/s, the steady state shear strength increases with sliding velocity, i.e. the samples are velocity-strengthening. At higher velocities, the samples become weaker with increasing velocity, i.e. the samples are velocity-weakening.

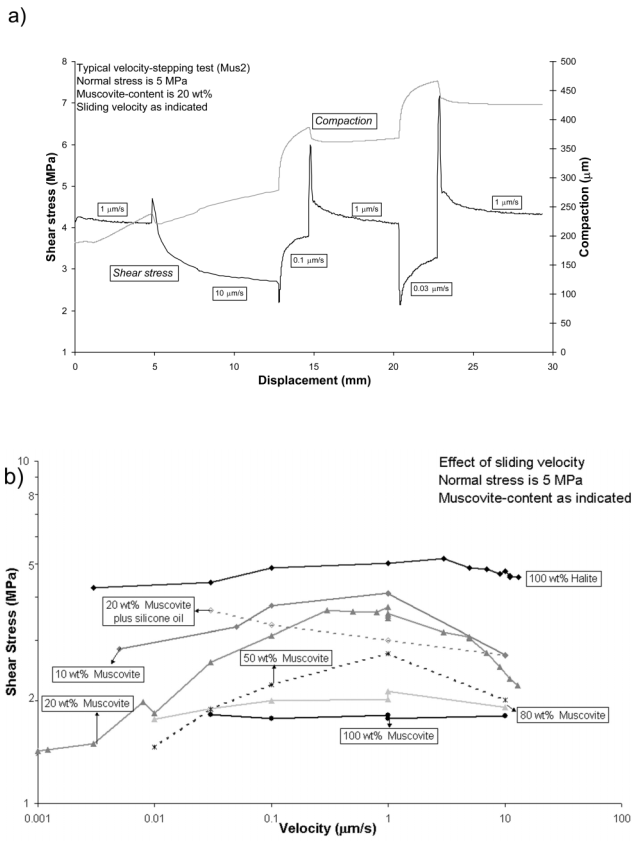

Figure 4.7: Effect of sliding velocity on steady state shear strength of gouges.
a) Shear stress and compaction strain versus sliding displacement for a 20 wt% muscovite sample (Mus2), subjected to velocity stepping at a normal stress of 5 MPa.
b) Steady state shear stress versus sliding velocity plot using representative data from velocity-stepping experiments.

4.3.5. Wet stage: Effect of muscovite-content

The effect of muscovite content on steady state shear stress is plotted in Figure 4.8, by combining shear stress data obtained from different samples at fixed sliding velocities and at a fixed normal stress of 5 MPa. The curves for samples deformed at low and high velocities show a systematic decrease of steady state shear stress supported with increasing muscovite-content, notably up to a muscovite-content of 30 wt%. Above 30 wt% muscovite, the steady state shear strength of the mixed samples is similar to that of the pure muscovite (see also Figure 4.7b). Samples deformed at intermediate sliding velocities of ~ 1 μm/s show a more continuous decrease in strength with muscovite content (Figure 4.8).

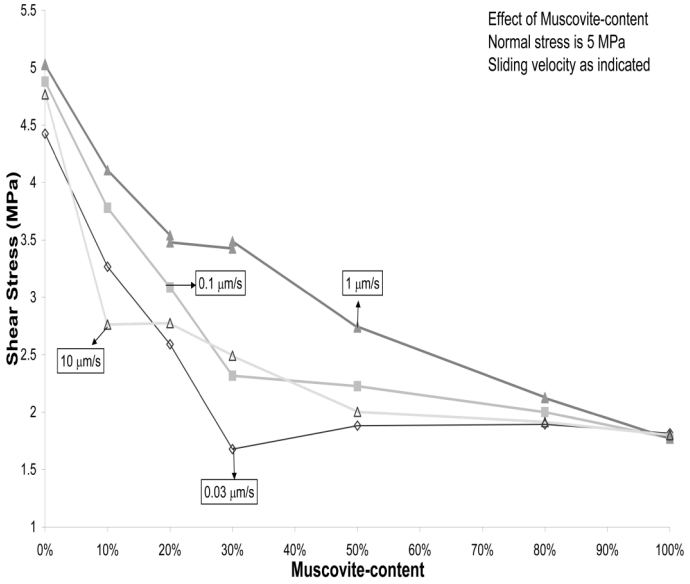

Figure 4.8: Effect of muscovite content on steady state shear strengths of gouges at different sliding velocities. Normal stress is 5 MPa in all experiments.

4.4. Microstructural Observations

The microstructure developed in the dry run-in stage of our experiments was investigated using the sample obtained from experiment Mus24 (20 wt% muscovite), which was terminated directly after the dry run-in. Its microstructure is illustrated in Figures 4.9a and b. The gouge shows numerous halite clasts (30 vol%) which are little affected by the deformation, as evidenced by their resemblance to the starting halite grains, and by the absence of intragranular fractures. These are embedded in a fine-grained mixture of halite and muscovite. The halite grains in the matrix are around 10 μm in size and therefore significantly finer than the starting grain size fraction (60-110 μm). The muscovite grains appear little affected by deformation and their size is similar to the starting grain size fraction. Some regions of the gouge (~20 vol.%, especially near the edges of the gouge) are relatively enriched in muscovite and contain fewer halite clasts than other regions. In plane polarized light (Figure 4.9a), the dry sheared gouge appears structureless with no clear foliation. However, with crossed polarizers the muscovite flakes are seen to define a weak, anastomosing foliation orientated at ~30 ° to the fault zone boundaries (Figure 4.9b). Some halite clasts are crudely elongated within this foliation. A sharp, continuous shear band was observed parallel and adjacent to the lower shear zone boundary of sample Mus24 (Y-shear, see arrows in Figure 4.9b). No such feature was present near the upper boundary. This boundary-parallel Y-shear mainly consists of fine, aligned muscovite flakes and is ~5-15 μm thick.

The wet-deformed samples show little or no evidence for boundary-parallel faults (Y-shears). Instead, these samples show a complex range of microstructures that depend on wet sliding velocity. Figures 4.10a-d illustrate the microstructures developed in four samples deformed to ~30 mm of wet displacement at sliding velocities of 0.03, 0.1, 5 and 13 μm/s (Mus5, 23, 7, and Mus8, respectively) after the dry run-in stage. This range of velocities covers both the velocity-strengthening and the velocity-weakening regimes of Figure 4.7b. Unlike the dry-sheared sample, the sample deformed wet at the lowest sliding velocity (Mus5, Figure 4.10a) shows a strongly foliated microstructure with only a few (~10 vol%) asymmetric sigmoidal halite clasts and has the general appearance of an S-C mylonite. The fine-grained matrix consists of an intercalation of muscovite (~10 μm) and halite grains (~15-30 μm, see Figure 4.11a), in which the muscovite flakes together with elongated halite grains define the main foliation at an angle of ~25 ° to the shear zone boundary. With increasing velocity (i.e. going from Figure 4.10a to d), the number and volumetric fraction of halite clasts increases and the gouge becomes less well foliated and more chaotic. The shape of the halite clasts progressively changes from sigmoidal forms at 0.03 and 0.1 μm/s (Figure 4.10a, b) to grains with a much more blocky and angular appearance at velocities of 5 and 13 μm/s. Indeed, the microstructure evolves from one with a foliated mylonitic character at low sliding velocities ($\leq$ 0.1 μm/s) to an almost structureless cataclastic microstructure at high velocities ($\geq$ 5 μm/s). The sample deformed

at the highest sliding velocity (Mus8, Figure 4.10d)) shows almost no foliation but is characterized by angular halite clasts embedded in a fine-grained structureless matrix. The matrix consists of a poorly sorted mixture of fine halite with muscovite flakes coating all grain boundaries (Figure 4.11b).

For samples Mus5 and Mus23 (constant sliding velocity tests) we determined halite grain sizes using manual tracings and image analysis. It was found that the halite grain size was more or less log-normally distributed in these samples with an average grain size of 20 μm and a relative standard deviation of 0.8.

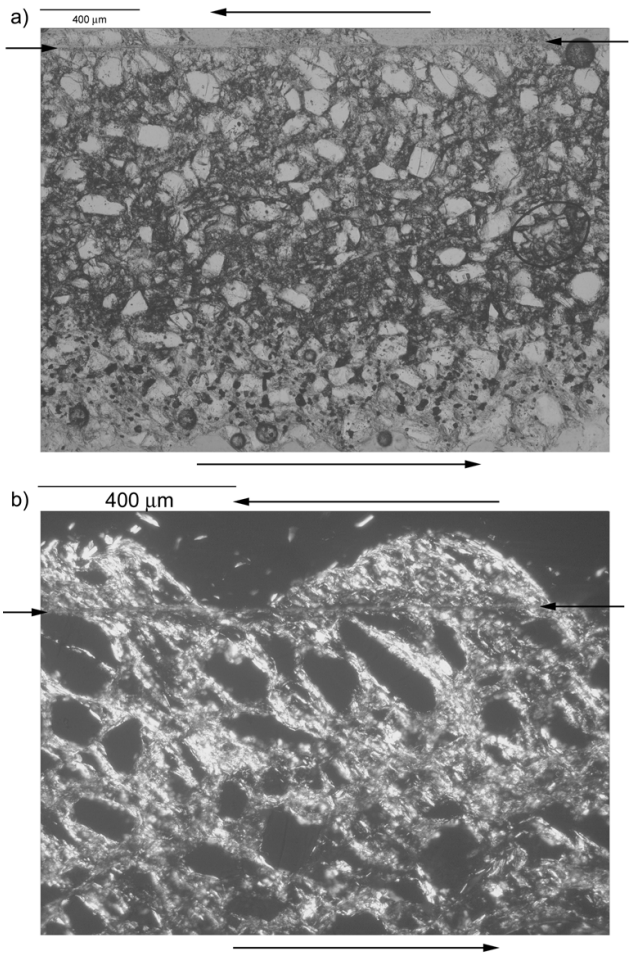

Figure 4. 9: Optical micrographs showing microstructures developed in the initial dry run-in stage of deformation, sample Mus24 (20 wt% muscovite, shear strain is ~40)
a) Plane polarized light: note chaotic structure with halite clasts embedded in a fine halite-muscovite matrix. A boundary parallel Y-shear is evident (small arrows). Shear sense as indicated.
b) Crossed polarized light: note weak foliation and Y-shear developed at the boundary of the gouge (small arrows). Shear sense as indicated.

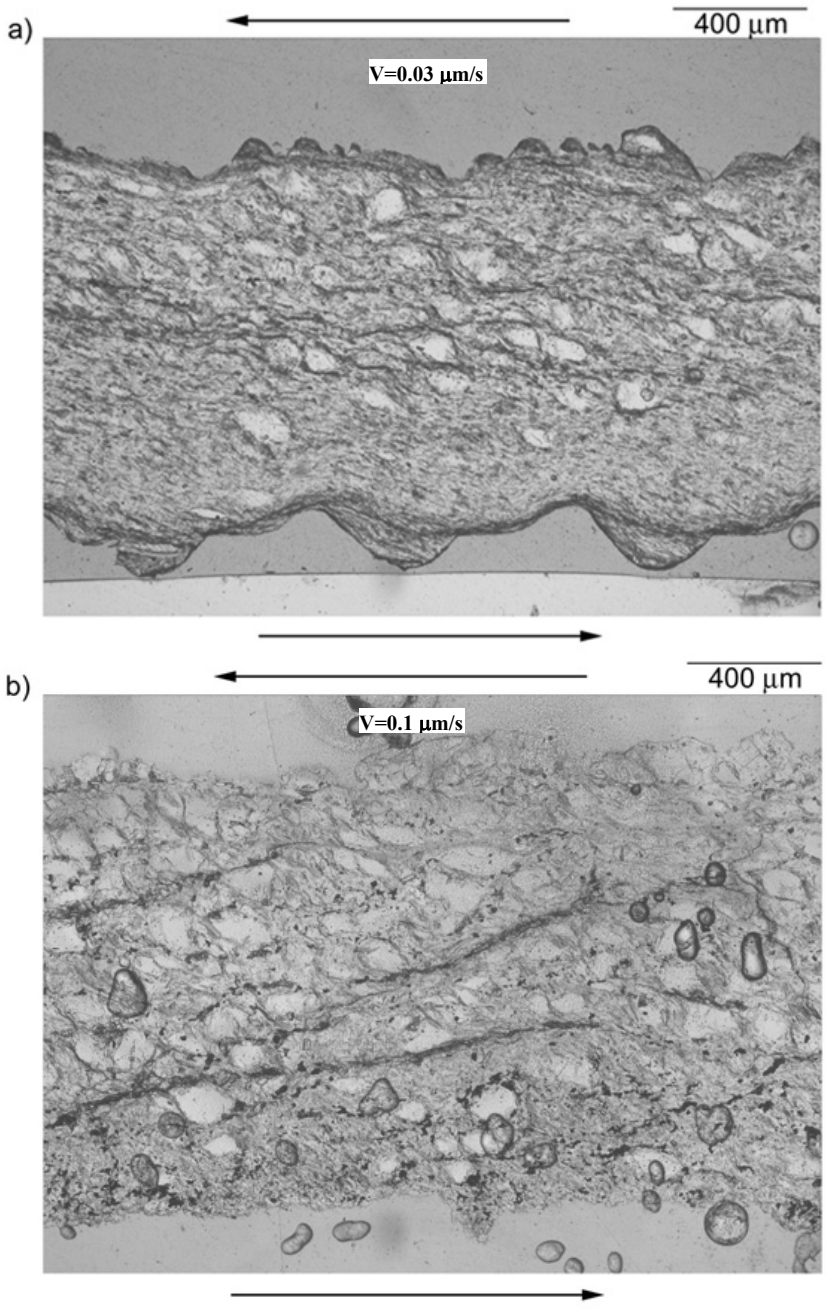
a)
400 µm
V=0.03 µm/s
b)
400 µm
V=0.1 µm/s

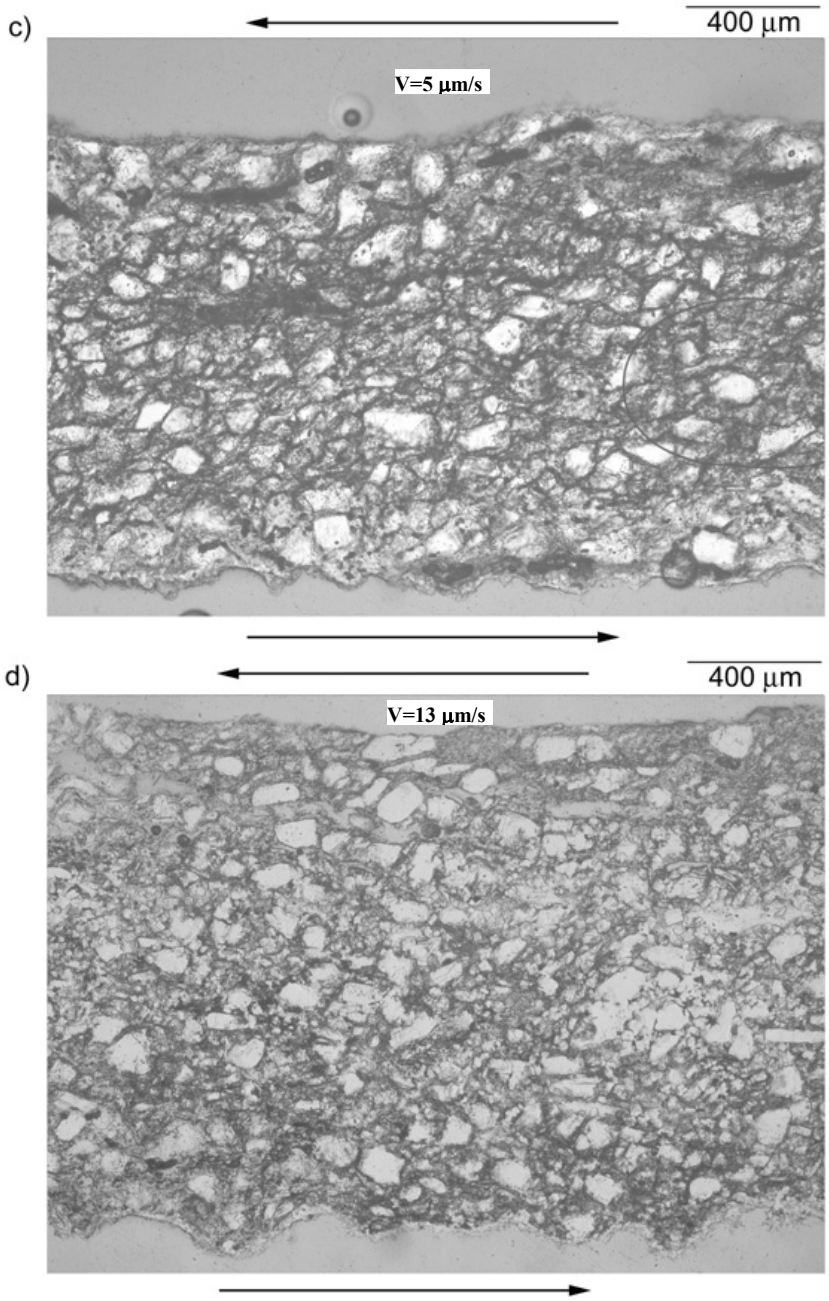

Figure 4.10: Microstructural development with increasing sliding velocity in samples deformed wet at velocities of 0.03 (a, Mus5), 0.1 (b, Mus24), 5 (c, Mus7) and 13 µm/s (d, Mus8). Muscovite content is 20 wt%, normal stress is 5 MPa and total (wet) shear strain is ~25 (see also Table 1). Note progression from a mylonitic structure at low velocity to a cataclastic structure at high velocity. Shear sense as indicated.

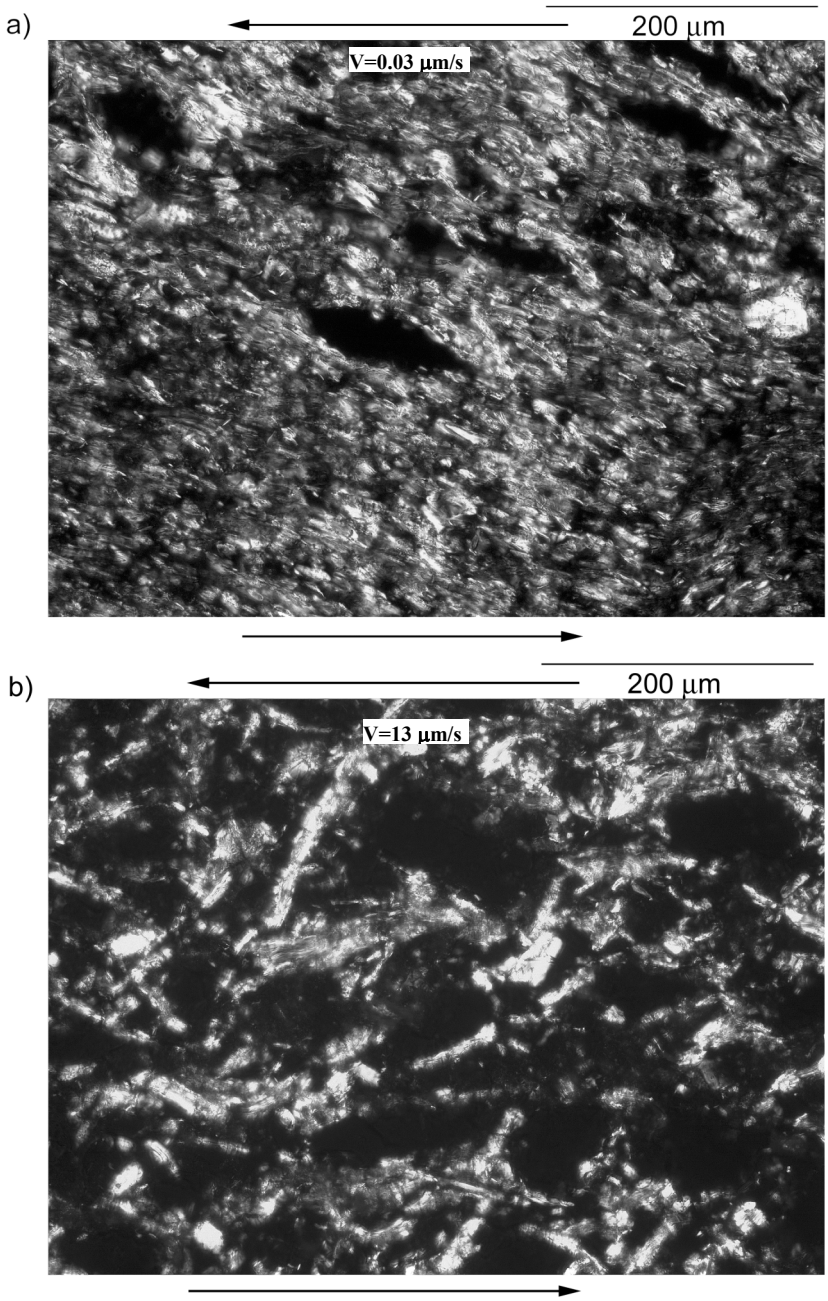

Figure 4.11: Optical micrographs showing matrix microstructure in samples deformed at (a) 0.03 µm/s (Mus5) and (b) 13 µm/s (Mus8). Note the change from a foliated to a structureless matrix. Shear sense as indicated.

4.5. Discussion

The aim of the present experiments was to test the microphysical model for steady-state frictional-viscous flow of foliated fault rock, developed by Bos and Spiers (2002b), for sliding velocities covering all behavioral regimes predicted by the model and for a realistic phyllosilicate grain size. In the following we compare our experimental data and microstructural observations with those of Bos and coworkers (2000a, 2000b, 2001, 2002b) and with the Bos-Spiers model. In subsequent sections, we go on to reformulate part of the model and extend it to account for effects of crystal plastic flow within the phyllosilicate foliation, in addition to the mechanisms of frictional slip, pressure solution and dilatation already incorporated. Finally, we apply the new model to predict steady state strength profiles in crustal faults and we examine the implications thereof.

4.5.1. Dry sliding behaviour

Samples deformed in the dry run-in stage of our experiments showed marked slip weakening after the initial peak strength (Figure 4.4a), plus an overall tendency for decreasing strength with increasing muscovite content. Those with intermediate muscovite content (10-50 wt%) exhibited stick-slip behaviour after displacements of ~15 mm, but showed little effect of muscovite content on peak stick-slip strength.

This behaviour is closely similar to that reported by Bos et al (2000a) for halite plus kaolinite gouges, indicating that the phyllosilicate grain size and type does not strongly influence dry slip. Our microstructural observations (Figure 4.9) demonstrate significant grain size reduction by cataclasis in the halite during the dry run-in stage plus the development of a weak foliation oblique to the shear plane. The stick-slip behaviour of intermediate muscovite-content (10-50 wt%) samples, for displacements beyond 15 mm displacement, corresponds to the presence of a through-going boundary-parallel shear (Y-shear, cf. Mus24, Figure 4.9). Localised slip on a Y-shear is often associated with onset of unstable (stick-slip) sliding (Chester and Logan, 1990; Bos et al., 2000b), so we infer that slip on the boundary-parallel shear occurred after ~15 mm of displacement. The fact that the peak strength of the mixtures during stick-slip did not depend on the muscovite-content, was probably due to the fact that slip was localised on a muscovite-enriched boundary-parallel shear. Stable sliding prior to stick-slip behaviour may have involved more distributed deformation, presumably by cataclasis, grain size reduction and redistribution of material, leading to the formation of the observed foliation or anastomosing muscovite network. Despite the fact that most deformation in the dry run-in stage of samples with intermediate muscovite contents (10-50 wt%) was localised on a boundary parallel shear, the anastomosing network of muscovite flakes was therefore present at the start of the wet stage of the experiments.

4.5.2. Wet sliding behaviour

From the wet runs on pure halite and pure muscovite, and from the single test on material consisting of 20% muscovite with halite plus silicone oil, it is evident that the steady state shear strength of these samples show little or no dependence on sliding velocity (Figure 4.7b). This suggests purely frictional behaviour as reported by Bos et al (2000a) for pure salt and pure kaolinite, with a coefficient of friction ($\mu = \tau/\sigma_n$) of ~0.8 for halite and 0.3 for muscovite (cf. 0.2 for kaolinite, Bos et al 2000a). In contrast, all salt-muscovite plus brine samples showed a pronounced velocity strengthening up to ~0.3 μm/s with a broad maximum in strength at velocities of ~0.3-1 μm/s and velocity weakening at higher velocities (Figure 4.7b). In broad terms then, the data obtained for muscovite and halite samples show two regimes of behaviour: a low rate, velocity-strengthening regime, and a high rate, velocity-weakening regime. Note that across the entire range of velocities investigated, the steady state strength of most halite-muscovite samples is intermediate between that of pure halite and pure muscovite with a clear decrease in strength as muscovite content increases (Figures 4.7b and 4.8).

Halite-muscovite samples deformed in the low rate, velocity strengthening regime show no slip weakening in the shear stress versus displacement curves (Figure 4.5a). However, their steady state strength is strongly dependent on both normal stress (σ_n) and in a highly non-linear way on sliding velocity (see Figures 4.6b and 4.7b). This "frictional-viscous" behaviour, and the strongly foliated mylonitic microstucture that develops in this regime, are closely similar to those found by Bos et al (2000a) in halite-kaolinite gouge at similar velocities and normal stresses (Figure 4.12). Such behaviour does not occur in our pure, wet halite or pure, wet muscovite samples, nor in the oil-flooded sample in which pressure solution is not possible. The observed frictional-viscous behaviour therefore seems to require the presence of a foliated, halite-plus-muscovite microstructure as well as conditions favourable for pressure solution of the halite. As for halite-kaolinite gouges (Bos et al., 2000a), we infer that the mechanism of deformation in the low velocity regime must be one of frictional sliding on/in the anastomosing muscovite foliae, with accommodation of ensuing geometric misfits by pressure solution of the intervening halite.

One important feature of our results for the halite-muscovite gouges, seen at velocities below those investigated by Bos et al (2000a, i.e. below 0.03 μm/s), is a clear change in the sensitivity of steady state strength to sliding velocity. At the lowest velocities reached, our data show strengths slightly below that of pure muscovite, with almost no dependence on sliding velocity (Figures 4.7b and 4.12). This decrease in the sensitivity of steady state strength to velocity towards very low sliding velocities was not observed by Bos et al (2000a, 2002b), but is predicted by their microphysical model for pressure solution-accommodated slip in a foliated fault rock. The Bos-Spiers model predicts rate-independent sliding behaviour at the lowest velocities (Regime 1). Here, pressure solution accommodation is predicted to be so easy that frictional sliding on the foliation controls the strength. As the sliding velocity increases, however, pressure solution accommodation

begins to contribute to the bulk strength leading to truly frictional-viscous behaviour (Regime 2). The present results therefore seem to confirm the validity of regimes 1 and 2 of the Bos-Spiers model for the lower sliding velocities accessed here.

At velocities of 0.3-1 μm/s our wet halite-muscovite samples show a broad maximum in steady state strength, and at velocities above 1 μm/s wet samples show strong velocity weakening. In this range of velocities, slip weakening and finally stick-slip becomes important (Figure 4.5a), and the samples are characterized by a structureless microstructure, rather than a foliated one, resembling that of a cataclasite (Figures 4.10c and 4.10d). At sliding velocities above ~1 μm/s the steady state strength of the samples remains linearly related to normal stress, but the coefficient of friction ($\mu = \tau/\sigma_n$) decreases with increasing sliding velocity.

The data presented by Bos et al (2000a, 2002b) for wet halite-kaolinite gouges at velocities of 0.3-10 μm/s are significantly different from ours in that they show an increase in strength to a more or less constant value at 1-10 μm/s with no significant velocity weakening (Figure 4.12). This strength plateau was interpreted by Bos et al (2000a, 2002b) to correspond to the onset of dilatational processes within the gouge, as slip on the anastomosing foliation becomes too fast to be accommodated by pressure solution in the halite. Such behaviour is described by Regime 3 of the Bos-Spiers model. It seems reasonable to suppose that at sufficiently high velocities, deformation of the gouge will indeed occur by a cataclastic process, involving disruption of any foliation produced during the dry run-in or earlier slow wet sliding, grain rotation, grain sliding and microfracturing. That such processes operated in our experiments is also supported by our microstructural observations that show a chaotic microstructure at the highest sliding velocity.

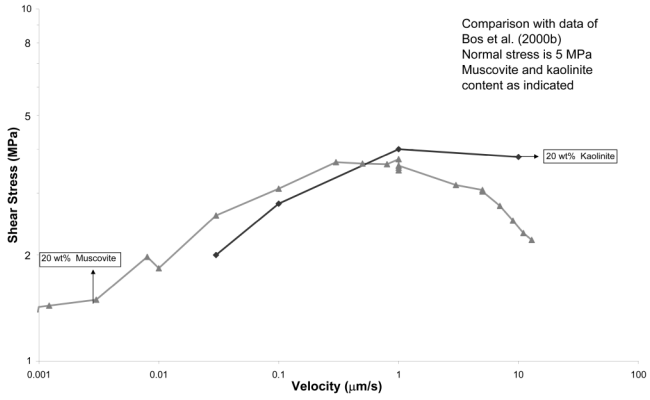

Figure 4. 12. Comparison of our experimental data on muscovite-halite mixtures with date of Bos et al (2000a) on kaolinite-halite mixtures.

However, purely cataclastic deformation is not expected to show a rate-dependence, whereas we found a very strong, inverse dependence of steady state shear strength on velocity (Figure 4.7b). This could be explained by severe grain size reduction in the halite, enhancing pressure solution rates and making it again possible for pressure solution to operate at a significant rate, accomodating slip at geometric obstacles. However, since the velocity weakening behaviour that we observed is reversible with velocity stepping direction, we believe that this is not likely. Another possible explanation is that deformation becomes localized in weak zones in the gouge at high velocities. However, we found little microstructural evidence for Y-shears or other signs of localised deformation in the high velocity samples examined (though one sample did show stick-slip which is suggestive of localisation). Clearly, more data are required to explain this velocity weakening effect. We will adress this in a future paper incorporating the results of slide-hold-slide experiments in this regime.

4.6. Revised model for frictional-viscous flow of foliated fault rock

4.6.1. Viscous-dilatational coupling

We have argued above that the Bos-Spiers model for Regimes 1 and 2 is consistent with the behaviour seen at low velocities in our experiments (<0.3 μm/s). The original model is based on the foliated steady-state microstructure shown in Figure 4.2, and on the mechanical analogue diagram of Figure 4.2c. An expression for the resistance to steady state slip on phyllosilicate foliae, was proposed by Bos and Spiers (2002b), with pressure solution accommodation at low rates and dilatation at high rates:

$$\tau = \tau_{gb} + \left(\frac{1}{\tau_{ps}} + \frac{1}{\tau_{dil}} \right)^{-1} \tag{4.2}$$

where τ is the total shear stress supported by the shear zone, τ_{gb} is the frictional shear stress generated by sliding on/within the phyllosilicate foliae, τ_{ps} is the shear stress offered by pressure solution (dissolution, diffusion and precipitation) of the intervening soluble grains, and τ_{dil} is the shear stress contribution due to dilatational accommodation of slip on the foliation (modelled as work against the normal stress).

The bracketed term $\tau_u \equiv \left(\frac{1}{\tau_{ps}} + \frac{1}{\tau_{dil}} \right)^{-1}$, on the right of the equation, is an approximation for the stress (τ_u) supported by the upper branch in the mechanical analogue diagram of Figure 4.2c. This approximation, $\tau_u \approx \tau$, was employed by Bos and Spiers (2002b) to smooth out the abrupt transition from a pressure solution controlled strength of the upper branch of $\tau_u \approx \tau_{gb}$ when $\tau_{ps} \approx \tau_{dil}$ (Regime 2), to a dilatation controlled strength at the limiting value of $\tau_u = \tau_{dil}$ when $\tau_{ps} \geq \tau_{dil}$ (regime 3). The approximation is accurate for $\tau_{ps} >> \tau_{dil}$ and for $\tau_{dil} >> \tau_{ps}$, but is physically unfounded and inaccurate by a factor of 2 when $\tau_{ps} = \tau_{dil}$, since at

this point $\tau = \tau_{dil} / 2$ whereas $\tau_u = \tau_{dil}$. The transition from pressure solution-controlled strength ($\tau_u = \tau_{ps}$) to dilatation controlled strength at the limiting value of $\tau_u = \tau_{dil}$, in the region $\tau_{ps} \geq \tau_{dil}$, is better described by re-defining the bracketed term in equation (4.2). Then, our model for frictional-viscous flow now takes the form

$$\tau = \tau_{gb} + \left\{ \left(\tau_{ps} \right)^{-n} + \left(\tau_{dil} \right)^{-n} \right\}^{-\frac{1}{n}} \tag{4.3}$$

For large values of the exponent n (e.g.. n=20), this equation faithfully reproduces the sharp transition from pressure solution to dilatation controlled strength, while still allowing the strength behaviour of the system to be represented using a simple continuous function (equation 4.3).

In Figure 4.13, we plot equation (4.3) as a function of sliding velocity for n-values of 1 (which is equivalent to the original model of Bos and Spiers, 2002b as described by equation (4.2)) and 20, and we compare the results with our experimental data on strength versus velocity for samples deformed at velocities below 1 μm/s (i.e. those showing a foliation). In plotting equation (4.3), we used parameter values to describe pressure solution in halite taken from Spiers et al. (1990). The grain size of the intervening halite grains was taken to be 30 μm on the basis of our microstructural observations (Figure 4.10). For the coefficient of frictional sliding on the phyllosilicate foliation we took a value of 0.31 obtained for pure muscovite plus brine from our own tests. Based on our microstructural observations, we took a value of 25° for the angle of dilatation. Increasing the value of n from 1 to 20 clearly demonstrates the much sharper change from Regime 2 (pressure solution dominated) to Regime 3 (dilatation dominated). The revised model with n=20 fits the experimental data at the lowest and highest velocities, but at intermediate velocities (0.02-0.2 μm/s) the revised model (n=20) predicts higher values for the steady state shear strength, and a sharper increase in strength than we observed. However, the model is derived for a single-valued grain size of the soluble phase (Bos and Spiers, 2002b). Incorporating a grain size distribution into the revised model, requires solving equation (4.3) for each incremental grain size class and volume-averaging their stress contributions accordingly. Assuming a homogeneous deformation rate in the soluble phase, this can be done numerically following the method described by Freeman and Ferguson (1981) and Ter Heege et al. (2004).We performed such a calculation, taking n=20, for a population of 1000 grains, randomly generated via a log-normal distribution, consistent with that seen in samples Mus5 and Mus23. The result of this simulation is compared with our single-valued grain size calculation (n=20) and experimental data in Figure 4.13. The distributed grain size leads to a smoother transition between regime 2 and regime 3, bringing the model and experimental data into good agreement over the entire range of velocities below ~1 μm/s. We accordingly infer that the discrepancy between our revised model (n=20), for a single-valued grain size, and our experimental data may indeed be due to the effects of the distributed grain size of our samples. The implication is that our revised model applied for a single-valued grain size offers a realistic prediction of steady state frictional-viscous

behaviour of foliated fault gouge, but that the predicted transition from Regime 2 to Regime 3 is too sharp. The excellent fit of the original Bos-Spiers model (equation 4.2, or 4.3 with n=1) to data obtained in Regime 2 at velocities of 0.02-0.2 μm/s (Figure 4.13) may thus have been largely fortuitous.

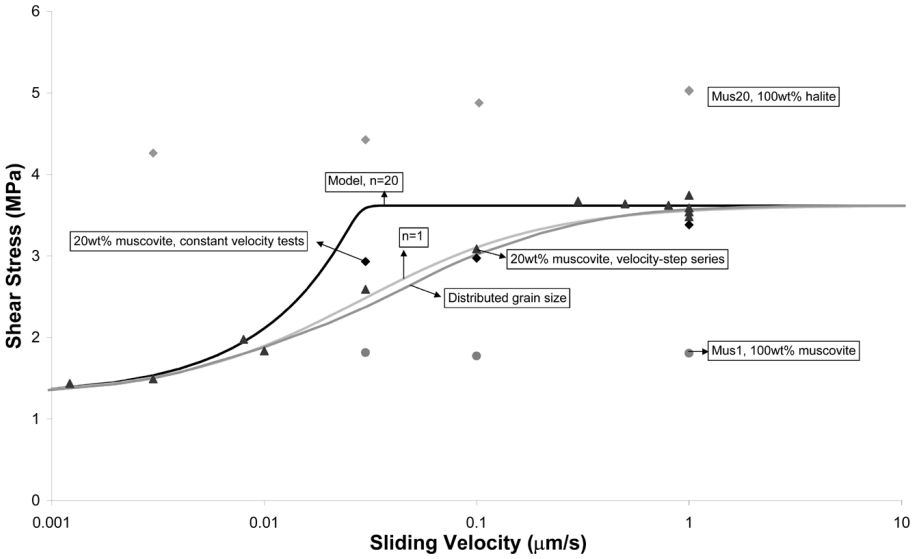

Figure 4.13: Comparison of representative experimental data with the different microphysical models. The halite grain size used in the model calculation is 30 μm and the angle of dilatation used is 25°. For the distributed grain size simulation a log-normal distribution was used with a mean grain size of 20 μm and a relative standard deviation of 1. Dilatation angle in this model is 25°.

4.6.2. Incorporation of phyllosilicate plasticity

To apply our re-formulated microphysical model (equation 4.3, n=20) to faults cutting the middle and lower crust, we need to include the possibility of plastic flow in the phyllosilicate foliae, operating concurrently with frictional slip. This can easily be incorporated in the model using the following equation describing the mechanical analogue diagram of Figure 4.14:

$$\tau = \left\{ \left(\tau_{gb}\right)^{-m} + \left(\tau_{pl}\right)^{-m} \right\}^{-\frac{1}{m}} + \left\{ \left(\tau_{ps}\right)^{-n} + \left(\tau_{dil}\right)^{-n} \right\}^{-\frac{1}{n}} \qquad (4.4)$$

Here τ_{gb}, τ_{ps}, τ_{dil} and n are the same as in equation (4.3), τ_{pl} is the shear strength contribution offered by plastic flow in the phyllosilicate foliae and m (=20) is an exponent, like n, that allows for a sharp, but continuous transition from frictional slip to plastic flow in the foliation. To our knowledge, the only phyllosilicates for which a flow equation has been determined are biotite single crystals (Kronenberg et al., 1990), 75 wt% biotite schist (Shea and Kronenberg, 1992) and muscovite single crystals (Mares and Kronenberg, 1993). As there are large uncertainties in the flow behaviour determined for muscovite (Mares and Kronenberg, 1993) and since our model is concerned with plastic flow in pure phyllosilicate foliae, we used the following equation determined for compressive deformation of biotite at 45° to (001) at temperatures of 20-400° (Kronenberg et al., 1990) as a first step to incorporating phyllosilicate plasticity in our frictional-viscous flow model:

$$\dot{\varepsilon} = C \cdot \exp(\alpha \cdot \sigma_d) \exp(-Q / RT) \qquad (4.5)$$

In this equation, $\dot{\varepsilon}$ is the axial strain rate (s^{-1}), σ_d is the applied differential stress ($\sigma_1 - \sigma_3$), T is the absolute temperature, R is the gas constant, Q is an apparent activation energy and C and α are empirical constants. Rearranging equation (4.5) and converting it for simple shear by dislocation slip on (001) leads to the relation

$$\tau_{pl} = \frac{1}{\alpha} Log \left\{ \frac{3^{\frac{1}{2}} \dot{\gamma}_{pl}}{C \cdot \exp(-Q / RT)} \right\} \qquad (4.6)$$

Note that the shear strain rate, $\dot{\gamma}_{pl}$, in this equation is the shear strain rate within the phyllosilicate foliae, defined as $\dot{\gamma}_{pl} = \dot{\gamma} / R$, where $\dot{\gamma}$ is the bulk shear strain rate of the gouge and R is ratio of the thickness of the phyllosilicate foliae to the total gouge thickness.

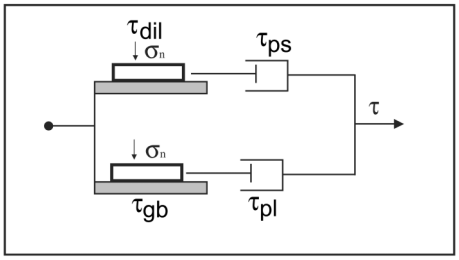

Figure 4.14: Mechanical analogue diagram for the postulated shear deformation process at zero porosity including plastic flow of the phyllosilicate foliae. τ_{pl} is the shear contribution offered by plastic flow in the phyllosilicate foliae (regime A), τ_{gb} is the shear stress contribution offered by frictional sliding on the phyllosilicate foliae (regime B), τ_{ps} is the shear stress contribution offered by pressure solution of the soluble solid (regime C), τ_{dil} is the shear contribution offered by dilatation on the foliation (work against the normal stress, regime D) and σ_n is the normal stress on the gouge.

Given appropriate constitutive parameters allowing computation of τ_{gb}, τ_{pl}, τ_{ps} and τ_{dil}, equation (4.4) allows the steady state strength of a foliated quartz-mica or other similar fault rock to be modelled for deformation by plastic and/or frictional slip on the anastomosing phyllosilicate foliation, with accommodation by pressure solution of the intervening mineral phase or by dilatation. From inspection of Figure 4.14 and the new model embodied by equation (4.4), it is evident that the model predicts four possible regimes of frictional and/or viscous behaviour with increasing strain rate, in which strength is controlled respectively by A) plastic flow in the phyllosilicate foliae, B) frictional slip in the phyllosilicate foliae, C) pressure solution of the soluble mineral phase and D) dilatational cataclasis. We will refer to these as Regimes A-D hereforth. Note that the model addresses steady state velocity strengthening behaviour only, and does not include velocity weakening behaviour of the type seen in our experiments at rapid sliding velocities where cataclastic flow destroys the foliation seen at low velocities.

4.7. Strength profiles for phyllosilicate-bearing mature crustal fault zones

4.7.1. Model application and predictions

We now construct crustal fault strength profiles using equation (4.4) and the appropriate constitutive equations for each process involved, assuming a foliated quartz-mica fault rock. Following Bos and Spiers (2002b), we apply the revised model to four different tectonic settings: (1) a transcrustal strike-slip fault zone (such as the San Andreas fault zone), (2) a normal fault zone accommodating crustal extension, (3) a thrust fault zone deforming under high pressure, low temperature conditions typical of a subduction setting, and (4) a thrust fault zone deforming under intermediate conditions typical of continent-continent collision zones. The geothermal gradients used in these models are 25 °C/km, 35 °C/km, 15 °C/km and 25 °C/km, respectively. Crustal density is taken to be 2.75 g/cm^3 and pore pressure is assumed hydrostatic at all depths. At upper crustal levels, we will assume pure frictional behaviour with an average friction coefficient of 0.75 (Byerlee, 1978). The minimum shear stress to activate frictional sliding is given by

$$\tau_{dil} = \tfrac{1}{2}(\sigma_1 - \sigma_3)\sin\left[\tan^{-1}(1/\mu)\right] \quad (4.7)$$

where σ_1-σ_3 is the minimum differential stress to activate sliding, which is different for each tectonic setting (Sibson, 1977; see also Bos and Spiers, 2002b). Turning to the constitutive behaviour of the fault rock (equation 4.3), for frictional sliding in/on the phyllosilicate foliae ($\tau_{gb}=\mu\sigma_n$), we used the friction coefficient (μ) of muscovite as determined in this study, which is similar to that determined for biotite by Kronenberg et al. (1990). For the plasticity of the phyllosilicate at stress τ_{pl} we used equation (4.6) and the parameter values for single crystal biotite given by Kronenberg et al. (1990). We took the ratio R of equation (4.6) as 0.1. Though Bos and Spiers (2002b) used a diffusion-controlled pressure solution equation for quartz in their study, recent data suggest that interface reaction is likely to be rate limiting in quartz (Renard et al., 1997; Renard et al., 1999; Renard et al., 2000b; Renard et al., 2001; Niemeijer and Spiers, 2002; Niemeijer et al., 2002; Alcantar et al., 2003 and Chapters 2 and 3). We therefore took dissolution/precipitation as the rate controlling process in our calculation of τ_{ps} in equation (4.4) using

$$\tau_{ps} = \frac{ARTd}{B^2 k_{s,p}\Omega_s}\dot{\gamma} \quad (4.8)$$

Here A is a constant reflecting the proportion of grain contacts actively dissolving at any instant of time (taken as 1), B is the grain aspect ratio (taken as 5), d is the grain size (taken as 50 μm), Ω_s is the molar volume of quartz and $k_{s,p}$ is the phenomenological rate coefficient for dissolution (subscript s) or precipitation (p). We used an empirical equation for k_s as a function of temperature determined by Rimstidt and Barnes (1980). To describe crystal plastic flow at greater depth we use the creep equation for wet quartz of Luan and Paterson (1992), rewritten for the case of simple shear.

In Figure 4.15, we show crustal strength profiles resulting from equation (4.3) for the four different tectonic regimes. The profiles have been constructed using strain rates of 10^{-10} and 10^{-12} s^{-1}, equivalent to a fault zone of 10 to 1000 meters wide sliding at 30 mm per year. These rates were chosen by reasoning that the narrow, upper-crustal portions of major faults experience higher average strain rates (e.g.. 10^{-10} s^{-1}) than the broader mid-crustal reaches (e.g.. 10^{-12} s^{-1}; Sibson, 1977; Bos and Spiers, 2002b). Note in Figure 4.15 that Byerlee's law plus the dislocation creep equation used for pure wet quartz for the strain rates shown (shaded lines), together represent a "classical" two-mechanism crustal strength profile, with the brittle-ductile transition located at depths of 8-15 km and peak crustal strengths at these depths of 50-200 MPa. By contrast, our model for foliated (i.e. high-strain) phyllosilicate-bearing fault zones predicts a significant truncation of the brittle-ductile transition in all tectonic regimes, reducing the peak crustal strengths to values between 15 and 90 MPa and reducing mid-crustal load-bearing capacity by 50-70%. For a fault zone in a strike-slip setting with a geothermal gradient of 25 °C/km, such as the San Andreas Fault, the peak strength of 30 MPa predicted by our frictional-viscous model occurs at the fully ductile transition from Regime B (frictional sliding with pressure solution accommodation) to dislocation creep of quartz at a depth of ~14 km, assuming a strain rate

there of 10^{-12} s^{-1} due to widening of the shear zone with depth (Sibson, 1977). The predicted brittle-ductile transition (i.e. the transition from cataclastic Regime D to Regime C in our model), which is much sharper than given by the earlier model of Bos and Spiers (2002b), occurs at a depth of ~3.5 km and has a peak strength of ~20 MPa. This marks the predicted transition from seismic to aseismic slip, since the deformation behaviour below this depth is dominated by velocity-strengthening viscous processes (Regimes A-C). Note however that the brittle-ductile transition is likely to be less sharp than predicted, due to the effects of distributed grain sizes, as discussed earlier.

The extension of our model to incorporate the possibility of plastic flow of the phyllosilicates does not significantly modify the predicted crustal strength profiles compared with the earlier work of Bos and Spiers (2002b). The only tectonic regime where this has a clear effect is the high pressure, low temperature (subduction) setting (Figure 4.15c). Here, the inclusion of the plasticity of biotite reduces the predicted peak strength at the transition to homogeneous plastic flow of wet quartz from ~120 MPa to ~90 MPa. It should be noted, however, that the experimental flow law for biotite (Kronenberg et al., 1990) is less well constrained than experimental flow laws for quartz. Clearly, more data are needed on plastic flow in phyllosilicates to evaluate their role in determining the rheology of foliated fault rock.

Pressure solution controlled slip on the foliation in high-strain phyllosilicate-bearing fault zones (Regime C behaviour) is relatively unimportant in our predicted strength profiles. The zone where crustal strength is dominated by pressure solution is relatively narrow (~2-5 km). We have to bear in mind, however, that the parameters describing pressure solution are relatively poorly constrained (e.g. see Renard et al., 2000a, see also Chapters 2 and 3; Bos and Spiers, 2002b; Niemeijer and Spiers, 2002; Niemeijer et al., 2002, see also Chapters 2 and 3) and that the use of different estimates for reaction control can result in differences in the predicted strength τ_{ps} of perhaps 1 order of magnitude. In addition, variations in grain size (< 50 μm) and/or strain rate will influence the depth range over which fault slip is controlled by pressure solution processes.

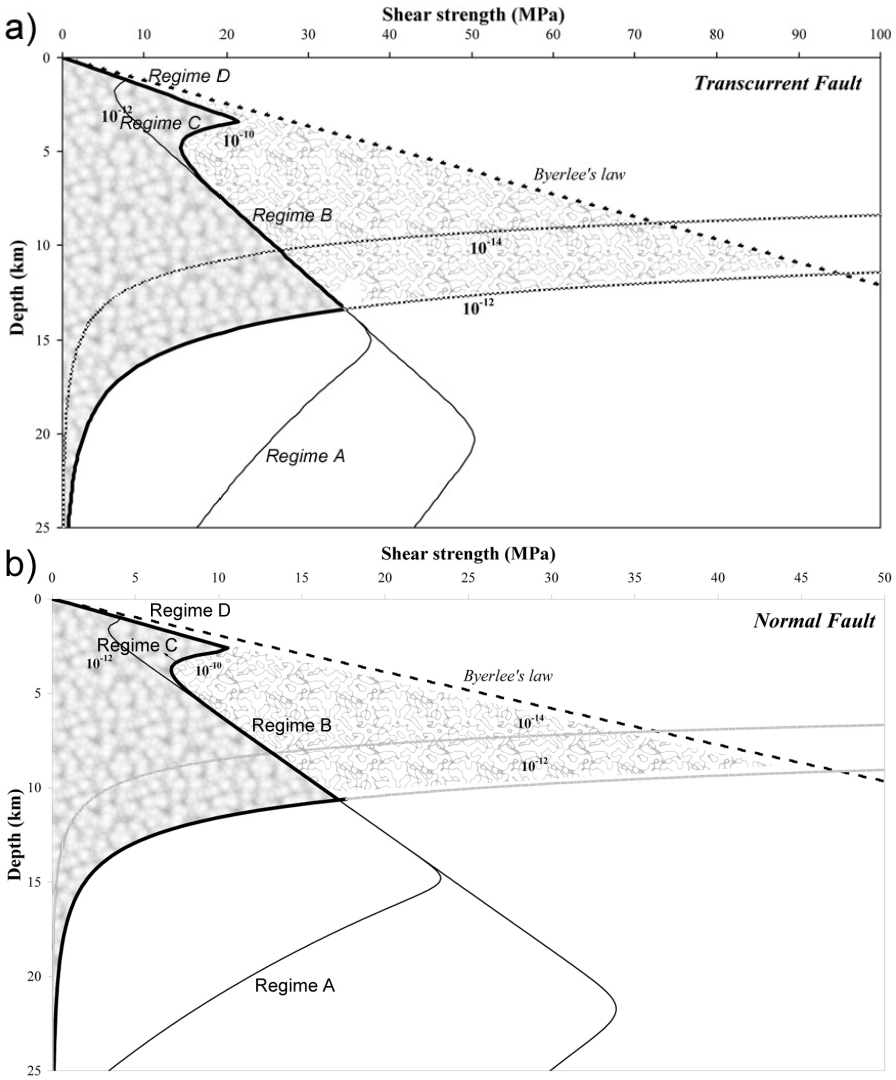
a)
Shear strength (MPa)
0
10
20
30
40
50
60
70
80
90
100
Depth (km)
0
5
10
15
20
25
Regime D
Regime C
Regime B
Regime A
Byerlee's law
Transcurrent Fault
10-12
10-10
10-14
10-12
b)
Shear strength (MPa)
0
5
10
15
20
25
30
35
40
45
50
Depth (km)
Regime D
Regime C
Regime B
Regime A
Byerlee's law
Normal Fault
10-12
10-10
10-14
10-12

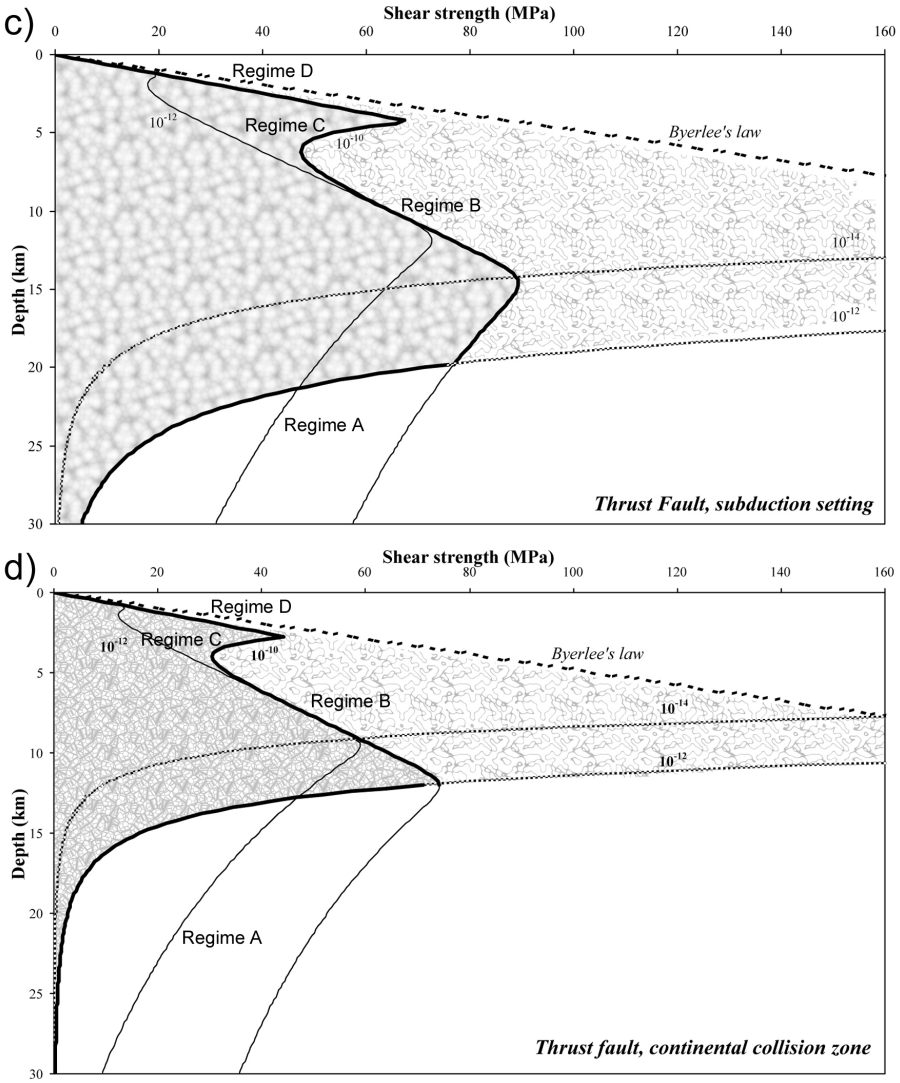

Figure 4.15: Crustal strength profiles for four different tectonic regimes. Geothermal gradients used are 25, 35, 15 and 25 °C/km for cases A, B, C, and D respectively. The grain size used is 50 μm in all cases. Regime A: plastic flow in the phyllosilicate foliae. Regime B: frictional sliding in/over the phyllosilicate foliae. Regime C: pressure solution-controlled strength. Regime D: Sliding accomodated by dilatation.

4.7.2. Further considerations and implications

Our improved microphysical model for frictional-viscous flow of high-strain (mature) phyllosilicate-bearing fault zones, predicts significant weakening compared to "classical" two-mechanism strength profiles. While the predicted brittle-ductile transition and the transition to quartz plasticity are presumably too sharp, the predicted average shear strength is roughly consistent with the low values for the San Andreas Fault inferred from heat flow measurements (Lachenbruch and Sass, 1980) and stress orientation data (Zoback, 2000; Townend and Zoback, 2001). Moreover, the predicted brittle-ductile transition depth of 3-5 km is consistent with the conclusion drawn from recent field studies of phyllosilicate-bearing mylonite zones, that progressive localization of deformation into such zones leads to a shallowing of the brittle-ductile transition from 10-15 km to ~5 km (Imber et al., 1997; Stewart et al., 2000). We are suggesting, therefore, that localization of continental fault zones may involve progressive weakening from the intact two-mechanism strength profile down to one described by our model, as the core of the fault zone is gradually converted into (overprinted by) a foliated, phyllosilicate-bearing mylonite at depths of 5-15 km and into a cataclastic equivalent at shallower levels. This does not exclude other mechanisms of fault zone weakening, such as fluid overpressuring effects (Hickman et al., 1995; Rutter et al., 2001), but it does seem consistent with field observations, at least on long-lived reactivated fault zones and in natural low angle normal faults (Imber et al., 1997; Stewart et al., 2000; Holdsworth et al., 2001; Collettini and Holdsworth, 2004; Jefferies et al., 2006, in press).

Despite this consistency with field observations, our predicted strength profiles display one major inconsistency with seismological observations on the depth distribution of seismicity on mature faults (e.g. Scholz, 2002). Our steady state model would suggest that crustal seismogenesis should be limited to the upper 5 km with frictional-viscous flow precluding seismicity at greater depths, whereas the observed distribution of seismicity typically extends to depths of 10-15 km (Sibson, 1977; Scholz, 2002). This problem requires detailed examination. We suggest, however, that the discrepancy lies in the complex anastomosing internal structure and compositional heterogeneity of (mature) fault zones. This complexity will inevitably lead to the development of internal stress concentrations around geometric irregularities or "rigid" lenses of more intact or stronger rock, as fault motion proceeds, producing local brittle failure. A mature fault zone, consisting of an anastomosing three dimensional network of weak, aseismically creeping mylonitic/phyllonitic strands with intervening strong lenses and by locked portions of widely varying length scale, would accordingly produce seismic events of varying magnitude and depth right down to the classical brittle-ductile transition (Holdsworth, 2004). Finally, note that the seismicity observed along active weak low angle normal faults has been related to hydrofracturing (Collettini and Barchi, 2004; Collettini and Holdsworth, 2004; Collettini et al., 2005)

A similar argument has recently been put forward by Faulkner et al. (2003) who studied the Carboneras fault in southeastern Spain. This ancient, large displacement (>40 km) strike-slip fault is approximately 1 km wide and is composed of continuous strands of phyllosilicate-rich fault gouge that bound lenses of variably broken-up protolith. The gouge strands are no wider than 5 metres and link up to form an anastomosing network with a width of ~1 km. Faulkner et al. (2003) suggest that these strands which are capable of accomodating large amounts of strain through aseismic creep, while the intervening lenses of (more or less) intact protolith are the possible sites of stress build-up and of large seismic moment earthquakes. Notably, several geophysical observations (see Faulkner et al., 2003 and references therein) suggest that the San Andreas fault zone around Parkfield with creeping and "locked" segments has a similar anastomosing fault structure at depth.

4.8. Conclusions

Room temperature rotary shear experiments have been performed on simulated fault gouge consisting of halite-muscovite mixtures at sliding velocities of 0.001-13 μm/s and normal stresses of 1-9 MPa. The aim was to test the model for steady-state frictional-viscous flow of foliated phyllosilicate-bearing fault rock developed by Bos and Spiers (2002b), over a wide range of sliding velocities and using a realistic phyllosilicate grain size. A unnecessary and physically unrealistic approximation in the model has been removed and the model has been extended to include the possibility of plastic flow in the phyllosilicates. The revised model was then applied to construct strength profiles for mature phyllosilicate-bearing continental fault zones. The following conclusions can be drawn:

1. At sliding velocities of <~0.5 μm/s, halite-muscovite mixtures develop an anastomosing muscovite foliation and deform by a combination of frictional sliding in/on the muscovite foliation with accommodation by pressure solution of the intervening halite grains. The general behaviour is similar to that of halite-kaolinite mixtures implying that the grain size and type of phyllosilicate has little effect on the sliding behaviour.
2. At low velocities (<0.5 μm/s), our revised model describes the observed behaviour well, assuming frictional behaviour in the phyllosilicate foliation only. At the lowest velocities, the strength of the synthetic fault gouge is purely frictional and consistent with purely frictional sliding in/on the foliation. This confirms the predictions of our model at velocities that had not been explored previously.
3. At velocities higher than 0.5 μm/s, a gradual transition to velocity-weakening behaviour and cataclastic microstructures was observed in our halite-muscovite samples, whereas halite-kaolinite samples show constant strength. A transition to dilatational/cataclastic flow at constant shear stress is predicted by our model, but the velocity-weakening we observed is not. More research is necessary to determine the operative deformation mechanisms and to evaluate the possible implications of such behaviour for seismogenesis.

4. Extending our model to foliated, phyllosilicate-bearing quartz-mica fault rocks in mature continental fault zones predicts a significant truncation of classical two-mechanism crustal strength profiles as well as a strength reduction of the upper crust of 50-70%. The strength-depth profiles predicted by our model suggest that frictional slip and plastic deformation on and within the phyllosilicate foliation will be the main factors controlling the strength of phyllosilicate-bearing fault rocks. While pressure solution is important in accommodating this process, it may be relatively unimportant in controlling strength. Flow laws for phyllosilicates need to be better constrained for future modelling.
5. Our revised model predicts the possibility of seismogenic slip on continental phyllosilicate-bearing fault to a depth of only 3-5 km, whereas seismicity is observed to depths of 5-15 km. We suggest that in such faults, seismicity in this depth range may be triggered at geometric irregularities or at “rigid” lenses of intact or stronger rock within the anastomosing internal structure of the heterogeneous fault zone.

Chapter 5

VELOCITY DEPENDENCE OF STRENGTH AND HEALING BEHAVIOUR IN SIMULATED PHYLLOSILICATE-BEARING FAULT GOUGE

This chapter has been accepted for publication in the Deformation mechanisms, Rheology and Tectonincs conference volume 2005, Tectonophysics as: Niemeijer, A.R. and Spiers, C.J., Velocity dependence of strength and healing behaviour in simulated phyllosilicate-bearing fault gouge.

Abstract

Despite the fact that phyllosilicates are widespread in fault zones, little is known about the strength of phyllosilicate-bearing fault rocks under brittle-ductile transitional conditions. In this study, we explored the steady state strength and healing behaviour of a simulated phyllosilicate-bearing fault rock, i.e. muscovite plus halite and brine, using a rotary shear apparatus. While 100% halite and 100% muscovite samples exhibit rate-independent frictional/brittle behaviour, the strength of mixtures containing 10-50% muscovite is both normal stress and sliding velocity dependent. At low velocities (<1 μm/s), strength increases with increasing velocity and normal stress, and a mylonitic foliation develops. This behaviour results from pressure solution in the halite grains, which accommodates frictional sliding on the phyllosilicate foliation. The pervasive muscovite foliation, which coats all halite grains, prevents significant healing. At high velocities (>1 μm/s), velocity-weakening frictional behaviour occurs, along with the development of a structureless, intermixed, cataclastic microstructure. The steady state porosity of samples deformed in this regime increases with increasing sliding velocity. We propose that this behaviour involves competition between dilatation due to granular flow and compaction due to pressure solution. Towards higher sliding velocities, dilatation increasingly dominates over pressure solution compaction, so that porosity increases and frictional strength decreases. During periods of zero slip, pressure solution compaction occurs, causing a significant strength increase on reshearing. Our results imply that cataclastic overprinting of mylonitic rocks in natural fault zones does not require any changes in temperature or effective pressure conditions, but can simply result from oscillating fault motion rates. Our healing data suggest that foliated, aseismically creeping fault segments will remain weak and aseismic, whereas segments that have slipped seismically will rapidly re-strengthen and remain in the unstable, velocity-weakening regime.

5.1. Introduction

In the past few decades considerable experimental effort has been focused on quantifying the frictional behaviour of faults. Results from room temperature and/or dry sliding experiments on bare rock interfaces and simulated gouge-filled faults have typically shown static and dynamic sliding friction at 0.6-0.9 times the applied normal stress (e.g. Byerlee, 1967; Dieterich, 1972; Jackson and Dunn, 1974; Byerlee, 1978). Early experiments on bare rock surfaces by Dieterich (1972) and many others (e.g. Byerlee, 1967; Byerlee and Summers, 1975; Rummel et al., 1978; Ruina, 1983) have shown an increase in static friction, that is the maximum friction following a "hold" period of zero slip, with increasing hold duration. These experiments also show a decrease in dynamic friction with increasing sliding velocity, a phenomenon known as velocity-weakening. By contrast, simulated fault gouges (e.g. Marone et al., 1990; Chester and Higgs, 1992; Chester, 1994; Blanpied et al., 1995) in general show a lower rate of increase in static friction with hold duration.

Moreover, they show an increase in dynamic friction with increasing sliding velocity for pervasive shear over a wide range of sliding velocities, i.e. a velocity-strengthening effect. With ongoing shear displacement, however, simulated fault gouges exhibit a transition from velocity-strengthening to velocity-weakening behaviour associated with localization of shear.

Reduction of dynamic friction through velocity-weakening behaviour is a requirement to produce unstable slip on a fault, i.e. a stick-slip event in the laboratory or an earthquake in nature, and is therefore of major interest in relation to seismogenesis. Increasing static friction during periods of zero slip, otherwise known as strength recovery or fault healing, is also of major interest in relation to understanding the earthquake cycle (e.g. Marone et al., 1995; Becker and Schmeling, 1998). A coupled description of static and dynamic friction in relation to fault slip behaviour was first established with the development of the rate-and state friction (RSF) laws by Dieterich (1979) and Ruina (1983). These have been successfully applied to quantify the effects seen in numerous rock friction experiments and have shown that static friction and its time dependence represent a special case of velocity-dependent friction.

Significantly, most previous studies of friction on bare fault surfaces and simulated gouge-filled faults have focused on room temperature experiments (e.g. Dieterich, 1978, 1979; Marone et al., 1990; Kilgore et al., 1993; Beeler et al., 1994; Beeler et al., 1996; Mair and Marone, 1999). Such experiments exclude the hydrothermal fluid-rock interactions that are known to be important in the upper to middle crustal depth range corresponding to the seismogenic zone and its base at the brittle-ductile transition (e.g. Imber et al., 2001; Rutter et al., 2001). Effects of fluid-rock interaction have been demonstrated in several experimental studies on gouge-filled faults (e.g. Chester and Higgs, 1992; Chester, 1994; Cox, 1994; Tullis, 1994; Blanpied et al., 1995; Karner et al., 1997; Kanagawa et al., 2000; Nakatani and Scholz, 2004) and have a clear influence on the sliding and healing behaviour. These effects include stabilization of sliding behaviour (i.e. a transition from velocity-weakening to velocity-strengthening) and a stronger healing propensity often attributed to solution transfer effects (e.g. Olsen et al., 1998; Nakatani and Scholz, 2004). However, systematic analysis and quantification of these effects, the micromechanical processes involved and their relevance for nature is lacking. Indeed, most experiments performed on simulated gouge under wet, reactive conditions have focused on pure single phase materials or else are influenced by incomplete mineral reactions. They are also limited in the duration and in the total amount of strain that could be reached, so that the internal microstructural development is highly immature (Blanpied et al., 1991; Cox, 1994; Blanpied et al., 1995; Karner et al., 1997; Olsen et al., 1998; Kanagawa et al., 2000; Nakatani and Scholz, 2004). By contrast, natural fault rocks often contain a significant proportion of weak phyllosilicates, either inherited from the host rock or formed by mineral reactions, which form an interconnected network or foliation indicative of high shear strain. Such foliations have often been suggested as an explanation for the observed weakness of some faults, such as the San Andreas Fault and others (e.g.Wintsch et al., 1995; Imber et al., 2001;

Holdsworth, 2004), though it remains unclear how these weak faults may be capable of producing large earthquakes.

Recent large strain, rotary shear experiments, performed by Bos, Niemeijer and Spiers (Bos et al., 2000a, b; Bos and Spiers, 2000, 2001, 2002b, a; Niemeijer and Spiers, 2005, see Chapter 4) on rock analogue materials consisting of halite plus phyllosilicate mixtures have shown large effects of phyllosilicate content and foliation development. These experiments were done under simulated brittle-ductile transitional conditions where cataclasis and solution transfer operate in the halite, without the operation of plastic processes such as dislocation creep. At low sliding velocities, combined slip on the developing phyllosilicate foliation and solution-transfer of intervening halite clasts yield velocity-strengthening behaviour plus slow healing characteristics. A microphysical model for the inferred deformation process predicts low steady state fault strength and aseismic slip in mature phyllosilicate-bearing faults at mid-crustal depths (Bos and Spiers, 2002b; Niemeijer and Spiers, 2005 and Chapter 4).

Similar experiments performed by Niemeijer and Spiers (2005 and Chapter 4) on wet halite/muscovite mixtures, but at higher sliding velocities, have recently revealed dramatic velocity-weakening behaviour, not seen in the two end-member compositions. Such behaviour may also be important in natural fault rocks containing phyllosilicates. If so, it could play a significant role in controlling seismogenesis and the entire the seismic cycle on faults under the reactive hydrothermal conditions of the brittle-ductile transition. However, the microphysical mechanisms underlying the observed velocity-weakening behaviour are not yet understood. Moreover, the healing behaviour in the velocity-weakening regime is unknown and the relevance to nature is unverified.

In this study, we have investigated the large strain sliding and the healing behaviour of simulated faults containing halite-muscovite gouges at velocities covering both the velocity-strengthening and velocity-weakening regimes. Under the chosen conditions, pressure solution, cataclasis and phyllosilicate foliation development and destruction are active, as anticipated for nature in the brittle-ductile transition. Our aim is to determine the healing behaviour of the mixtures as a function of sliding velocity and to explain the microphysical mechanisms responsible for the observed velocity-weakening and healing effects. Finally, we speculate on the possible implications of our results for natural faults, assuming that the processes observed in our experiments also occur in natural fault zones.

5.2. Experimental Method

The experiments were performed at room temperature on simulated, muscovite-halite fault gouges, using a rotary shear apparatus located in an Instron 1362 loading frame to apply normal load to the simulated fault. Tests were done both dry and in the presence of brine. The apparatus has been described in detail elsewhere (Bos et al., 2000a; Niemeijer and Spiers, 2005 and Chapter 4). In brief, the sample assembly consists of a pair of toothed stainless steel rings (the wall rock rings of Figure 5.1, teeth height=~0.1 mm) sandwiching a

layer of halite-muscovite gouge. The assembly is sealed, using O-rings, between an inner steel confining ring and an outer steel confining ring, which houses a pore fluid in- and outlet. Within the rotary-shear machine, the sample assembly is rigidly gripped by a stationary upper forcing block and a lower forcing block linked to a servo-controlled drive system. The servo-controlled drive is used to apply rotational sliding velocities of 0.001-10 μm/s to the gouge with a resolution of 0.0003 μm/s. Shear displacement is measured using a potentiometer with a resolution of 0.001 mm, geared to the lower (rotating) forcing block Shear stress on the gouge is measured using a torque gauge couple, with a resolution of 0.01 MPa, mounted on the upper forcing block. Normal stress is applied using the Instron loading ram and can be held constant to within ~0.02 MPa. Most of the present experiments where conducted under a normal stress of 5 MPa. Displacement occurring normal to the fault zone is measured using a Linear Variable Displacement Transducer or LVDT (1 mm full scale, 0.01 % resolution) located in the centre of the sample assembly.

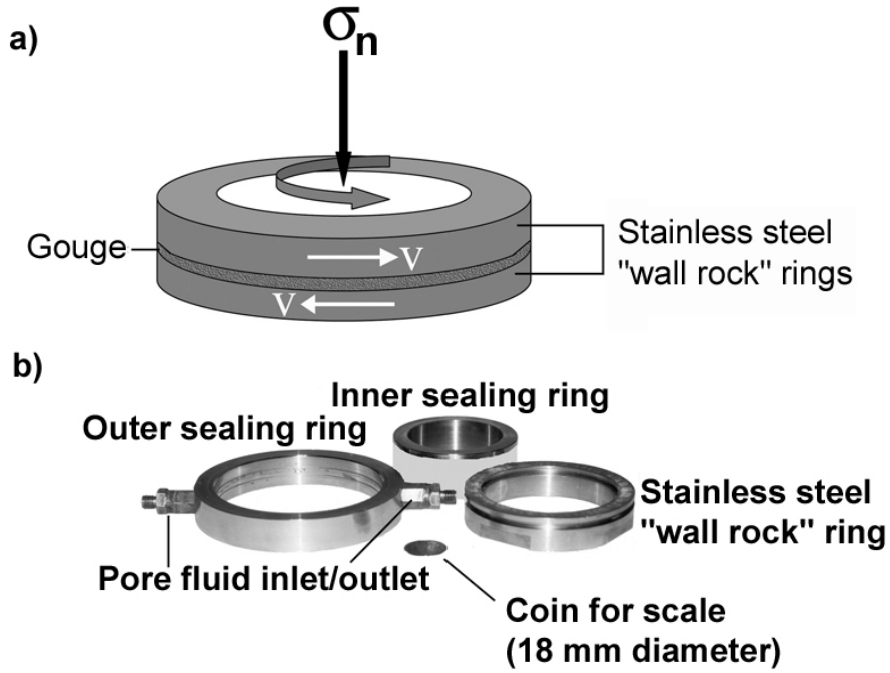

Figure 5.1: a) Schematic diagram of the rotary shear sample assembly used in this study. Granular fault gouge is sheared between annular stainless steel wall rock rings at controlled velocity v and normal stress σ_n. Gouge dilatation/compaction is measured using anLVDT located in the centre of the sample assembly. b) Photograph of the wall-rock rings and the sealing rings that constitute the sample assembly.

Sample material consisted of mixtures of granular halite with a median grain size of 100 μm (determined using a Malvern particle sizer), plus 10-80 wt% muscovite with a median equivalent spherical diameter of 13 μm (as stated by the supplier, Internatio B.V.). Pure halite and pure muscovite samples were used for control experiments. In setting up each run, about 8 grams of material were loaded into the sample assembly, yielding an initial gouge thickness of ~ 2 mm. All samples were then subjected to dry compaction, under a normal load of 1 MPa for ~15 minutes. Except where otherwise specified (Table 5.1), samples were subsequently dry-sheared to a displacement around ~50 mm at a velocity of 1 μm/s and 5 MPa normal stress. This was done to produce a reproducible microstructure. In most experiments, the pore fluid system was then connected to the sample assembly, which was in turn evacuated and flooded with saturated brine (i.e. saturated with respect to the NaCl in the gouge). The pore fluid was subsequently kept at atmospheric pressure by means of evaporation-proof draining to air.

Two broad categories of experiments were performed to investigate the effects of sliding velocity, composition and normal stress.

a) Continuous sliding experiments carried out in velocity stepping mode, normal stress stepping mode, or at constant velocity and constant normal stress.

b) Slide-hold-slide experiments, performed using different sliding velocities and constant normal stress.

The continuous sliding experiments consisted of 24 separate experiments. These included a series of 11 velocity-stepping experiments performed on brine-flooded samples of different composition (0, 10, 20, 50, 80 and 100 wt% muscovite). The tests were carried out by shearing at a constant sliding velocity of 1 μm/s until a steady state shear stress level was attained, usually after a displacement of ~3 mm. The velocity was then stepped up or down and the new sliding velocity held constant until a new steady state shear stress level was reached. The aim of this series was to determine the rate dependence of steady state shear strength for a range of gouge compositions. Most of these tests were carried out at a constant normal stress of 5 MPa, though the normal stress was also stepped in a few cases to determine its effect on gouge shear strengths. In addition, four stress-stepping experiments were performed at constant sliding velocity on wet samples with 20 wt% muscovite using the same experimental procedure, but without the dry run-in phase. A further series of 5 large displacement experiments was carried out on wet samples with 20 wt% muscovite at a constant sliding velocity of 0.03, 0.1, 1, 5 and 13 μm/s and at a constant stress of 5 MPa (including a dry run-in phase). These were done to investigate the high strain microstructure (shear strain of 30). The remaining continuous sliding tests consisted of 4 control experiments, performed dry and using silicone oil instead of brine. For more details, we refer to our previous paper dealing with velocity-stepping experiments on the same material (Niemeijer and Spiers, 2005 and Chapter 4).

The slide-hold-slide (SHS) experiments (Table 5.2) were carried out with the aim of investigating the transient and healing behaviour of mixtures containing 80 wt% halite and 20 wt% muscovite plus brine at different sliding velocities. This series of 5 tests

involved the same initial dry compaction and shearing procedure described above, followed by a wet "run-in" sliding stage at 1 μm/s, until a steady state shear stress level was reached. The sliding velocity was then stepped to a chosen SHS reference sliding velocity until a new steady state shear stress was reached. The rotary drive was then halted and the sample allowed to "stress relax" for a chosen hold time. After the desired hold, sliding was restarted at the same reference velocity, by switching on the motor, and continued until steady state was re-attained. This slide-hold-slide procedure was repeated 2 or 3 times for reference SHS sliding velocities of 0.01, 0.03, 0.1, 1, 2, 3, 5 and 10 μm/s, using hold periods of 60 s, 600 s, 1200 s and 6000 s. We employed slide-hold-slide cycles at different reference velocities within individual tests in order to avoid any effects of sample variability and to investigate the influence of increasing displacement (shear strain). An exception to the above SHS procedure is test shs3, which was slid directly after the dry run-in stage at the desired reference sliding velocity of 10 μm/s.

At the end of all experiments, sliding was halted and the normal load was removed. Residual brine was flushed rapidly from the sample assembly with hexane and the entire assembly was removed from the testing machine and dried at 50 ºC for ~ 2 hours. Finally, the sample was extracted and impregnated with blue-stained epoxy resin. Standard thin sections were cut parallel to the sliding direction and normal to the shear plane.

The final porosities of the gouge samples studied in all constant velocity tests (mus5, mus6, mus7, mus8, Mus23) and all slide-hold-slide tests were determined by image analysis of thin sections and Thermo Gravimetric Analysis of propylene carbonate-saturated samples. Porosity determination using image analysis was done by defining a pixel threshold for detecting pores filled with blue-stained resin in 10 microstructural images at the same magnification. The images were converted to a black-and-white image using the UTHSCA ImageTool and a manual grey scale threshold. The porosity was obtained from the relative proportion of black pixels, yielding an area-based porosity. Porosity determinations using TGA were conducted by evacuating of about 0.1 grams of sample material and subsequently impregnating this with propylene carbonate. Propylene carbonate is a liquid with a high boiling point (240 ºC) which does not dissolve halite in significant amounts. The sample was then placed in a DuPont Instruments 1090 Thermal Gravimetric Analyzer and heated at a rate of 10 ºC per minute up to a temperature of 130 ºC at which point significant evaporation starts. It was then kept at this temperature for 40 minutes, while the weight loss was continuously measured. The porosity was determined by assuming a constant surface evaporation rate at 130 º C, so that deviations from a linear weight loss must be due to evaporation from the pores. The weight loss due to evaporation from the pores was then used to determine the porosity of the sample. Measurements for each sample were repeated three times. The absolute standard error in our TGA porosity determination is about 1.5 %. Values obtained from TGA agree well with those available from image analysis.

5.3. Results

Table 5.1 lists the 24 continuous sliding experiments, along with corresponding data on dry run-in displacement, normal stress, sliding velocity, total wet displacement and final gouge thickness (cf. Niemeijer and Spiers, 2005 and Chapter 4). A similar list of the 5 slide-hold-slide experiments and supporting data is given in Table 5.2.

Table 5.1: List of the 26 velocity-stepping, constant velocity and normal stress stepping experiments performed plus corresponding experimental conditions. Note that σ_n is the normal stress on the fault.
n.d. : not determined
** : total shear displacement after the dry run-in stage*

Sample Code	Composition Muscovite : Halite	Dry run-in displacement(mm)	Fluid	σ_n stepping sequence (MPa)	Velocity-stepping sequence (μm/s)	Total shear displacement *	Final Gouge thickness (μm)
Hal1	0% : 100%	0	brine	1, 0.5, 2, 3, 1	1	29.38	n.d.
Mus1	100% : 0%	69	brine	5, 7, 9, 5, 3, 1	1, 10, 0.1, 1, 0.03, 1	40.01	1028
Mus2	10% : 90%	59	brine	5, 9, 1, 5	1, 10, 0.1, 1, 0.03, 1	44.18	1470
Mus3	20% : 80%	49	brine	5	1, 0.8, 0.5, 1, 0.1, 0.03, 0.3, 1, 0.01, 0.003, 0.008, 0.3, 1	44.96	1318
Mus4	20% : 80%	61	brine	5	1, 3, 5, 7, 9, 11, 13, 11, 9, 7, 5, 3, 1, 5, 10	171.04	975
Mus5	20% : 80%	50	brine	5	0.03	35.35	967
Mus6	20% : 80%	50	brine	5	1	30.10	1142
Mus7	20% : 80%	50	brine	5	5	30.11	1135
Mus8	20% : 80%	53	brine	5	13	30.05	1295
Mus9	20% : 80%	0	brine	5, 4, 3, 2, 1	1	32.43	1212
Mus10	20% : 80%	0	brine	5, 4, 3, 2, 1	5	38.87	1361
Mus11	20% : 80%	0	brine	5, 4, 3, 2, 1, 2, 3, 4, 5	10	60.14	1376
Mus12	20% : 80%	0	silicone oil	5	1, 10, 0.1, 1, 0.03, 1, 3, 5, 1, 0.1	44.62	1007
Mus13	20% : 80%	0	none	5	1, 10, 0.1	38.05	n.d.
Mus14	30% : 70%	45	brine	5	1, 10, 0.1, 1, 0.03, 1, 3, 5, 10, 1	33.72	n.d.
Mus15	30% : 70%	66	brine	5	1, 10, 0.1, 1, 0.03, 1, 10, 1, 3, 1, 0.01	50.53	997
Mus16	20% : 80%	0	none	5	1, 10, 0.1, 1, 0.03, 1, 10, 1, 0.1	38.46	1555
Mus17	20% : 80%	0	brine	5	1, 0.001	8.27	880
Mus20	0% : 100%	54.8	brine	5	1, 10, 0.1, 1, 0.03, 1, 3, 5, 7, 9, 11, 13, 11, 1, 0.01, 0.003	106.51	1100
Mus21	80% : 20%	50.3	brine	5	1, 10, 0.1, 1, 0.03, 1, 0.00	30.91	793
Mus22	50% : 50%	55.5	brine	5	1, 10, 0.1, 1, 0.03, 1, 0.01	47.05	955
Mus23	20% : 80%	49.5	brine	5	0.1	30.3	1026
Mus24	20% : 80%	51.8	none	5	1	-	1568
Mus25	20% : 80%	0	brine	5, 4, 3, 2, 1	0.03	30	1300

Table 5.2:
List of slide-hold-slide experiments performed plus corresponding experimental conditions.
**: sliding interval without hold*

Sample Code	Composition Muscovite : Halite	Dry run-in displacement (mm)	Fluid	Normal Stress (MPa)	Velocity-stepping sequence (μm/s)	Hold Periods (s)	Total wet shear displacement	Final Gouge thickness (μm)
shs1	20% : 80%	51.3	brine	5	1*, 3, 5, 0.05*, 10, 1, 5	60, 600, 60	95.27	1077
shs2	20% : 80%	55.61	brine	5	1*, 0.1, 0.01	600, 1200, 6000	27.73	1008
shs3	20% : 80%	50.5	brine	5	10, 5	60, 600, 6000	60.22	1015
shs4	20% : 80%	57.6	brine	5	1*, 0.03, 0.1, 1, 0.1*, 5	60, 600, 6000	86.49	903
shs5	20% : 80%	50.12	brine	5	1*, 0.1*, 2, 0.1*, 10	60, 600, 6000	82.49	963

5.3.1 Porosity data

The final porosities of the samples obtained from our constant velocity tests (Mus5, Mus6, Mus7, Mus8 and Mus23) and slide-hold-slide tests, as measured using image analysis and TGA, are listed in Table 5.3. The final porosity of the gouges was also calculated from our mechanical compaction data using the gouge composition and the measured initial thickness of the sample assembly. However, in numerous cases we found negative values for the final porosity calculated in this way, probably due to minor material loss from the edges of the samples during the experiments. We accordingly corrected our mechanical compaction data for material loss, using the gouge composition and the measured initial

thickness of the sample assembly. However, in numerous cases we found negative values for the final porosity calculated in this way, probably due to minor material loss from the edges of the samples during the experiments. We accordingly corrected our mechanical compaction data for material loss, using a linear fit of compaction strain versus displacement obtained from experiment Mus12 in which silicone oil was used as the pore fluid. Pressure solution compaction does not occur under these conditions, because halite is not soluble in silicone oil. The porosity (Porosity –Exp) values listed in Table 5.3 are the values obtained from the thus corrected compaction data. They agree well with the porosities determined using both image analysis and TGA. Note that the final porosity of the gouges increases systematically with increasing sliding velocity (Figure 5.2).

Table 5.3:
Porosity values determined for a selected number of experiments using our experimental compaction data (porosity Exp) corrected for minor material loss, image analysis (porosity I.A.) and Thermo Gravimetric Analysis (porosity TGA) plus their standard deviations (S.D.)
n.d.: not determined

Experiment	Velocity (μm/s)	Porosity Exp	Porosity IA	S.D.	Porosity TGA	S.D.
shs1	1*, 3, 5, 0.05*, 10, 1, 5	10.73	n.d.	n.d.	9.91	0.02
shs2	1*, 0.1, 0.01	0.30	n.d.	n.d.	1.85	0.11
shs3	10, 5	8.31	n.d.	n.d.	7.65	0.20
shs4	1*, 0.03, 0.1, 1, 0.1*, 5	3.52	n.d.	n.d.	5.38	1.26
shs5	1*, 0.1*, 2, 0.1*, 10	5.79	n.d.	n.d.	6.33	1.26
mus5	0.03	1.58	n.d.	n.d.	1.37	0.28
mus23	0.1	3.27	n.d.	n.d.	3.14	1.24
mus6	1	4.82	n.d.	n.d.	5.26	1.52
mus7	5	8.66	9.05	1.42	8.99	2.16
mus8	13	12.46	13.37	4.50	12.15	0.76

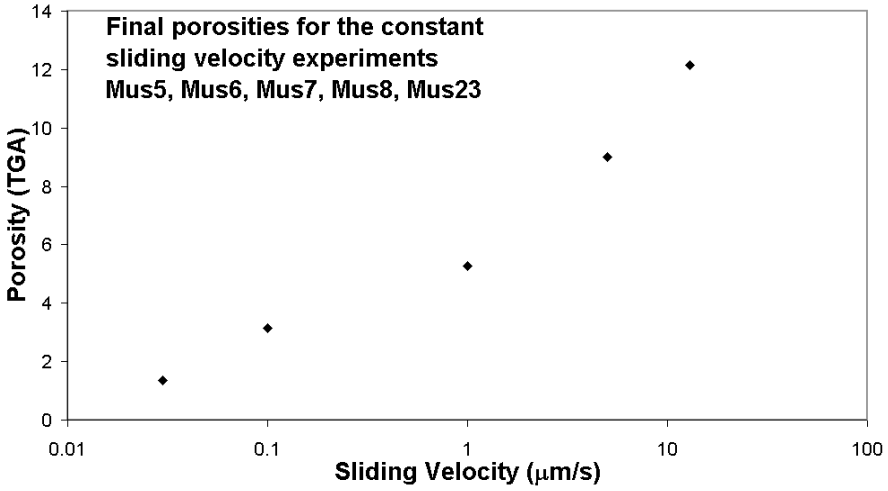

Figure 5.2: Plot showing measured final porosity (TGA) versus sliding velocity for the 5 constant sliding velocity experiments (Mus5, Mus6, Mus7, Mus8 and Mus23)

5.3.2 Velocity-stepping data

We present data from a typical velocity-stepping experiment (Mus2) in Figure 5.3a. In all such experiments, upon a change in sliding velocity, an instantaneous effect on the measured shear stress (strength) was observed. This was followed by a gradual approach to a new steady state strength as seen in conventional rate-and state-dependent friction experiments (Dieterich, 1979; Ruina, 1983; Marone, 1998b; Scholz, 1998). Sample compaction rate was observed to increase sharply upon a step down in velocity and to decrease and even become negative upon a step up in velocity.

Representative results from the complete set of velocity-stepping tests, showing the dependence of steady state shear strength of our gouge samples on sliding velocity, are presented in Figure 5.3b. The pure muscovite sample (Mus1) showed no measurable velocity-dependence of steady state shear strength (~1.8 MPa) over the entire velocity range (0.03-10 μm/s) investigated. The pure halite sample showed a very slight velocity dependence, with the steady state shear strength increasing from a value of ~ 4.3 MPa at a velocity of 0.003 μm/s to a maximum of ~ 5.2 MPa at 3 μm/s. At higher velocities, the steady state strength decreased slightly, falling to around 4.6 MPa at the highest velocity (13 μm/s).

In contrast to the pure end-members, all mixed muscovite-halite samples show a pronounced dependence of steady state shear strength on sliding velocity, reaching a maximum strength at ~ 1 μm/s (Figure 5.3b). In addition, strength clearly decreases with increasing muscovite-content. All halite-muscovite mixtures are weaker than the pure halite sample over the entire velocity range investigated, while at the lowest sliding velocities investigated, samples with 20-50 wt% muscovite are even weaker than the pure muscovite sample. The velocity dependence of shear strength is most pronounced in mixtures with low to intermediate muscovite content (i.e. 10 wt% to 50 wt%). The samples with 20 wt% muscovite increased over 250% in strength, from a minimum value of ~1.4 MPa at 0.001 μm/s to a maximum of ~3.7 MPa at 1 μm/s. At higher sliding velocities, the steady state strength decreased again, reaching a value of ~2.2 MPa at 13 μm/s. Two regimes of behaviour could thus be distinguished for the halite-muscovite samples, namely a velocity-strengthening regime at low sliding velocities (< 1 μm/s) and a velocity-weakening regime at high sliding velocities (≥ 1μm/s).

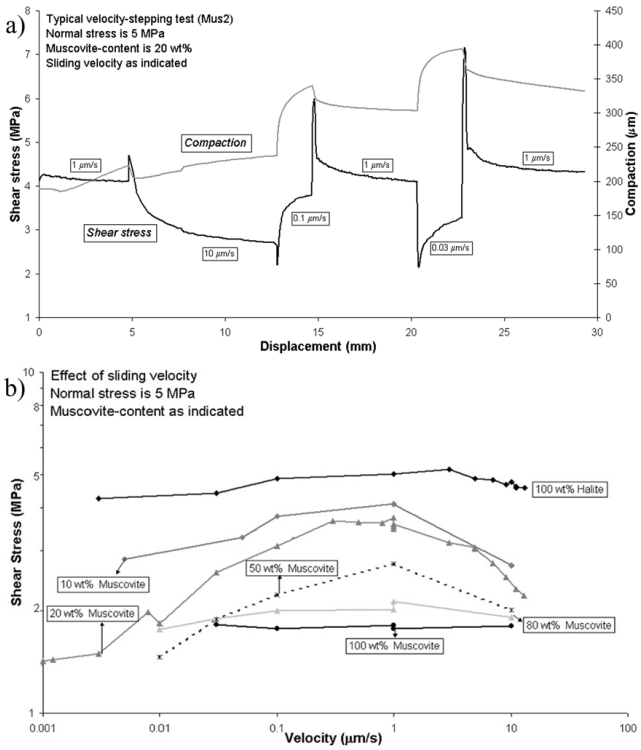

Figure 3. a) Measured shear stress (strength) and fault normal compaction versus sliding displacement for a 20 wt% muscovite sample (Mus2), subjected to velocity stepping at a normal stress of 5 MPa.
b) Measured steady state shear stress (strength) versus sliding velocity data from the complete set of velocity-stepping experiments (Table 5.1: cf. chapter 4).

5.3.3 Slide-hold-slide data

In Figure 5.4, we present typical shear stress and normal displacement versus time data sets extracted from the complete sequence of SHS cycles performed within experiments shs2 and shs5 (see Table 5.2). Note that the experimental data shown are for displacements beyond both the dry and wet run-in stages. The steady state sliding behaviour obtained prior to and between hold periods was generally similar to that observed in the velocity-stepping experiments, both in terms of steady state shear stress levels and in terms of strain weakening and transient response to velocity-steps. An exception was sample shs3 (wet run-in at 10 µm/s), which showed significantly lower steady state shear stress values (~ 30%) than those determined in the velocity-stepping series, as well as regular stick-slip cycles during sliding at 10 µm/s.

All SHS cycles showed rapid shear stress relaxation from the instant that the drive motor was halted (see Figure 5.4 and 5.5). In addition, significant compaction and shear displacement were observed during the hold periods. At low SHS reference velocities (< 1 μm/s), the shear stress drops at a low rate, and only small amounts of horizontal and vertical displacement are accumulated. With increasing SHS reference velocity, the shear stress relaxation rate during individual hold periods increases, with a maximum observed at 1 μm/s (though the lowest shear stress level was observed in the sample deformed at 10 μm/s). Both horizontal (shear) and vertical (compaction) displacement accumulated during hold periods increase with increasing SHS reference velocity. Shear displacement, for example, is approximately half an order of magnitude larger at a SHS reference velocity of 10 μm/s than at 0.1 μm/s, while compaction is even one order of magnitude larger.

Upon re-shear, distinctly different behaviour was observed for SHS cycles performed in the velocity-strengthening regime (sliding velocity <1 μm/s) than for SHS cycles in the velocity-weakening regime (sliding velocity ≥ 1 μm/s). When sliding was re-started in the low velocity regime, a more or less gradual increase in shear stress occurred until a steady state shear stress was achieved at a similar level to the shear stress prior to the hold period (see Figures 5.4a and 5.4b). Dilatation, recovering about 80% of the compaction that occurred during the hold, was observed upon re-shear. In the high velocity regime, on the other hand, a sharp peak in shear stress was observed upon re-shear, accompanied by significant dilatation usually recovering all of the compaction that occurred during the hold (Figure 5.4c and 5.4d). After the peak, the shear stress rapidly decreased to a steady state level similar to that prior to the hold period.

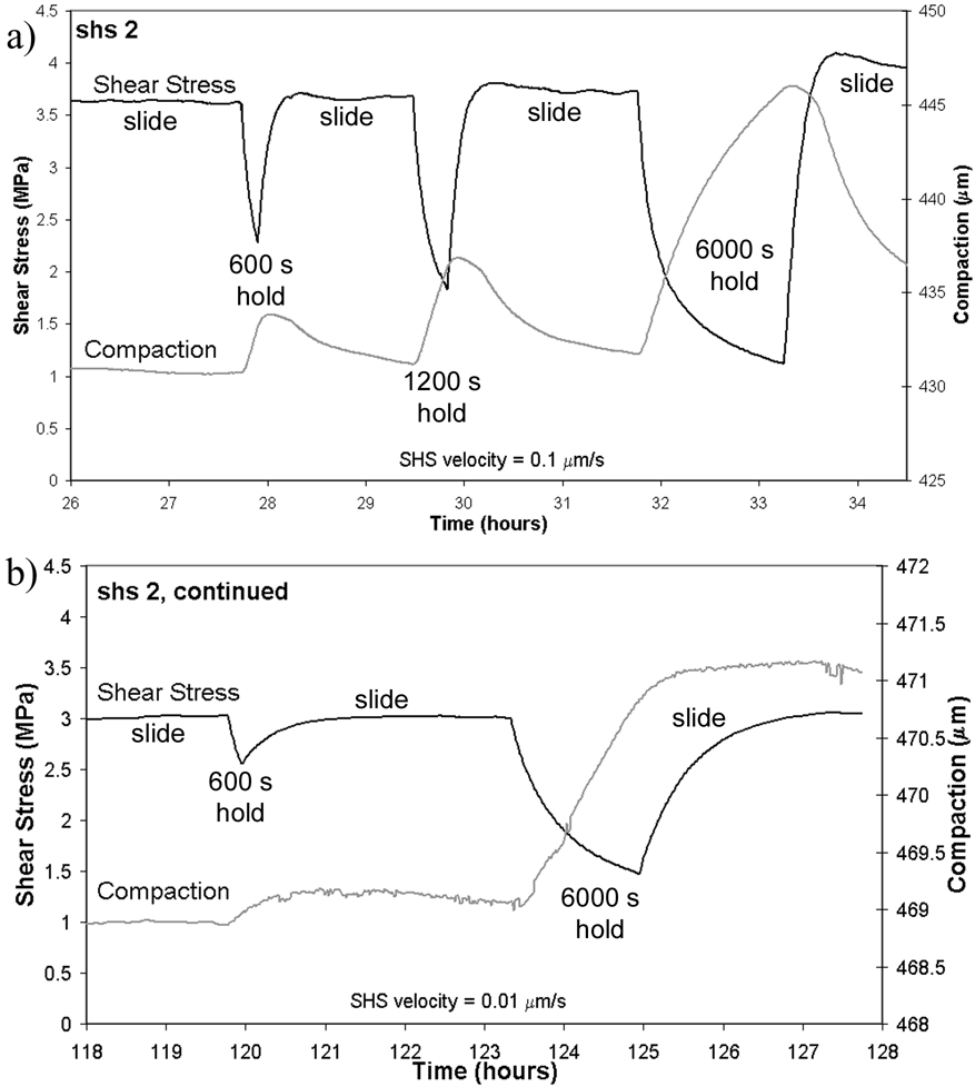
a)
shs 2
Shear Stress
slide
slide
slide
slide
600 s
hold
6000 s
hold
Compaction
1200 s
hold
SHS velocity = 0.1 μm/s
Shear Stress (MPa)
Compaction (μm)
Time (hours)
b)
shs 2, continued
Shear Stress
slide
slide
slide
600 s
hold
Compaction
6000 s
hold
SHS velocity = 0.01 μm/s
Shear Stress (MPa)
Compaction (μm)
Time (hours)

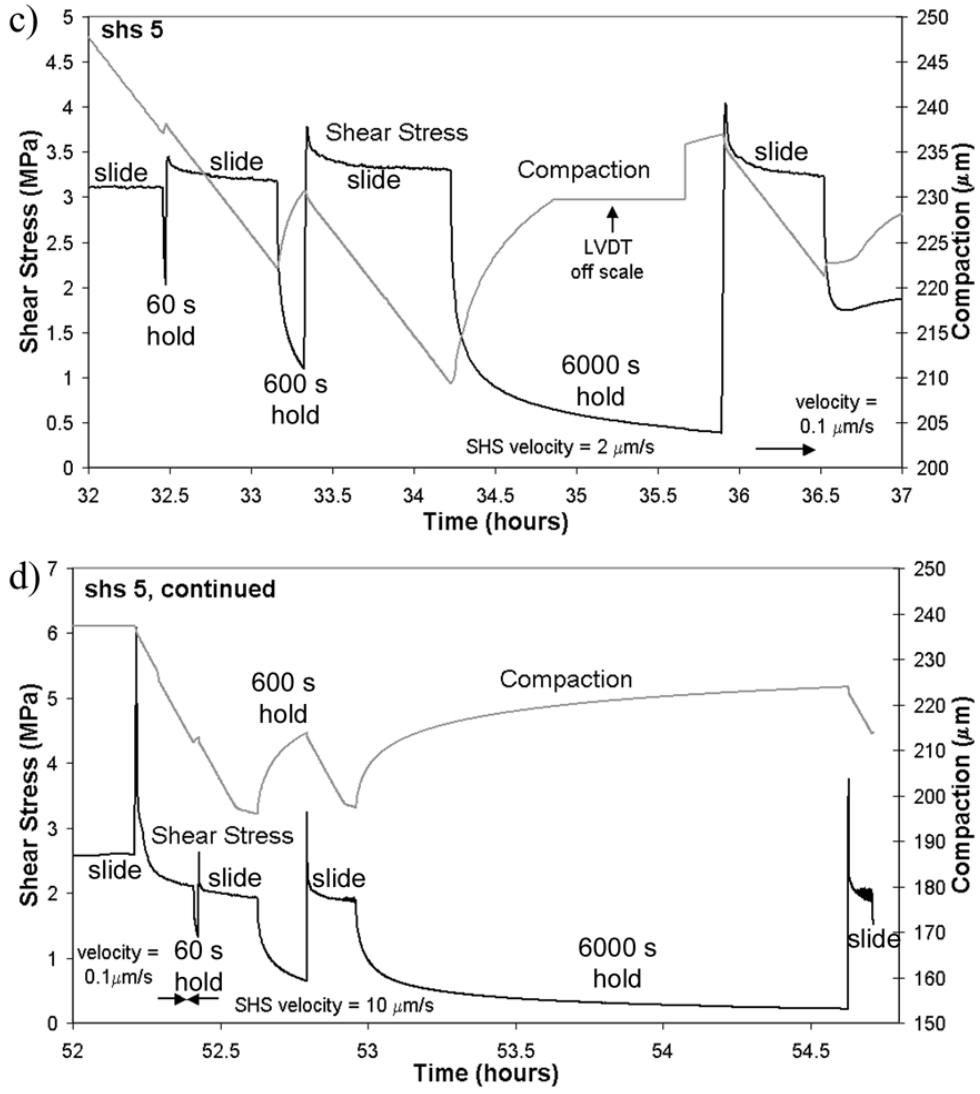

Figure 5.4: Typical shear stress and compaction versus time data obtained for SHS cycles performed within experiments shs 2 (a,b) and shs 5 (c,d). Note that the slide periods are characterized by near steady state stress levels, while the intervening hold periods show stress relaxation and enhanced compaction. Compaction is represented in μm of displacement measured normal to the fault zone. Normal stress is 5 MPa and muscovite-content is 20 wt% in all cases.

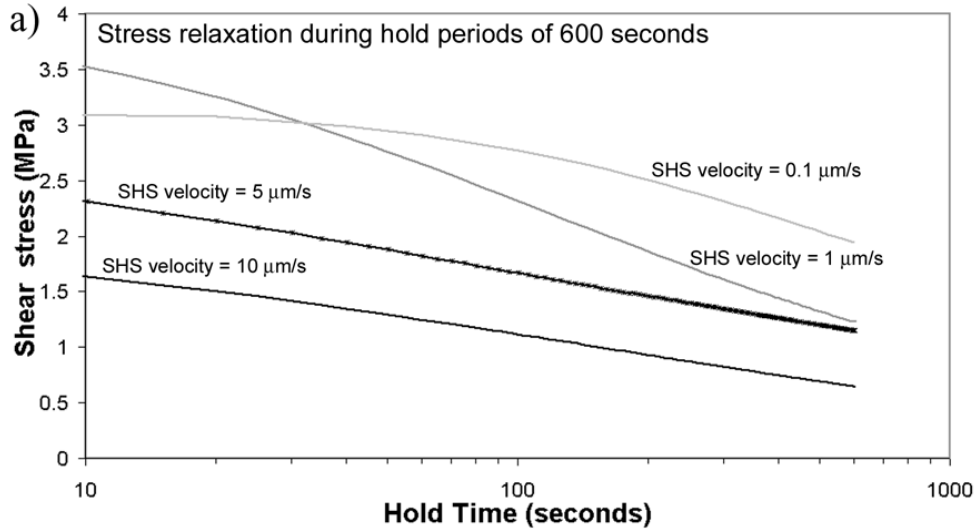
a)
Stress relaxation during hold periods of 600 seconds
Shear stress (MPa)
Hold Time (seconds)
SHS velocity = 0.1 μm/s
SHS velocity = 1 μm/s
SHS velocity = 5 μm/s
SHS velocity = 10 μm/s
0
0.5
1
1.5
2
2.5
3
3.5
4
10
100
1000

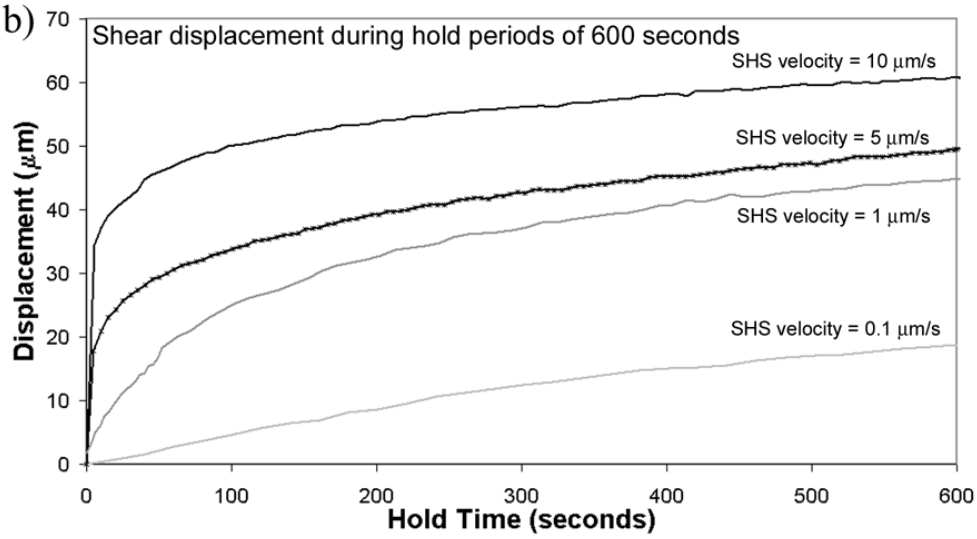
b)
Shear displacement during hold periods of 600 seconds
Displacement (μm)
Hold Time (seconds)
SHS velocity = 10 μm/s
SHS velocity = 5 μm/s
SHS velocity = 1 μm/s
SHS velocity = 0.1 μm/s
0
10
20
30
40
50
60
70
0
100
200
300
400
500
600

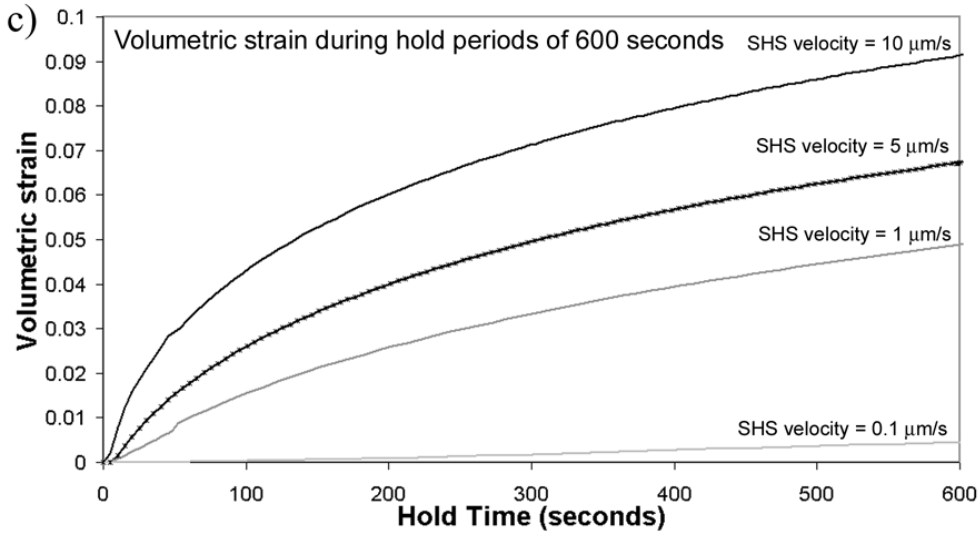

Figure 5.5: Hold period data. Evolution of shear stress (a), shear displacement (b) and volumetric strain (c) during hold periods of 600 seconds for samples containing 20 wt% muscovite and 80 wt% halite tested in SHS mode at different SHS reference velocities (samples shs4 and shs 5).

5.3.4 Microstructural observations

The starting microstructure of the wet samples prior to brine addition was investigated using a sample extracted from an experiment that was terminated directly after the dry run-in stage, i.e. after a dry shear strain of ~50 (sample Mus24, Niemeijer and Spiers, 2005 and Chapter 4 – see Figure 5.6). In this sample, halite clasts with a size close to the starting grain size fraction (60-110 μm) are obvious and represent ~30 vol% of the gouge. These appear to be little affected by deformation, since they are mostly equiaxial. However, the matrix of the sample consists of a fine-grained mixture of halite and muscovite. Some regions of the gouge (~20 vol%, especially near the edges of the gouge) are relatively enriched in muscovite and contain fewer halite clasts than other regions. Such regions sometimes form narrow poorly defined zones lying in the Riedel shear orientation, i.e. inclined at 20-30 º to the shear direction. Locally, the matrix also shows a weak foliation orientated at 30° to the fault zone boundary (Figure 5.6b), defined by muscovite grains interleaved with comminuted halite grains, some of which show a weak elongation within this foliation. A sharp, continuous, 5-15 μm wide boundary-parallel shear band, mainly consisting of aligned muscovite flakes, is observed near the lower shear zone boundary of sample Mus24 (see arrows, Figure 5.6a and 5.b). It was inferred in an earlier paper (see Chapter 4) that this shear band was probably produced during the last part of the dry run-in,

since at this time stick-slip cycles occurred which are well-known to be associated with shear localization (Chester and Logan, 1990; Marone, 1998b; Bos et al., 2000b).

In Figures 5.7a-c and 5.8a-c, we show the microstructures developed in three constant sliding velocity (0.03, 5 and 13 μm/s) experiments in which the samples were deformed wet to a shear strain of ~30. Sample Mus 5, deformed at 0.03 μm/s, shows a wavy foliation defined by aligned muscovite flakes plus intervening halite grains (see Figure 5.7a). The overall grain size of the halite is significantly reduced in comparison with the starting material, although numerous larger clasts are still present. These larger clasts consist of elongated grains often with long tails that sometimes show trails of fluid inclusions (Figure 5.8a), suggesting the presence of an overgrowth. The matrix makes up approximately 80 vol% of the gouge and consists of a foliated intercalation of muscovite flakes and fine halite grains. No apparent porosity is visible in the thin section, indicating that it is very low (see also Table 5.3).

Samples Mus7 and Mus8, deformed wet at higher sliding velocities (5 and 13 μm/s) are relative structureless on the microscopic scale and show a large variation in halite grain size (Figures 5.7b-c). The larger clasts in these samples are blocky and irregular compared to the clasts in the low velocity sample. The matrix muscovite grains do not define a clear foliation. They usually coat the smaller halite grain boundaries but not the entire surface of larger clasts. In contrast to the low velocity samples, considerable porosity is developed, especially at the highest velocity (Mus8, see Table 5.3). The porosity is both distributed over the sample as well as locally clustered to form zones of higher porosity. Besides the difference in porosity, there is little further difference in the microstructures of sample Mus7 (5 μm/s, Figure 5.7b, 5.8b) and Mus 8 (13 μm/s, Figures 5.7c and 5.8c).

In Figures 5.9a and 5.10a, we show the microstructure of slide-hold-slide sample shs2, which was deformed to a shear strain of ~28 in the low-velocity regime (< 1 μm/s). The microstructure is relatively homogeneous and consists of a matrix of highly intercalated halite and muscovite grains, with numerous tailed or sigmoidally shaped halite clasts. A clear, anastomosing foliation can be observed, which is mostly defined by the muscovite flakes and the shape of the intervening halite clasts. Almost all halite grain boundaries are coated with muscovite flakes. The sample shows no evidence for boundary-parallel shear bands.

Figures 5.9b and 5.10b show the microstructure of sample shs4 which was deformed to a shear strain of ~85 in both velocity regimes. The appearance of this gouge is very heterogeneous. The overall halite grain size is significantly reduced in comparison to sample shs2. However, there are still a number of larger, sigmoidally shaped or tailed halite clasts present. Some of these clasts show intragranular fractures (Figure 5.10b). The matrix consists of regions of very fine-grained mixtures of halite and muscovite and regions with less muscovite and more porosity. Some of the more porous zones appear aligned in a poorly defined Riedel shear orientation.

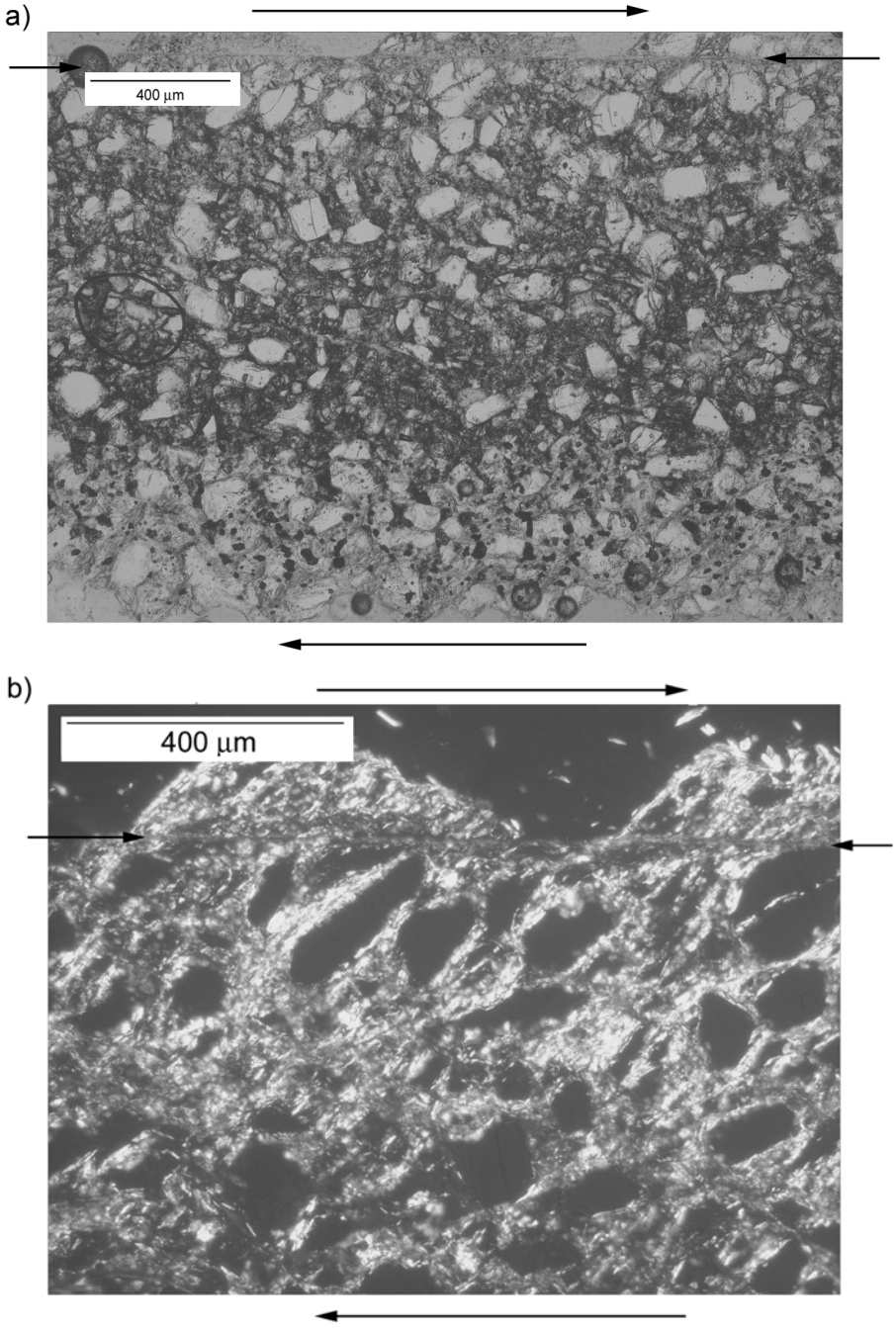

Figure 5.6: Optical micrographs showing microstructures developed in the initial dry run-in stage of deformation, sample Mus24 (20 wt% muscovite, shear strain is ~40).
a) Plane polarized light: note chaotic structure with halite clasts embedded in a fine halite-muscovite matrix. A boundary parallel Y-shear is evident (small arrows). Shear sense as indicated.
b) Crossed polarized light: note weak foliation and Y-shear developed at the boundary of the gouge (small arrows). Shear sense as indicated. See also chapter 5.

a)

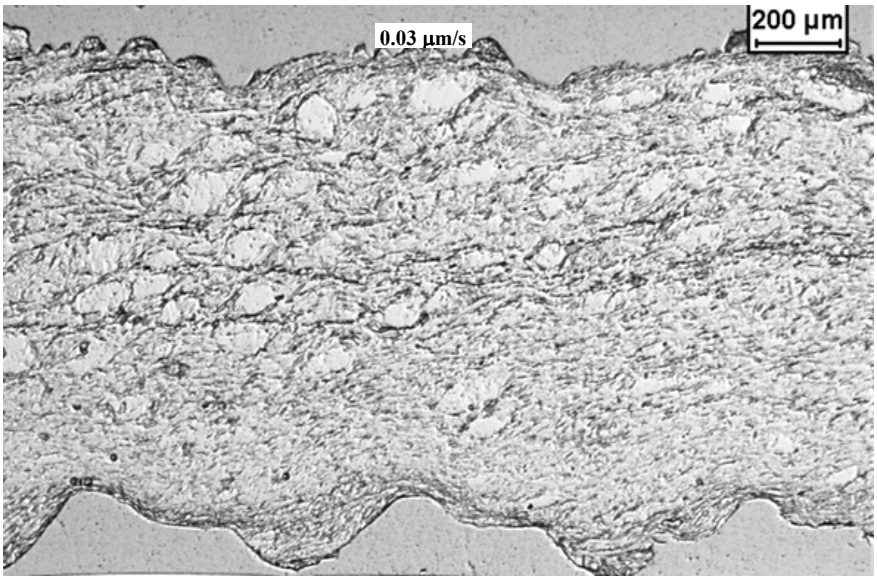

b)

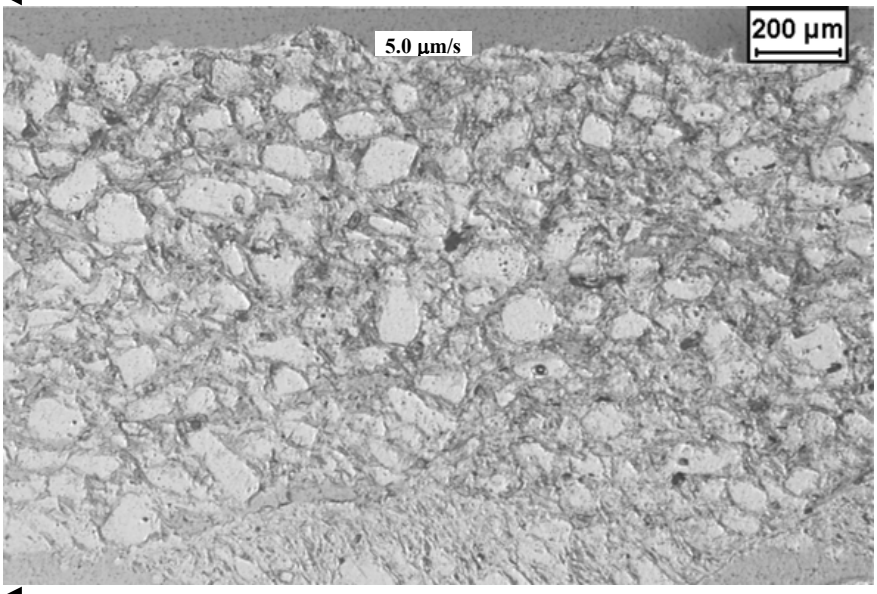

c)

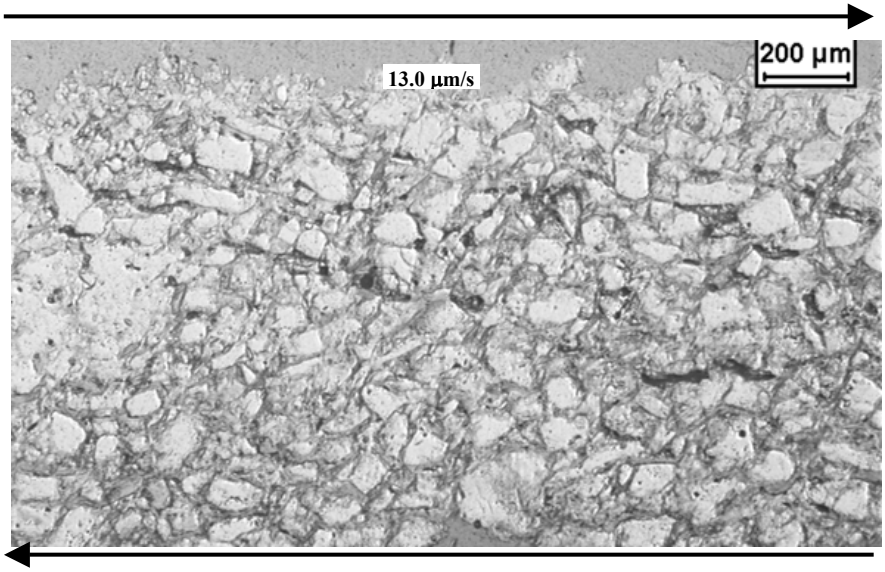

Figure 5. 7: Optical micrographs showing microstructures developed in the constant sliding velocity tests, samples Mus5, Mus 7 and Mus 8 (20 wt% muscovite, shear strain is ~30). Shear sense as indicated
a) Plane polarized light, sliding velocity is 0.03 µm/s,note well developed foliation and absence of porosity.
b) Plane polarized light, sliding velocity is 5 µm/s, note chaotic appearance and presence of porosiy.
c) Plane polarized light, sliding velocity is 13 µm/s, note chaotic appearance and presence of porosiy

a)

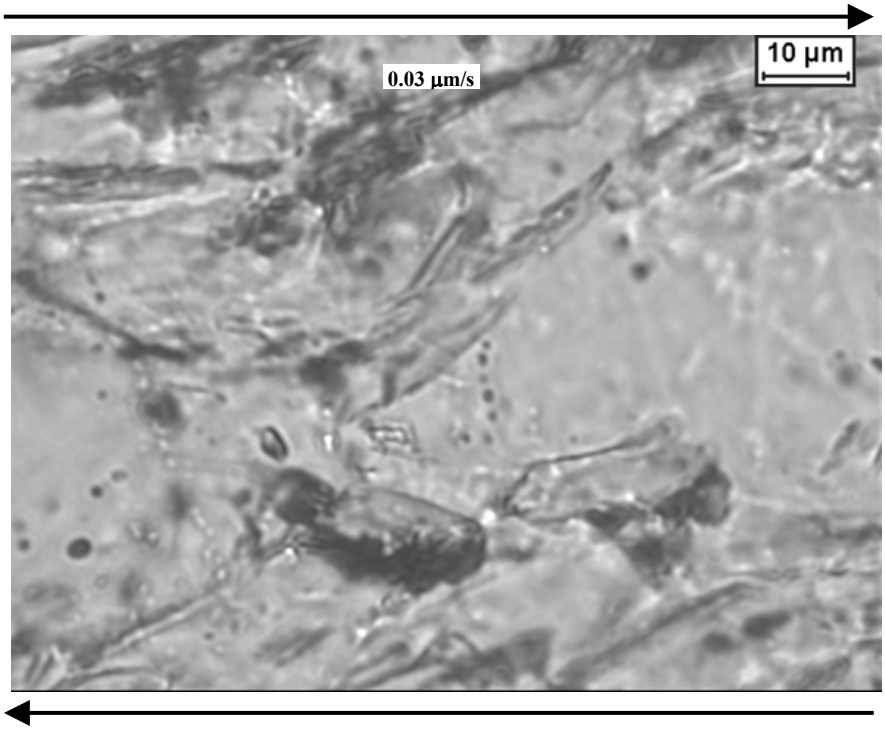

b)

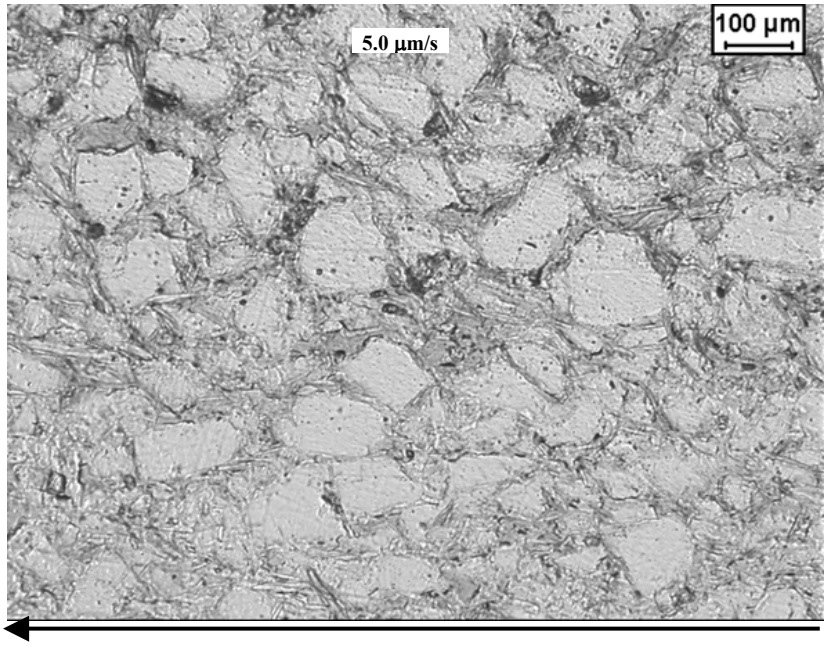

c)

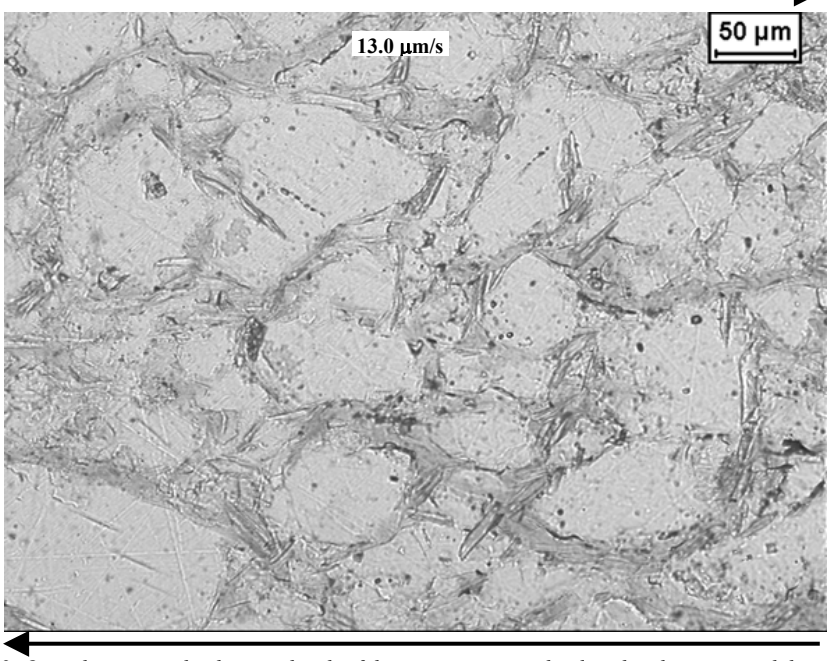

Figure 5.8: Optical micrographs showing details of the microstructures developed in the constant sliding velocity tests, samples Mus5, Mus 7 and Mus 8 (20 wt% muscovite, shear strain is ~30).Shear sense as indicated
a) Plane polarized light, sliding velocity is 0.03 µm/s, note long tail of halite clast..
b) Plane polarized light, sliding velocity is 5 µm/s, note the high porosity.
c) Plane polarized light, sliding velocity is 13 µm/s, note the high porosity.

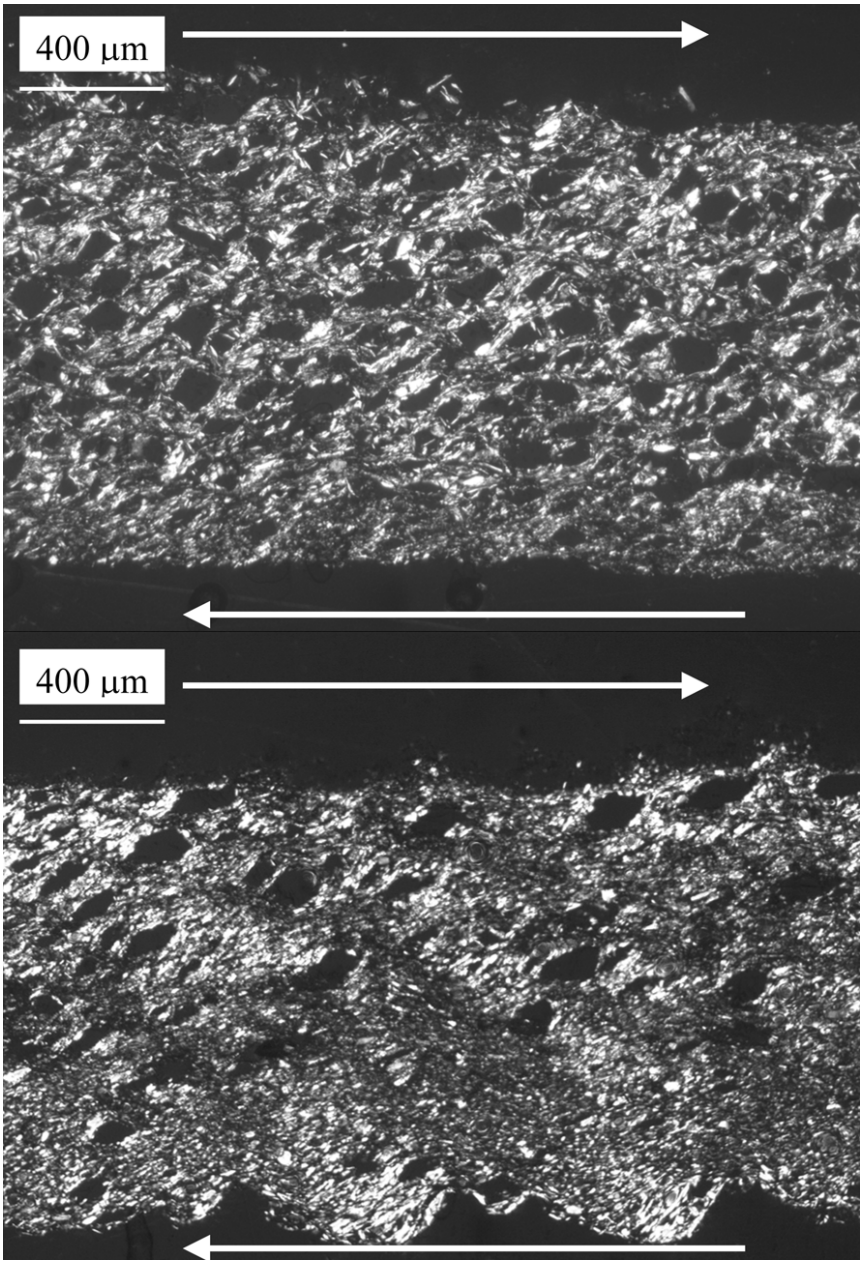

Figure 5.9: Crossed polarized light optical micrographs showing microstructures developed in SHS tests shs2 and shs4.
a) Sample shs 2. Note foliation orientated at an angle of ~20° to the fault zone boundary. Numerous asigmoidally shaped halite clasts, showing long tails are evident. Shear strain is ~ 25 and shear sense as indicated.
b) Sample shs4. Note heterogeneous appearance of the gouge, with zones of finely-grained mixtures of halite and muscovite and zones with larger halite clasts embedded in muscovite. The wavy foliation is orientated at an angle of ~10° to the fault zone boundary. Shear strain is 85 and shear sense as indicated.

a)

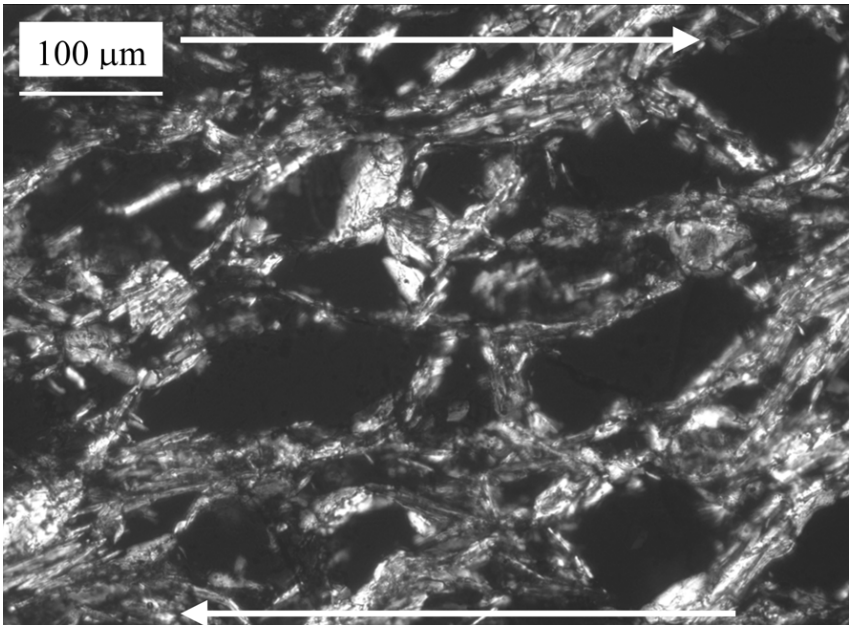

b)

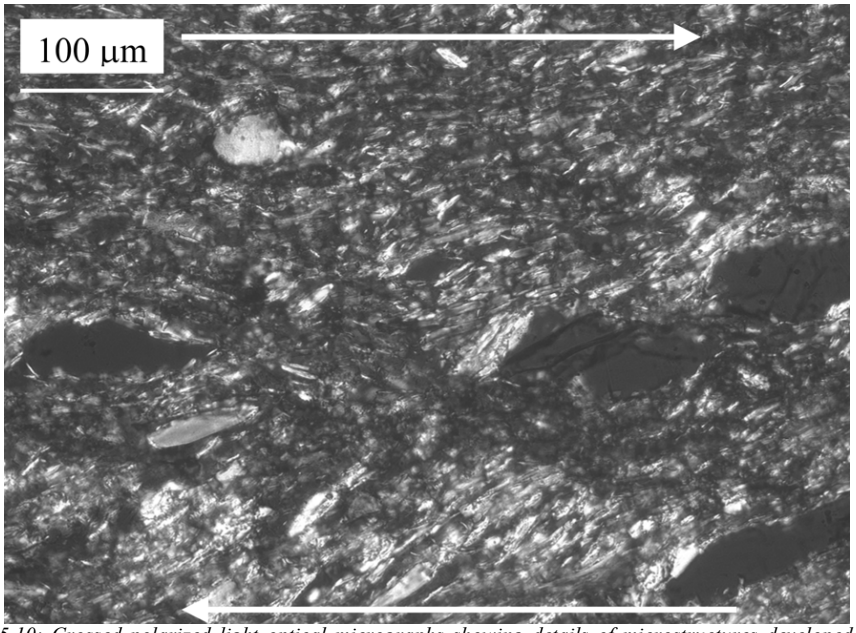

Figure 5.10: Crossed polarized light optical micrographs showing details of microstructures developed in SHS tests shs2 and shs4.
a) Sample shs2. Note long tails in most halite grains. All halite grains are coated with muscovite flakes. Shear strain is ~25 and shear sense as indicated
b) Sample shs4. Note small grain size of halite grains in the matrix. Large halite clasts show several intragranular fractures. Shear strain is 85 and shear sense as indicated.

5.4. Discussion

The aim of the present work is to investigate the large strain slip and healing behaviour of halite-muscovite fault gouges in both the velocity-strengthening and in the velocity-weakening regimes, to explain any differences in behaviour in terms of the microphysical mechanisms involved, and to speculate on the possible implications of our results for natural fault zones. In order to set about interpreting our results, we begin by considering a number of important theoretical concepts relating to the strength and healing of gouge-filled faults. We then proceed to consider the microphysical mechanism that might be responsible for the observed velocity-weakening under steady state conditions. We go on to compare and mechanistically analyse the strength recovery behaviour seen in slide-hold-slide experiments performed in both the velocity-strengthening and the velocity-weakening regimes. Finally, we will discuss some of the implications that our work may have for deformation of natural phyllosilicate-bearing fault zones under hydrothermal conditions.

5.4.1. Theoretical considerations

Following Lehner (1995) and Bos and Spiers (2000; 2002a), and taking into account possible changes in grain boundary and pore wall surface areas, the combined energy and entropy balance for a representative volume of fault rock during deformation can be written as:

$$\tau \dot{\gamma} + \sigma_n \dot{\varepsilon} = \dot{f} + \dot{\Delta} + \dot{A}_{gb}\gamma_{gb} + \dot{A}_{sl}\gamma_{sl} \tag{5.1}$$

assuming a closed system with respect to solid mass. In this relation, τ is the shear stress acting on the fault rock, $\dot{\gamma}$ is the shear strain rate, σ_n is the effective normal stress on the fault (compressive positive), $\dot{\varepsilon}$ is the normal strain rate (compaction positive), $\dot{f}$ is the rate of change of Helmholtz free energy of the solid phase per unit volume, $\dot{\Delta}$ denotes the volume specific energy dissipation rate by all irreversible processes, $\dot{A}_{gb}$ is the rate of change in grain boundary surface area per unit volume, γ_{gb} is the grain boundary surface energy, $\dot{A}_{sl}$ is the rate of change of solid-liquid interfacial area per unit volume and γ_{sl} is the solid-liquid interfacial energy. For clarity, note that the left-hand side of (5.1) represents the rate at which work is done on unit volume of fault rock by the externally applied stresses. The right-hand side represents the sum of the energy dissipation rates of all microscale processes operating per unit volume (Δ), plus changes in the Helmholtz free energy stored in

the solid part of the system, plus changes in surface energy caused by changes in grain boundary and pore wall area. Dividing now by $\dot{\gamma}$ (Bos and Spiers, 2000, 2002a), the measured shear stress or shear strength can be written:

$$\tau = \tau_x - d\varepsilon/d\gamma\,\sigma_n \tag{5.2}$$

where $\frac{d\varepsilon}{d\gamma}$ represents an instantaneous dilatation angle $\tan\psi = \frac{d\varepsilon}{d\gamma}$ analogous to that familiar in soil mechanics (e.g. Paterson, 1995), and where

$$\tau_x = \frac{df}{d\gamma} + \frac{d\Delta}{d\gamma} + \frac{dA_{gb}}{d\gamma}\gamma_{gb} + \frac{dA_{sl}}{d\gamma}\gamma_{sl} \tag{5.3}$$

The quantity τ_x can be interpreted as representing the contribution to measured shear stress of all energy dissipation and storage processes operating in the gouge. Ignoring minor changes in Helmholtz free energy, it is evident from (5.2) and (5.3) that strengthening of a homogeneously deforming granular fault gouge may occur for three basic reasons. First, gouge compaction may increase the packing density so that upon reshearing the gouge needs to dilate, requiring work against the normal stress ($\frac{d\varepsilon}{d\gamma}\sigma_n$). Second, the gouge may strengthen through an increase in contact bonding between particles in the gouge. The increased bonding may increase the grain boundary friction coefficient and/or the grain boundary cohesion. This then increases the average contact sliding strength in the gouge and thereby the total frictional dissipation ($\frac{d\Delta}{d\gamma}$) due to intergranular slip on re-shearing. Third, the gouge may strengthen by an increase in grain contact area (relative to pore wall area) which may be disrupted on re-shear. This increases strength only when the sliding contact has a cohesive strength. In general, fault gouge healing will be a combination of the three.

5.4.2 Steady state behaviour: Velocity-strengthening vs. velocity-weakening

Our results from the velocity-stepping experiments have shown two clear regimes of steady state behaviour for the halite-muscovite mixtures: velocity-strengthening at velocities below 1 μm/s and velocity-weakening at velocities above 1 μm/s. We have shown here and in our previous work (Bos and Spiers, 2002b; Niemeijer and Spiers, 2005 and Chapter 4) that the velocity-strengthening regime is associated with intense phyllosilicate foliation development.

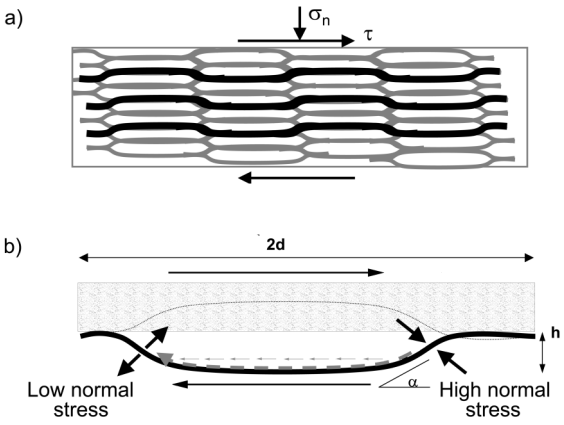

Figure 5.11 a) Schematic diagram of the model microstructure proposed by Bos and Spiers (2002b), showing a contiguous, anastomosing network of phyllosilicates surrounding elongate grains of a soluble solid. The shear strength of the gouge is determined by the combined resistance to shear offered by the serialtransport processes of frictional sliding on the phyllosilicate foliae, pressure solution in the halite and dilatation on the foliation (work done against the normal stress).
b) Schematic drawing of representative grain element of matrix, showing an active sliding surface in black. Shear sense is right-lateral. The diffusive mass flux from source to sink regions is indicated by a dashed arrow. The foliation waves have amplitude h, the grains have long axis d. The leading edge of the grain is inclined at an angle α to the horizontal (Figure from Bos and Spiers, 2002b).

In our previous paper, we presented strong evidence that this regime is characterized by a steady state flow mechanism involving frictional sliding on the foliation accommodated by pressure solution of the intervening halite grains. A microphysical model was presented that is capable of predicting the observed velocity-strengthening behaviour. The model is based on a steady state microstructure (Figure 5.11), where the phyllosilicate foliation wraps around elongate halite grains. The shear stress supported by the gouge at a particular sliding velocity is then the sum of the shear stress for sliding on the foliation plus the shear stress taken up by driving pressure solution. The strengthening with increasing velocity is caused by an increasing influence of pressure solution on the total shear stress, i.e. increasing dissipation by pressure solution.

We argue here that the switch to velocity-weakening behaviour occurs when the rate of pressure solution is too slow to accommodate the imposed shear displacement and the gouge has to dilate to accommodate slip, causing the onset of cataclasis. This argument is based on the observation that the velocity-weakening regime is associated with a chaotic cataclastic microstructure (see Figures 5.7b,c and 5.8b,c). However, purely cataclastic deformation is not expected to show a strong rate-dependence, whereas we have found a marked, inverse dependence of steady state shear strength on velocity (Figure 5.3b). This velocity weakening effect could potentially be explained by severe grain size reduction in the halite with increasing velocity, thus enhancing pressure solution rates in the halite and reducing the stress required for pressure solution to accommodate slip on phyllosilicates. However, since the velocity weakening behaviour that we observe is reversible with velocity-stepping direction (see Figure 5.4a), we believe that an effect of grain size reduction thereby enhancing pressure solution rates, can be ruled out. Another possibility is that the proportion of healed, cohesive contacts decreases with increasing sliding velocity, due to a shorter average contact lifetime (*cf.* Dieterich-type healing). However, if this is the explanation of the velocity-weakening, the same would occur in the pure halite sample, but we did not observe a strong velocity-weakening in this sample. Moreover, the lack of

healing observed in halite-kaolinite samples (Bos and Spiers, 2000) and in our low velocity samples, implies that phyllosilicate-halite contacts do not heal readily. Therefore, we believe that a Dieterich-type healing mechanism cannot explain the observed strong velocity-weakening.

On the basis of the chaotic, intermixed, cataclastic microstructures, we propose instead the hypothesis that the velocity-weakening regime is due to competition between a) shear-induced dilatation caused by granular flow of the gouge and b) compaction of the gouge through pressure solution of the halite. Such a mechanism should lead to an increase in porosity with increasing shear rate, at steady state, as granular dilatation becomes more effective compared to compaction by pressure solution. This will produce a decrease in mean grain contact area and intergranular slip-surface inclination/amplitude (dilatancy angle for granular flow). A decrease of the average inclination of actively sliding grain contacts (i.e. the dilatancy angle for granular flow) will lower the normal force on the contacts, thereby reducing the friction on the contacts. Focusing first on the steady state behaviour, the proposed mechanism should thus lead to:

1. Increasing steady state porosity with increasing steady state velocity
2. Zero compaction rate at mechanical steady state
3. A decrease in granular dilatancy angle with increasing steady state sliding velocity.

The first of these is confirmed by the porosity measurements made on samples deformed at constant sliding velocity, i.e. at 0.03, 0.1, 1, 5 and 13 μm/s and 5 MPa normal stress (see Figure 5.2). The final porosity of these samples increases from near-zero at the lowest sliding velocity to ~ 13% at the maximum sliding velocity. Zero compaction rate was almost never measured, however. This could be due to the fact that we did not achieve true steady state in our experiments, or more likely because of minor but ongoing material loss from the simulated fault zone. Direct determination of the granular dilatancy angle from our compaction data is not possible because our volumetric data are a combined signal of compaction by pressure solution and dilatation by granular flow. We therefore evaluate our hypothesis further by qualitatively testing its implications versus our observations in slide-hold-slide tests.

5.4.3. Slide-hold-slide and healing behaviour– velocity-strengthening regime

Our SHS results for the velocity-strengthening regime (<1 μm/s), characterized by foliation development, show an increase in compaction rate and gradual shear stress relaxation during the hold periods plus a gradual increase in shear strength upon re-shear accompanied by significant dilatation (Figures 5.4a, 4b and Figure 5.5a). The re-shearing behaviour has been analysed by calculating the dilatation rate $\frac{d\varepsilon}{d\gamma}$ and τ_x for an SHS reference velocity of 0.1 μm/s and a hold period of 6000 s (Figure 5.12a). This shows that there is hardly any peak discernible for the shear stress (τ) or for τ_x, whereas the dilatation

rate $\frac{d\varepsilon}{d\gamma}$ shows a broad maximum. This implies that most of the strength recovery was due to dilatational work done against the normal stress. This behaviour resembles that for foliated clay-bearing synthetic fault gouges reported earlier by Bos and Spiers (2000). These authors explained the observed compaction and stress relaxation as caused by the operation of pressure solution. The absence of a peak strength upon re-shear was explained by a low proportion of healing-prone halite-halite grain contacts due to the presence of a pervasive phyllosilicate foliation. The absence or low amount of healing of these gouges was thus attributed to the absence of contact strengthening and/or increase during the hold periods. Since the behaviour seen in our SHS tests in the velocity-strengthening regime is identical, the same explanation would seem to apply.

a)

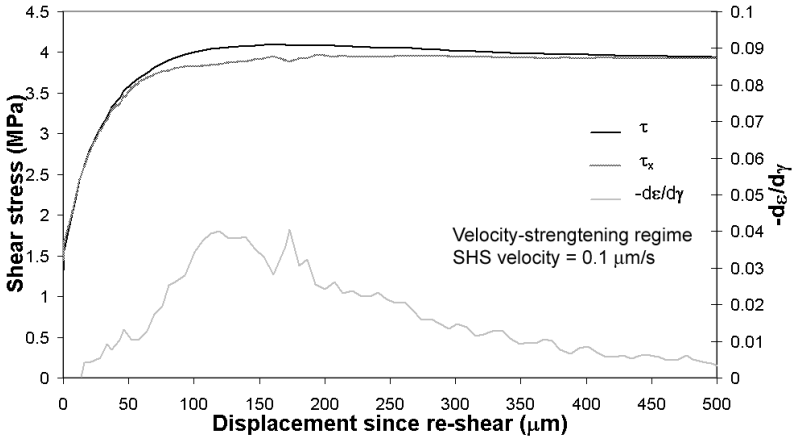

b)

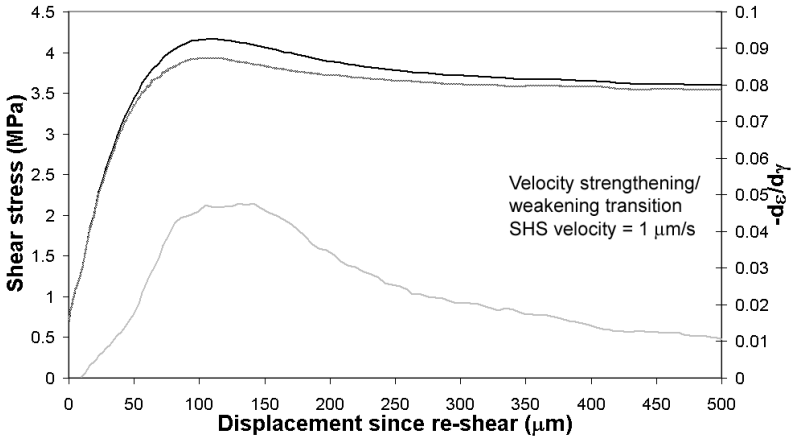

c)

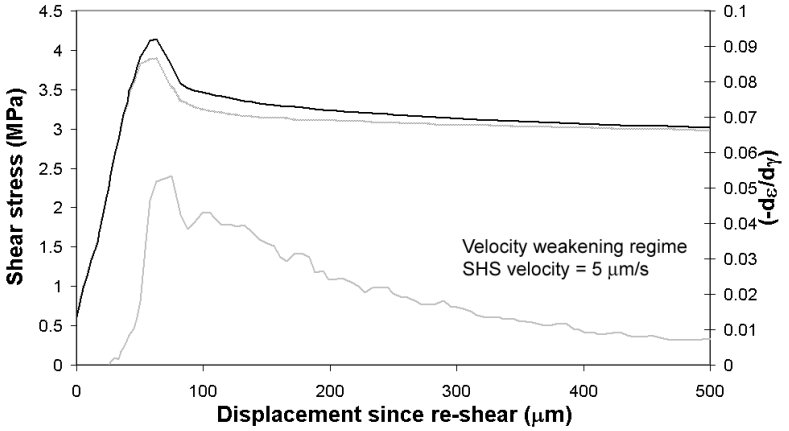

d)

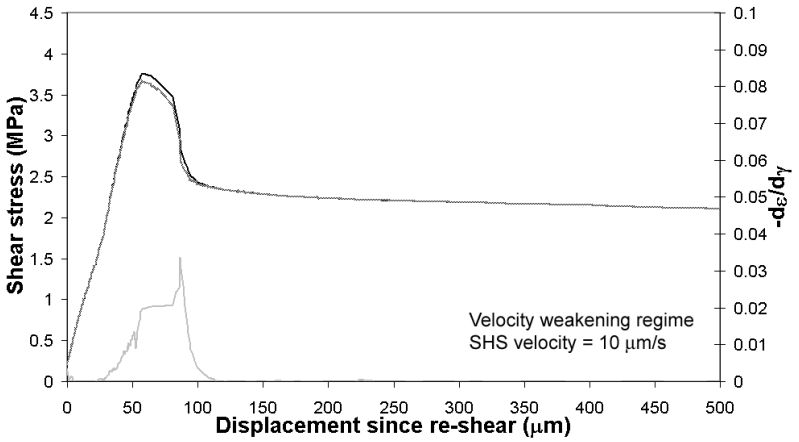

Figure 5.12: Plots showing the evolution of shear stress, τ_x and dilatation rate $-d\varepsilon/d\gamma$ vs displacement since re-shear after a hold period of 6000 seconds for samples containing 20 wt% muscovite, 80 wt% halite plus brine (shs4 and shs 5). a) SHS reference velocity of 0.1 μm/s. b) SHS reference velocity of 1 μm/s. c) SHS reference velocity of 5 μm/s. d) SHS reference velocity of 10 μm/s.

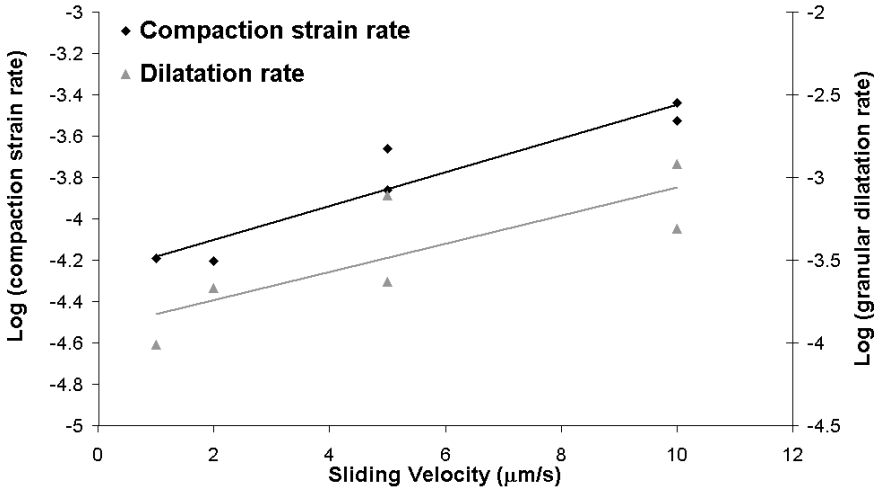

Figure 5.13: Plot of volumetric strain rate at the start of hold periods of 6000 seconds and granular dilatation rates just prior to hold periods of 6000 seconds as a function of SHS reference velocity. Data are derived from experiments shs4 and shs5.

5.4.4. Slide-hold-slide and healing behaviour – velocity-weakening regime

Our SHS results for the velocity-weakening regime (≥ 1 μm/s) samples shs1, shs4 and shs5) show increasing syn-hold compaction with increasing SHS reference velocity (Figure 5.5c), as well as rapid shear stress relaxation during hold periods (Figure 5.5a) and a strong increase in shear strength on re-shearing (Figure 5.11b-d). This results in a peak strength which gradually decays to a steady state value, the peak being accompanied by only minor dilatation. If we assume that the steady state velocity-weakening behaviour is indeed due to the mechanism of compaction *vs.* dilatation inferred in section 4.2, then in the SHS experiments, the faster syn-hold compaction observed for higher SHS reference velocities (Figure 5.5c) can be explained by a higher porosity being maintained during faster steady state sliding. This would result in a higher pressure solution compaction rate than at low sliding velocity, due to the smaller grain contact area and the higher grain contact stress (e.g. Niemeijer et al., 2002; Spiers et al., 2004 and Chapter 2)

Support for our hypothesis that gouge behaviour is controlled by competition between pressure solution compaction and dilatation due to granular flow can be obtained by a comparison of pre-hold and syn-hold compaction behaviour. Our qualitative model implies that 1) The compaction rate at the start of and during individual hold periods should increase systematically with increasing gouge porosity and SHS reference velocity and 2) the granular dilatation rate (i.e. the granular dilatancy angle) just prior to the hold period should increase with pre-hold steady state porosity and hence SHS reference velocity. The granular dilatation rate just prior to the hold can be obtained by subtracting the volumetric strain rate just after the start of the hold from the volumetric strain rate just before the start

of the hold. The results are shown in Figure 5.13 and indeed show an increasing compaction rate and dilatation rate with increasing SHS sliding velocity.

We now analyse the effects of reshearing on strength seen in the velocity-weakening regime. To do this we again use the measures of strength τ and τ_x introduced in section 5.4.1. In Figure 5.12b-d, we show representative data on the evolution of τ, τ_x and the measured dilatation rate $(-d\varepsilon/d\gamma)$ with displacement for three different sliding velocities after a hold period of 6000 seconds. The curves for τ_x correspond to the measured shear stress τ almost perfectly at all SHS velocities. This means that dilatational work ($\sigma_n \cdot \dot{\varepsilon}$) contributes negligibly to strength evolution and that strength is determined by dissipative processes or changes in stored energy within the system. Note that the peak in dilatation rate consistently postdates the peaks in τ and τ_x by ~20 μm in displacement, which again implies that dilatation contributes almost negligibly to strength evolution. Instead, virtually all strengthening is caused by an increase in τ_x.

As explained earlier, this implies that strengthening was either due to an increase in average contact strength, thereby increasing the amount of frictional dissipation through intergranular slip, or due to an increase in average grain contact area relative to pore wall area. We can not distinguish between the two on the basis of our mechanical results, although the increase of the amount of compaction during hold periods with increasing SHS velocity might indicate a larger increase in contact area with increasing SHS velocity. The observed increase in strengthening with increasing SHS velocity might be explained by an increase in contact area during hold periods.

In analysing SHS tests, it is customary to define the degree of restrengthening or healing ($\Delta\mu$) as the difference between the peak shear stress and steady state shear stress prior to each hold period, normalized with respect to the applied normal stress. Figure 5.14a shows how this depends on hold time for our complete set of SHS experiments (with the exception of SHS reference velocities of 0.01 and 0.03 μm/s, which were similar to the results for 0.1 μm/s and of test shs3). The linearised healing rate ($\Delta\mu$ per order of magnitude of healing time, i.e. the slope in Figure 5.13a) is also indicated. The healing rate is observed to increase steadily with increasing pre-hold sliding velocity, with the healing rate at 10 μm/s being almost 1.5 orders of magnitude higher than at 0.1 μm/s. In Figure 5.14b we show the dependence of $\Delta\mu_x$ (the difference between the peak and steady state values of τ_x, normalized by the normal stress) as a function of hold time. Again, an increase in healing rate is observed with increasing sliding velocity. In Figure 5.14c we show the maximum measured dilatation rate $(-d\varepsilon/d\gamma)$as a function of hold time. No clear dependence of maximum dilatation rate on hold time or sliding velocity is visible, although dilatation rate tends to be higher after longer hold times. Figure 14d shows the dependence of $\Delta\mu$, $\Delta\mu_x$ and $-(d\varepsilon/d\gamma)_{max}$ on SHS sliding velocity for a fixed hold period of 6000 seconds. This illustrates nicely that with increasing SHS sliding velocity, healing rates increase as a result of faster compaction due to higher steady state porosity being sustained at high SHS sliding velocity.

a)

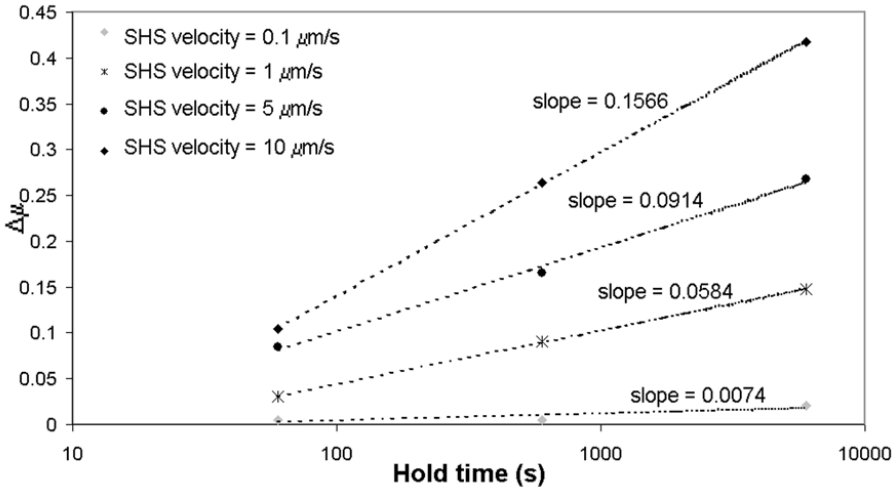
SHS velocity = 0.1 μm/s
SHS velocity = 1 μm/s
SHS velocity = 5 μm/s
SHS velocity = 10 μm/s
slope = 0.1566
slope = 0.0914
slope = 0.0584
slope = 0.0074
Δμ
0.45
0.4
0.35
0.3
0.25
0.2
0.15
0.1
0.05
0
10
100
1000
10000
Hold time (s)

b)

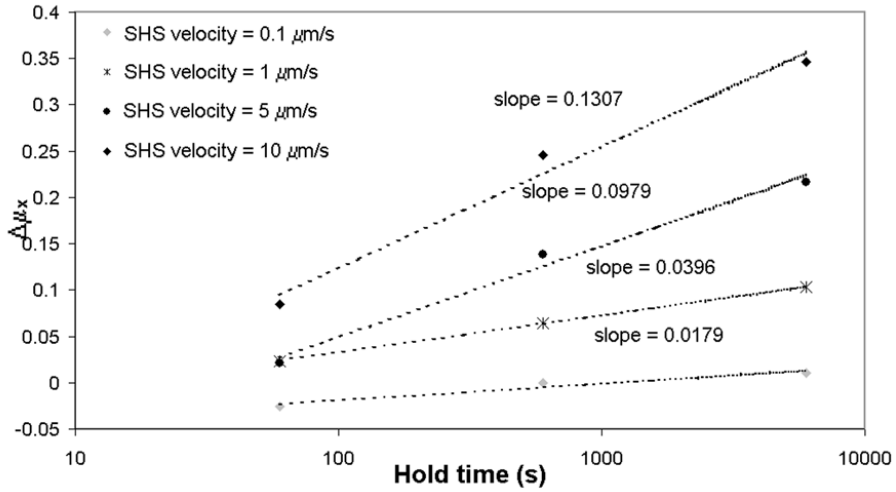
SHS velocity = 0.1 μm/s
SHS velocity = 1 μm/s
SHS velocity = 5 μm/s
SHS velocity = 10 μm/s
slope = 0.1307
slope = 0.0979
slope = 0.0396
slope = 0.0179
Δμx
0.4
0.35
0.3
0.25
0.2
0.15
0.1
0.05
0
-0.05
10
100
1000
10000
Hold time (s)

c)

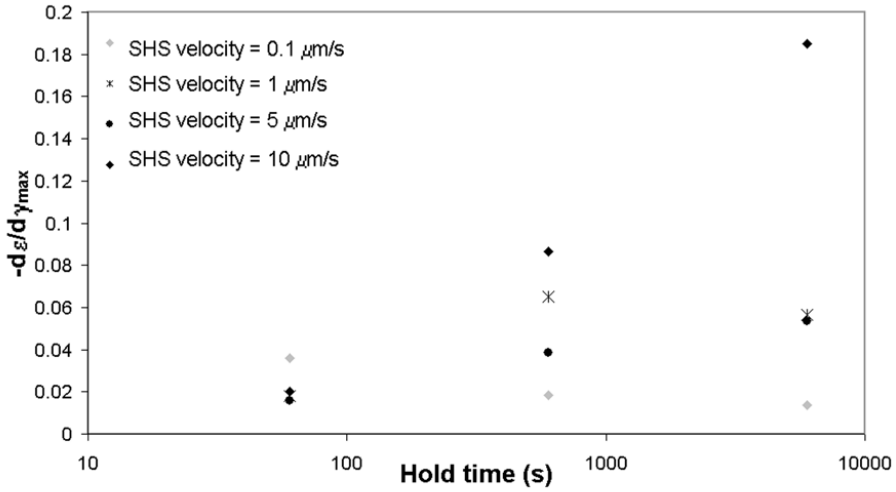

d)

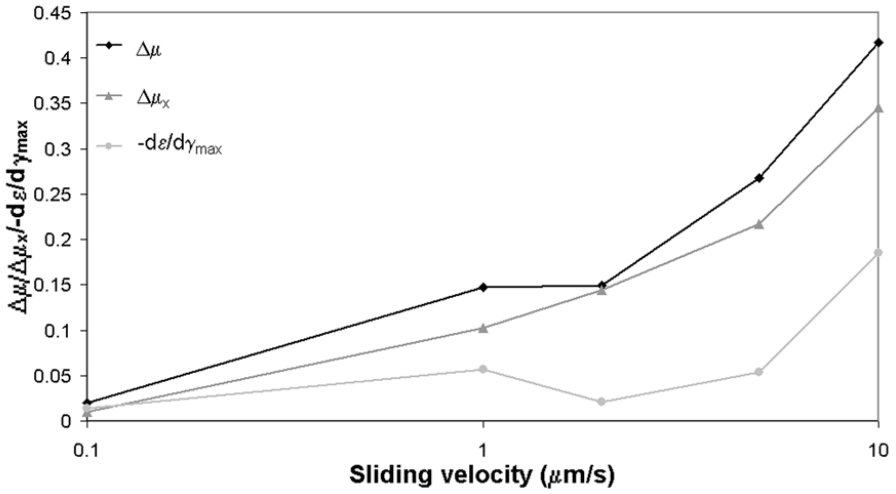

Figure 5.14: Plots showing extent of healing for different hold times and SHS reference velocities.
a) Plot of $\Delta\mu$ vs. hold time for different SHS reference velocities.
b) Plot of $\Delta\mu_x$ (see equation 5) vs. hold time for different SHS reference velocities.
c) Plot of maximum dilatation vs. hold time for different SHS reference velocities.
d) Plot of the three healing parameters as a function of SHS reference velocity for a hold period of 6000 seconds.

In summary, Figures 5.12 and 5.14 show that at low sliding velocities, post-hold strengthening is minor and mostly due to dilatation. We infer that changes in τ_x, i.e. in contact friction and/or strength, are unimportant and do not influence strengthening in the low velocity regime. This is because there are few halite-halite contacts to be disrupted, as concluded by Bos and Spiers (2000) for NaCl plus kaolinite. At high sliding velocities, however, restrengthening is almost entirely (~90%) due to an increase in τ_x (or $\Delta\mu_x$, see Figures 5.12b-d and Figure 5.14b). This is due to a decrease in porosity which causes an increase in the dilatancy angle for granular flow, hence an increased contact friction. Increased cohesive strength at halite/halite contacts may also play a role in this regime.

We will now discuss sample shs3. In this case, there was no initial wet sliding stage at low sliding velocity and stick-slip cycles occurred after a short amount of slip. The absence of initial slow sliding apparently resulted in a loose gouge where localization could easily be achieved, as evidenced by the occurrence of stick-slip similar to the deformation during part of the dry run-in stage (Niemeijer and Spiers, 2005 and Chapter 4)

5.4.5. Effects of muscovite versus kaolinite

It will be evident from the above that our results for the halite-muscovite mixtures in the velocity strengthening regime are closely similar to that reported by Bos et al. ((2000a; 2000b; 2000; 2002a) for halite plus kaolinite. There are some important differences however. The main difference between the present experiments and the previous work of Bos and coworkers lies in the effect of using of muscovite instead of kaolinite as the phyllosilicate phase. Surprisingly, the different phyllosilicate phase has led to a different mechanical behaviour in the high velocity regime. First, our muscovite-bearing mixtures have shown strongly velocity-weakening behaviour at high velocities, whereas Bos et al. ((2000a; 2000b) reported only a slight velocity-effect at sliding velocities above 1 μm/s for salt-kaolinite mixtures. Second, our samples in the velocity-weakening regime heal significantly faster than kaolinite-bearing samples, even when there is no foliation present in the kaolinite-salt mixtures (Bos and Spiers, 2002a). The explanation of these marked differences in mechanical behaviour may lie in the fact that Bos used a sub micron grain size for his kaolinite phase and we used muscovite grains with a median grain size of 13 μm. In the kaolinite-bearing samples dilatation is less effective, since the sub micron kaolinite grains are easily bent and smeared out, whereas in the muscovite-bearing samples the large muscovite flakes form true barriers for granular flow, so that dilatation is much more effective. Therefore, a larger amount of porosity is created and sustained in the muscovite-bearing samples during steady state shearing. The presence of more porosity results in higher restrengthening for these samples.

5.4.6. Implications

Many natural fault zones exhumed from brittle-ductile transitional depths contain significant amounts of phyllosilicates. Moreover, pressure solution and cataclasis are known to be important deformation mechanisms in fluid-rich rocks at such depths (e.g. Rutter and Mainprice, 1979; Passchier and Trouw, 1996; Holdsworth et al., 2001; Imber et al., 2001). The present results accordingly imply a possible influence of phyllosilicate content, foliation development, cataclasis and pressure solution on mid-crustal fault mechanics, including both steady state and transient aspects. We therefore speculate upon the following possible implications of our present work, although we are aware that a microphysical model, and/or experiments under hydrothermal conditions on real fault rock materials such as quartz plus muscovite, are needed to validate extrapolation of our results to nature.

A first and obvious implication is that the occurrence of brittle deformation textures (i.e. cataclasites) together with ductile deformation textures (i.e. mylonites) does not necessarily imply a change in deformation temperature or effective pressure conditions. Equally, our results indicate that an increase in shear strain rate, through an increase in fault displacement rate or a decrease in fault zone width, can create chaotic, cataclastic gouges by causing a transition from velocity-strengthening (stable) fault creep to a granular flow process accompanied by pressure solution compaction. Because this process is velocity-weakening, self-enhancing behaviour is initiated leading to an instability and possibly a seismic event. Similarly, oscillating fault motion rate can easily produce multiple cataclastic overprinting of mylonitic rocks.

Secondly, it is worth noting that the healing rates we measured at the highest sliding velocity are about one order of magnitude higher than healing rates of quartz-feldspar gouges determined at room temperature and/or dry (e.g. Dieterich, 1972; Beeler et al., 1994; Marone, 1998a). A direct comparison of our healing data with estimates of fault-healing rates based on earthquake stress drop observations would not be appropriate. However, since the same mechanisms operate under upper to mid-crustal conditions, healing of natural fault zones can be expected to be dominated by solution-transfer processes and the transition from velocity-strengthening to velocity-weakening would also occur when pressure solution is too slow to accommodate the imposed displacement.

Finally, the present data on the rates of restrengthening of our simulated fault gouges in the velocity-strengthening and velocity-weakening regimes imply a strong effect of the velocity history of a fault gouge on its healing rate and seismicity. A mature phyllosilicate-bearing fault rock can be expected to slip aseismically at low rates with low friction and a low healing propensity forming a mylonitic fault rock. At high strain rates, however, the same fault rock might slip seismically with high friction and a high healing propensity, forming a chaotic, cataclastic fault rock. In such a scenario, the geometry and heterogeneity of the fault zone, together with pore fluid pressure and/or composition, will initially determine which parts of the fault zone can slip aseismically and which parts might slip seismically. With ongoing displacement, stably sliding portions will tend to remain

weak and stable, while unstable portions will rapidly heal and thus remain strong and unstable.

5.5. Conclusions

In this study, we have investigated the large strain sliding and healing behaviour of simulated fault gouge using a muscovite-halite system where pressure solution, cataclasis and phyllosilicate foliation development and/or destruction are active, as anticipated for nature in the brittle-ductile transition. We investigated the steady state sliding behaviour and performed a series of slide-hold-slide tests to investigate the transient behaviour of the gouges in both the velocity-weakening and velocity-strengthening regimes reported previously. Our aim was to explain the observed velocity-weakening and healing behaviour in terms of a microphysical mechanism. We also aimed to speculate on the possible implications of our work for phyllosilicate-bearing natural fault zones under hydrothermal conditions. The following conclusions were reached:

1. Synthetic fault gouges composed of muscovite plus halite are characterized by a strong velocity-dependence of shear strength, showing velocity-strengthening behaviour at low velocities ($< 1\mu m/s$) and velocity-weakening at high velocities ($\geq 1\ \mu m/s$).
2. In the low velocity regime, halite-muscovite gouges develop a mylonitic microstructure and deform by slip on the muscovite foliation with accommodation by pressure solution of the intervening halite grains. These gouges show little or no healing in slide-hold-slide tests, probably due to the low porosity (low compaction potential) of these samples and the absence of halite-halite contacts than can heal by solution transfer processes.
3. In the high velocity regime, halite-muscovite gouges develop a chaotic, intermixed, cataclastic microstructure due to deformation by granular flow involving pervasive intergranular sliding plus competition between intergranular dilatation and pressure solution controlled compaction. A higher porosity develops towards higher sliding velocities due to an increase in the relative importance of dilatation compared to compaction. The increase in porosity at high sliding velocity causes reduced intergranular friction due to a lower inclination of sliding grain contacts (i.e. dilatancy angle for granular flow) which leads to the observed velocity-weakening.
4. Gouges deformed in the high velocity regime exhibit strong, velocity-dependent healing in slide-hold-slide tests, as a result of compaction during the hold period. This increases the inclination of sliding contacts (i.e. dilatancy angle) and increases intergranular friction. An increase in cohesive strength of halite-halite contacts through cementation might also play a role in the restrengthening.

5. The overprinting of mylonitic rocks by cataclasites does not necessarily require a history of uplift, since such overprinting relations can be formed by changing the strain rate in the fault zone. Multiple overprinting of cataclasites and mylonites more likely implies a history of highly variable fault displacement rates than a complex uplift history.
6. The large difference between healing rates in the low velocity and high velocity regimes observed in the present experiments implies that mature phyllosilicate-bearing fault zones might slip aseismically where a mylonitic foliation with a low healing and low restrengthening potential is developed. In contrast, other parts of the fault zone, where a cataclastic microstructure is developed with a high healing and high restrengthening potential, will tend to slip seismically.

Chapter 6

FRICTIONAL BEHAVIOUR OF SIMULATED QUARTZ FAULT GOUGES UNDER HYDRO-THERMAL CONDITIONS: RESULTS FROM ULTRA-HIGH STRAIN ROTARY SHEAR EXPERIMENTS

Abstract

Numerous experimental studies have been conducted to explore the frictional behaviour and healing properties of simulated gouge-filled faults and bare rock surfacess. Most of these studies, however, do not take the effects of fluids into account, though it has long been recognized that fluids might play an important role. Moreover, most studies have been severely limited in the total shear strain that could be reached. In this study, we report ultra-high strain experiments performed on simulated quartz fault gouges under hydrothermal conditions using a rotary shear apparatus. Our experiments were conducted at normal stresses of 20-100 MPa, a fluid pressure of 200 MPa, temperatures of 400-600 ºC, sliding velocities of 0.01-1 μm/s, reaching total total shear strains up to 50. The experiments show strain hardening up to a shear strain γ of 0.6-1.8, followed by strain weakening of up to 30% towards a steady state value attained at a γ of ~8-12. While the low strain behaviour seen in our tests is similar to previous results, the total strain weakening is much larger as a result of the larger strains achieved. The steady state shear strength tends to increase with decreasing grain size, increasing sliding velocity, and decreasing temperature. The microstructure of the deformed quartz gouge is characterised by the presence of a through-going boundary-parallel Y-shear. Some samples also show Riedel shears oriented oblique to the shear zone boundary. Deformation in these tests was largely by cataclastic processes, with most displacement being accommodated along the boundary-parallel Y-shear, causing the strong weakening observed. Intergranular pressure solution did not contribute significantly to shear strain accommodation, but appears to play a role in smoothening and weakening the localised slip surface and in controlling gouge compaction.

6.1. Introduction

In order to model geodynamic processes such as mountain building, rifting and continental break-up, detailed knowledge of the rheology of the Earth's crust and upper mantle is necessary. Numerous experiments have therefore been conducted to decipher the mechanical behaviour and strength properties of rock materials as a function of strain rate, temperature, confining pressure, fluid pressure, fluid composition and strain (Carter and Kirby, 1978; Rutter and Mainprice, 1978; Goetze and Evans, 1979; Kirby, 1980; Shimamoto and Logan, 1981; Chester and Logan, 1990; Shea and Kronenberg, 1993; Kohlstedt et al., 1995). Brittle failure tests and simulated fault sliding experiments have shown that rocks are generally expected to slide frictionally on pre-existing faults, under upper crustal conditions, at steady state shear stress levels of ~0.6-0.9 times the normal stress, with low sensitivity to changes in sliding rate, temperature and mineralogy (for a review, see Byerlee, 1978; Scholz, 2002). With increasing depth and thus overburden pressure, shear stress levels in the crust are accordingly predicted to increase. At depths in

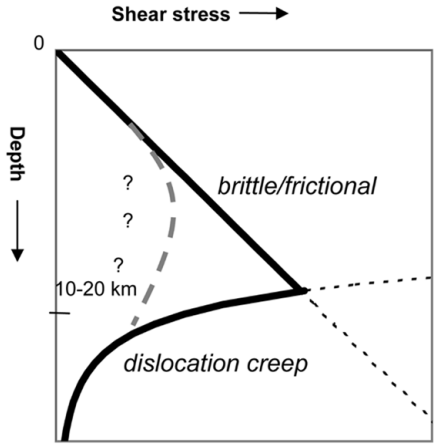

Figure 6.1: Schematic of classical crustal strength profile, showing brittle-frictional behaviour dominating at upper crustal levels and dislocation creep determining crustal strength at deeper levels (solid lines). The thick dashed line represents the widely expected effects of fluid-assisted deformation mechanisms on crustal strength (Figure after Bos et al. 2000b).

excess of 10-15 km, however, high pressure and temperature deformation experiments have shown that thermally-activated, ductile deformation processes, such as dislocation creep, become easier than and hence dominate over brittle/frictional sliding (Goetze and Evans, 1979; Hirth and Tullis, 1992; Luan and Paterson, 1992; Gleason and Tullis, 1995; Kohlstedt et al., 1995; Küster and Stöckhert, 1999; McKenzie and Jackson, 2002). The underlying experimental data have led to the construction of crustal strength profiles, such as that illustrated in Figure 6.1 (e.g. Sibson, 1977, 1983; Schmid and Handy, 1991).

It has long been recognized that strength profiles are probably an oversimplification of the rheology of major fault zones, especially at brittle-ductile transition depths of 10-15 km near the base of the seismogenic zone (e.g. Rutter and Mainprice, 1979; Sibson, 1983; Rutter and Brodie, 1991). The experiments which form the basis for the brittle part of such profiles have been mostly conducted using single phase rock materials or under conditions where chemical, fluid-rock interaction is absent or unimportant (e.g. Byerlee, 1967; Tullis and Yund, 1977). Moreover, most sliding experiments performed to date have been limited to low shear strains ($\gamma < 5$), which are insufficient to produce a mature or steady state microstructure showing a realistic internal structure or foliation (e.g. Logan and Rauenzahn, 1987; Chester, 1994a). Significantly, field and microstructural observations of the widespread occurrence of quartz veins, slickenfibres, pressure solution seams, hydration reactions and phyllosilicate foliation development in exhumed mid-crustal fault zones (Cox, 1994a; Wintsch et al., 1994; Hickman et al., 1995; Wintsch et al., 1995; Imber et al., 1997; Holdsworth et al., 2001; Imber et al., 2001; Wintsch and Yi, 2002; Holdsworth, 2004) indicate a major role of fluid-rock reactions and solution transfer processes at these depths.

It has accordingly been suggested that solution-transfer processes may have a key influence on the strength and sliding behaviour of fault rocks, promoting easy creep at low sliding rates in the mid/upper crust (e.g. Rutter and Mainprice, 1979; Lehner and Bataille, 1984/85; Bos et al., 2000a, b; Bos and Spiers, 2001). At the same time, pressure solution compaction has been suggested to play an important role in the "healing" or restrengthening of crustal fault rocks between earthquakes (e.g. Byerlee, 1994; Bos and Spiers, 2000, 2002a; Niemeijer et al., 2002; Nakatani and Scholz, 2004). Therefore, to describe the rheology of fault rocks in the brittle-ductile transition, and to model the seismic cycle, an understanding

of the effects of solution-transfer processes in active fault zones under hydrothermal conditions is necessary.

Previous laboratory studies of fault rock strength under hydrothermal conditions have focused on pre-faulted sandstones and on simulated fault gouges of granitic composition, or of pure quartz, at temperatures up to 900 ºC (Blanpied et al., 1991; Chester and Higgs, 1992; Rutter and Maddock, 1992; Chester, 1994a; Blanpied et al., 1995; Blanpied et al., 1998a; Blanpied et al., 1998b; Kanagawa et al., 2000; Nakatani and Scholz, 2004). These have shown that gouge strengths, expressed in terms of a coefficient of friction μ, decrease with increasing temperature and/or decreasing sliding velocity. Dry control experiments have shown similar frictional strengths, but without the strong healing effects observed in slide-hold-slide tests on wet samples (e.g. Nakatani and Scholz, 2004). However, the predominant microstructures in the generally low strain experiments done on wet samples ($\gamma < 5$) have shown evidence mainly for cataclastic deformation, with few indications for the operation of solution-transfer processes, through microstructures such as grain indentation, growth of new grains or overgrowths. Therefore, the effect of solution-transfer processes on gouge strength remains unclear, especially at high shear strains, which have yet to be explored.

In this chapter, we report experiments on simulated fault gouges of pure quartz performed in a newly constructed, hydrothermal rotary shear apparatus, capable of reaching ultra high shear strains (γ over 50) under high pressure and temperature conditions (effective normal stresses up to 100 MPa, fluid pressures up to 200 MPa and temperatures up to 600 ºC). A previous experimental study by Niemeijer et al. (2002, see also chapter 2) on the compaction behaviour of granular quartz demonstrated that pressure solution operates at measurable rates at temperatures in the range 400-600 ºC, a confining pressure of 300 MPa and fluid pressures of 150-250 MPa. Here, we aim to investigate the effects on fault friction of temperature, starting grain size, normal stress and fault sliding velocity under similar conditions, and thereby to establish the effects of solution transfer processes on the sliding behaviour of pure quartz gouges at shear strains up to 50.

6.2. Experimental Apparatus

The present series of experiments was performed in a hydrothermal, rotary shear apparatus located inside an Instron 1362 loading frame, used to apply normal load to the simulated fault (Figures 6.2 and 6.3). In Figure 6.2a, we show a schematic diagram of the hydrothermal rotary shear cell. The apparatus was designed and built at the HPT laboratory in Utrecht and was commissioned for use in February 2005. With reference to Figure 6.2a, the rotary cell consists of a compound pressure vessel (A) housing a pair of opposing internal pistons (H + I), which sandwich a thin layer of simulated fault gouge (J). The pressure vessel is sealed by means of upper and lower sealing heads (G +L), held in place by threaded closure nuts (D+M). Water is used to pressurize the vessel and, having direct

access to the sample, provides the pore fluid pressure. The required effective normal stress is applied to the gouge by axially loading the piston assembly, from the top, via a pressure-compensated piston (E), sealed in the upper sealing head by three dynamic O-rings. The sample is sheared by rotating the vessel plus internally fixed lower piston, while holding the pressure-compensated piston (E) plus coupled upper piston (H) stationary (zero rotation with respect to the Instron frame). Grip on the pressure-compensated piston is provided by an external upper forcing block, which is equipped with both a torque cell and an axial load cell assembly fixed to the upper Instron cross-head (Figure 6.3a). Rotation of the vessel and lower internal piston is driven, through a lower forcing block, by a servo-controlled motor and gearbox system located on the Instron ram (Figure 6.3a). The sample and surrounding pore fluid medium are heated internally by means of a sheathed "thermocoax" heating element (C in Figure 6.2a, see also Figure 6.3b). Temperatures up to 700 ºC, pore fluid pressures up to 300 MPa, normal stresses up to 300 MPa, displacement rates of 0.0003 to 3 μm/s and a maximum displacement of ~100 mm (approximately 1.5 revolutions) can be achieved.

In detail, the sample is contained between raised toothed rings (~height ~0.2 mm) machined on the faces of the two opposing internal pistons (see Figures 6.2b and 6.3c; inner radius is 11 mm and outer radius is 14 mm). The sample material is kept in place by an inner and an outer confining ring of stainless steel fitted closely over the toothed section of the pistons. The piston material is the nickel superalloy, René-41, which has a higher thermal expansion coefficient (13.5×10^{-6} K^{-1} at 500 º) than stainless steel (12×10^{-6} K^{-1} at 500 ºC), so that at operating temperature (400-600 ºC) we expect an even closer fit. In preparing a sample for testing, gouge material is deposited between the confining rings on the toothed section of the lower internal piston (Figures 6.2b and 6.3c). The upper internal piston is then located over the rings and twisted half a revolution to distribute the material evenly over the gouge zone. The two internal pistons are attached to each other by a load-released clamping mechanism (Figure 6.2b), so that the piston assembly can be lifted and placed in the vessel. An insulating mullite tube, sealed in a welded stainless steel can, is located over the top piston to prevent convection in the pore fluid. The piston-sample assembly is attached to the pressure-compensated piston by means of a keyway and locked by a screw. Note that the upper sealing head is sealed against the pressure vessel by means of a single, static, O-ring seal ,and is water cooled by means of internal channels machined in the vicinity of the inner seals. One port in the upper sealing head provides access for the pore fluid system, two are cooling water conduits and a final port provides access for a thermocouple, whose active tip is located ~5 mm below the simulated fault gouge. The coiled furnace element which surrounds the sample region is insulated from the vessel wall by a tube of mullite sheathed in a sealed, stainless steel (316) can (Figure 6.3b). Mirroring the sealing arrangement at the top of the vessel (Figure 6.3b), one O-ring seals the lower sealing head into the vessel. Two ports in the lower head provide access for one thermocouple, measuring the temperature at the seal, plus a control thermocouple located in the furnace coil. A third port provides access

for the power line to the furnace. The outside wall of the vessel is sheathed in a water-cooling jacket. In assembling the apparatus in preparation for an individual experiment, the complete upper head and piston-sample assembly is lowered into a rotation-proof slot at the bottom of the water-primed pressure vessel. The entire vessel with the piston assembly is then closed, using the upper closure nut, and loaded using a fork lift onto a basal support, or lower forcing block, positioned in the Instron loading frame (Figure 6.3a). The protruding top of the piston assembly is then located firmly and rigidly into the upper forcing block, which is connected to the torque and axial force gauges. The lower forcing block is coupled to the underlying servo-controlled, rotational drive system, which is in turn rigidly coupled to the vertical loading ram of the Instron (Figure 6.3a). The rotational drive is used to apply the rotational sliding velocities of 0.0003-3 μm/s to the gouge.

As already indicated, the entire vessel rotates in the Instron loading frame, with the pressure-compensated piston and hence top inner piston being held stationary. Shear displacement is measured using a potentiometer with a resolution of 0.001 mm, geared to the lower (rotating) forcing block. Shear stress is measured externally, with a resolution of 0.2 MPa, using the torque gauge couple mounted on the upper forcing block. Normal stress is applied using the Instron loading ram. It is measured externally using a 100 kN Instron load cell and can be held constant to within ~0.2 MPa. Corrections for seal friction were applied as described in section 6.3.4. Internal shear and normal force gauges are under construction but were not available for the present work. Fluid pressure is applied to the water in the pressure vessel using a manually driven pump and is measured using a pressure transducer with a resolution of 0.001 MPa. The temperatures of the lower seal, the furnace element and the sample are continuously measured to within 1 ° C. Displacement and hence compaction/dilatation normal to the simulated fault gouge is measured externally using the position transducer (LVDT) of the Instron loading ram (resolution of 0.01 mm), correcting for the machine stiffness.

a)

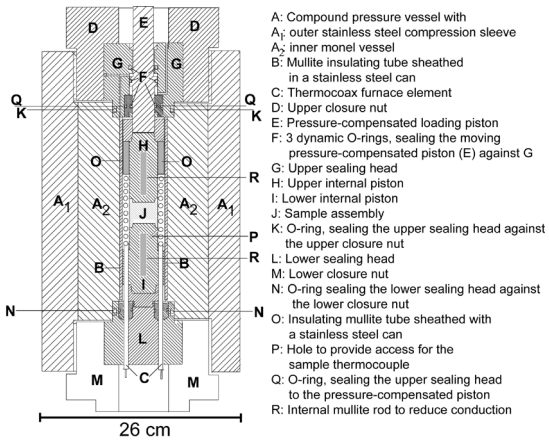

b)

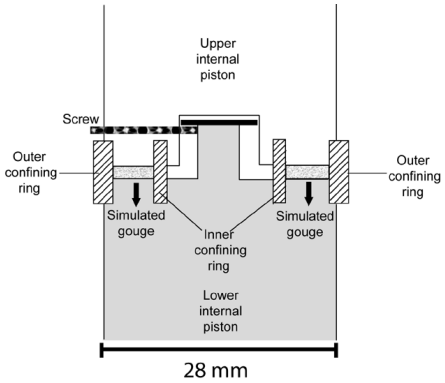

Figure 6.2: a) Schematic cross-sections of hydrothermal rotary shear celll with all internal components and O-ring seals (approximate scale only).
b) Internal pistons with load-released clamping mechanism (approximate scale only).

a)

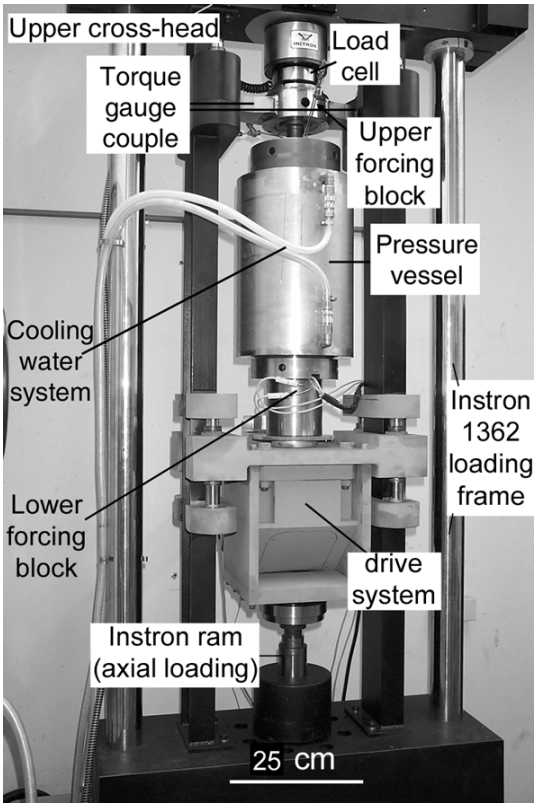

b)

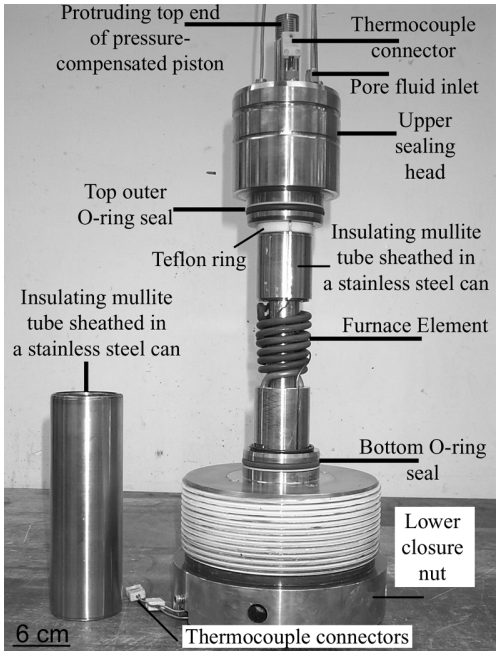

c)

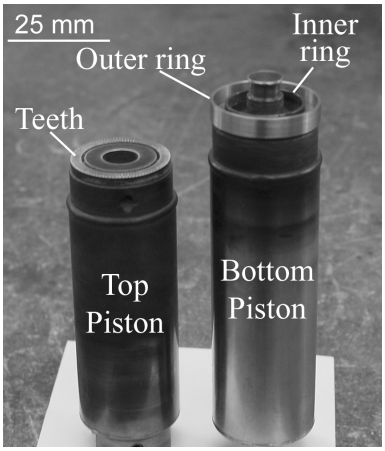

Figure 6.3: Photographs of
a) pressure vessel located inside the Instron loading frame (approximate scale only).
b) the two internal pistons assembled with the pressure-compensated piston plus upper sealing head. Note also the two insulating mullite tubes sheathed with stainless steel and the furnace element (normally located inside the pressure vessel (approximate scale only).
c) the two internal pistons plus sample-confining rings (approximate scale only).

6.3. Experimental Method

6.3.1 Sample preparation and installation

Sample material consisted of pure natural quartz powder supplied by the U.S. Silica Company. Four different initial grain sizes (median diameters, d_i) were used. These were 5 μm (Min-u-Sil 15), 8.0 μm (Min-u-Sil 30), 12 μm (Sil-co-Sil 49) and 22 μm (Sil-co-Sil125). In setting up individual experiments, about ~ 0.5 grams of material is loaded onto the bottom internal piston, with the two stainless steel confining rings in place (Figure 6.3c; note that the same inner confining ring is used for each test, but the outer confining ring is renewed each time). The top piston is located into the confining rings from above and the two pistons plus intervening sample are clamped together, as described earlier (Figure 6.2b). The piston-sample assembly is then rotated manually to distribute the gouge evenly and attached to the pressure-compensated piston plus upper sealing head. The initial gouge thickness is ~800 μm.

As already indicated, after pre-filling the vessel with distilled water to ~ 20 vol%, the entire sealing head and piston assembly (see Figure 6.3b) is loaded into the vessel. The assembly is then pushed tightly into the vessel and the large upper closure nut is screwed on, thereby removing any residual air from the vessel through the pore fluid pressure port on top of the upper sealing head. The entire vessel is subsequently placed into the Instron loading frame, and the pore fluid and cooling systems are attached to the ports on the top of the vessel, i.e. on the upper sealing head (see Figure 6.3a). The loading ram of the Instron is now advanced upwards until the pressure-compensated piston locks into the upper forcing block. The water cooling system is then turned on, typically at a flow rate of 5 l/min.

6.3.2 Testing procedure

In the present experiments, after loading the vessel into the Instron frame, a fluid pressure of ~ 10 MPa was applied by pumping distilled water into the pore fluid system (vessel). The furnace was then switched on and an effective normal load of usually 20 or 100 MPa applied. During the heating procedure, the fluid pressure increased, reaching ~200 MPa at 500 ºC. Any overpressure which occurred during heating was corrected by withdrawing water from the system. The desired test temperature was usually reached within 15 minutes. The system was then left to equilibrate for ~ 30 minutes before the rotary drive was switched on at 1 μm/s for a displacement of 5-10 mm. After this first shear displacement at constant sliding velocity, constant normal stress, constant temperature and constant fluid pressure, we performed a variety of normal stress stepping sequences as well as a number of velocity-stepping and temperature-stepping sequences. Effective normal stress was stepped using stress intervals of 20 MPa. Displacement intervals of at least 1 mm were used in all stepping sequences, which was always sufficient to reach steady state shear stress levels. We explored temperatures of 400-600 ºC, effective normal stresses of 20-100 MPa, a fluid pressure of 200 MPa and sliding velocities of 0.01-1 μm/s.

6.3.3 Test termination

Tests were terminated by switching off the rotary drive and then the furnace, which resulted in a rapid decrease in fluid pressure. After approximately 45 minutes, the entire system reached room temperature, at which point the axial load was removed and the cooling water circulation stopped. In all experiments with this machine, the pore fluid and cooling systems are finally disconnected and the entire vessel is taken out of the Instron loading frame. The upper closure nut plus the piston assembly are then removed from the vessel, and the inner piston pair is removed from the pressure-compensated piston plus sealing head. The clamped inner pistons are then carefully separated from each other, exposing the sample. In the present tests, the pistons and sample material were then left to dry in an oven at 60 ºC for ~ 60 minutes. The simulated fault gouge sample usually adhered

to one of the two pistons, mostly the lower piston to which the rings were attached. In some cases, it proved impossible to remove the sample intact, but in most cases substantial pieces of fault gouge were successfully recovered. These typical measured 400-600 μm in thickness. These were impregnated with epoxy resin and standard thin sections cut, normal to the shear direction, for analysis using optical and electron microscopy.

6.3.4. Accounting for seal and ring friction

In order to measure the shear stress sustained by the gouge samples, it is necessary correct the externally measured shear stress for the frictional force exerted by the dynamic seals on the pressure-compensated piston, as well as for any frictional force exerted by the confining rings surrounding the sample. Since the shape and size of the (outer) confining rings is slightly variable, the friction due to the rings will vary from experiment to experiment, as will the seal friction, to some extent. However, the frictional forces offered by the seals and confining rings are not likely to depend strongly on applied normal stress. In the absence of internal force measurement (under construction), we have therefore assumed that the slope of the uncorrected shear stress vs. normal stress data (i.e. the coefficient of friction) obtained from stress-stepping tests directly reflects the friction coefficient of the sample.

We tested this assumption by shearing two opposing ring-shaped samples of molybdenum-disulphide bearing PEEK (Polyether etherketone or Vitrex) in our apparatus at room temperature and at a fluid pressure of 200 MPa. The friction coefficient of this material is reported by the manufacturer to be 0.1. We prepared two thin rings of this plastic-like material and fitted them tightly into the pistons, in the position normally occupied by the gouge samples. Our data for the material show an excellent linear relation between shear and normal stress and a coefficient of friction of 0.091, which closely agrees with the manufacturer's value. A similar procedure employed using crushed talc as sample material yielded a coefficient of friction of 0.23 at room temperature compared with a value of 0.18-0.20 reported in the literature (Moore and Lockner, 2004). We therefore conclude that linear fits to the uncorrected shear stress and normal stress data obtained in our experiments on quartz gouge yield true friction coefficients for the sample material. In the present study, we have accordingly focused on obtaining friction coefficient data for our samples using this method. In order to be able to compare frictional shear stress values from experiment to experiment as well as possible, we corrected our shear stress data for seal and confining ring friction using the apparent cohesion measured in the normal stress stepping sequences, thereby ignoring any (minor) cohesion exerted by the samples. Note that the "corrected shear stress" data thus obtained can be regarded as a measure of friction coefficient if normalized with respect to effective normal stress. Hence, curves of corrected shear stress versus displacement are equivalent to the μ versus displacement curves

frequently presented in fault rock friction studies for experiments at constant effective normal stress. Uncorrected shear stress values are reported for the two velocity and temperature-stepping experiments that were performed, since normal stress was not stepped in these tests.

Aside from the effect on measured shear stress, friction of the O-ring seals also influences the normal stress experienced by the sample. From hysteresis seen in the normal displacement signal at constant normal, and taking an observed rate dependence of seal friction into account, we estimate that the relative error in normal stress, due to variations in normal load, fluid pressure and frictional resistance of the O-ring seals during slow vertical movement of the piston, is less then 5%.

6.4. Results

Table 6.1 lists all our experiments and the corresponding experimental conditions along with data on the total shear displacements achieved. Recall that all experiments on the quartz gouge were performed at 400-600 ºC, normal stresses in the range 20-100 MPa and a fluid pressures of 200 MPa, using sliding velocities of 0.01-1 μm/s. Recall also that the samples were first sheared through an initial displacement of typically 10 mm at constant effective normal stress (20 or 100 MPa), before the various normal stress stepping, velocity stepping and temperature stepping a sequences were carried out. Note that as the gouges were initially ~ 0.8 mm thick, the initial 10 mm displacement represents a minimum shear strain γ of 12.5. All shear strains reported here are minimum values based on the initial gouge thickness.

Table 6.1: List of the 12 normal stress-stepping experiments and 2 temperature/velocity-stepping experiments reported here plus the corresponding experimental conditions. Note that all samples were initially sheared at constant effective normal stress for at least 5 mm of shear displacement. Sliding velocity is 1 μm/s in all experiments. Grain size reported is the initial median grain size as given by the manufacturer (U.S. Silica Company).

Sample	Initial median grain size (μm)	Temperature (°C)	P_{fluid} (MPa)	Effective normal stress (MPa)	Sliding velocity (μm/s)	Total displacement (mm)
AN-20	PEEK	25	200	4, 8, 12, 16, 20, 25, 30, 34, 38, 42, 50, 60, 68, 76, 84 ,94, 100	1	10.49
AN-01	12	500	200	100, 80, 40, 60, 20, 40, 60 , 80, 100	1	16.72
AN-03	12	500	200	100, 80, 40, 60, 20, 40, 60 , 80, 100	1	19.64
AN-04	12	500	200	100	1, 0.1, 0.01, 0.3, 1, 0.03, 1	18.08
AN-08	5	500-450-400-500	200	100	1, 0.03	14.82
AN-09	5	500	200	100, 80, 40, 60, 20, 40, 60 , 80, 100 (2x)	1	36.86
AN-12	5	600	200	20, 40, 60, 80, 100, 80, 60, 40, 20 (2x)	1	45.53
AN-22	5	400	200	20, 40, 60, 80, 100, 80, 60, 40, 20	1	17.39
AN-23	22	500	200	20, 40, 60, 80, 100, 80, 60, 40, 20	1	19.04
AN-24	12	500	200	20, 40, 60, 80, 100, 80, 60, 40, 20	1	18.43
AN-25	5	500	200	20, 40, 60, 80, 100, 80, 60, 40, 20	1	17.78
AN-26	22	500	200	100, 80, 40, 60, 20, 40, 60 , 80, 100	1	18.48
AN-28	8	500	200	20, 40, 60, 80, 100, 80, 60, 40, 20	1	17.84
AN-29	5	500	200	20, 40, 60, 80, 100, 80, 60, 40, 20	1	18.96

6.4.1. Initial shearing at fixed effective normal stress

6.4.1.1. Effect of temperature

In Figures 6.4a and 6.4b, we show the corrected shear stress and compaction versus displacement curves for samples AN-22 AN-25 and AN-12, deformed at 20 MPa effective normal stress and at temperatures of 400, 500 and 600 ºC, respectively. Note that as the samples were ~ 0.8 mm thick, the initial 10 mm displacement represents a shear strain γ of 12.5. All samples show a rapid increase in load supported up to a shear displacement of ~0.8 mm (γ=1). After this point, sample AN-22, deformed at 400 ºC, shows a broad "yield point" reaching a more or less steady state strength by 1.5 mm displacement (γ=1.8). The higher temperature samples show a sharper peak strength with significant subsequent weakening, approaching steady state at 5-8 mm displacement (γ=6-10). From Figure 6.4b, we observe that the measured compaction decreases with increasing temperature. Sample AN-22 (400 ºC) compacts throughout the entire 10 mm of displacement imposed. By contrast, samples AN-25 (500 ºC) and AN-12 (600 ºC) initially dilate (negative compaction) somewhat, after which sample AN-25 "compacts" slightly and sample AN-12 remains more or less constant in thickness.

6.4.1.2 Effect of grain size

Figure 6.5a shows the corrected shear stress versus displacement curves for samples AN-23 (d_i = 22 μm), AN-24 (d_i = 12 μm), AN-25 (d_i = 5 μm) and AN-28 (d_i = 8 μm), which were all deformed at a temperature of 500 ºC, a sliding velocity of 1 μm/s, an effective normal stress of 20 MPa and a fluid pressure of 200 MPa. All samples show an initial peak strength (AN-at a displacement of around 0.5-1 mm (γ=0.6-1.2). Sample AN-28 (d_i = 8 μm) shows the highest peak strength, followed by samples AN-25 (d_i = 5 μm), AN-23 (d_i = 22 μm) and AN-24 (d_i = 12 μm). Beyond this point, all samples show weakening, approaching steady state only after 6-8 mm of displacement |(γ=7.5-10). Final steady state strength reached after ~10 mm of displacement (γ=12.5) systematically increases with increasing initial grain size, although the differences are small (~ 1 MPa).

In Figure 6.5b we show corrected shear stress versus displacement curves for samples AN-01 (d_i = 12 μm), AN-03 (d_i = 12 μm), AN-09 (d_i = 5 μm) and AN-26 (d_i = 22 μm). These samples were deformed at a temperature of 500 ºC, a sliding velocity of 1 μm/s, a fluid pressure of 200 MPa and a normal stress of 100 MPa (see Table 6.1). All samples show much higher strength than those tested at 20 MPa effective normal stress. All, except AN-09, show a broad yield point at a displacement of ~1 to 1.5 mm (γ=1.2-1.8) followed by continuous weakening up to a displacement of 10 mm. The sample with the finest grain size

(AN-09) shows no peak strength and continues to strengthen up to a displacement of 6.5 mm. No systematic dependence of final strength on initial grain size is observed.
In Figures 6.6a and 6.6b, we show the compaction versus displacement curves for the same samples represented in Figures 6.5a and 6.5b. All samples deformed at 20 MPa effective normal stress (AN-23, AN-24, AN-25 and AN-28, Figure 6.6a) show initially small amounts of dilatation, up to a displacement of around 0.5 mm, followed by 0.02-0.07 mm of compaction continuing up to a displacement of 5-7 mm. No systematic dependence of compaction on starting grain size is visible at 20 MPa effective normal stress. In Figure 6.6b, we observe that the sample with the finest grain size (AN-09, d_i = 5 μm), deformed at 100 MPa effective stress, shows considerable dilatation in the first mm of the experiment. The other samples show either dilatation (AN-01) or compaction (AN-03 and AN-26) in the first mm of the experiment. Beyond 1 mm of displacement, all samples tested at 100 MPa effective normal stress show compaction. The amount of compaction at a given displacement tends to increase with increasing grain size.

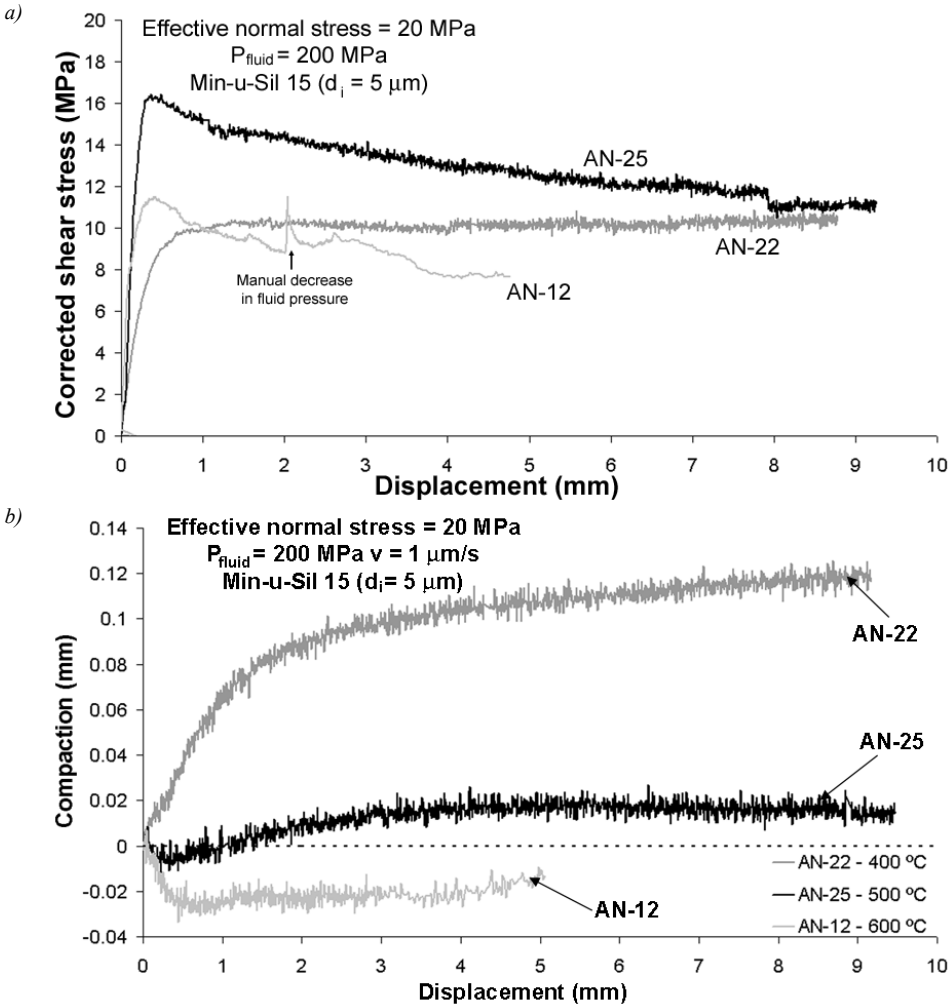

Figure 6.4:

a) Corrected shear stress versus displacement plot for samples AN-22, AN-25 and AN-12,which consisted of min-u-sil 15 (initial median grain size of 5 μm) and were deformed at 400, 500 and 600 ºC, respectively. Effective normal stress was 20 MPa and fluid pressure 200 MPa.

b) Compaction versus displacement plot for the same experiments.

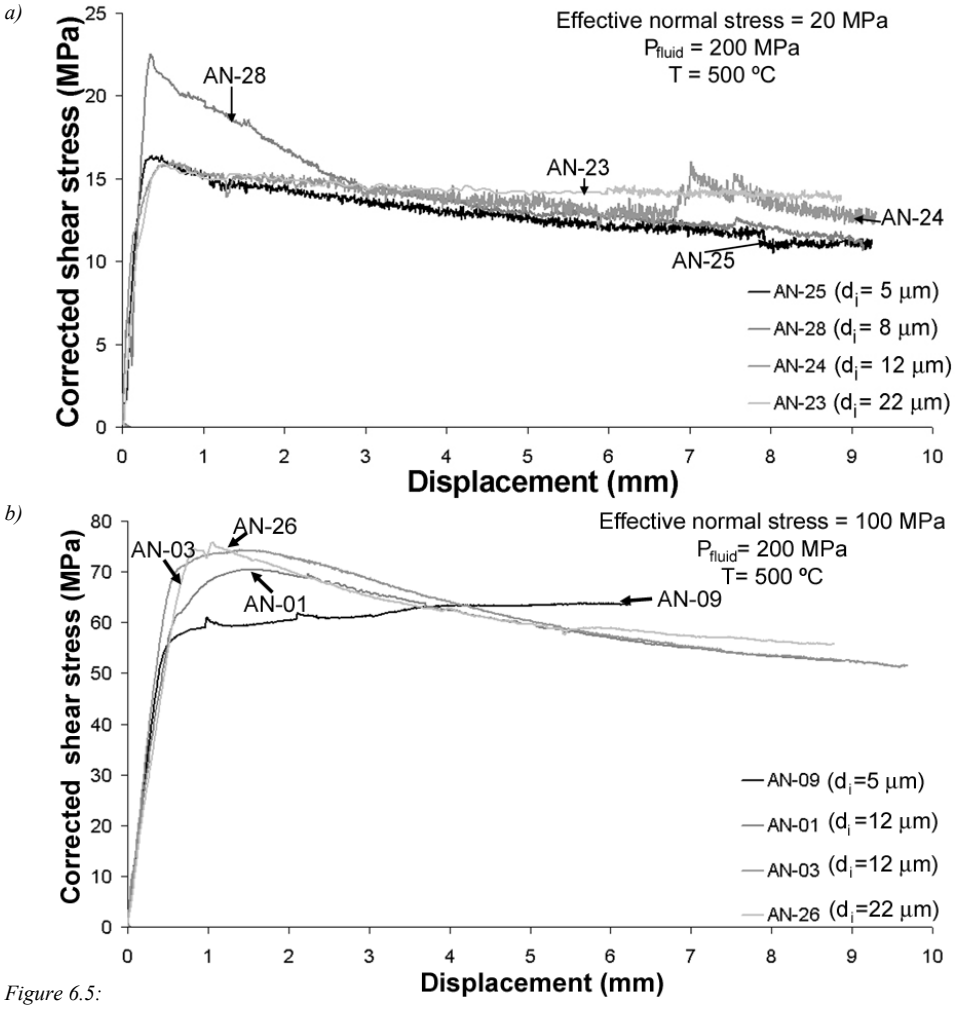

Figure 6.5:

a) Corrected shear stress versus displacement plot for samples AN-23, AN-24, AN-25 and AN-28, which were all deformed at a temperature of 500 ºC, a sliding velocity of 1 µm/s, an effective normal stress of 20 MPa and a fluid pressure of 200 MPa.

b) Corrected shear stress versus shear displacement plot for samples AN-01, AN-03, AN-09 and AN-26, which were deformed at a temperature of 500 ºC, a sliding velocity of 1 µm/s, a fluid pressure of 200 MPa and an effective normal stress of 100 MPa

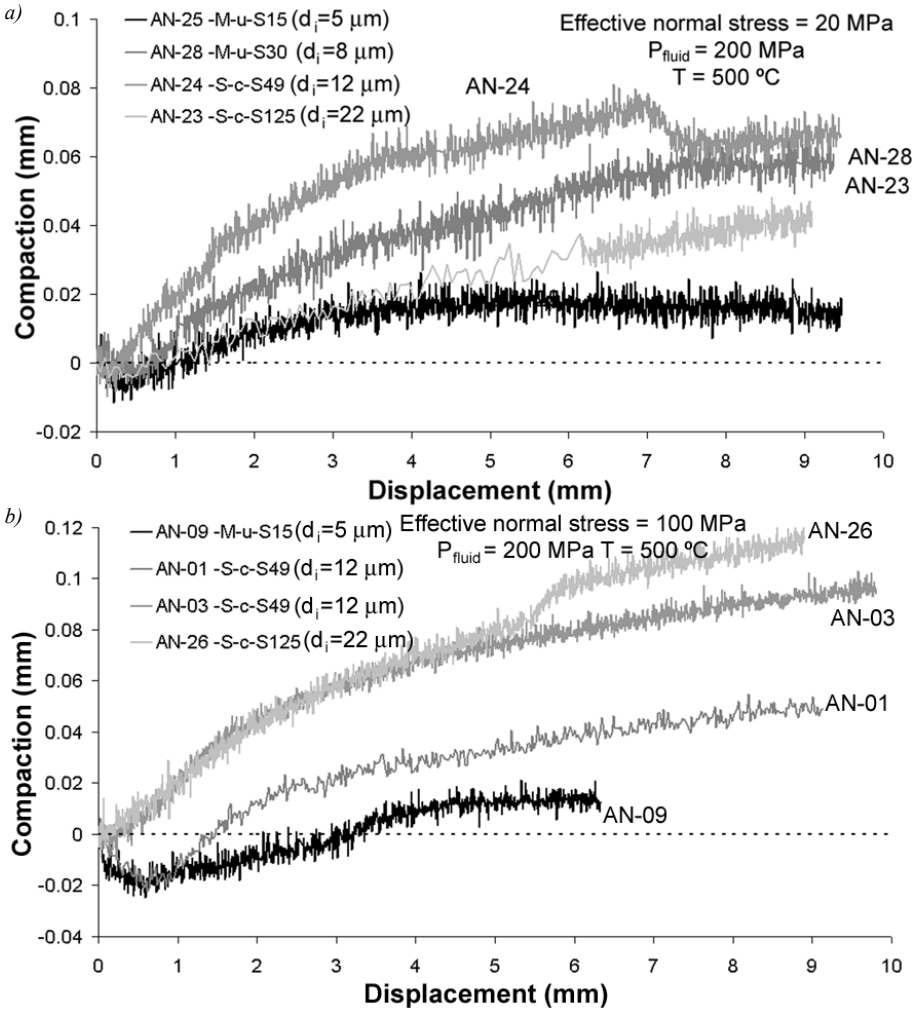

Figure 6.6:

a) Compaction versus displacement plot for samples AN-23, AN-24, AN-25 and AN-28, which were all deformed at a temperature of 500 ºC, a sliding velocity of 1 μm/s, an uncorrected effective normal stress of 20 MPa and a fluid pressure of 200 MPa.

b) Compaction versus displacement plot for samples AN-01, AN-03, AN-09 and AN-26, which were deformed at a temperature of 500 ºC, a sliding velocity of 1 μm/s, a fluid pressure of 200 MPa and an effective normal stress of 100 MPa

6.4.1.3. Effect of effective normal stress

Comparing samples of the same grain size (Figures 6.5a and 6.5b), but deformed at different normal stresses (20 MPa and 100 MPa), we see that the 100 MPa samples are 4 times stronger than the 20 MPa samples. We also observe a striking difference in behaviour between the samples with the finest grain size (AN-25 and AN-09). At 20 MPa effective stress, sample AN-25 shows a peak strength followed by strong weakening up to a displacement of 7 mm. At 100 MPa effective normal stress, however, sample AN-09 shows no peak strength and continues to strengthen up to 6 mm of displacement. Other samples of the same grain size show no large differences in the form of shear stress vs. displacement curve. All show a broad yield point followed by weakening. The amount of weakening is slightly higher in the experiments at 100 MPa effective normal stress (30% vs. 20% for an initial grain size of 12 μm, and 27% vs. 13% for an initial grain size of 22 μm). The volumetric behaviour of the two sets of samples is similar, but the total amount of compaction is higher (~ 20%) in the high effective normal stress samples (compare Figure 6.6a and 6.6b).

6.4.2 Normal stress stepping and steady state friction data

In our stress stepping experiments, the initial run-in of 10 mm displacement was followed by instantaneously stepping the effective normal stress using a step size of 20 MPa. The stress was cycled both up and down. In most cases, a more or less steady state shear stress was achieved within a 1 mm displacement interval. Figure 6.7a shows typical stepping data obtained in experiment AN-25. We plot uncorrected stress data, as these are what we used to determine friction coefficients (see Section 6.3.4). We observed an almost instantaneous response of shear stress upon each step in normal stress, and a systematic increase in shear stress supported with increasing effective normal stress. In Figure 6.7b, we plot the corresponding compaction versus displacement data for AN-25, correcting the compaction data for machine stiffness as mentioned previously. The plot illustrates the behaviour seen in most samples, i.e. that the sample compacts with increasing normal stress and dilates with decreasing normal stress. The compaction rate per unit displacement also increases with increasing normal stress and the dilatation rate increases with decreasing normal stress. The observed dilatation with decreasing normal stress did not recover all of the compaction that occurred during the stepping up of normal stress, so that at the end of the stepping sequence a net compaction (0.05 mm in AN-25) has occurred. Figure 6.7c shows an uncorrected shear stress versus effective normal stress plot for sample AN-25, constructed using data points taken at the end of each step in normal stress. The sample shows a linear relation between shear and normal stress, which can be described by a Coulomb-type criterion given by

$$\tau = \mu^{ss} \cdot \sigma_n + C \quad (6.1)$$

Here μ^{ss} is a steady state internal friction coefficient of the sample and C represents a combination of the internal cohesion of the simulated gouges plus a normal-stress-insensitive contribution due to the friction exerted by the O-ring seals and confining rings. Recall that in our stepping experiments, friction exerted by the O-ring seals and confining rings contributes to the measured shear stress, but not to steady state internal friction coefficient of our sample (see section 6.3.4). All steady state friction coefficient and cohesion values obtained from linear fits to our stress-stepping data are given in Table 6.2.

In Figure 6.8 we summarize our entire set of steady state friction coefficient results by plotting the average friction coefficients, obtained from stepping the normal stress up and down, against temperature and starting grain size. Error bars correspond to the standard error for the two values obtained for each friction coefficient (step-up and step-down). In some cases, we performed two stepping cycles on the same sample at fixed conditions, so that the average friction coefficient and standard error are based on four values (samples AN-09, AN-12, AN-01+AN-03 and AN-25+AN29). Figure 6.8a shows that the steady state friction coefficient tends to decrease with increasing temperature, decreasing from 0.71 to 0.54 in the temperature 400-600 ºC. Figure 6.8b suggests a decrease in steady state friction coefficient (from 0.64 to 0.52) with increasing initial grain size (5 μm to 22 μm) at high initial effective normal stress (100 MPa). No clear trend is visible for samples deformed at 20 MPa effective normal stress.

a)

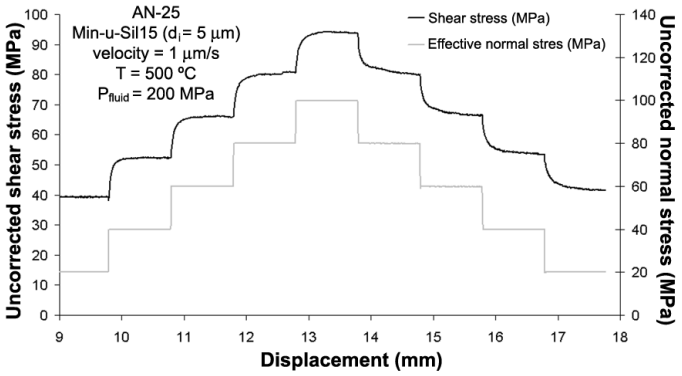

b)

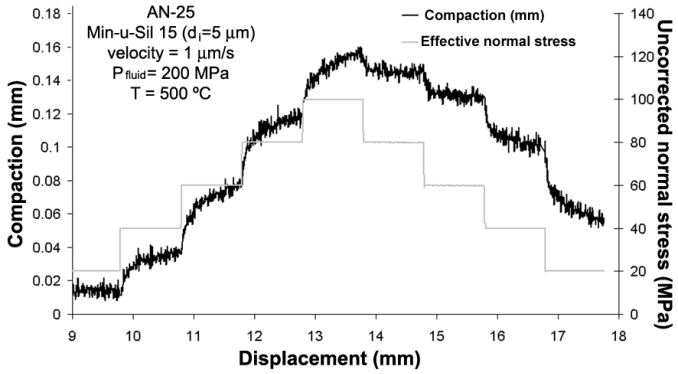

c)

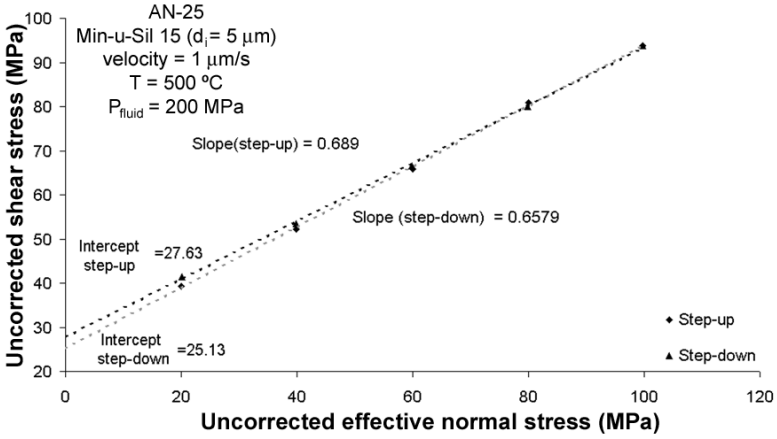

Figure 6.7:

a) Typical stress-stepping data obtained in experiment AN-25, consisting of Min-u-Sil 15 (initial median grain size of 5 μm)which was deformed at 500 ºC, a sliding velocity of 1 μm/s and a fluid pressure of 200 MPa..

b) Compaction versus displacement plot for the same experiment.

c) Uncorrected shear stress versus uncorrected effective normal stress. Note the excellent linear fits.

Table 6.2: List of the results of the linear fits to uncorrected shear stress vs. normal stress data for all (12) stress-stepping experiments performed. The displacement reported is the displacement at the start of the normal stress stepping sequence. Shear displacement during the stress-stepping intervals is at least 1 mm. Note that the cohesion reported is a combination of the internal cohesion of the sample plus a contribution of the O-rings seal and confining ring friction at zero effective normal stress.

Sample	Displacement at start of stepping up (mm)	Friction coefficient (step-up)	Cohesion (MPa) (step-up)	Displacement at start of stepping up (mm)	Friction coefficient (step-down)	Cohesion (MPa) (step-down)
AN-20	2.3	0.0910	17.7	-	-	-
AN-01	14.5	0.4679	32.1	9.2	0.5834	28.4
AN-03	14.4	0.5546	26.8	10.4	0.5274	27.6
AN-09	10.4	0.6211	31.6	6.4	0.6593	33.5
AN-09	30.9	0.5317	34.7	26.7	0.6297	34.5
AN-12	5.5	0.5783	28.4	12.1	0.5997	25.0
AN-12	30.8	0.5355	28.5	38.7	0.4942	31.4
AN-22	9.3	0.7333	28.5	13.3	0.6933	33.5
AN-23	10.3	0.6837	23.6	14.1	0.6918	21.2
AN-24	10.1	0.7105	20.4	14.1	0.6994	19.2
AN-25	9.8	0.6890	25.1	13.8	0.6579	27.6
AN-26	14.4	0.4652	28.2	10.6	0.582	26.7
AN-28	10.8	0.5929	26.2	14.8	0.5995	23.6
AN-29	9.8	0.7252	29.2	13.8	0.7064	28.6

a)

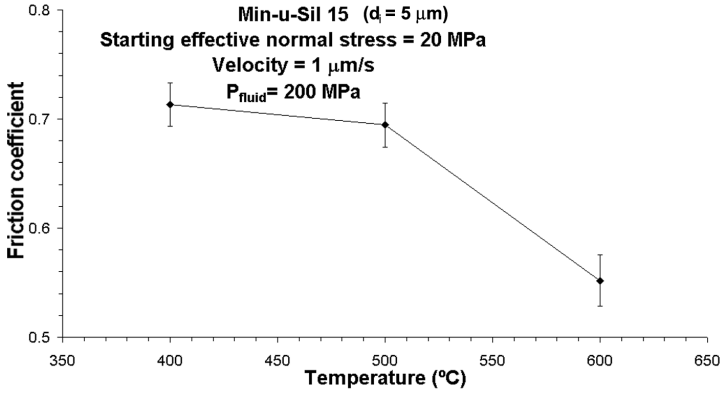

b)

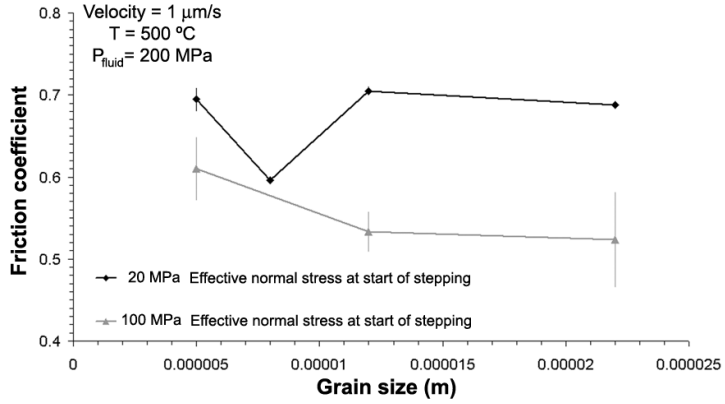

Figure 6.8: Friction coefficients plus corresponding standard errors as determined in stress-stepping experiments as a function of
a) Temperature
b) Initial median grain size

6.4.3 Velocity and temperature-stepping data

In Figure 6.9 we show the uncorrected shear stress vs. displacement data for the two velocity-stepping and temperature-stepping tests we performed. Sample AN-04 consisted of Sil-co-sil 49 with an initial median grain size of 12 μm. For this sample, the sliding velocity was stepped from 1 to 0.1, 0.01, 0.3, 1, 0.03 and 1 μm/s at a constant temperature of 500 ºC (Figure 6.9a). The initial sliding at a velocity of 1 μm/s for a displacement of 4.5 mm was unstable (stick-slip behaviour), but was stabilized by a 10-fold decrease in sliding velocity. Note that the shear strength of the sample drops almost instantaneously upon a step down in sliding velocity, and vice versa.

Sample AN-08 consisted of Min-u-sil 15 with an initial median grain size of 5 μm. For this sample, we observed upon a step in temperature, an instantaneous change in fluid pressure, which was corrected immediately by manually pumping fluid into or out of the system. During the temperature-stepping, we observed unstable sliding (stick-slip behaviour). There is not a large response of the shear strength of the sample upon a change in temperature. The changes in shear strength measured can be mostly related to the changes in fluid pressure though the data do show a tendency for strain hardening to be favoured towards lower temperature. The single step down in sliding velocity, performed on sample AN-08, resulted in a rapid decrease in shear stress by about 30% (Figure 6.9b), with ongoing continuous weakening for several millimetres after the step.

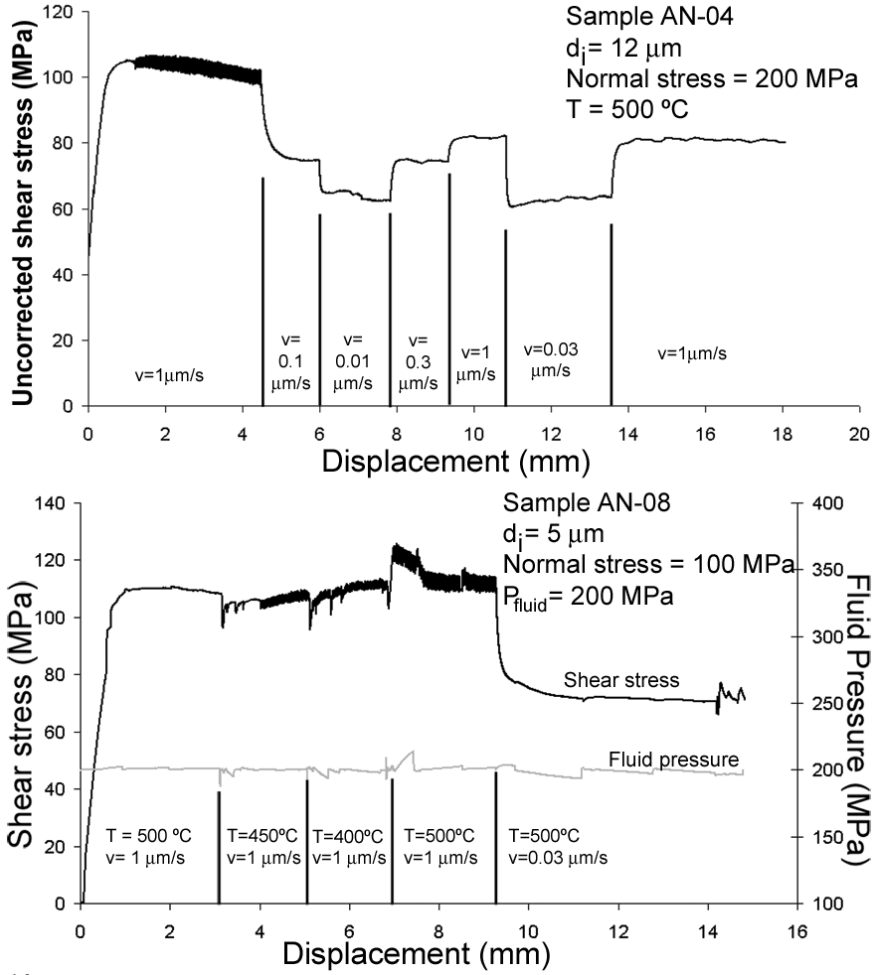

Figure 6.9:

a) Uncorrected shear stress versus shear displacement plot for sample AN-04, consisting of Sil-co-sil 49 (initial median grain size of 12 μm) This was deformed at a temperature of 500 ºC, a fluid pressure of 200 MPa and a normal stress of 100 MPa and sliding velocities of 1, 0.1, 0.01, 0.3, 1, 0.03 and 1 μm/s. b) Uncorrected shear stress versus shear displacement plot for sample AN-08, consisting of Min-u-sil 15 (initial median grain size of 5 μm. This was deformed at a temperature of 400-500 ºC, a fluid pressure of 200 MPa and a normal stress of 100 MPa and sliding velocities of 1 and 0.03 μm/s.

6.4.4. Microstructural Observations

All samples tested exhibited closely similar microstructures, regardless of temperature, fluid pressure and effective normal stress. These are illustrated in Figure 6.10a-c and 11a-d, which show representative microstructures seen in samples AN-09 (d_i = 5 μm), AN-28 (d_i = 12 μm) and AN-23 (d_i = 22 μm). These samples were slid for a total shear displacement of ~18 mm (γ=22.5) at effective normal stresses stepped in the range 20-100 MPa, a fluid pressure of 200 MPa and a sliding velocity of 1 μm/s (Table 6.1).

In all experiments performed, the samples could be relatively easily separated from the upper piston along the piston-gouge interface. The thus exposed upper surface of the gouges was always flat and shiny. In thin section, this top region of the gouges is characterized by the presence of a sharp, flat, through-going, boundary-parallel zone (thickness < 5 μm) with concentrations of fine-grained material (d < 0.5 μm) filling up surface roughness (Figure 6.10a-c). There are no impressions of the teeth of the pistons in this upper zone, contrary to the lower gouge-piston boundary where these impressions are generally still present (Figure 6.10a). The upper interface of the sample was thus interpreted to be a boundary-parallel Y-shear (Chester and Logan, 1990; Hoogerduijn Strating and Vissers, 1994; Bos et al., 2000b; Kanagawa et al., 2000) in which deformation was concentrated at some point during the experiments. No evidence was found for the development of Y-shears at the lower piston-gouge interface. A few samples also show a number of dilated zones in the typical Riedel shear orientation at an angle of 30 º to the fault gouge boundary, which curve towards and into upper the Y-shear (Figures 6.10a and 10b). The spacing of these Riedel shears, as seen in the microstructure of sample AN-09 (Figure 6.10a), is probably related to the teeth spacing on the lower piston. The average grain size of all samples is typically around ~2-5 μm and is significantly reduced compared to the initial grain sizes of 5-22 μm (Figure 6.11). This is mostly the result of the presence of numerous very fine grains (< 1 μm), whereas the larger grains reflect more the initial grain size (distribution). The shape of these larger grains is angular, with numerous inter- and intragranular fractures (Figures 6.11b, 11c and 11d). The small grains tend to be more rounded and show few such fractures (Figure 6.11d). No shape preferred orientation of fragments was observed.

In all samples, the average porosity is low (~10-15%), the spaces between larger grains being filled with numerous very fine fragments (< 1 μm). Porosity decreases towards the boundary-parallel Y-shear (Figure 6.10c) to values as low as 4%, while the amount of fine-grained material increases. Also, the number of fine grains seems to increase closer to the Riedel shears. Occasional grain-to-grain indentation and truncation features are apparent, especially in the finer fragments (Figures 6.11a-c). There was no indication for undulatory extinction in any of the samples.

a)

b)

c)

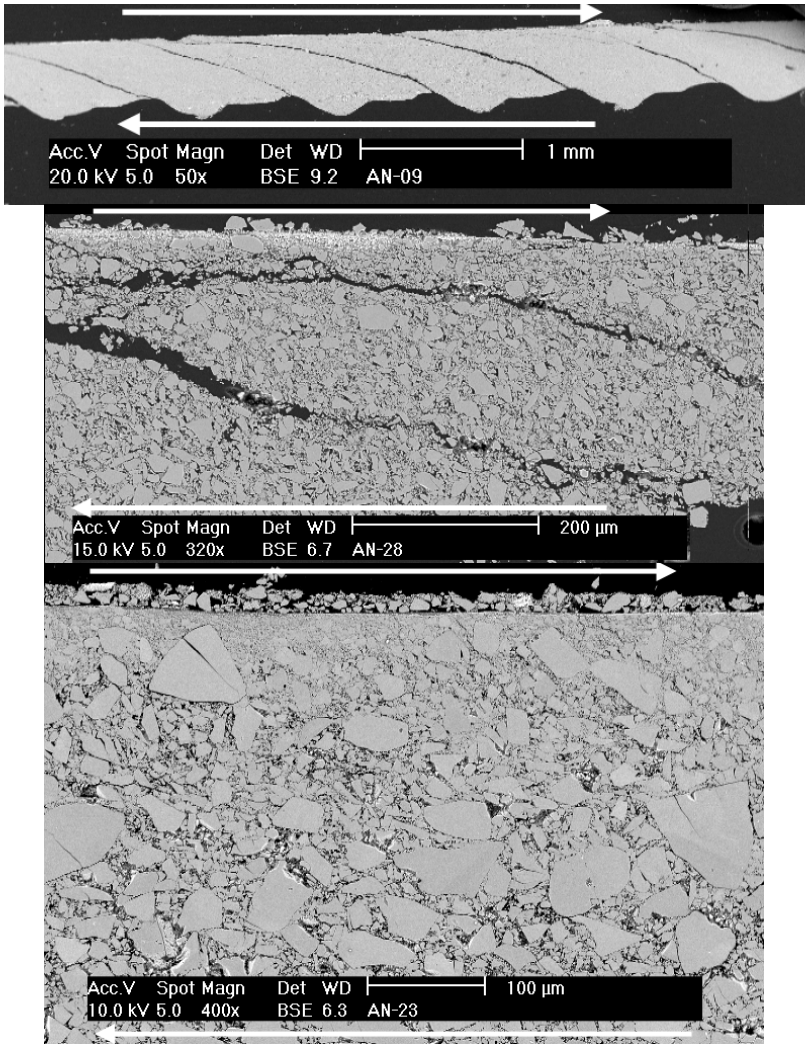

Figure 6.10: Electron backscatter images showing typical gouge microstructures.
a) Typical regular dilatational Riedel shears oblique to the shear zone boundary, curving towards and into a through-going Y-shear at the upper surface. The Riedel spacing may be related to the location of the sample-gripping teeth. Sample AN-09, with a starting grain size of 5 µm and deformed at 500 ºC, initial normal stress of 100 MPa and fluid pressure of 200 MPa. Total displacement is 18 mm and shear sense as indicated.
b) Riedel shears oblique to the shear zone boundary, curving towards and into a sharp, through-going Y-shear at the upper surface. Sample AN-28, with a starting grain size of 12 µm and deformed at 500 ºC, initial normal stress of 20 MPa and fluid pressure of 200 MPa. Total displacement is 18 mm and shear sense as indicated.
c) Sharp continuous Y-shear (upper surface), showing a lower porosity (<5%) close to the Y-shear than in the center of the gouge zone (10-15%). Also note large variation in grain size and intragranular fractures in the larger grains. Sample AN-23, with a starting grain size of 22 µm and deformed at 500 ºC, initial normal stress of 50 MPa and fluid pressure of 200 MPa. Total displacement is 19 mm and shear sense as indicated.

a)

b)

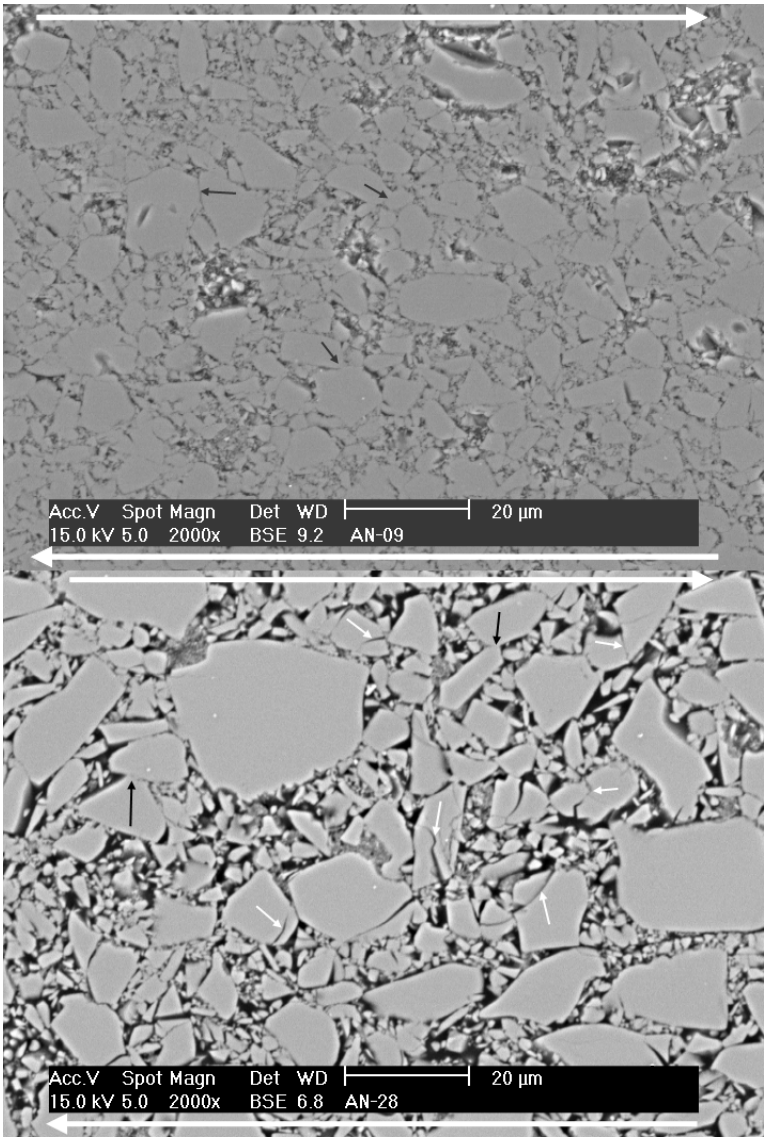
Acc.V Spot Magn Det WD 20 µm
15.0 kV 5.0 2000x BSE 9.2 AN-09
Acc.V Spot Magn Det WD 20 µm
15.0 kV 5.0 2000x BSE 6.8 AN-28

c)

d)

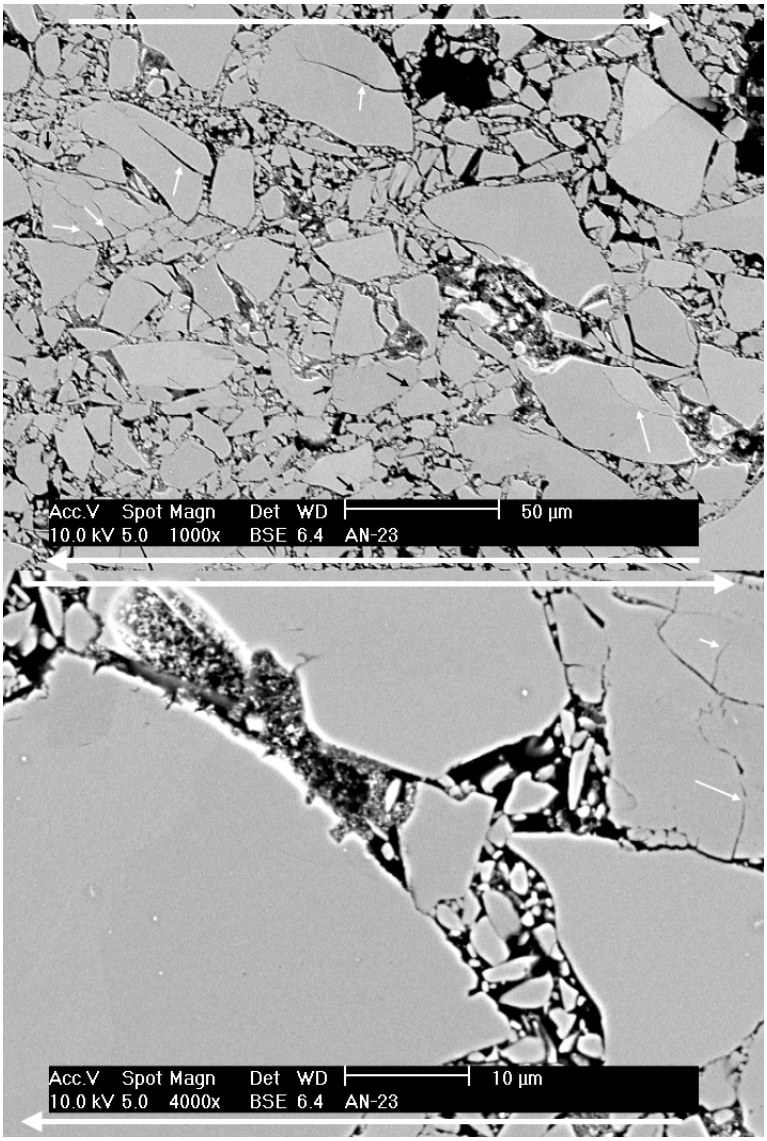

Figure 6.11: Electron backscatter image showing details of the microstructures of
a) sample AN-09. Note the low porosity, long grain boundaries and occasional indentations (black arrows)
b) sample AN-28. Note the low porosity intragranular and transgranular fractures (white arrows) and grain-to-grain indentations (black arrows).
c) sample AN-23. Note the low porosity, intragranular and transgranular fractures (white arrows) and grain boundary interpenetration (black arrows).
d) Sample AN-23. Note the irregular grain boundaries, intragranular and transgranular fractures (white arrows) and distrubition of rounded fine particles.
For the experimental conditions, see Table 6.1 and in all images shear sense is as indicated.

6.5. Discussion

The aim of the present experiments was to determine the high shear strain behaviour of simulated quartz gouges under hydrothermal conditions, investigating the effects of strain (γ up to 50), effective normal stress (20-100 MPa), temperature (400-600 ºC), sliding velocity (0.01-1 μm/s) and initial grain size (5-22 μm). In almost all experiments, significant strain weakening (15-30 %) occurred after initial "failure" of the samples, reaching steady state values at shear strains of ~10-15. Failure of the gouges was associated with a switch from minor dilatation (or zero compaction), during the first mm of the displacement, to subsequent compaction. The steady state strength increases linearly with effective normal stress. In broad terms, our results show that the steady state friction coefficient of pure quartz gouges varies between ~0.5 and 0.7 under the conditions studied. A decrease in sliding velocity leads to an instantaneous decrease in shear strength. A decrease in temperature appears to cause an increase in steady state friction coefficient in experiments performed at different temperatures, but the results from the single temperature-stepping test show no clear effect on the steady state strength. Some evidence exists for a slight decrease in steady state friction coefficient with increasing initial grain size, but the effect is not clear. We will now attempt to explain these findings and to speculate on the controlling microscale processes.

6.5.1. Stress-strain behaviour and possible deformation mechanisms

The initial phase of deformation of our samples consists of continuous slip hardening until the peak shear strength is reached after a displacement of ~0.5-1 mm (γ=0.6-1.2, see Figures 6.4 and 6.5). The slip hardening was accompanied by minor dilatation or zero compaction. This phase of initial shear displacement in the approach to peak strength ("failure") is presumably mostly accommodated by grain crushing, grain rotation and intergranular grain sliding. After the peak shear stress, the gouges continuously weaken over a displacement of up to ~ 8 mm (γ=10) and displacement normal to the gouge switches to continuous compaction. The characteristic softening occurring in all but one sample (sample AN-09) seems likely to be associated with localization of slip along the interface between the top-piston and the gouge samples (Y-shear development), since localization requires strain softening (see also Gu and Wong, 1994; Sleep et al., 2000). However, sample AN-09 (consisting of Min-u-sil 15 and deformed at 1 μm/s, 200 MPa fluid pressure and 100 MPa normal stress) also shows indications for the presence of a boundary-parallel Y-shear, though it showed no weakening. Therefore, it remains questionable at which point during the experiment the Y-shears were actually developed, how much shear strain was taken up by them, what their internal strength properties are, and what the effect of their development on macroscopic shear strength is. It is possible that the Y shears form at the peak stress

without always producing on-going macroscopic weakening if independent hardening effects are sufficiently competitive.

A possible explanation for the weakening observed beyond the peak stress may lie in a reduced contribution of cataclasis and an increasing contribution of solution-transfer processes to the observed deformation, either within the developing Y-shear or independently in the body of the gouge. Solution-transfer or pressure solution processes are known to be faster for smaller grain sizes and may therefore be expected to become more important after initial grain size reduction, perhaps smoothening and weakening the Y-shear or weakening the bulk gouge by promoting granular flow (cf. Paterson, 1995). However, enhanced solution-transfer processes will also lead to compaction of the gouge, which will thus become denser and stronger with increasing displacement as reported by Bos et al. (2000b) for shear of wet halite aggregates. It therefore seems more likely that strain weakening is related to Y-shear activity. An additional possibility might be that the gouge is weakened by the ongoing development of strain softening Riedel shears, with slip on these being accommodated by pressure solution enhanced deformation of the intervening cataclastically refined gouge, though Riedel shears were developed in only 3 samples As these samples did not showed more or less weakening than the other samples, weakening as a result of Y-shear activity still seems most likely.

6.5.2. Insights from the effects of temperature, grain size and sliding velocity

We now examine what more we can infer about operative microscale processes from the effects of temperature, grain size and sliding velocity in our experiments. The three experiments performed at different fixed temperatures show a decreasing steady state friction coefficient with increasing temperature. This trend is not seen in our single temperature-stepping test. However, this may be due to difficulties in attaining steady state, so we focus on the tests done at fixed temperatures. The decrease in steady state friction coefficient and the increase in strain softening with increasing temperature seen in these experiments can potentially be explained by decreasing friction along localised Y slip surface(s) due to smoothening by the removal of asperities by solution-transfer processes. Riedel-shearing with enhanced accommodation by pressure solution remains a possibility too, though its occurrence in only 3 samples makes this unlikely. Note that, the largest amount of compaction observed in the samples tested at 400, 500 and 600 ºC was in that deformed at 400 ºC, while the other two samples (500 and 600 ºC) showed nearly isovolumetric behaviour. This suggests that initial, pre-shearing compaction may have played a role in controlling the shear behaviour of the higher temperature samples.

The trend observed in the experiments with varying initial grain size indicates a slight decrease in steady state friction coefficient for an increasing initial grain size at high effective normal stress, with no clear effect at low normal stress. However, we also observed a strong weakening in almost all of these samples, which suggests localization of deformation into a boundary-parallel Y-shear. In this case, the initial grain size should

indeed have little effect on the observed steady state friction coefficient. A coarser initial grain size might even lead to more initial cataclasis, producing finer fragments and hence more effective smoothening and weakening of the Y-shear due to solution transfer activity. If the observed strain weakening were due to the development of Riedel-shears with accommodation by pressure solution compaction/deformation, then initially samples should tend to be stronger, which does not seem consistent with our data on the effect of grain size. Turning finally to our velocity-stepping data, we observed a decrease in sliding friction with decreasing sliding velocity. We can explain this trend by a relative increase in solution-transfer activity per unit displacement. A localised Y-slip surface would then be smoothened and weakened by increased dissolution of asperities at lower sliding velocities (cf. Dieterich and Kilgore, 1994), which broadly fits our observations. At the same time Riedel-shearing with accommodation by pressure solution deformation should also get easier with decreasing velocity. On the basis of our data, then, the most likely explanation for the observed strain weakening and effects of temperature, initial grain size and sliding velocity on steady state frictional strength is one of localized Y-shear development with internal weakening by solution-transfer processes.

6.5.3. Comparison with previous work

We will now compare our experimental work with data from saw-cut type shear experiments done by previous authors on simulated quartz gouges. Kanagawa et al. (2000) performed a number of sliding experiment on simulated quartz gouges consisting of Min-u-Sil 5 and Sil-co-Sil 250 (median grain size of 2 and 45 μm, respectively) in the presence of either water or argon at a pore fluid pressure of 200 MPa, a confining pressure of 300 MPa, a temperature of 927 ºC and sliding velocities of 0.13-6.68 μm/s. They used a triaxial testing apparatus with a cylinder of quartz sandstone (Fontainebleau sandstone) containing an initially 1 mm thick layer of simulated quartz gouge inserted into a saw cut inclined at 30 º to the cylinder axis. The nature of the triaxial set-up limits the maximal axial displacement to ~ 2 mm, which corresponds to a shear strain of ~ 2. The experimental conditions of Kanagawa et al. (2000) were thus comparable to our conditions, though the temperature was higher, and the total shear strain achieved was much lower. In addition, compaction could not be measured during shear.

Kanagawa and coworkers observed different mechanical sliding behaviour for samples deformed with argon (dry) versus water (wet) as the pore fluid. The dry samples showed slip hardening with a decreasing slip hardening rate with increasing displacement. The friction coefficient of these samples at the end of the tests was 0.65-0.68 at a displacement of 1.5 mm. The microstructures of the dry samples showed pronounced grain crushing and comminution, Riedel shears and high porosity domains in the Riedel shear orientation.

In contrast, Kanagawa's wet samples showed two types of deformation behaviour dependent on the starting grain size and the sliding velocity (v). Coarse gouges deformed at high sliding velocities exhibited a sharp peak stress followed by slip softening and subsequent stable sliding with a friction coefficient of 0.45 (at v = 0.6 μm/s or $\dot{\gamma}$ = 6 x 10^{-4} s^{-1}) and 0.58 (at v = 6.68 μm/s or $\dot{\gamma}$ = 6.68 x 10^{-3} s^{-1}). The gouges always showed a continuous slip surface along the interface between gouge layer and upper sandstone forcing block. Riedels shear were not developed within the gouge layer and the gouge was strongly cohesive. Grains were interlocking and their boundaries interpenetrating. Porosity varied from 8 to 12 %. On the other hand, fine gouges and coarse gouges deformed wet at low sliding velocity exhibited slip hardening after a poorly defined yield point and reached maximum friction coefficients of 0.68-0.71. Microstructural observations indicated that the gouges were strongly compacted and very cohesive. The grains in the gouge appeared subequant in shape and showed large contact areas. Riedel shears were present in the gouge, but no significant grain comminution or fracturing occurred along them. Two-dimensional porosity measurements of these gouges yielded porosities of 5-12 %, with the coarse gouge having the lowest porosity.

In summary of their main results for wet samples at shear strains up to 1 or 2, Kanagawa et al. (2000) observed a transition from slip hardening (with Riedel-shearing) to slip softening (with Y-shear localization) as sliding velocity and grain size increased. Kanagawa's coarse dry samples notably showed strain hardening, Riedel shearing and no Y-shears, suggesting that the Y-shearing was responsible for the strain weakening in the wet tests and that presence of water is required for Y-shear development and on-going activity. Clearly, our strain softening data and microstructural observations obtained at a shear strain rate of 5x10^{-5}-5x10^{-3} s^{-1}, d_i of 5-22 μm and temperatures of 400-600 ºC most resemble that of Kanagawa's coarse gouges (45 μm) deformed wet at high sliding velocities ($\dot{\gamma}$ = 6x10^{-4} - 6x10^{-3} s^{-1}). Though they were unable to measure compaction/dilatation, Kanagawa et al. suggest that the initial slip hardening in these samples was the result of shear-induced compaction by grain comminution, producing large relative load-bearing contact area. They also implied that this compaction eventually resulted in localization of slip along the gouge/forcing block interface, thus accommodating the imposed shear displacement and resulting in subsequent slip softening. Most of our tests show initial dilatation or virtually no volume change during the loading stage, with most compaction occurring after the peak stress, so we reject the possibility that strong compaction is responsible for the initial loading characteristics. Instead, we propose that the initial loading behaviour involves cataclastic/granular flow, accompanied by dilatation. The pre-peak loading stage is thus interpreted as analogous to the mechanical behaviour of soils. From soil mechanics, it is known that densely packed granular media initially show dilatation and/or particle fracture,

leading to a peak stress and followed by slip softening and a decreasing contribution of dilatational work to observed shear strength. In our experiments and Kanagawa's experiments, initial compaction during the heating and equilibration stage of test preparation may have produced a dense, overcompacted gouge that dilated during initial shear, resulting in a peak stress followed by slip weakening. In soil mechanics steady state sliding is usually achieved after a shear strain of ~ 0.5-1, whereas we observe continued slip weakening, probably as a result of localization of deformation along the boundary-parallel Y-shear seen in all our samples. The fact that Kanagawa et al. (2000) obtained Y-shears in wet samples, but not in dry one tested under similar conditions, supports our suggestion that strain weakening associated with the Y-shears is related to the action of water, e.g. through effects such as solution transfer.

Most of the peak shear strengths we measured occur after a displacement of ~0.5-1.5 mm (γ=0.6-1.8), which is near the maximum displacement that Kanagawa et al could reach and well beyond their peak strengths for coarse samples deformed fast (see AN-01, Figure 6.12). Therefore, we suggest that the fine gouges of Kanagawa et al, which exhibited only slip hardening (inferred to be due to compaction through solution-transfer processes), might simply not have reached the point of localization and subsequent weakening. This is supported by Figure 6.13, where we compare friction coefficients from our experiments, conducted at an effective normal stress of 100 MPa and a temperature of 500 ºC, with those of Kanagawa's fine and coarse gouges deformed at 923 ºC and 300 MPa confining pressure at similar strain rates. From this figure, we can clearly see that our samples increase in strength over the strain interval of γ=0.5-1.0 reached in Kanagawa's fine gouge, but weaken substantially at the higher shear strains not reached by Kanagawa et al. We conclude that our results are in broad agreement with the coarse and fine experiments of Kanagawa et al. (2000), taking into account the differences in temperature, experimental set-up and total shear strains reached.

Chester and Higgs (1992) performed triaxial shear experiments on wet, ultrafine (< 1 μm) and thin (0.2 mm) quartz gouges at temperatures of 25-600 ºC, confining pressures of 150 MPa, fluid pressure of 100 MPa and an axial displacement rate of 4 x 10^{-4} mm/s. Like us, they found a decrease in friction coefficient with increasing temperature for temperatures above 300 ºC, but observed slip hardening up to the maximum shear strain they reached (γ=5). Based on microstructural observations of Riedel shears, vein quartz, preferred orientations and low porosity, they inferred that deformation involved cataclasis and a solution-precipitation process. We suggest that their experiments would eventually also slip soften if shearing had continued to larger displacements, as in our tests.

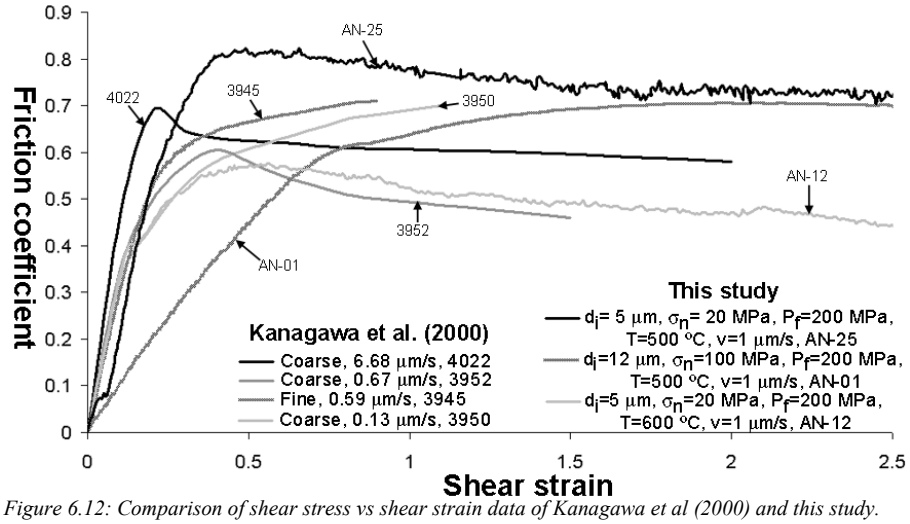

Figure 6.12: Comparison of shear stress vs shear strain data of Kanagawa et al (2000) and this study.

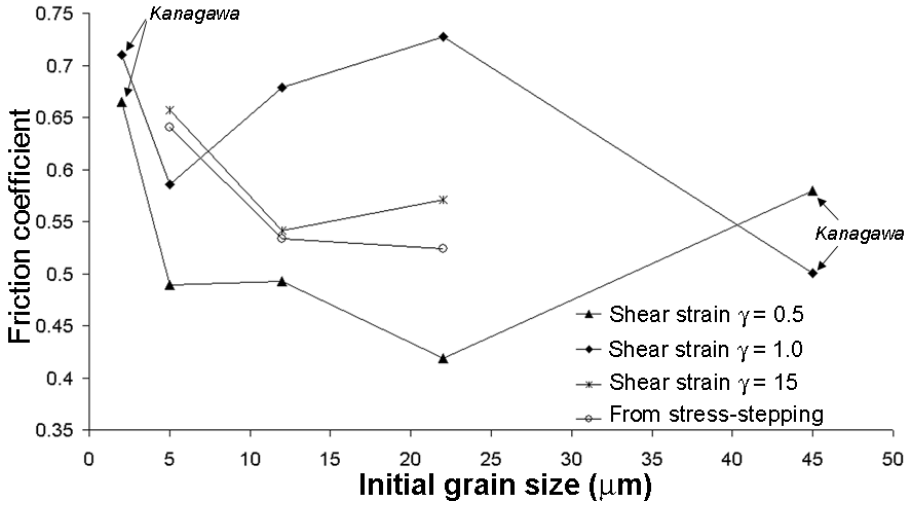

Figure 6.13: Plot of friction coefficients vs. grain size for this study and Kanagawa et al. (2000) for different shear strains. Our data are from experiments AN-01, AN-03, AN-09 and AN-26, all deformed at 500 ºC, 100 MPa effective normal stress, 200 MPa fluid pressure and $\dot{\gamma}$ *of ~* 10^{-3} s^{-1}*. Kanagawa's data are from experiments 3945 (fine, 2 μm) and 4022 (45 μm), which were both deformed at 927 ºC, 300 MPa confining pressure, 200 MPa fluid pressure and* $\dot{\gamma}$ *of* 0.6×10^{-3} s^{-1}.

Room temperature experiments on quartz gouges by Marone and Scholz (1989) and Morrow and Byerlee (1989) at similar effective normal stresses (12.5-100 MPa) and sliding velocities (10^{-2}-30 μm/s) have demonstrated that porosity and particle-size distribution have a strong effect on the evolution of the strength of these gouges. Both studies showed soil mechanics type behaviour in that overconsolidated (overcompacted) quartz gouges dilate and show a peak strength during initial shearing and subsequently slip weaken. These effects did not occur in samples sheared at lower effective normal stress.

In summary, it is important to recall that porosity at the start of the sliding in our tests is probably rather low (5-10%) depending on initial grain size, effective normal stress, temperature and pre-test equilibration time. Our "overcompacted" gouges show initial slip hardening as a result of net dilatancy, similar to previous experimental studies (Marone and Scholz, 1989; Morrow and Byerlee, 1989; Chester and Higgs, 1992; Kanagawa et al., 2000). Subsequent shearing past the peak shear stress leads to localised slip along a boundary-parallel Y-shear and, in some cases, Riedel shears, accompanied by strong slip weakening. Steady state strength of the gouges is most probably related to the strength of the localised Y-slip surfaces, in which solution-transfer activity probably acts as a weakening agent by smoothing the surface.

6.5.3. Implications for crustal faults under hydrothermal conditions

Previous experimental work and modelling studies (Rutter and Mainprice, 1979; Chester and Higgs, 1992; Rutter and Maddock, 1992; Chester, 1994b; Cox, 1994b; Chester, 1995) have shown that solution-transfer effects may be very important in controlling the sliding behaviour of crustal faults under hydrothermal conditions. The present experiments indicate that solution-transfer effects are indeed active. However, no evidence was found for a pressure-solution creep controlled gouge strength (cf. Rutter and Mainprice, 1979). Instead, gouge strength seemed to be controlled by localization of slip into discrete Y-shears and the strength of the Y-slip surface. Solution-transfer or related processes have been inferred to be important in adjusting the strength of the localised slip surface, probably by asperity removal through dissolution. Our findings imply that chemical effects on friction can act together with cataclastic processes to cause significant strain softening (up to 30%) in gouge-bearing faults, under brittle-ductile transitional conditions compared with "traditional" rock strength data obtained under dry and room temperature conditions. Most importantly, our results have shown that these strain softening effects are only seen at relatively high shear strains (γ>0.5-1). Future experimental and modelling studies of fault slip and localization should take this findings into account. More work is needed to determine the RSF behaviour at high shear strains.

6.6. Conclusions

We have performed a series of ultra high strain (γ=50) sliding experiments on simulated quartz gouge using a hydrothermal ring shear apparatus operated at a fluid pressure of 200 MPa, normal stresses of 20-100 MPa, temperatures of 400-600 ºC and sliding velocities of 0.01-1 μm/s. From previous work, we know that solution-transfer processes are active under these experimental conditions. Our aim was to investigate the influence of such solution-transfer processes on the sliding behaviour and strength of simulated quartz gouges. The following conclusions were reached:

1. Initial shear deformation in quartz gouges is dominantly accommodated by cataclastic processes and dilatation which result in marked, initial strengthening towards a peak/yield strength at a shear strain of 0.6-1.8.
2. Progressive shear deformation results in subsequent weakening, most probably as a result of slip localization on a boundary-parallel slip surface. Slip weakening within such localized surfaces or Y-shears is likely to be due to solution-transfer processes, acting to remove asperities by dissolution.
3. Slip weakening up to 30% occurred in the present experiments, reaching a steady state value at γ=8-12. The measured steady state friction coefficients in the quartz gouges (0.5-0.7) correspond well with previous experimental studies, conducted at hydrothermal conditions, though much lower shear strains were generally reached in these and steady state was often not reached.
4. The steady state strength of quartz gouges tends to increase with increasing sliding velocity, decreasing temperature and decreasing grain size under the conditions studied.
5. Our results imply that significant slip weakening and localization can occur in natural quartz-rich fault gouges at high shear strains. Future experimental and modelling studies should take this into account. More work is needed to determine the RSF parameters of simulated fault gouges to high shear strains.

Chapter 7

A MICROPHYSICAL MODEL OF VELOCITY WEAKENING IN PHYLLOSILICATE-BEARING FAULT GOUGES

Abstract

Previous rotary shear experiments performed on a fault gouge analogue system consisting of muscovite plus halite and brine, have shown that the presence of the phyllosilicate phase and operation of pressure solution have large effects on the sliding behaviour of the gouge under conditions where cataclasis and solution transfer can operate in the halite matrix phase. Our experiments have shown that while 100% halite and 100% muscovite samples exhibit rate-independent frictional/brittle behaviour, the strength of mixtures containing 10-30% muscovite is both normal stress and sliding velocity dependent. At high velocities (>1 μm/s), unusually marked velocity-weakening frictional behaviour occurs, along with the development of a structureless, cataclastic microstructure. In this paper, a micromechanical model is developed in an attempt to explain this behaviour. The model assumed a granular flow process involving competition between intergranular dilatation and compaction by pressure solution. The predictions of the model agree well with the experimental results. Extension of this model to quartz-mica systems implies that the presence of phyllosilicates can strongly promote (unstable) velocity weakening behaviour at rapid slip rates on natural faults, under mid-crustal conditions. Static stress drop predictions based on the model agree reasonably with estimates from seismic observations. Our results may help explain the discrepancy between laboratory-derived rate-and-state friction parameter values for dry, low strain and/or single phase rock systems, with the values for natural fault rocks inferred from seismological data.

7.1. Introduction

In recent decades, a great deal of experimental effort has been focused on quantifying the frictional behaviour of faults, in order to address the issue of seismogenesis and the seimic cycle. Of particular interest in this research is the phenomenon of velocity weakening. Velocity weakening occurs when fault rock strength decreases with increasing displacement rate and it is a prerequisite for generating a slip instability. i.e. an earthquake.

Laboratory results obtained from mostly room temperature and/or dry sliding experiments on bare rock interfaces and gouge-filled faults have typically shown stable, velocity-strengthening sliding friction at 0.6-0.8 times the applied normal stress(e.g. Byerlee, 1967; Dieterich, 1972; Jackson and Dunn, 1974; Byerlee, 1978; Scholz, 2002). Velocity-weakening is usually observed in such experiments in association with localisation of deformation along boundary-parallel shear bands (Chester and Logan, 1990; Bos et al., 2000b). Laboratory data on gouges and bare rock surfaces also show important time-dependent (transient) effects when sliding velocity is changed.

Quantitative analysis of the mechanical data is usually done using the so called rate-and-state variable friction laws (RSF laws hereafter), developed by Dieterich (1978, 1979) and Ruina (1983). Dieterich (1978, 1979) proposed that the time or rate dependence of frictional strength is due to processes that affect the real area of contact of the sliding

surfaces. During a period of reduced slip rate or of zero slip, the real area of contact is envisaged to increase due to creep of the existing contact points or asperities. Upon shearing at fast rate, the resistance offered by the increased contact area requires a large applied shear stress to be overcome ("the direct effect"). This shear stress then evolves towards a new steady state value during which a new population of contact points is created ("the evolution effect", see Figure 7.1). Velocity strengthening occurs when the steady state contact area at higher velocity is larger and velocity weakening occurs when the steady state contact area at higher velocity is lower. This type of behaviour can be expressed in a mathematical form using the relation:

$$\mu = \mu_0 + a \ln\left(\frac{V}{V_0}\right) + b \ln\left(\frac{V_0 \theta}{D_c}\right) \tag{7.1}$$

which fits a wide range of experimental data well but has no mechanistic basis (Dieterich, 1978, 1979; Ruina, 1983). Here μ is the instantaneous friction coefficient (shear stress divided by the normal stress), μ_0 is a reference friction coefficient at a reference sliding velocity V_0, V is the instantaneous sliding velocity, a is a parameter that reflects the magnitude of the direct effect (second right hand term), b reflects the magnitude of the stress drop associated with the evolution effect, θ is a (micro)physical state variable that represents the state of the sliding surface, and D_c is a characteristic sliding distance over which the evolution effect takes place. Stable, velocity strengthening slip occurs when $(a-b) \geq 0$ and unstable, velocity weakening slip will occur when $(a-b) < 0$.

Although the RSF equations are purely empirical, they are widely used to model earthquake and faulting phenomena (e.g. Cao and Aki, 1986; Dieterich, 1994; Ben-Zion and Rice, 1995; Ben-Zion and Rice, 1997; Sleep, 1997; Marone, 1998b; Beeler et al., 2001; Scholz, 2002). Application of RSF parameters to natural conditions is done without much consideration of the (micro)physical processes involved in natural fault zones under hydrothermal, mid-crustal conditions. Use of laboratory-derived *a*- and *b*-values of the order of 0.01-0.02 and 0.0-0.02, respectively, usually gives reasonable modelling results, but the critical displacement parameter, *Dc*, typically has to be set in the range of 0.01-0.1, contrary to the laboratory-derived values of 1-10 μm.

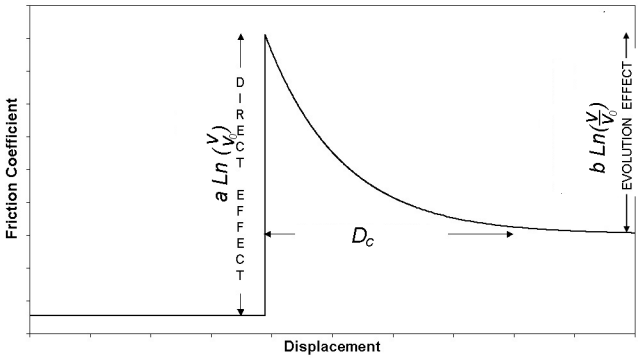

Figure 7.1.: Plot showing the effect of a step in sliding velocity on the friction coefficient for a hypothetical velocity-strengthening material.

Despite the fact that modelling results obtained using these values of a, b and D_c compare favourably with field-derived data on post-seismic creep displacement, moment and rupture area (Stuart and Tullis, 1995; Tullis, 1996; Ben-Zion and Rice, 1997), static stress drops, which are directly related to the value of (a-b), predicted from models based on laboratory-derived RSF parameters are not compatible with field observations (i.e. heat flow and stress orientation data) of the absolute strengths of mature fault zones. Controversy therefore remains in the application and up-scaling of laboratory-derived RSF parameters to natural situations. The central problem is finding a physical basis to extrapolate laboratory values of the RSF parameters a, b and D_c to the spatial and temporal scales relevant to natural faults. Laboratory studies are limited in total displacement and roughness of the gouge zone which means that processes such as wear, fault zone widening, shear localization and microstructural development can not easily be taken into account. Time and strain limitations also mean that effect of fluid-rock interaction, phyllosilicate production and foliation development are not sufficiently well understood to be reliably accounted for by extrapolating and upscaling of a, b and D_c values to nature.

To investigate the effects of fluid, strain, microstructural development and the presence of phyllosilicates, we recently conducted an experimental study on simulated phyllosilicate-bearing fault-rock analogues (halite-muscovite plus saturated brine, see Niemeijer and Spiers 2005 and chapters 4 and 5). In the pure end-member samples we observed velocity strengthening or velocity neutral behaviour at rapid sliding rates. In contrast, the mixtures of salt and muscovite showed strong velocity weakening. We observed (a-b)-values around 0.1 and critical displacements of 0.5-1 mm, which is an order of magnitude higher than previously reported values. The associated high velocity microstructures were chaotic, with a cataclastic appearance and evidence for the operation of pressure solution. We also observed an increasing porosity with increasing sliding velocity. We interpreted the observed deformation behaviour to be the result of competition between shear-induced intergranular dilatation and normal stress driven compaction via pressure solution, with muscovite preventing intergranular healing. Since many fault zones

are phyllosilicate-rich, the question arises as to whether such effects will occur in natural fault rocks. If so, their role might be very important in bringing about velocity weakening and hence seismogenesis.

In this chapter, we attempt to assess the possible role of phyllosilicates in causing velocity weakening of faults under conditions where pressure solution processes are active. To do so, we present a simple microphysical model, incorporating the proposed competition between dilatation and compaction and compare the predicted steady state strengths with our experimental results for the salt/muscovite plus brine system. We go on to extrapolate the model to quartz-muscovite fault gouges under natural conditions, using the appropriate kinetic equations for compaction of quartz by pressure solution. We finally predict the static stress drop expected when a rupture propagates from a strong asperity within a fault zone into velocity-weakening muscovite-bearing fault rock, comparing our results with data on stress drops retrieved from analysis of seismic data from a variety of tectonic regimes.

7.2. The velocity weakening effect in simulated phyllosilicate-bearing fault gouge

Before attempting to construct a microphysical model for the velocity-weakening process of interest, it is useful to recap on the experiments showing this dramatic effect. Niemeijer and Spiers (2005, see also chapters 4 and 5) performed high strain rotary shear experiments on fault gouges consisting of halite-muscovite mixtures flooded with saturated brine. For mixtures in the range10-50 wt% muscovite, we observed a strong dependence of shear strength on sliding velocity and on normal stress (Figure 7.2). In contrast, samples consisting of pure halite or pure muscovite showed almost no dependence of shear strength on sliding velocity. For a simulated fault gouge consisting of 20 wt% muscovite and 80 wt% halite, the steady state shear strength increases, with increasing sliding velocity, from a minimum value of 1.8 MPa to a peak value of 4 MPa (at a normal stress of 5 MPa) and subsequently decreases to a minimum value of 2 MPa. In Figure 7.3, we show the typical microstructures, characteristic for the two different velocity regimes. In the velocity-strengthening regime, the gouge is dense and apparently mylonitic, with a continuous, anastomosing foliation, consisting of aligned muscovite flakes and intervening, elongated halite grains. In contrast, the typical microstructure in the velocity-weakening regime is chaotic, with no foliation and a large variation in grain size. Moreover, gouge porosity determinations made after deformation show an increase steady state porosity with increasing sliding velocity, especially in the velocity-weakening regime (Figure 7.4). Following Bos and Spiers (2000a; 2002b), Niemeijer and Spiers (2005, see also chapters 4 and 5) proposed that deformation in the velocity-strengthening regime is accommodated by slip on/over the muscovite foliation, accommodated by pressure solution of (solution-transfer around) the intervening halite grains. The displacement rate is so slow in this regime, that the tendency for dilatation by slip on/in the foliation is largely countered by compaction through pressure solution, so the porosity remains low (1-3%). A microphysical

model for this type of behaviour was developed by Bos and Spiers (2002b) and improved by Niemeijer and Spiers (2005, see chapter 4). For the velocity weakening regime, Niemeijer and Spiers (2005, see chapter 5) proposed that deformation occurs by pervasive granular flow of the halite/muscovite mixtures, with an ongoing competition between shear-induced intergranular dilatation and compaction via solution-transfer processes. Such competition implies to an increase in steady state porosity with increasing sliding velocity, hence a decrease in effective sliding contact area, in dilatation angle and/or in contact strength (due to reduced time-dependent healing), thus producing the observed velocity-weakening and volumetric behaviour (Figures 7.2 and 7.4). In the following, we will set-up a microphysical model describing this competition between dilatation and compaction and compare the results with our experimental data.

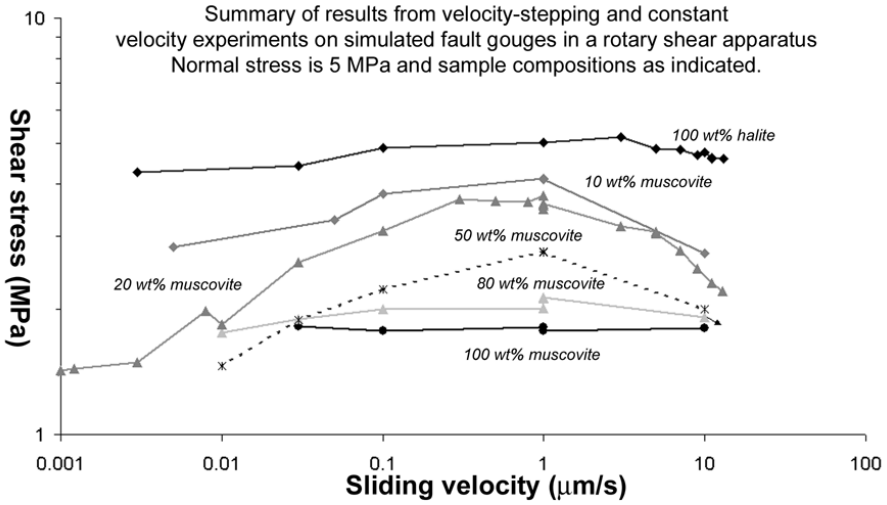

Figure 7.2.: Plot of steady state stress vs. sliding velocity for a set of brine-flooded rotary shear experiments at 5 MPa normal stress.

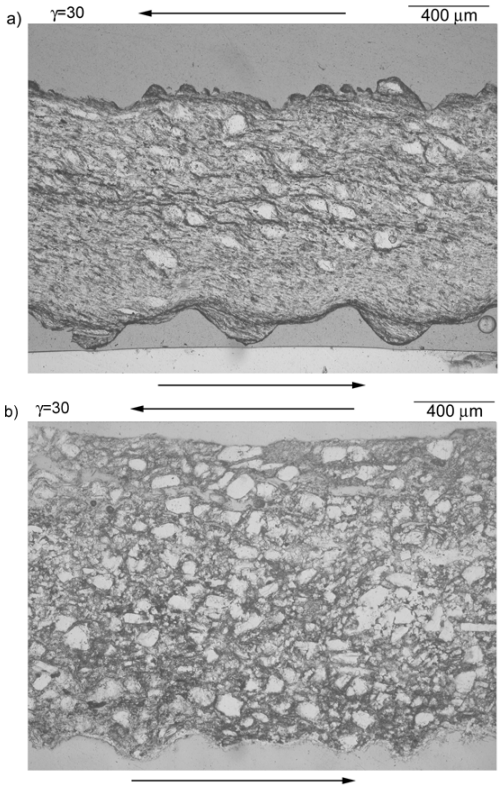

Figure 7.3.: Typical microstructures characteristic of the two velocity regimes
a) Low sliding velocity (0.03 μm/s). Note the anastomosing muscovite foliation with intervening halite clasts. Total strain and shear sense as indicated
b) High sliding velocity (13 μm/s). Note the chaotic microstructure and high porosity. Total strain and shear sense as indicated.

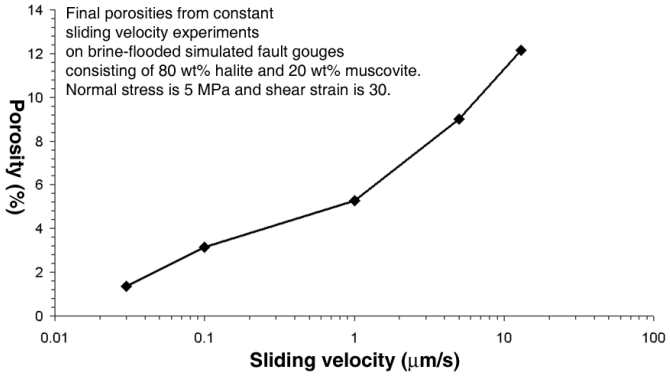

Figure 7.4.: Plot of final porosity of constant sliding velocity experiments on simulated fault gouge of salt-muscovite mixtures with 20 wt% muscovite vs. sliding velocity.

7.3. Model development

In order to develop a model for the behaviour inferred to occur in our halite-muscovite gouges at high sliding velocities, i.e. in the velocity-weakening regime, we start by defining a microstructural model for granular gouge. We then set up equations relating porosity evolution to the two volume-changing deformation mechanisms that are assumed to operate, namely granular flow and pressure solution. We next proceed to derive relations for the contact forces operating in our gouge and the shear resistance offered to purely granular flow. After a consideration of energy conversation and dissipation relations, finally we obtain our equations for the steady state shear strength of our modelled gouge, which we compare with our experimental results.

7.3.1 Microstructural model and associated state variables

The essential elements of the gouge microstructure that we assume in our model are shown in Figure 7.5. For geometric simplicity, the volume fraction of muscovite is considered negligible with respect to the total gouge volume, which is reasonable for a volume percentage of muscovite up to perhaps 15%.

Shear deformation of the gouge is envisaged to occur predominantly by a process of uniformly distributed granular flow involving grain neighbour swapping plus frictional slip on the intergranular muscovite. Slip on the inclined contacts (average inclination angle ψ) leads to dilatation with dilatancy angle ψ.Pressure solution on these, as well as surrounding contacts, causes a component of both compaction and shear deformation. The microstructure is viewed as an idealized snapshot in time of a self-randomizing system whose average porosity and average dilatancy angle ψ evolve with on-going shear, depending on the competition between dilatation and compaction.

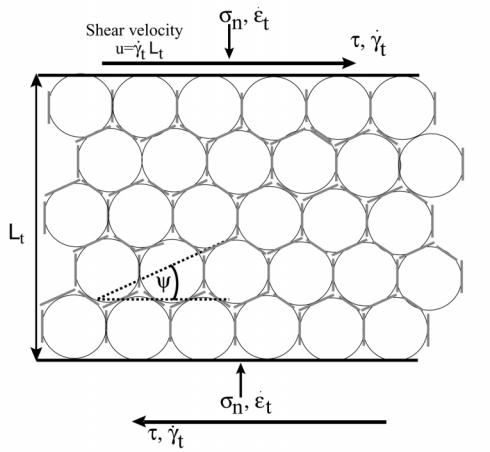

Figure 7.5.: Assumed two-dimensional geometry of a gouge sliding at high sliding velocities by granular flow. Gray lines indicate phyllosilicate, ψ is the dilatancy angle

To quantify the evolution of dilatation rate, intergranular stresses and compaction rate by intergranular pressure solution, relations must now be obtained linking the relevant microstructural state variables of average dilatancy angle (ψ) and average grain contact area (A_c) to porosity (ϕ). A similar problem is encountered in critical state soil mechanics in modelling the shearing behaviour of sands from the over- or underconsolidated state towards the critical state at which shear strength and porosity remain constant. In soil mechanics, this evolution is usually modelled using a discrete element approach to granular flow (Muqtadir and Desai, 1986; Brown and Shie, 1990; Chen and Martin, 2002; Yang and Jeremic, 2002) but such approaches have so far been restricted to considering mainly elastic/frictional interactions between grains. We have therefore chosen to establish a very simple set of microstructural equations relating $\tan\psi$ and A_c to porosity ϕ. While these are a clear oversimplification, and may not be fully internally consistent with the assumed microstructural model, they do embody the trends known to occur in granular media and they satisfy a number of important microstructural constraints.

In establishing our microstructural relations, we first assume that compaction by pressure solution ensures that the model gouge porosity never exceeds the critical state value for pure granular flow. This implies that the granular flow component of our models always tends to produce dilatation and that $\tan\psi \geq 0$. Thus at typical critical state porosities ϕ_c of say 40%, $\tan\psi = 0$. On the other hand, at zero porosity, two extreme gouge microstructures can be envisaged in 2-D, as shown in Figure 7.6. At the onset of granular flow, these microstructures imply dilatancy angles given as $\tan\psi = \frac{1}{\sqrt{3}}$ and $\tan\psi = \sqrt{3}$ (Figure 7.6a and 7.6b respectively).

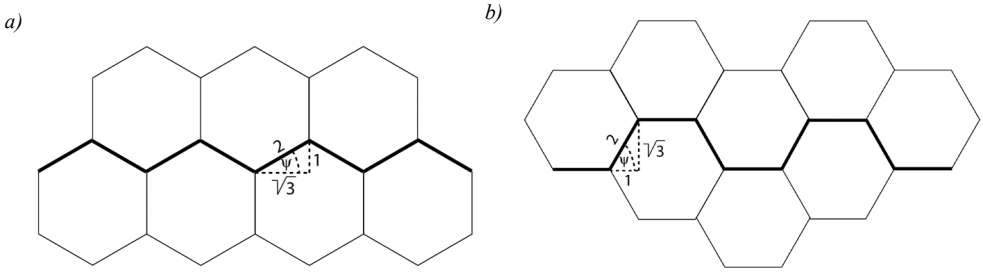

Figure 7.6.: Microstructural geometries for an aggregate of two-dimensional grains with zero porosity. Bold lines indicate the sliding surfaces.

To capture the tendency for the dilatancy angle to decrease with increasing porosity, as seen in shear tests on sub-critical granular media (Bouckovalas et al., 2003; Xenaki and Athanasopoulos, 2003), we accordingly assume that $\tan\psi$ can be approximated by a function of the form

$$\tan\psi = H(q - 2\phi)^n \tag{7.2}$$

where H takes values in the range $1/\sqrt{3}$ to $\sqrt{3}$ and q = 2ϕ_c ($q \approx$ 0.8-1). This describes a monotonic decrease in $\tan\psi$ as ϕ increases, while satisfying the constraints that $\tan\psi \approx 1$ when ϕ is 0 and $\tan\psi = 0$ when $\phi = \phi_c$. In the absence of any constraints on n, we take n = 1 for present purposes. Use of equation (7.1) is then equivalent to defining the microstructural properties of the gouge such that (7.1) is obeyed. Note, however, that in principle, a best fit value of n could be determined empirically for any gouge deforming by granular flow only.

To describe how the average grain-to-grain contact area (A_c) depends on gouge porosity, we adopt a similar approach. We assume that $A_c \rightarrow$ 0 at high porosities approaching critical state values ϕ_c of say 35-45%. At zero porosity, we assume that $A_c \rightarrow \frac{1}{z} \cdot \pi d^2$, where z is the average grain packing coordination number, d is the average grain diameter and πd^2 is the equivalent surface area of a spherical grain of diameter d. At intermediate porosities of 5-35 %, an analysis of the geometry of a simple cubic, or body-centered cubic pack of initially spherical grains compacting isotropically by pressure solution (Renard et al., 1999; Renard et al., 2000a; Gundersen et al., 2002) shows that the relation between contact area and porosity is well described by the relation

$$A_c = k\pi d^2 \left(q - 2\phi\right) \tag{7.3}$$

where q again takes a value of 0.8-1 and $k \approx 1/z$ (see Spiers et al., 2004). This relation satisfies the requirement that $A_c \rightarrow 0$ as $\phi \rightarrow \phi_c$ and $A_c \rightarrow \frac{1}{z} \cdot \pi d^2$ as $\phi \rightarrow 0$, and has been used a mean of approximating grain contact area in previous models of compaction by pressure solution (Spiers et al., 2004). We use it here assuming that it also holds for the average grain contact area in a gouge material undergoing simultaneous granular flow plus compaction by pressure solution.

7.3.2. Kinematic relations for gouge deformation by granular flow plus pressure solution

With reference to Figure 7.5, it is evident that shearing of a fault gouge that can deform by combined granular flow plus pressure solution will lead to total normal and shear strain rates given by:

$$\dot{\varepsilon}_t = \dot{\varepsilon}_{ps} + \dot{\varepsilon}_{gr} \qquad \text{and} \qquad \dot{\gamma}_t = \dot{\gamma}_{ps} + \dot{\gamma}_{gr} \qquad (7.4a,b)$$

where compaction is taken positive and the subscripts *ps* and *gr* represent the strain rate contributions by pressure solution and granular flow, respectively. Following the classical soil mechanics approach to granular flow (see also Paterson, 1995), dilatation due to the granular flow component of deformation can be described using the relation:

$$\dot{\varepsilon}_{gr} = \frac{d\varepsilon_{gr}}{dt} = \left(\frac{d\varepsilon_{gr}}{d\gamma_{gr}} \right) \frac{d\gamma_{gr}}{dt} = -(\tan\psi)\dot{\gamma}_{gr} \qquad (7.5)$$

where ψ is of course the dilatancy angle for pure granular flow. Combining this with (7.4a) we get

$$\dot{\varepsilon}_t = \dot{\varepsilon}_{ps} - (\tan\psi)\dot{\gamma}_{gr} \qquad (7.6)$$

In the case of rapid shear, the shear strain rate contribution due to pressure solution processes in (7.4b) will be negligible compared with the contribution due to granular flow, so that $\dot{\gamma}_t \approx \dot{\gamma}_{gr}$. Thus we get

$$\dot{\varepsilon}_t \approx \dot{\varepsilon}_{ps} - (\tan\psi)\dot{\gamma}_t \qquad \text{and} \qquad \dot{\varepsilon}_{gr} \approx -(\tan\psi)\dot{\gamma}_t \qquad (7.7a,b)$$

Since pressure solution compaction rates increase with increasing porosity through the associated decrease in contact area, equation (7.6a) demonstrates that rapid shearing of a dense gouge will cause dilatation until a steady state is reached where pressure solution balances dilatation. For these steady state conditions, where net compaction is zero, equation (7.7a) accordingly yields

$$\dot{\varepsilon}_{ps} = (\tan\psi)\,\dot{\gamma}_t \tag{7.8}$$

On combining with equation (7.2) for the relation between dilatancy angle and porosity, and taking $n = 1$ in (7.12, this gives

$$\dot{\varepsilon}_{ps} = \dot{\gamma}_t\, H(q - 2\phi) \tag{7.9}$$

for the balance between pressure solution compaction and granular dilatation at steady state.

7.3.3. Rate of compaction by pressure solution

To obtain expressions for $\dot{\varepsilon}_{ps}$, the compaction rate of the gouge due to pressure solution, we assume that the gouge compacts like an isotropic material, so that the effects of normal stress and shear stress can be considered separately. Under these conditions, pressure solution compaction normal to the gouge will be similar to uniaxial compaction under an effective normal stress, σ_n. Previous analyses of pressure solution compaction using equation (7.3) to describe the porosity dependence of mean grain contact area within a compacting granular material (Spiers et al., 2004) have yielded the following results:

$$\dot{\varepsilon}_s = A_s \frac{I_s}{d}\frac{\sigma_e \Omega_s}{RT} f_s(\phi) \text{ for dissolution control} \quad \text{(a)}$$

$$\dot{\varepsilon}_d = A_d \frac{(DCS)}{d^3}\frac{\sigma_e \Omega_s}{RT} f_d(\phi) \text{ for grain boundary diffusion control} \quad \text{(b)} \qquad (7.10a,b,c)$$

$$\dot{\varepsilon}_p = A_p \frac{I_p}{d}\frac{\sigma_e \Omega_s}{RT} f_p(\phi) \text{ for precipitation control} \quad \text{(c)}$$

Here, $\dot{\varepsilon}_x$ represents volumetric strain rate (s^{-1}) for the cases of dissolution, diffusion or precipitation control (subscripts x=s,d,p), the A_x are geometric constants, I_s and I_p are the velocities of dissolution and precipitation, respectively (m/s), d is the grain size (m), σ_e is the applied effective stress (Pa), Ω_s is the molar volume ($m^3 mol^{-1}$), R is the universal gas constant ($Jmol^{-1}K^{-1}$), T is the absolute temperature (K), $f_x(\phi)$ are dimensionless functions of porosity (ϕ) that account for changes in grain contact area, transport length and pore wall area, D is the diffusion coefficient in the grain boundary fluid ($m^2 s^{-1}$), C is the solubility of the solute in the grain boundary fluid ($m^3 \cdot m^{-3}$) and S is the effective thickness of the grain boundary fluid (m). For porosities in the range 5-40%, it is easily shown that the geometry of a regular grain pack implies that:

$$f_s \approx \frac{1}{(q-2\phi)} \quad \text{(a)} \quad f_d \approx \frac{1}{(q-2\phi)^2} \quad \text{(b)} \quad f_p \approx \frac{2\phi}{(q-2\phi)^2} \quad \text{(c)} \qquad (7.11a,b,c)$$

as indicated by Spiers et al. (2004).

7.3.4. Porosity and dilatancy angle at steady state

Inserting the above expressions for pressure solution compaction rate into equation (7.8) we can now obtain results describing the steady state porosity developed when pressure solution is controlled by dissolution, diffusion and precipitation, respectively:

$$\phi_{ss} \approx \frac{1}{2}\left\{ q - \left(A_s \frac{I_s}{d} \cdot \frac{\sigma_e \Omega_s}{R \cdot T} \cdot \frac{1}{\dot{\gamma}_t \cdot H} \right)^{\frac{1}{2}} \right\} \quad \text{(a)}$$

$$\phi_{ss} \approx \frac{1}{2}\left\{ q - \left(A_d \frac{DCS}{d^3} \cdot \frac{\sigma_e \Omega_s}{R \cdot T} \cdot \frac{1}{\dot{\gamma}_t \cdot H} \right)^{\frac{1}{3}} \right\} \quad \text{(b)} \qquad (7.11)$$

$$\frac{(q - 2\phi_{ss})^3}{2\phi_{ss}} \approx A_p \cdot \frac{I_p}{d} \cdot \frac{\sigma_e \Omega_s}{R \cdot T} \frac{1}{\dot{\gamma} H} \quad \text{(c)}$$

We can also equation (7.2) to obtain the dilatancy angle ψ_{ss} at steady state for each rate controlling process

$$\tan \psi_{ss} \approx H \left(A_s \frac{I_s}{d} \cdot \frac{\sigma_e \Omega_s}{R \cdot T} \cdot \frac{1}{\dot{\gamma}_t \cdot H} \right)^{\frac{1}{2}} \quad \text{(a)}$$

$$\tan \psi_{ss} \approx H \left(A_d \frac{DCS}{d^3} \cdot \frac{\sigma_e \Omega_s}{R \cdot T} \cdot \frac{1}{\dot{\gamma}_t \cdot H} \right)^{\frac{1}{3}} \quad \text{(b)} \qquad (7.12)$$

$$\tan \psi_{ss} \approx H \left(2\phi_{ss} \cdot A_p \cdot \frac{I_p}{d} \cdot \frac{\sigma_e \Omega_s}{R \cdot T} \frac{1}{\dot{\gamma} H} \right)^{\frac{1}{3}} \quad \text{(c)}$$

7.3.5 Contact forces and shear resistance to granular flow

Our next step is to find the forces and stresses on inclined grain contacts and an expression for the shear resistance to pure granular flow. We use the assumed 2-D geometry shown in Figure 7.7 to estimate the contact forces and stresses in our model gouge. Recall that shear deformation is assumed to involve a main flow mechanism of self-randomising grain neighbour swapping with slip on the inclined contacts. Assuming further that grain rotation effects can be neglected when the bulk of the imposed shear displacement is accommodated on the inclined contacts, then the forces acting on each individual grain can be written as:

$$F_h = \tau x^2 \qquad \text{and} \qquad F_v = \sigma_n x^2 \tag{7.13a,b}$$

Force balance considerations normal and parallel to the sliding contacts require that:

$$\tilde{f}_n = F_v \cos\psi + F_h \sin\psi \quad \text{and} \quad \tilde{f}_s = F_h \cos\psi - F_v \sin\psi \tag{7.14a,b}$$

Here, the tilde embellishment (~) denotes the forces on the contacts and the subscripts *n, s, v* and *h* correspond to normal, shear, vertical and horizontal, respectively. Combining equations (7.13) and (7.14) gives:

$$\tilde{f}_n = \sigma_n x^2 \cos\psi + \tau x^2 \sin\psi \qquad \text{and} \qquad \tilde{f}_s = \tau x^2 \cos\psi - \sigma_n x^2 \sin\psi \tag{7.16a,b}$$

To a first approximation, if the grain size of the "spherical" grain is d, we have $x \approx d$. Using our expression for the contact area (A_c) obtained assuming grain-to-grain truncation by pressure solution compaction (equation 7.2), the contact stresses are now given by

$$\tilde{\sigma}_n = \frac{\tilde{f}_n}{A_c} = \frac{\tilde{f}_n}{d^2 k\pi(q-2\phi)} = \frac{1}{k\pi(q-2\phi)}\left(\sigma_n \cos\psi + \tau \sin\psi\right) \tag{7.17}$$

$$\tilde{\tau} = \frac{\tilde{f}_s}{A_c} = \frac{\tilde{f}_s}{d^2 k\pi(q-2\phi)} = \frac{1}{k\pi(q-2\phi)}\left(\tau \cos\psi - \sigma_n \sin\psi\right) \tag{7.18}$$

Now, individual contacts must satisfy a slip criterion during granular flow which we assume to have the form of a Coulomb-type criterion given as

$$\tilde{\tau} = \tilde{S}_0 + \tilde{\mu}\tilde{\sigma}_n \qquad \text{or} \qquad \tilde{f}_s = \tilde{f}_0 + \tilde{\mu}\tilde{f}_n \tag{7.19a,b}$$

where $\tilde{f}_0 = \tilde{S}_0 A_c = k\pi d^2 (q-2\phi)\cdot \tilde{S}_0$ and $\tilde{S}_0$ is the cohesion of grain contacts. This represents slip on or within the muscovite-coated contact, whichever is weaker. From (7.17), (7.18) and (7.19) it follows that

$$\frac{\left(\tau \cos\psi - \sigma_n \sin\psi\right)}{k\pi(q-2\phi)} = \tilde{S}_0 + \frac{\tilde{\mu}(\sigma_n \cos\psi + \tau \sin\psi)}{k\pi(q-2\phi)} \tag{7.20}$$

or

$$\tau = \left(\frac{k\pi(q-2\phi)\tilde{S}_0}{\cos\psi - \tilde{\mu}\sin\psi} \right) + \frac{(\sin\psi + \tilde{\mu}\cos\psi)}{(\cos\psi - \tilde{\mu}\sin\psi)}\sigma_n \tag{7.21}$$

which, since $\tan\psi = H(q-2\phi)$, yields

$$\tau = \frac{k\pi}{H}\left(\frac{\tan\psi}{\cos\psi - \tilde{\mu}\sin\psi} \right) \cdot \tilde{S}_0 + \frac{(\sin\psi + \tilde{\mu}\cos\psi)}{(\cos\psi - \tilde{\mu}\sin\psi)}\sigma_n \tag{7.22}$$

for the shear resistance to pure granular flow in a gouge of a given porosity and average grain contact area $A_c = k\pi(q-2\phi)$.

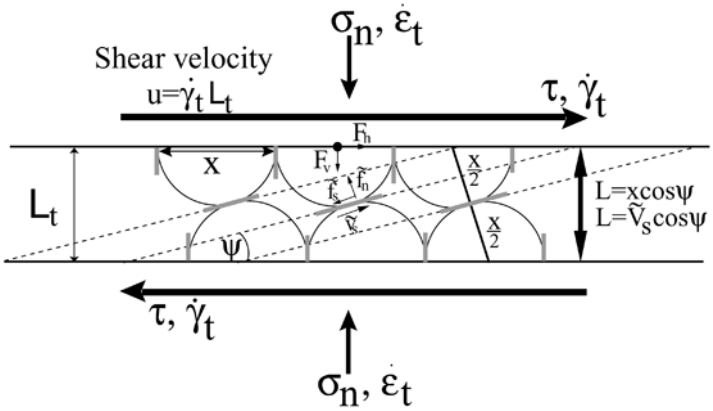

Figure 7.7.: Assumed two-dimensional geometry of a gouge sliding at high sliding velocities by granular flow. Contact forces and geometries are indicated. Gray lines indicate phyllosilicates.

7.3.6 Energy balance and dissipation

Following Lehner (1990, see also chapter 5), the combined energy and entropy balance for unit volume of deforming (shearing) fault gouge as represented in Figure 7.5 can be written

$$\tau\dot{\gamma}_t + \sigma_n\dot{\varepsilon}_t = \dot{f} + \dot{\Delta} \tag{7.23}$$

where $\dot{f}$ is the rate of change of Helmholtz free energy of the solid per unit volume of gouge and $\dot{\Delta}$ is the total dissipation by irreversible microscale processes operating. Under conditions of steady state deformation it is reasonable to suppose that $\dot{f} \approx 0$, as there will be little change in the thermodynamic state of the solid and the solid mass per unit volume will be constant. If the gouge can deform by the combined (parallel) processes of frictional

granular flow and pressure solution, $\dot{\varepsilon}_t$=0 and, separating the compaction and shear components of pressure solution, we can now write

$$\tau \dot{\gamma}_t = \dot{\Delta}_{fr} + \dot{\Delta}_{ps}^{comp} + \dot{\Delta}_{ps}^{shear} \tag{7.24}$$

where $\dot{\Delta}_{fr}$ is the dissipation due to frictional sliding on inclined contacts (Figure 7.5), $\dot{\Delta}_{ps}^{comp}$ is the dissipation due to the compactional component of pressure solution and $\dot{\Delta}_{ps}^{shear}$ is the dissipation due to shear by pressure solution. In the last relation, $\dot{\Delta}_{fr}$ can be written

$$\dot{\Delta}_{fr} = \dot{\Delta}_c N_c \tag{7.25}$$

where $\dot{\Delta}_c$ is the dissipation rate per sliding (inclined) contact and N_c is the number of contacts per unit volume of fault gouge. Now, $\dot{\Delta}_c = \tilde{f}_s \tilde{v}_s$ where $\tilde{v}_s$ is the average frictional slip velocity on the inclined contacts. In addition, with reference to Figure 7.7, it is easily seen that the number of sliding contact per unit area of fault zone with thickness $L=x\cos\psi$ is ~$1/x^2$, so that number of contacts per unit volume of gouge is given $N_c \approx 1/x^3 \cos\psi$. Hence we obtain from (7.25)

$$\dot{\Delta}_{fr} = \frac{\tilde{f}_s \tilde{v}_s}{x^3 \cos\psi} \tag{7.26}$$

Again from the geometry of Figure 7.7, it is also seen that the frictional shear velocity $u = \tilde{v}_s \cos\psi = L\dot{\gamma}_{gr} = x\dot{\gamma}_{gr}\cos\psi$, which yields

$$\tilde{v}_s = x\dot{\gamma}_{gr} \text{ q} \tag{7.27}$$

so that

$$\dot{\Delta}_{fr} = \frac{\tilde{f}_s \cdot \dot{\gamma}_{gr}}{x^2 \cos\psi} \approx \frac{\tilde{\tau} \cdot A_c \cdot \dot{\gamma}_{gr}}{d^2 \cos\psi} \tag{7.28}$$

Using our expression for the contact area (7.3) plus the Coulomb-type criterion for slip on inclined grain contacts (7.19) and our expression for normal stress on these contacts (7.17), this gives

$$\frac{\dot{\Delta}_{fr}}{\dot{\gamma}_{gr}} = \frac{k\pi(q-2\phi)}{\cos\psi} \cdot \tilde{S}_0 + \tilde{\mu}\sigma_n + \tilde{\mu}\tau\tan\psi \tag{7.29}$$

Assuming now that all mechanical work in driving deformation by pressure solution is fully dissipated through the associated microscale processes of dissolution, grain boundary

diffusion and precipitation on pore walls, and assuming that the gouge behaves as an isotropic material with respect to pressure solution, we can write

$$\dot{\Delta}_{ps}^{comp} = \sigma_n \dot{\varepsilon}_{ps} \quad \text{and} \quad \dot{\Delta}_{ps}^{shear} = \tau \dot{\gamma}_{ps} \tag{7.30a,b}$$

Combining (7.24), (7.29) and (7.30), then yields

$$\tau \dot{\gamma}_t = \frac{k\pi(q-2\phi)}{\cos\psi} \cdot \tilde{S}_0 \dot{\gamma}_{gr} + \tilde{\mu}\sigma_n \dot{\gamma}_{gr} + \tilde{\mu}\tau \tan\psi \dot{\gamma}_{gr} + \sigma_n \dot{\varepsilon}_{ps} + \tau \dot{\gamma}_{ps} \tag{7.31}$$

which using $\dot{\gamma}_t = \dot{\gamma}_{ps} + \dot{\gamma}_{gr}$ (7.4b) and $\dot{\varepsilon}_{ps} = (\tan\psi)\dot{\gamma}_{gr}$ at steady state (see equation 7.7) becomes

$$\tau = \frac{k\pi(q-2\phi)}{(\cos\psi - \tilde{\mu}\sin\psi)} \cdot \tilde{S}_0 + \left(\frac{\tilde{\mu}\cos\psi + \sin\psi}{\cos\psi - \tilde{\mu}\sin\psi} \right) \sigma_n \tag{7.32}$$

Finally, using $\tan\psi = H(q-2\phi)$ (equation 7.1) we obtain

$$\tau = \frac{k\pi}{H} \left(\frac{\tan\psi}{\cos\psi - \tilde{\mu}\sin\psi} \right) \cdot \tilde{S}_0 + \frac{(\sin\psi + \tilde{\mu}\cos\psi)}{(\cos\psi - \tilde{\mu}\sin\psi)} \sigma_n \tag{7.33}$$

The above equation for steady state granular with pressure solution is identical to the expression (equation 7.22) that we obtained for the shear resistance offered by a gouge deforming by granular flow alone. This reflects the fact that pressure solution operates in parallel with the time-independent process of frictional granular flow. Under these circumstances the shear stress required to drive granular flow depends only on the dilatancy angle ψ which itself depends on the porosity ϕ. The role of pressure solution in determining the shear strength is simply one of determining the steady state porosity, where dilatation by granular flow is balanced by pressure solution compaction.

7.3.7. Final assembly of the model

The above equation for steady state shear strength due to combined granular flow and pressure solution (equation 7.33) can be combined with equations (7.11) and (7.12) for the steady state values of porosity and dilatancy angle to describe gouge behaviour for the limiting cases of dissolution, diffusion and precipitation controlled pressure solution. The relevant form of equation (7.33) for the steady state case is then best written

$$\tau = \frac{k\pi}{H} \left(\frac{\tan\psi_{ss}}{\cos\psi_{ss} - \tilde{\mu}\sin\psi_{ss}} \right) \cdot \tilde{S}_0 + \frac{(\sin\psi_{ss} + \tilde{\mu}\cos\psi_{ss})}{(\cos\psi_{ss} - \tilde{\mu}\sin\psi_{ss})} \sigma_n \tag{7.34}$$

where ψ_{ss} is given by equation (7.12).

7.4. Model predictions and comparison with experiments

In the following, we apply our model to predict the behaviour of our halite/muscovite gouges, and we compare the results with our experimental results. For the kinetics of pressure solution compaction in the halite-muscovite system, we have used the pressure solution parameters taken from the compaction experiments by Spiers et al. (1990). We assume grain sizes of 20-40 μm in accordance with grain sizes observed after deformation. In line with values expected for a simple grain pack, we have taken the geometrical constant q to be 0.8 (about twice the maximum likely porosity of ~0.4), H to lie in the range $1/\sqrt{3}$ to $\sqrt{3}$ and k to be 1/6. We have taken the grain boundary friction coefficient to be 0.2, 0.3 and 0.4, which includes the value of 0.3 measured for muscovite in the pure muscovite tests (see Niemeijer and Spiers, 2005 and chapter 4).

In Figure 7.8, we show the results given by our microphysical model, along with our experimental data for the sample containing 20 wt% muscovite (equivalent to ~13 vol% for a gouge with 15 % porosity). In Figure 7.8a, we show the variation of the model predictions with varying grain size. It shows that the variation in predicted shear stresses is not strongly dependent on grain size and that a grain size of 20-30 μm would fit best with our experimental data. The overall trend of the model is somewhat flatter than the experimental data show, but this might be an effect of variable grain size in the experiments. Figure 7.8b shows the variation of the model predictions as a function of the grain boundary friction coefficient. The plot shows a relatively strong dependence of the predicted shear stress on the friction coefficient, especially at high sliding velocities. In contrast, the shear stresses predicted using our microphysical model do not depend strongly on the geometrical term H or the grain boundary cohesion, S_0, as shown in Figures 7.8c and 7.8d.

In summary, our simple microphysical model is capable of predicting the observed velocity weakening to within ~0.2 MPa, choosing mid range values of grain size, grain boundary friction coefficient, H and S_0. However, across the entire range of velocities modelled, the predictions are strongly dependent on the grain boundary friction coefficient, which is poorly known in the experimental gouges, because the relative strength and importance of halite-halite contacts (cemented and uncemented), halite-muscovite contacts and muscovite-muscovite contacts are unknown. Still, noting that the friction coefficient for pure muscovite gouge is 0.31, and that this value explains the frictional behaviour of foliated halite/muscovite gouges at low velocities (Niemeijer and Spiers, 2005 and chapter 4), this first modelling attempt yields convincing results with respect to the velocity weakening trend observed in high sliding velocity experiments on our analogue gouges.

a)

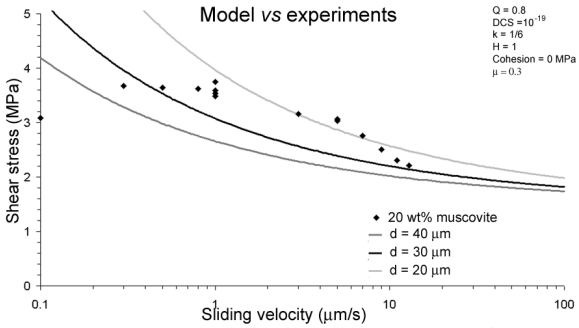

b)

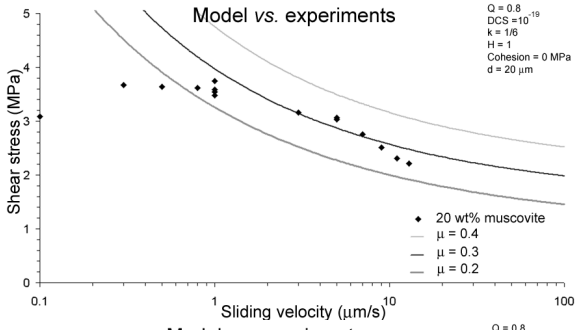

c)

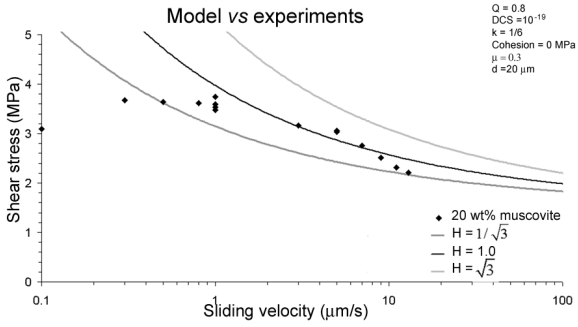

d)

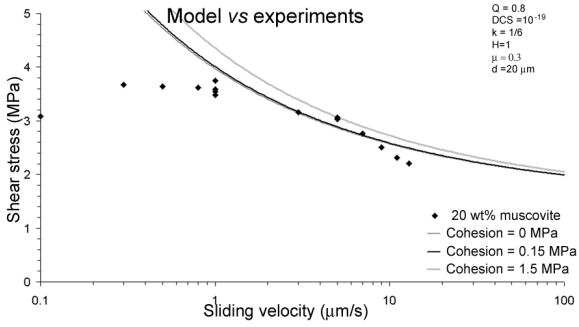

Figure 7.8.: Shear stress vs sliding velocity graph, showing the experimental data for a sample containing 20 wt% muscovite and the predicted model curves.

a) Model predictions using variable grain sizes
b) Model predictions using variable grain boundary friction coefficients
c) Model predictions using variable values for the geometrical constant H
d) Model predictions using variable values for grain boundary cohesion S_0

7.5. Model predictions for natural conditions and implications for seismogenesis

We now apply both our low velocity model (Niemeijer and Spiers, 2005 and also chapter 4) and the high velocity model reported in this chapter to the case of a quartz-muscovite fault gouge deforming at mid-crustal conditions, i.e. an effective normal stress of 100 MPa, temperatures of 200, 300 and 400 ºC and a grain size of 50 μm, roughly consistent with a depth of ~8-10 km. Note that we have used the friction coefficient obtained for our pure muscovite test at room temperature (μ=0.31). The temperature dependence of the high strain friction coefficient of muscovite under hydrous conditions seems to be unknown, though some data exist that suggests no strong temperature dependence (Mariana, 2002). Previous work on pressure solution compaction in quartz sands (Niemeijer et al., 2002, see chapter 2) has shown that pressure solution is probably dissolution rate controlled under upper to mid-crustal conditions, so we have used the dissolution rate law reported by Rimstidt and Barnes (1980) to describe the rate limiting step of pressure solution.

Our results are shown in Figure 7.9 as a plot of friction coefficient versus strain rate. This shows that the predicted friction coefficient of a quartz-muscovite fault gouge at a very low strain rate is lower than the friction coefficient assumed for pure muscovite gouge. This reflects a property of our low velocity slip model, in which frictional slip occurs only horizontal portions of the phyllosilicate foliation (see Bos and Spiers, 2002b and chapter 4; Niemeijer and Spiers, 2005) we have assumed that only a proportion of all phyllosilicate slip planes is active. With increasing bulk shear strain rate, the friction coefficient of our simulated quartz-muscovite fault gouge increases (velocity-strengthening, *cf.* regime 2 described by the model of Niemeijer and Spiers, 2005, see also chapter 4). At a constant strain rate in this regime, the friction coefficient is observed to decrease with increasing temperature. At strain rates of ~10^{-7},10^{-5} and 10^{-4} s^{-1} for temperatures of 200, 300 and 400 ºC, respectively, a transition to velocity-weakening occurs as described by the model developed in this chapter. This velocity-weakening continues for over 4 orders of magnitude in strain rate. Eventually, the model predicts a velocity-independent strength equal to the frictional strength of pure muscovite gouges. Clearly, high shear strain experiments are needed on quartz-muscovite gouges, at high pressures and temperatures, to test the models illustrated in Figure 7.9. Nonetheless, the predicted velocity effects are large compared with laboratory measurements for pure quartz gouge (at least one order of magnitude), so that further attention is justified.

Finally, let us consider a crustal fault zone consisting of quartz-muscovite gouge sliding at an aseismic creep rate and deforming in the velocity-strengthening field corresponding to the microphysical model put forward by (Niemeijer and Spiers, 2005, see also chapter 4) and which can be used to predict the steady state shear stress for such a fault zone. Now, let us assume that some part of the fault zone is locally locked, perhaps due to the absence of muscovite or due to a geometric irregularity, such that aseismic creep is resisted in that segment of the fault. The local shear stress then builds up, until failure

occurs. In the case that this leads to rupture of the aseismically creeping section, the aseismically deforming gouge will be forced into the high sliding velocity regime. Assuming that the gouge now deforms via a granular flow mechanism with competition between dilatation and compaction, we can use our model for the associated velocity weakening to estimate the shear stress for coseismic slip at typical coseismic rates. If we assume that the size of the asperity is small with respect to the rupture length (area) of the aseismically creeping section, then the static stress drop of the seismic event will be the difference between the stress state of the aseismically creeping section before and during the rupture. Now, the static stress drop for a seismic event can be estimated from GPS measurements and/or seismological observations of fault slip and length. We can compare these estimates with the predictions from our two microphysical models, noting that the geophysical estimates actually give an average value for the rupture zone, instead of the value of stress drop at one point (Scholz, 2002).

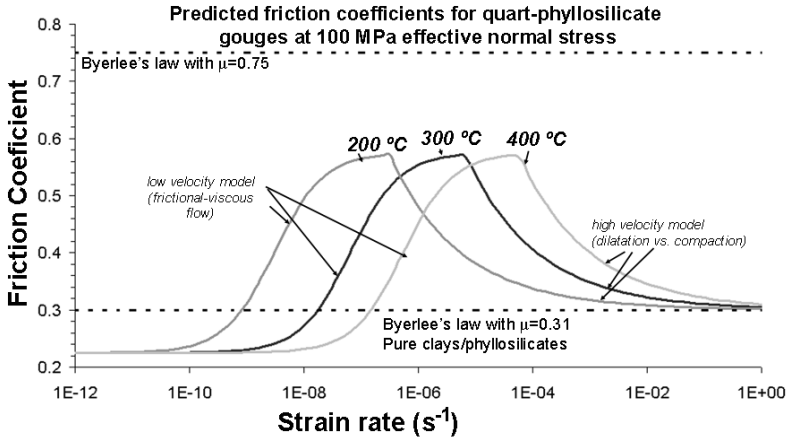

Figure 7.9: Models predictions of friction coefficients for a wide range of strain rate using a grain size of 30 μm, an effective normal stress of 100 MPa and temperatures of 200, 300 and 400 ºC.

In Figure 7.10 we show the model results for the above scenario. In our calculation, we have assumed an aseismic creep rate of 10^{-3} μm/s (or 30 mm/year) and a coseismic slip rate of 1 m/s, based on GPS measurements across the San Andreas Fault and previous estimates of coseismic slip rates (e.g. Scholz, 2002; Becker et al., 2004). We have again used the dissolution rate law reported by Rimstidt and Barnes (1980) to describe the rate limiting step of pressure solution (Niemeijer et al., 2002, see also chapter 2). As phyllosilicates have been reported to both increase (Dewers and Ortoleva, 1991; Bjørkum, 1996; Renard et al., 2001) and decrease IPS compaction rates(Niemeijer and Spiers, 2002, see also chapter 3), we also show model curves for increased (10 times) and decreased (10 times) dissolution rates (see Figure 7.10). The grain size used in all model curves is 50 μm, which is reasonable for a natural fault rock (Imber et al., 2001; Wibberley and Shimamoto, 2003). We also show static stress drop estimates for earthquakes obtained from the analysis of strong ground motion data, geodetic data, aftershock area and from the corner frequency of the corresponding high-resolution (source spectrum) seismic data (Kanamori, 1994; Ide et al., 1996; Hough, 1997; Bouchon et al., 1998; McGarr and Fletcher, 2002).

With reference to Figure 7.10, the microphysical models predict that a drop in stress will occur to depths up to 4 km for a thick fault zone (10 m) and to depths up to 14 km for a thin fault zone (1 mm). The transition from a predicted stress drop to a (physically infeasible) stress rise occurs at depths ranging from 2 to 4 km for the thick fault zone models, and at depths ranging from 6 to 14 km for the thin fault zone models. The predicted maximum stress drops (1 to 4 MPa for the thick fault zone and 4 to 12 for the thin fault zone) agree relatively well with static stress drop estimates from earthquakes covering a large magnitude range (Kanamori, 1994; McGarr and Fletcher, 2002; Scholz, 2002; Abercrombie and Rice, 2005; Duni and Kuka, 2005; Konstantinou et al., 2005; Kumar et al., 2005). Our calculations showed that the kinetics of the dissolution reaction have a strong effect on absolute maximum value of the stress drop. One order of magnitude change in dissolution rate was found to change the maximum stress drop by as much as 3 MPa. Also, the depth to which seismic slip may propagate (i.e. the switch from velocity-weakening to velocity strengthening) is very much dependent on the width of the deforming zone and on the kinetics of dissolution of quartz. For thick fault zones, the model predicts that seismic slip will not propagate to depths over 4 km, whereas the depth to which seismic slip may propagate under fast kinetic conditions in a thin fault zone may reach 14 km. Comparing the two tectonic regimes, the predicted maximum static stress drop is expected to be the largest in a transcurrent fault regime. No statistical evidence of static stress drops exist to date (that we are aware of) that confirms or rejects such a difference between the different tectonic settings.

The present results of our microphysical model imply that, if similar micromechanical processes operate in natural, quartz-rich fault gouges, the presence of phyllosilicates and the operation of pressure solution may enhance velocity weakening by up to one order of magnitude. Extrapolation of our models to natural conditions, to generate maximum static stress drop estimates as a function of depth, yields results which are

reasonably consistent with estimates of static stress drop from seismic data (Figure 7.10). Moreover, the results imply that we can only reliably extrapolate RSF parameters for quartz-phyllosilicate fault gouges to natural conditions if we can characterize the fault zone in terms of the composition of the fault rock and local pressure solution kinetics. Extending our model to address transient effects in the velocity-weakening regime, involving competition between compaction and dilatation, will in future allow us to predict the a, b and D_c parameters, used in RSF descriptions, on the basis of the micro scale processes that occur. It is expected that predicted critical displacement, D_c, for a fault gouge will depend on the amount of time necessary to re-establish steady state porosity and thus on the rate of pressure solution compaction and the rate of dilatation (i.e. on $\tan\psi$).

a)

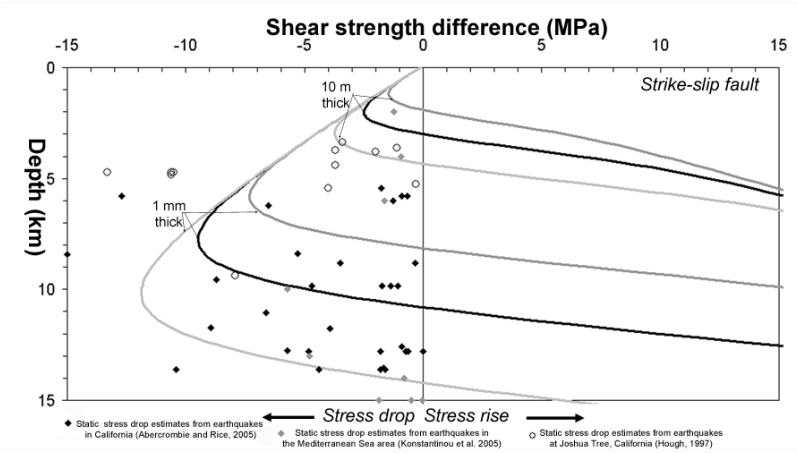

b)

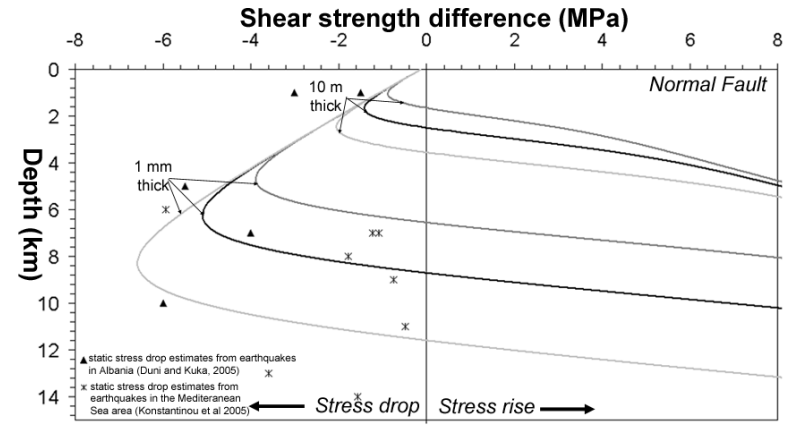

Figure 7.10.: Stress drop vs. depth plots for 2 different tectonic settings using the microphysical models for low velocity frictional-viscous flow behaviour and high velocity granular flow-type behaviour. We assumed a coseismic slip rate of 1 m/s, an overburden density of 2750 kg/m^3 and a hydrostatic fluid pressure (λ=0.36). Three different dissolution rates were used, which are Rimstidt and Barnes' dissolution rate equation (black lines), 10 times this dissolution rate (dark gray lines) and 0.1 times (light gray line). We determined stress drops for a fault zone thickness of 1 mm and 10 m. Also shown are static stress drop estimates for various earthquakes.

a) Strike-slip fault setting. Geothermal gradient is 25 ºC/km.

b) Normal fault setting. Geothermal gradient is 35 ºC/km.

7.6. Conclusions

In order to understand the seismic cycle and seismogenesis better, an improved knowledge of the phenomenon of velocity weakening slip is required. Previous work using high strain rotary shear experiments, has demonstrated unusually strong velocity weakening at high sliding velocity, as the result of addition of weak phyllosilicates to simulated (halite) fault rock under conditions where solution-transfer processes, cataclasis and foliation development/destruction occur. The inferred deformation mechanism was granular flow with ongoing competition between shear-induced dilatation and compaction by solution-transfer processes. In this paper, we have presented a simple microphysical model for this high velocity, velocity weakening behaviour. The following conclusions were reached:

1. A simple microphysical model based on competition between shear-induced dilatation and compaction by time-dependent pressure solution is capable of predicting the velocity-weakening behaviour observed in high strain rotary shear experiments on brine-flooded fault rock analogue (halite-muscovite) samples.
2. Extrapolation of the model to upper and mid crustal conditions suggests that strong velocity weakening, due to granular flow with competition between dilatation and compaction is also possible in quartz-phyllosilicate fault gouges under these conditions.
3. Application of the velocity weakening model to crustal faults, along with an earlier developed velocity strengthening model for slow deformation, predicts static stress drops for seismic events which are in reasonable agreement with estimates from seismological observations.
4. High strain experiments on simulated fault gouges consisting of quartz-phyllosilicate mixtures, performed under hydrothermal conditions, are needed to test the model.

If similar processes are verified in quartz-phyllosilicate mixtures, the present model should be extended to include transient sliding behaviour. The resulting model will be capable of predicting values for RSF parameters for natural fault rocks and will thus yield a microphysically based RSF model for quartz-phyllosilicate fault gouges.

Chapter 8

GENERAL CONCLUSIONS AND SUGGESTIONS FOR FUTURE RESEARCH

8.1. Conclusions

In this thesis, the results of an experimental study, aimed at investigating the effects of intergranular pressure solution (IPS) and phyllosilicates on slip and compaction behaviour of gouge-bearing faults, have been reported. The general aims of the work were a) to characterize IPS compaction in quartz and quartz-muscovite aggregates, b) to investigate the sliding and healing behaviour of simulated fault rock analogue materials, c) to test and improve microphysical models of frictional-viscous flow and d) to experimentally investigate the high strain shearing behaviour of simulated fault gouges of quartz under hydrothermal conditions. In relation to these aims, I reach the following main conclusions.

1. Experimental characterization of intergranular pressure solution (IPS) in quartz.

Isostatic compaction experiments on quartz sands under hydrothermal conditions up to 600 ºC, a confining pressure of 300 MPa and fluid pressures of 150-250 MPa have indicated that IPS is controlled by quartz dissolution at grain contacts under these conditions. Existing microphysical models for this process show reasonable agreement with the experimental results, at least down to porosities of ~15%. At lower porosities, rates slow dramatically as a result of either a switch in rate-controlling mechanism, internal healing of the grain boundary structure or due to contamination of the pore fluid by dissolution of the copper capsules used in our experiments. Our findings imply that IPS compaction under natural conditions is most likely to be controlled by dissolution within grain contacts and that pore fluid chemistry will thus have a strong effect on IPS compaction rates.

2. Effect of muscovite on IPS compaction rates in quartz

Similar isostatic compaction experiments performed on quartz-muscovite mixtures under hydrothermal conditions have demonstrated that the presence of muscovite in amounts of 5-20 wt% hinders IPS compaction rate by a factor of 3-10. This retardation is believed to be

the result of either dissolution of the mica, releasing Al^{3+} into the pore fluid and thus hindering the dissolution of quartz, or possibly a reduction in precipitation area by the presence of muscovite in the pores.

3. Steady state mechanical behaviour of halite-muscovite fault gouge analogue

High strain, rotary shear experiments, on halite-muscovite mixtures flooded with saturated brine have demonstrated distinctly different sliding behaviour for different sliding velocities. A low sliding velocity regime has been identified, where a strong muscovite foliation develops. In this regime, frictional-viscous deformation occurs by frictional sliding in/on the muscovite foliation, with accommodation by pressure solution of the intervening halite grains, in a manner similar to that reported for halite-kaolinite gouges by Bos and coworkers (2000, 2001, 2002). The steady state strength of the gouge in this regime increases with increasing sliding velocity (velocity-strengthening). A high sliding velocity regime has also been identified, where deformation involves granular (cataclastic) flow, producing a relatively chaotic granular microstructure. The mechanical behaviour seen in this regime is determined by competition between shear-induced intergranular dilatation and pressure solution controlled compaction. The steady state strength of the gouges in this regime decreases with increasing sliding velocity (velocity-weakening). This is due to an increase in porosity and thus a decrease in dilatancy angle for granular flow, which in turn reduces grain boundary shear resistance. In contrast, pure halite and pure muscovite samples did not show a significant velocity dependence. The results imply that phyllosilicates may be capable of producing marked velocity weakening effects in natural quartz-rich fault rocks. In addition, they imply that, if in natural fault rocks a cataclastic microstructure is observed in the vicinity of a mylonitic microstructure, this does not necessarily mean a change in pressure and temperature conditions. A change in strain rate can just as easily produce the two different microstructures.

4.Healing behaviour of halite-muscovite fault gouge analogue

Aside from the above steady state tests, slide-hold-slide tests on simulated fault rocks, consisting of halite-muscovite mixtures, have demonstrated an important effect of sliding velocity on the observed healing (i.e. strength recovery) rate. In the low velocity regime, healing is virtually zero, due to the low porosity and presence of a pervasive muscovite foliation, which inhibits compaction and cementation of the halite grains. In the high velocity regime, healing is significant and healing rate increases with increasing sliding velocity. This is due to the higher steady state porosity sustained at higher sliding velocity. The higher porosity enhances IPS compaction rates during periods of zero slip (hold

periods), thereby enhancing healing effects through compaction and contact cementation during hold periods. If similar microphysical processes operate in natural phyllosilicate bearing fault gouges, the observed increase in healing rate with increasing sliding velocity implies a strong effect of the velocity history of a fault gouge on its healing and restrengthening behaviour. This in turn implies that, an aseismically creeping fault segment will not restrengthen, while a seismically slipping segment will.

5. Microphysical modelling

The microphysical model put forward by Bos and Spiers for the type of mechanism inferred for the low velocity regime seen in our halite-muscovite experiments (i.e. describing frictional-viscous flow of foliated fault rock) has been reformulated and extended to include the possibility of crystal plastic flow in the phyllosilicates. The model predictions agree well with our experimental data for the halite-muscovite system under room temperature conditions where plasticity in the muscovite plays no role. Extrapolation of the model to quartz-phyllosilicate fault rock under mid-crustal depth conditions predicts a significant truncation of classical strength profiles (factor 2-5), as pressure solution enables low stress slip on/in the phyllosilicate foliation at depths greater than 3-5 km. In addition, a completely new microphysical model has been developed, describing the steady state competition between shear-induced dilatation and pressure solution controlled compaction in phyllosilicate-bearing fault gouge deforming in the velocity weakening regime seen in our experiments. The model predictions compare reasonably well with our experimental data for the halite-muscovite system. Extrapolation of the model to natural conditions for quartz-phyllosilicate fault rocks predicts a significant velocity weakening effect at depths of 5-10 km for strain rates larger than 10^{-6} s^{-1}, due to the presence of phyllosilicates and the operation of pressure solution. This effect is much larger than velocity weakening effects reported earlier in friction experiments on quartz/granite gouges and may have significant implications for seismogenesis. Also, the model predicts average static stress drops (maxima) for earthquakes, which are within the range inferred from seismological observations.

6. Sliding behaviour of simulated quartz gouges under hydrothermal conditions

Rotary shear experiments have been performed on simulated quartz gouges (initial grain size of 5 to 22 μm) under hydrothermal conditions at temperatures of 400-600 ºC, effective normal stresses of 20-100 MPa, a fluid pressure of 200 MPa and sliding velocities of 0.01-1 μm/s. Shear strains γ up to 25 or even 50 were reached, which is well beyond the maximum

values of ~1-5 previously achieved. The results show a broad yield/peak stress at γ is 0.6-1.8, followed by steady slip weakening (up to 30%) towards near steady state values at shear strains γ of 10-15. Steady state friction coefficients obtained from stress-stepping at a velocity of 1 μm/s lie between 0.5 and 0.7. The friction coefficient is observed to increase with decreasing temperature and grain size. On the basis of microstructural observations and previous work by other authors, we infer that the observed slip weakening is most likely caused by localisation of deformation along a boundary parallel Y-shear. Bulk deformation is mostly cataclastic, probably with some pressure solution acting to weaken the Y-shear slip surface at higher temperatures and lower sliding velocities. Our experiments show that even in quartz gouge that show initial slip hardening behaviour at shear strains up to 1.5, significant strain softening occurs at higher strains. This implies that chemical effects can act together with cataclastic processes to significantly weaken fault gouges at higher strains. These should be taken into account in future experimental and modelling studies of fault behaviour.

8.2. Suggestions for future research

The experiments described in this thesis leave behind a number of unsolved questions and new problems. These are summarized below and suggestions are made on how these may be addressed in future.

1. As seen in the present work on quartz sands, microphysical models for IPS compaction depend on knowing the kinetics of the three serial processes of dissolution, diffusion and precipitation. Present results have shown dissolution reaction control for quartz under the specific experimental and chemical conditions used, but we also found evidence for retardation by other effects at porosities <15%. Better quantification of the kinetic processes controlling IPS in a granular aggregate under realistic natural conditions, and the evolution of such processes with ongoing compaction, is therefore still needed, with special attention for effects of pure fluid chemistry. Several approaches can be taken to tackle this problem. First, geochemical experiments at high temperatures (e.g. 300 ºC) and fluid pressures (e.g. up to 100 MPa) can be done to quantify the dissolution and precipitation rates of natural quartz, systematically checking the influence of common pore fluid impurity ions. Second, internal grain boundary structure, dissolution kinetics and diffusive properties might be investigated by performing electrical resistivity and dissolution rate measurements on bi-crystal contacts during IPS (cf. De Meer et al., 2002; Spiers et al., 2004). Third, high resolution compaction experiments on ultra fine granular quartz sands can be performed under conditions where the results can be directly applied to determine the kinetics of the rate-controlling process. By systematically varying the grain size, it should be possible to quantify the kinetics of the three serial processes as a function of

temperature, fluid pressure and confining pressure, following the approach adopted here in Chapter 2.

2. While present results show a retarding effect of phyllosilicates on IPS compaction rates in quartz, the effect is still not unambiguously explained and our results contradict expectations from earlier work. The main problem is that the effect of phyllosilicates in compaction experiments might be chemical or physical. In order to devise more diagnostic experiments, careful consideration must be given to separating these effects. Purely chemical effects of phyllosilicate dissolution could be identified in future isostatic compaction experiments on pure granular quartz sands by externally equilibrating the pore fluid with respect to the phyllosilicate phase, and by comparing the results with those of control experiments done using pure water as pore fluid. Varying the pore fluid chemistry by addition of IPS-enhancing cation such as Ca^{2+}, K^{+} and Na^{+} and IPS-retarding cations such Al^{3+} or Fe^{3+} would also be useful. When straightforward chemical effects of phyllosilicate dissolution have been clearly identified or eliminated, physical effects of the presence of phyllosilicates within the samples can be investigated. Again, bi-crystal quartz-quartz and quartz-phyllosilicate experiments might be useful here, following the methods suggested under point 1.

3. The present study has shown that experiments on rock analogue materials are very useful to study microphysical processes under easily accessible conditions. However, systematic, high strain rotary shear experiments on quartz-phyllosilicate mixtures, under hydrothermal conditions, are still needed to establish whether low and high sliding velocity regimes of behaviour seen in our halite-muscovite mixtures also occur in more realistic fault gouge materials, under appropriate conditions. If so, the experimental results can then be compared to the predictions of the present microphysical models for steady state slip in the velocity strengthening and velocity weakening regimes, and any modifications or extension of the existing models carried out. If the models successfully reproduce the experimental data for realistic fault rocks, under steady state conditions, the geodynamical and seismological implications of the models need to be carefully investigated.

4. Given the relevance of velocity weakening to seismogenesis, a microphysical model should be constructed for the transient behaviour seen in the high velocity or velocity weakening regime of our halite-muscovite experiments. The present steady state model for this regime can be extended to the transient case, by obtaining expressions for porosity and dilatancy angle evolution under non steady state conditions. The results of such a model should enable us obtain a microphysical basis for predicting rate- and state friction parameters. Like the

steady state model, such a model should also be tested against experiments on natural systems. This would involve high strain, slide-hold-slide experiments on natural materials (e.g. quartz-muscovite mixtures) in a rotary shear set-up under hydrothermal conditions.

5. The microphysical models developed here for the low and high velocity regimes of behaviour of phyllosilicate-bearing fault gouge, require input data not only on the kinetics of IPS (see also point 1), but also on the sliding properties of grain contacts. The latter are not well known for quartz-phyllosilicate systems. Systematic sliding experiments are therefore needed to clarify and quantify the grain contact slip behaviour of quartz-quartz, quartz-phyllosilicate and phyllosilicate-phyllosilicate contacts under hydrothermal conditions. This will constrain the input parameters of the models for extrapolation to nature. Aside from the frictional slip behaviour expected at low temperatures and pressures, care should be taken in such work to account for other processes that might play a role at high temperatures, such as thermally activated grain boundary sliding, fluid film effect or pore fluid pressurization.

6. Upscaling of laboratory results to natural fault zones requires the internal structure, rock properties and structural evolution of such fault zones to be taken into account. Future numerical models of faulting and seismogenesis should aim to take the heterogeneity and anastomosing structure of fault zones into account, computing the macroscopic fault behaviour using microphysical models, such as those obtained here, to describe the rheology of the various internal fault rock segments.

REFERENCES

Abe, K., 1973. Tsunami and mechanism of great earthquakes. Physics of the Earth and Planetary Interiors, 7: 143-153.

Abercrombie, R.E. and Rice, J.R., 2005. Can observations of earthquake scaling constrain slip weakening? Geophysical Journal International, 162(406-424): 406-424.

Addis, M.A. and Jones, M.E., 1985. Volume changes during diagenesis. Marine and Petroleum Geology, 2: 241-246.

Alcantar, N., Israelachvili, J. and Boles, J., 2003. Forces and ionic transport between mica surfaces: Implications for pressure solution. Geochimica et Cosmochimica Acta, 67(7): 1289-1304.

Angevine, C.L., Turcotte, D.L. and Furnish, M.D., 1982. Pressure solution lithification as a mechanism for the stick-slip behavior of faults. Tectonics, 1: 151-160.

Atkinson, B.K. and Meredith, P.G., 1989. The theory of subcritical crack growth with applications to minerals and rocks. In: B.K. Atkinson (Editor), Fracture mechanics of rocks. Academic Press, London, pp. 111-166.

Barker, C.E. and Kopp, O.C., 1991. Luminescence microscopy and spectroscopy: Qualitative and quantitative applications. SEPM Short Course, 25.

Bauer, P., Palm, S. and Handy, M.R., 2000a. Strain localization and fluid pathways in mylonite: Inferences from in situ deformation of a water-bearing quartz analogue (norcamphor). Tectonophysics, 320(2): 141-165.

Bauer, P., Rosenberg, C. and Handy, M.R., 2000b. 'see-through' deformation experiments on brittle-viscous norcamphor at controlled temperature, strain rate and applied confining pressure. Journal of Structural Geology, 22(3): 281-289.

Beaumont, C., Kamp, P.J.J., Hamilton, J. and Fullsack, P., 1996. The continental collision zone, south island, new zealand: Comparison of geodynamical models and observations. Journal of Geophysical Research, 101(B2): 3333-3359.

Beaumont, C., Muñoz, J.A., Hamilton, J. and Fullsack, P., 2000. Factors controlling the alpine evolution of the central pyrenees inferred from a comparison of observations and geodynamical models. Journal of Geophysical Research, 105(B4): 8121-8145.

Becker, T.W., Hardebeck, J.L. and Anderson, G., 2004. Constraints on fault slip rate of the southern california plate boundary from gps velocity and stress inversions. Geophysical Journal International, 160(2): 634-650.

Becker, T.W. and Schmeling, H., 1998. Earthquake recurrence-time variations with and without fault-zone interactions. Geophys J Int, 135(1): 165-176.

Beeler, N.M., Hickman, S.H. and Wong, T.-f., 2001. Earthquake stress drop and laboratory-inferred interseismic strength recovery. Journal of Geophysical Research, 106(B12): 30701-30713.

Beeler, N.M., Tullis, T.E., Blanpied, M.L. and Weeks, J.D., 1996. Frictional behavior of large displacement experimental faults. Journal of Geophysical Research, 101(B4): 8697-8715.

Beeler, N.M., Tullis, T.E. and Weeks, J.D., 1994. The roles of time and displacement in the evolution effect in rock friction. Geophysical Research Letters, 21: 1987-1990.

Ben-Zion, Y. and Rice, J.R., 1995. Slip pattern and earthquake populations along different classes of faults in elastics solids. Journal of Geophysical Research, 100(B7): 12959-12983.

Ben-Zion, Y. and Rice, J.R., 1997. Dynamic simulations of slip on a smooth fault in an elastic solid. Journal of Geophysical Research, 102(B8): 17771-17784.

Bilek, S.L. and Lay, T., 2002. Tsunami earthquakes possibly widespread manifestations of frictional conditional stability. Geophysical Research Letters, 29(14): 10.1029/2002GL015215.

Birch, F., 1966. Compressibility; elastic constants. In: J.S.P. Clark (Editor), Handbook of physical constants, rev. Edn. Geological society of america memoir, pp. 97-173.

Bjørkum, P.A., 1996. How important is pressure in causing dissolution of quartz in sandstones. Journal of Sedimentary Research, 66(1): 147-154.

Blanpied, M.L., Lockner, D.A. and Byerlee, J.D., 1991. Fault stability inferred from granite sliding experiments at hydrothermal conditions. Geophysical Research Letters, 18: 609-612.

Blanpied, M.L., Lockner, D.A. and Byerlee, J.D., 1995. Frictional slip of granite at hydrothermal conditions. Journal of Geophysical Research, 100: 13045-13064.

Blanpied, M.L., Marone, C.J., Lockner, D.A., Byerlee, J.D. and King, D.P., 1998a. Quantitative measure of the variation in fault rheology due to fluid-rock interactions. Journal of Geophysical Research, 103(B5): 9691-9712.

Blanpied, M.L., Tullis, T.E. and Weeks, J.D., 1998b. Effects of slip, slip rate, and shear heating on the friction of granite. Journal of Geophysical Research, 103(B1): 489-511.

Bos, B., Peach, C.J. and Spiers, C.J., 2000a. Frictional-viscous flow of simulated fault gouge caused by the combined effects of phyllosilicates and pressure solution. Tectonophysics, 327: 173-194.

Bos, B., Peach, C.J. and Spiers, C.J., 2000b. Slip behavior of simulated gouge-bearing faults under conditions favoring pressure solution. Journal of Geophysical Research, 105(B7): 16669-16718.

Bos, B. and Spiers, C.J., 2000. Effect of phyllosilicates on fluid-assisted healing of gouge-bearing faults. Earth and Planetary Science Letters, 184: 199-210.

Bos, B. and Spiers, C.J., 2001. Experimental investigation into the microstructural and mechanical evolution of phyllosilicate-bearing fault rock under conditions favouring pressure solution. Journal of Structural Geology, 23(8): 1187-2002.

Bos, B. and Spiers, C.J., 2002a. Fluid-assisted healing processes in gouge-bearing faults: Insights from experiments on a rock analogue system. Pure and Applied Geophysics, 159: 2537-2566.

Bos, B. and Spiers, C.J., 2002b. Frictional-viscous flow of phyllosilicate-bearing fault rock: Microphysical model and implications for crustal strength profiles. Journal of Geophysical Research, 107(B2): 10.1029/2001JB000301.

Bouchon, M., Campillo, M. and Cotton, F., 1998. Stress field associated with the rupture of the 1992 landers, california, earthquake and its implications concerning the fault strength at the onset of the earthquake. Journal of Geophysical Research, 103(B9): 21091-21097.

Bouckovalas, G.D., Andrianopoulos, K.I. and Papadimitriou, A.G., 2003. A critical state interpretation for the cyclic liquefaction resistance of silty sands. Soil Dynamics and Earthquake Engineering, 23(2): 115-125.

Brown, D.A. and Shie, C.-F., 1990. Three dimensional finite element model of laterally loaded piles. Computers and Geotechnics, 10: 59-79.

Brudy, M., Zoback, M.D., Fuchs, K., Rummel, F. and Baumgärtner, J., 1997. Estimation of the complete stress tensor to 8 km depth in the ktb scientific drill holes: Implications for crustal strength. Journal of Geophysical Research, 102(B8): 18,453-18,475.

Burnham, C., Holloway, J.R. and Davis, N.F., 1969. Thermodynamics properties of water to 1,000 ºc and 10,000 bars. Geological Society of America Special Paper, 132: 96.

Butler, R.W.H., Holdsworth, R.E. and Lloyd, G.E., 1997. The role of basement reactivation in continental deformation. Journal of Geological Society of London, 154: 69-71.

Byerlee, J., 1978. Friction of rocks. Pure and Applied Geophysics, 116: 615-627.

Byerlee, J., 1994. The role of water in the evolution of large crustal faults such as the san andreas in california. In: S. Hickman, R. Sibson and R. Bruhn (Editors), The mechanical involvement of fluids in faulting. USGS Open File reports, Menlo Park, California, pp. 254-261.

Byerlee, J.D., 1967. Frictional characteristics of granite under high confining pressure. Journal of Geophysical Research, 72: 3639-3648.

Byerlee, J.D. and Summers, R., 1975. Stable sliding preceding stick-slip on fault surfaces in granite at high pressure. Pure and Applied Geophysics, 113: 63-68.

Caine, J.S., Evans, J.P. and Forster, C.B., 1996. Fault zone architecture and permeability structure. Geology, 24: 1025-1028.

Cao, T. and Aki, K., 1986. Seismicity simulation with a rate- and state-dependent friction law. Pure and Applied Geophysics, 124: 487-513.

Carter, N.L. and Kirby, S.H., 1978. Transient creep and semibrittle behavior of crystalline rocks. Pure and Applied Geophysics, 116: 807-838.

Cattin, R., Doubre, C., de Chabalier, J.-B., King, G., Vigny, C., Avouac, J.-P. and Ruegg, J.-C., 2005. Numerical modelling of quaternary deformation and post-rifting displacement in the asal-ghoubbet rift (djibouti, africa). Earth and Planetary Science Letters, 239(3-4): 352-367.

Chen, C.-Y. and Martin, G.R., 2002. Soil-structure interaction for landslide stabilizing piles. Computers and Geotechnics, 29(5): 363-386.

Chester, F.M., 1994a. Effects of temperature on friction: Constitutive equations and experiments with quartz gouge. Journal of Geophysical Research, 99(B4): 7247-7261.

Chester, F.M., 1994b. Rheologic model of crustal faults: Influence of fluids on strength and stability. In: S. Hickman, R. Sibson and R. Bruhn (Editors), The mechanical involvement of fluids in faulting. USGS Open File reports, Menlo Park, California, pp. 487-500.

Chester, F.M., 1995. A rheologic model for wet crust applied to strike-slip faults. Journal of Geophysical Research, 100: 13033-13044.

Chester, F.M., Evans, J.P. and Biegel, R.L., 1993. Internal structure and weakening mechanisms of the san andreas fault. Journal of Geophysical Research, 98(B1): 771-786.

Chester, F.M. and Higgs, N.G., 1992. Multimechanism friction constitutive model for ultrafine quartz gouge at hypocentral conditions. Journal of Geophysical Research, 97: 1859-1870.

Chester, F.M. and Logan, J.M., 1990. Frictional faulting in polycrystalline halite: Correlation of microstructure, mechanisms of slip, and constitutive behaviour. In: A.G. Duba, Durham, W.B., Handin, J.W. and Wang, H.F. (Editor), The brittle-ductile transition in rocks: The heard volume. Geophysical monograph, pp. 49-65.

Chester, J.S., Lenz, S.C., Chester, F.M. and Lang, R.A., 2004. Mechanisms of compaction of quartz sand at diagenetic conditions. Earth and Planetary Science Letters, 220(3-4): 435-451.

Cloetingh, S. and Burov, E.B., 1996. Thermomechanical structure of earopean continental lithosphere: Constrains from rheological profiles and eet estimates. Geophysical Journal International, 124: 695-723.

Collettini, C. and Barchi, M.R., 2004. A comparison of structural data and seismic images for low-angle normal faults in the northern appennines (central italy): Constraints on activity. In: G.I. Alsop, R.E. Holdsworth, K.J.W. McCaffrey and M. Hand (Editors), Flow processes in faults and shear zones. Special publications. The Geological Society of London, London, pp. 95-112.

Collettini, C., Chiaraluce, L., Pucci, S., Barchi, M.R. and Cocco, M., 2005. Looking at fault reactivation matching structural geology and seismological data. Journal of Structural Geology, 27(5): 937-942.

Collettini, C. and Holdsworth, R.E., 2004. Fault zone weakening and character of slip along low-angle normal faults: Insights from the zuccale fault, isle of elba, italy. Journal of Geological Society of London, 161(2004): 1039-1051.

Cox, S.F., 1994a. Deformation processes and controls on fault mechanics during fault-valve behavior in the wattle gully fault zone, central victoria, australia. In: S. Hickman, R. Sibson and R. Bruhn (Editors), The mechanical involvement of fluids in faulting. USGS Open File reports, Menlo Park, California, pp. 5-17.

Cox, S.F., 1994b. Low friction during sliding on simulated faults in porous quartz sandstone at hydrothermal conditions. In: S. Hickman, R. Sibson and R. Bruhn (Editors), The mechanical involvement of fluids in faulting. USGS Open File reports, Menlo Park, California, pp. 501-508.

Cox, S.F. and Paterson, M.S., 1991. Experimental dissolution-precipitation creep in quartz aggregates at high temperatures. Geophysical Research Letters, 18(8): 1401-1404.
De Boer, R.B., Nagtegaal, P.J.C. and Duyvis, E.M., 1977. Pressure solution experiments on quartz sand. Geochimica et Cosmochimica Acta, 41: 257-264.
De Meer, S. and Spiers, C.J., 1995. Creep of wet gypsum aggregates under hydrostatic loading conditions. Tectonophysics, 245: 171-183.
De Meer, S. and Spiers, C.J., 1997. Uniaxial compaction creep of wet gypsum aggregates. Journal of Geophysical Research, 102: 875-891.
De Meer, S., Spiers, C.J., Peach, C.J. and Watanabe, T., 2002. Diffusive properties of fluid-filled grain boundaries measured electrically during active pressure solution. Earth and Planetary Science Letters, 200(1-2): 147-157.
Deer, W.A., Howie, R.A. and Zussman, J., 1977. An introduction to the rock forming minerals, part 3: Sheet silicates. Longman Group Limited, Tenth Impression, London, pp. 193-205.
Dewers, T. and Ortoleva, P., 1991. Influences of clay minerals on sandstone cementation and pressure solution. Geology, 19: 1045-1048.
Dewers, T.A. and Hajash, A., 1995. Rate laws for water-assisted compaction and stress-induced water-rock interaction in sandstones. Journal of Geophysical Research, 100(B7): 13093-13112.
Dieterich, J., 1994. A constitutive law for rate of earthquake production and its application to earthquake clustering. Journal of Geophysical Research, 99(B2): 2601-2618.
Dieterich, J.H., 1972. Time-dependent friction in rocks. Journal of Geophysical Research, 77: 3690-3697.
Dieterich, J.H., 1978. Time-dependent friction and the mechanics of stick-slip. Pure and Applied Geophysics, 116: 790-806.
Dieterich, J.H., 1979. Modeling of rock friction 1. Experimental results and constitutive equations. Journal of Geophysical Research, 84: 2162-2168.
Dieterich, J.H. and Kilgore, B.D., 1994. Direct observation of frictional contacts: New insights for state-dependent properties. Pure and Applied Geophysics, 143(1/2/3): 283-302.
Dove, P.M., 1999. The dissolution kinetics of quartz in aqueous mixed cation solutions. Geochimica et Cosmochimica Acta, 63(22): 3715-3727.
Dove, P.M. and Nix, C.J., 1997. The influence of the alkaline earth cations, magnesium, calcium, and barium on the dissolution kinetics of quartz. Geochimica et Cosmochimica Acta, 61(16): 3329-3340.
Dove, P.M. and Rimstidt, J.D., 1994. Silica-water interactions. In: P.J. Heaney (Editor), Silica : Physical behavior, geochemistry and materials applications. Reviews in mineralogy. Mineralogical Society of America, Washington D.C., pp. 259-308.
Duni, L. and Kuka, N., 2005. Stress drop estimates from recent strong motion records in albania. Science and Technology for Safe Development of Lifeline Systems: 1-6.
Engelder, T. and Marshak, S., 1985. Disjunctive cleavage formed at shallow depths in sedimentary rocks. Journal of Structural Geology, 7: 327-343.
Evans, J.P. and Chester, F.M., 1994. Fluid-rock interaction and weakening in faults of the san andreas system: Inferences from san gabriel fault-rock geochemistry and microstructures. In: S. Hickman, R. Sibson and R. Bruhn (Editors), The mechanical involvement of fluids in faulting. USGS Open File reports, Menlo Park, California, pp. 514-532.
Farver, J.R. and Yund, R.A., 1991. Measurement of oxygen grain boundary diffusion in natural, fine-grained, quartz aggregates. Geochimica et Cosmochimica Acta, 55: 1597-1607.
Faulkner, D.R., Lewis, A.C. and Rutter, E.H., 2003. On the internal structure and mechanics of large strike-slip fault zones: Field observations of the carboneras fault in southeastern spain. Tectonophysics, 367(3-4): 235-251.
Fredrich, J.T. and Evans, B., 1992. Strength recovery along simulated faults by solution-transfer: Implications for diagenesis, lithification, and strength recovery., 33rd U.S. Symp. Rock. Mech., pp. 121-130.
Freeman, B. and Ferguson, C.C., 1981. Deformation mechanism maps and micromechanics of rocks with distributed grain sizes. Journal of Geophysical Research, 91: 3849-3860.
Gleason, G.C. and Tullis, J., 1995. A flow for dislocation creep of quartz aggregates determined with the molten salt cell. Tectonophysics, 247: 1-23.
Goetze, C. and Evans, B., 1979. Stress and temperature in the bending lithosphere as constrained by experimental rock mechanics. Geophys. J. R. astr. Soc., 59: 463-478.
Govers, R. and Wortel, M.J.R., 1995. Extension of stable continental lithosphere and the initiation of lithosphere scale faults. Tectonics, 14: 1041-1055.
Gratier, J.P. and Guiguet, R., 1986. Experimental pressure solution-deposition on quartz grains: The crucial effect of the nature of the fluid. Journal of Structural Geology, 8(8): 845-856.
Gratier, J.P., Muquet, L., Hassani, R. and Renard, F., 2005. Experimental microstylolites in quartz and modeled application to natural stylolitic structures. Journal of Structural Geology, 27(1): 89-100.
Gratier, J.-P., Renard, F. and Labaume, P., 1999. How pressure solution creep and fracturing processes interact in the upper crust to make it behave in both a brittle and viscous manner. Journal of Structural Geology, 21: 1189-1197.
Gu, Y. and Wong, T.-F., 1994. Development of shear localization in simulated quartz gouge: Effect of cumulative slip and gouge particle size. Pure and Applied Geophysics, 143(1/2): 387-423.
Gueydan, F., Leroy, Y.M. and Jolivet, L., 2001. Grain-size-sensitive flow and shear-stess enhancement at the brittle-ductile transition of the continental crust. International Journal of Earth Sciences (Geologische Rundschau), 90(1): 181-196.
Gueydan, F., Leroy, Y.M., Jolivet, L. and Agard, P., 2003. Analysis of continental midcrustal strain localization induced by microfracturing and reaction-softening. Journal of Geophysical Research, 107(B2): doi:10.1029/2001JB000611.
Gundersen, E., Dysthe, D.K., Renard, F., Bjørlykke, K. and Jamtveit, B., 2002. Numerical modelling of pressure solution in sandstone, rate-limiting processes and the effect of clays. In: S. De Meer, M.R. Drury, J.H.P. De Bresser and G.M.

Pennock (Editors), Deformation mechanisms, rheology and tectonics. Special publication. Geological Society of London, Noordwijk, pp. 41-60.
Han, J.-H. and Kim, D.-Y., 1998. Determination of three-dimensional grain size distribution by linear intercept measurement. Acta Materialia, 46(6): 2021-2028.
Handy, M.R., Wissing, S.B. and Streit, L.E., 1999. Frictional-viscous flow in mylonite with varied bimineralic composition and its effect on lithosperic strength. Tectonophysics, 303: 175-191.
Hardebeck, J.L. and Michael, A.J., 2004. Stress orientations at intermediate angles to the san andreas fault, california. Journal of Geophysical Research, 109(B11303): doi:10.1029/2004JB003239.
Heald, M.T., 1959. Significance of stylolites in permeable sandstones. Journal of Sedimentary Petrology, 29: 251-253.
Heidug, W.K., 1995. Intergranular solid-fluid phase transformations under stress: The effect of surface forces. Journal of Geophysical Research, 100(B4): 5931-5940.
Hickman, S., Sibson, R. and Bruhn, R., 1995. Introduction to special section: Mechanical involvement of fluids in faulting. Journal of Geophysical Research, 100(B7): 12,831-12,840.
Hickman, S.H., Barton, C.A., Zoback, M.D., Morin, R., Sass, J. and Benoit, R., 1997. In situ stress and fracture permeability along the stillwater fault zone, dixie valley, nevada. International Journal of Rock Mechanics and Mining Sciences, 34: 414.
Hickman, S.H. and Evans, B., 1992. Growth of grain contacts in halite by solution-transfer: Implications for diagenesis, lithification, and strength recovery. In: B. Evans and T.-f. Wong (Editors), Fault mechanics and transport properties of rocks. Academic Press, pp. 253-280.
Hickman, S.H. and Evans, B., 1995. Kinetics of pressure solution at halite-silica interfaces and intergranular clay films. Journal of Geophysical Research, 100(B7): 13113-13132.
Hickman, S.H. and Langbein, J., 2002. The parkfield experiment - capturing what happens in an earthquake. In: P.H. Stauffer (Editor). USGS, pp. 1-2.
Hirth, G., Teyssier, C. and Dunlap, J.W., 2001. An evaluation of quartzite flow laws based on comparisons between experimentally and naturally deformed rocks. International Journal of Earth Sciences (Geologische Rundschau), 90(1): 77-87.
Hirth, G. and Tullis, J., 1992. Dislocation creep regimes in quartz aggregates. Journal of Structural Geology, 14: 145-159.
Holdsworth, R.E., 2004. Weak faults - rotten cores. Science, 303: 181-182.
Holdsworth, R.E., Stewart, M., Imber, J. and Strachan, R.A., 2001. The structure and rheological evolution of reactivated continental fault zones: A review and a case study. In: J.A. Miller, R.E. Holdsworth, I.S. Buick and M.R. Handy (Editors), Continental reactivation and reworking. Special publication. The Geological Society of London, London, pp. 115-137.
Hoogerduijn Strating, E.H. and Vissers, R.L.M., 1994. Structures in natural serpentinite gouges. Journal of Structural Geology, 16(9): 1205-1215.
Hough, S.E., 1997. Empirical green's function analysis: Taking the next step. Journal of Geophysical Research, 102(B3): 5369-5384.
Houseknecht, D.W., 1987. Assesing the relative importance of compaction processes and cementation to reduction of porosity in sandstones. Bulletin of the American Association of Petroleum Geologists, 71: 633-642.
Ide, S., Takeo, M. and Yoshida, Y., 1996. Source process of the 1995 kobe earthquake: Determination of spatio-temporal slip distribution by bayesian modeling. Bulletin of the Seismological Society of America, 86(3): 547-566.
Iler, R.K., 1973. Effect of adsorbed alumina on the solubility of amorphous silica in water. Journal of Colloid and Interface Science, 43(2): 399-408.
Iler, R.K., 1979. The chemistry of silica. Wiley, New York.
Imber, J., Holdsworth, R.E., Butler, C.A. and Lloyd, G., 1997. Fault-zone weakening processes along the reactivated outer hebrides fault zone, scotland. Journal of Geological Society of London, 154: 105-109.
Imber, J., Holdsworth, R.E., Butler, C.A. and Strachan, R.A., 2001. A reappraisal of the sibson-scholz fault zone model: The nature of the frictional to viscous ("brittle-ductile") transition along a long-lived, crustal-scal fault, outer hebrides, scotland. Tectonics, 20(5): 601-624.
Israelachvili, J.N., 1992. Intermolecular and surface forces. Academic Press, San Diego, California.
Jackson, R.E. and Dunn, D.E., 1974. Experimental sliding friction and cataclasis of foliated rocks. International Journal of Rock Mechanics and Mining Science and Geomechanics Abstracts, 11: 235-249.
Jefferies, S.P., Holdsworth, R.E., Wibberley, C.A.J., Shimamoto, T., Spiers, C.J., Niemeijer, A.R. and Lloyd, G.E., 2006, in press. The nature and importance of phyllonite development in crustal-scale fault cores: An example from the median tectonic line, japan. Journal of Structural Geology: 1-16.
Kanagawa, K., Cox, S.H. and Zhang, S., 2000. Effects of dissolution-precipitation processes on the strength and mechanical behavior of quartz gouge at high-temperature hydrothermal conditions. Journal of Geophysical Research, 105: 11,115-11,126.
Kanamori, H., 1972. Mechanism of tsunami earthquakes. Physics of the Earth and Planetary Interiors, 6: 346-359.
Kanamori, H., 1994. Mechanics of earthquakes. Annual Reviews Earth and Planetary Science Letters, 22: 207-237.
Karner, S.L. and Marone, C., 2001. Frictional restrengthening in simulated fault gouge: Effect of shear load perturbations. Journal of Geophysical Research, 106(B9): 19319-19337.
Karner, S.L., Marone, C. and Evans, B., 1997. Laboratory study of fault healing and lithification in simulated fault gouge under hydrothermal conditions. Tectonophysics, 277: 41-55.
Kenis, I., Urai, J.L., van der Zee, W., Hilgers, C. and Sintubin, M., 2005. Rheology of fine-grained siliciclastic rocks in the middle crust--evidence from structural and numerical analysis. Earth and Planetary Science Letters, 233(3-4): 351-360.
Kilgore, B.D., Blanpied, M.L. and Dieterich, J.H., 1993. Velocity dependent friction of granite over a wide range of conditions. Geophysical Research Letters, 20(10): 903-906.

Kirby, S.H., 1980. Tectonic stresses in the lithosphere: Constraints provided by the experimental deformation of rocks. Journal of Geophysical Research, 85: 6353-6363.
Knauss, K.G. and Wolery, T.J., 1989. Muscovite dissolution kinetics as a function of ph and time at 70 °c. Geochimica et Cosmochimica Acta, 53: 1493-1501.
Knopf, A., 1929. The mother lode system of california. U.S. Geological survey professional paper, 157, 88 pp.
Koch, P.S., Christie, J.M., Ord, A. and George Jr., R.P., 1989. Effect of water on the rheology of experimentally deformed quartzite. Journal of Geophysical Research, 94: 13975-13996.
Kohlstedt, D.L., Evans, B. and Mackwell, S.J., 1995. Strength of the lithosphere: Constraints imposed by laboratory experiments. Journal of Geophysical Research, 100(B9): 17,587-17,602.
Konstantinou, K.I., Papadopoulos, G.A., Fokaefs, A. and Orphanogiannaki, K., 2005. Empirical relationships between aftershock area dimensions and magnitude for earthquakes in the mediterranean sea region. Tectonophysics, 403(1-4): 95-115.
Kronenberg, A.K., Kirby, S.H. and Pinkston, J., 1990. Basal slip and mechanical anisotropy of biotite. Journal of Geophysical Research, 95: 19257-19278.
Kumar, D., Sarkar, I., Sriram, V. and Khattri, K.N., 2005. Estimation of the source parameters of the himalaya earthquake of october 19, 1991, average effective shear wave attenuation parameter and local site effects from accelerograms. Tectonophysics, 407(1-2): 1-24.
Küster, M. and Stöckhert, B., 1999. High differential stress and sublithostatic pore fluid pressure in the ductile regime - microstructural evidence for short-term post-seismic creep in the sesia zone, western alps. Tectonophysics, 303: 263-277.
Lachenbruch, A.H. and Sass, J.H., 1980. Heat flow and energetics of the san andreas fault zone. Journal of Geophysical Research, 85: 6185-6222.
Lachenbruch, A.H. and Sass, J.H., 1992. Heat flow from cajon pass, fault strength, and tectonic implications. Journal of Geophysical Research, 97(B4): 4995-5015.
Lehner, F.K., 1990. Thermodynamics of rock deformation by pressure solution. In: D.J. Barber and P.G. Meredith (Editors), Deformation processes in minerals, ceramics and rocks. Unwin Hyman, London, pp. 296-333.
Lehner, F.K., 1995. A model for intergranular pressure solution in open systems. Tectonophysics, 245: 153-170.
Lehner, F.K. and Bataille, J., 1984/85. Nonequilibrium thermodynamics of pressure solution. Pure and Applied Geophysics, 122: 53-85.
Logan, J.M. and Rauenzahn, K.A., 1987. Frictional dependence of gouge mixtures of quartz and montmorillonite on velocity, composition and fabric. Tectonophysics, 144: 87-108.
Luan, F.C. and Paterson, M.S., 1992. Preparation and deformation of synthetic aggregates of quartz. Journal of Geophysical Research, 97(B1): 301-320.
Mair, K. and Marone, C., 1999. Friction of simulated fault gouge for a wide range of velocities and normal stresses. Journal of Geophysical Research, 104(B12): 28899-28914.
Mares, V.M. and Kronenberg, A.K., 1993. Experimental deformation of muscovite. Journal of Structural Geology, 15(9/10): 1061-1075.
Mariana, E., 2002. An experimental study of the deformation of white mica. unpublished PhD thesis, University of Manchester.
Marone, C., 1997. On the rate of frictional healing and the constitutive law for time- and slip-dependent friction. International Journal of Rock Mechanics and Mining Sciences, 34(3-4): 347.
Marone, C., 1998a. The effect of loading rate on static friction and the rate of fault healing during the earthquake cycle. Nature, 391: 69-71.
Marone, C., 1998b. Laboratory-derived friction laws and their application to seismic faulting. Annual Reviews Earth and Planetary Science Letters, 26: 643-696.
Marone, C., Raleigh, B. and Scholz, C.H., 1990. Frictional behavior and constitutive modeling of simulated fault gouge. Journal of Geophysical Research, 95(B5): 7007-7025.
Marone, C. and Scholz, C.H., 1989. Particle-size distribution and microstructures within simulated fault gouge. Journal of Structural Geology, 11(7): 799-814.
Marone, C., Vidale, J.E. and Ellsworth, W.L., 1995. Fault healing inferred from time dependent variations in source properties of repeating earthquakes. Geophysical Research Letters, 22(22): 3095-3098.
McGarr, A. and Fletcher, J.B., 2002. Mapping apparent stress and energy radiation over fault zones of major earthquakes. Bulletin of the Seismological Society of America, 92: 1633-1647.
McKenzie, D. and Jackson, J., 2002. Conditions for flow in the continental crust. Tectonics, 21(6): 1055, doi:10.1029/2002TC001394.
Miller, S.A., Ben-Zion, Y. and Burg, J.-P., 1999. A three-dimensional fluid-controlled earthquake model: Behavior and implications. Journal of Geophysical Research, 104(B5): 10621-10638.
Moore, D.E. and Lockner, D.A., 2004. Crystallographic controls on the frictional behavior of dry and water-saturated sheet structure minerals. Journal of Geophysical Research, 109(B03401): doi:10.1029/2003JB002582.
Morrow, C.A. and Byerlee, J.D., 1989. Experimental studies of compaction and dilatancy during frictional sliding on faults containing gouge. Journal of Structural Geology, 11(7): 815-825.
Mullis, A.M., 1993. Determination of the rate-limiting mechanism for quartz pressure solution. Geochimica et Cosmochimica Acta, 57: 1499-1503.
Muqtadir, A. and Desai, C.S., 1986. Three dimensional analysis of a pile-group foundation. International Journal for numerial and analytical methods in geomechanics, 10: 41-58.
Nakashima, S., 1995. Diffusivity of ions in pore water as a quantitative basis for rock deformation rate estimates. Tectonophysics, 245: 185-203.

Nakatani, M. and Scholz, C.H., 2004. Frictional healing of quartz gouge under hydrothermal conditions: 1. Experimental evidence for solution transfer healing mechanism. Journal of Geophysical Research, 109(B7): 10.1029/2001JB001522.
Newhouse, W.H., 1942. Ore deposits as related to structural features, 280. Princeton University Press, Princeton, New Jersey.
Nielsen, A.E., 1986. Mechanism and rate laws in electrolyte crystal growth from aqueous solution. In: J.A. Davis and K.Y. Hayes (Editors), Geochemical processes at mineral surfaces acs symposium series, pp. 600-614.
Niemeijer, A.R. and Spiers, C.J., 2002. Compaction creep of quartz-muscovite mixtures at 500 °c: Preliminary results on the influence of muscovite on pressure solution. In: S. De Meer, M.R. Drury, J.H.P. De Bresser and G.M. Pennock (Editors), Deformation Mechanisms, Rheology and Tectonics. Special Publication. Geological Society of London, Noordwijk, pp. 61-72.
Niemeijer, A.R. and Spiers, C.J., 2005. Influence of phyllosilicates on fault strength in the brittle-ductile transition:Insights from rock analogue experiments. In: D. Bruhn and L. Burlini (Editors), High-strain zones: Structure and physical properties. Special publication. Geological Society of London, Nice, pp. 303-327.
Niemeijer, A.R., Spiers, C.J. and Bos, B., 2002. Compaction creep of quartz sand at 400-600 °c: Experimental evidence for dissolution-controlled pressure solution. Earth and Planetary Science Letters, 195(3-4): 261-275.
Oelkers, E.H., Bjørkum, P.A., Walderhaug, O., Nadeau, P.H. and Murphy, W.M., 2000. Making diagenesis obey thermodynamics and kinetics: The case of quartz cementation in sandstones from offshore mid-norway. Applied Geochemistry, 15: 295-309.
Olsen, M.P., Scholz, C.H. and Léger, A., 1998. Healing and sealing of a simulated fault gouge under hydrothermal conditions: Implications for fault healing. Journal of Geophysical Research, 103(B4): 7421-7430.
Pashley, R.M. and Israelachvili, J.N., 1984. Molecular layering of water in thin films between mica surfaces and its relation to hydration forces. Journal of Colloid and Interface Science, 101(2): 511-523.
Passchier, C.W. and Trouw, R.A.J., 1996. Microtectonics. Springer-Verlag Berlin Heidelberg New York.
Paterson, M.S., 1995. A theory for granular flow accommodated by material transfer via an intergranular fluid. Tectonophysics, 245: 135-151.
Raj, R., 1982. Creep in polycrystalline aggregates by matter transport through a liquid phase. Journal of Geophysical Research, 87(B6): 4731-4739.
Renard, F., Brosse, É. and Gratier, J.P., 2000a. The different processes involved in the mechanism of pressure solution in quartz-rich rocks and their interactions. Spec. Publ. int. Ass. Sediment., 29: 67-78.
Renard, F., Dysthe, D., Feder, J., Bjørlykke, K. and Jamtveit, B., 2001. Enhanced pressure solution creep rates induced by clay particles: Experimental evidence in salt aggregates. Geophysical Research Letters, 28(7): 1295-1298.
Renard, F., Gratier, J.-P. and Jamtveit, B., 2000b. Kinetics of crack-sealing, intergranular pressure solution, and compaction around active faults. Journal of Structural Geology, 22: 1395-1407.
Renard, F., Ortoleva, P. and Gratier, J.-P., 1997. Pressure solution in sandstones: Influence of clays and dependence on temperature and stress. Tectonophysics, 280: 257-266.
Renard, F., Park, A., Ortoleva, P. and Gratier, J.-P., 1999. An integrated model for transitional pressure solution in sandstones. Tectonophysics, 312: 97-115.
Renton, J.J., Heald, M.T. and Cecil, C.B., 1969. Experimental investigation of pressure solution of quartz. Journal of Sedimentary Petrology, 39: 1107-1117.
Rice, J.R., 1992. Fault stress strates, pore pressure distributions, and the weakness of the san andreas fault. In: B. Evans and T.-F. Wong (Editors), Earthquake mechanics and transport properties of rocks. Academic Press, London, pp. 475-503.
Rimstidt, J.D. and Barnes, H.L., 1980. The kinetics of silica-water reactions. Geochimica et Cosmochimica Acta, 44: 1683-1699.
Ruina, A., 1983. Slip instability and state variable friction laws. Journal of Geophysical Research, 88(B12): 10,359-10,370.
Rummel, F., Alheid, H.J. and Frohn, C., 1978. Dilatancy and fracture induced velocity changes in rock and their relation to frictional sliding. Pure and Applied Geophysics, 116: 743-764.
Rutter, E.H., 1976. The kinetics of rock deformation by pressure solution. Philosophical Transactions of the Royal Society of London Abstracts, 283: 203-219.
Rutter, E.H., 1983. Pressure solution in nature, theory and experiment. Journal of Geological Society of London, 140: 725-740.
Rutter, E.H. and Brodie, K.H., 1991. Lithosphere rheology - a note of caution. Journal of Structural Geology, 13(3): 363-367.
Rutter, E.H., Holdsworth, R.E. and Knipe, R.J., 2001. The nature and tectonic significance of fault zone weakening: An introduction. In: R.E. Holdsworth, R.A. Strachan, J.F. Magloughlin and R.J. Knipe (Editors), The nature and tectonic significance of fault zone weakening. Geological society special publication. The Geological Society of London, London, pp. 1-12.
Rutter, E.H. and Maddock, R.H., 1992. On the mechanical properties of synthetic kaolinite/quartz fault gouge. Terra Nova, 4: 489-500.
Rutter, E.H., Maddock, R.H., Hall, S.H. and White, S.H., 1986. Comparative microstructures of natural and experimentally produced clay-bearing fault gouges. Pure and Applied Geophysics, 124: 3-30.
Rutter, E.H. and Mainprice, D.H., 1978. The effect of water on stress relaxation of faulted and unfaulted sandstone. Pure and Applied Geophysics, 116: 634-654.
Rutter, E.H. and Mainprice, D.H., 1979. On the possibility of slow fault slip controlled by a diffusive mass transfer process. Gerlands Beitrage Geophysik, 88(2): 154-162.
Rutter, E.H. and Wanten, P.H., 2000. Experimental study of the compaction of phyllosilicate-bearing sand at elevated temperature and with controlled pore water pressure. Journal of Sedimentary Research, 70(1): 107-116.
Saffer, D.M. and Marone, C., 2003. Comparison of smectite- and illite-rich gouge frictional properties: Application to the updip limit of the seismogenic zone along subduction megathrusts. Earth and Planetary Science Letters, 215(1-2): 219-235.

Schmid, S.M. and Handy, M.R., 1991. Towards a genetic classification of fault rocks: Geological usage and tectonophysical implications. In: D.W. Muller, J.A. McKenzie and H. Weissert (Editors), Controversies in modern geology. Academic Press, London, pp. 339-361.
Scholz, C.H., 1998. Earthquakes and friction laws. Nature, 391: 37-42.
Scholz, C.H., 2000. Evidence for a strong san andreas fault. Geology, 28(163-166): 2.
Scholz, C.H., 2002. The mechanics of earthquakes and faulting. Second edition. Cambridge University Press, Cambridge, U.K., 471 pp.
Schutjens, P.M.T.M., 1991. Experimental compaction of quartz sand at low effective stress and temperature conditions. Journal of Geological Society of London, 148: 527-539.
Schwarz, S. and Stöckhert, B., 1996. Pressure solution in siliciclastic hp-lt metamorphic rocks - constraints on the state of stress in deep levels of accretionary complexes. Tectonophysics, 255: 203-209.
Segall, P. and Rice, J.R., 1995. Dilatancy, compaction and slip instability of a fluid-infiltrated fault. Journal of Geophysical Research, 100(B11): 22155-22171.
Shea, W.T. and Kronenberg, A.K., 1992. Rheology and deformation mechanisms of an isotropic mica schist. Journal of Geophysical Research, 97: 15.201-15.237.
Shea, W.T. and Kronenberg, A.K., 1993. Strength and anisotropy of foliated rocks with varied mica contents. Journal of Structural Geology, 15: 1097-1121.
Shimamoto, T. and Logan, J.M., 1981. Effects of simulated clay gouges on the sliding behavior of tennessee sandstone. Tectonophysics, 75: 243-255.
Shimizu, I., 1995. Kinetics of pressure solution creep in quartz: Theoretical considerations. Tectonophysics, 245: 121-134.
Sibson, R.H., 1977. Fault rocks and fault mechanisms. Journal of the Geological Society of London, 133: 191-213.
Sibson, R.H., 1983. Continental fault structure and the shallow earthquake source. Journal of the Geological Society of London, 140: 741-767.
Sibson, R.H., 2001. Seismogenic framework for hydrothermal transport and ore deposition. Reviews in Economic Geology, 14: 25-50.
Sibson, R.H., Moore, J.M. and Ranklin, A.H., 1975. Seismic pumping - a hydrothermal fluid transport mechanism. Journal of the Geological Society of London, 131: 653-659.
Skinner, B.J., 1966. Thermal expansion. In: J.S.P. Clark (Editor), Handbook of physical constants, rev. Edn. Geological society of america memoir, pp. 75-97.
Sleep, N.H., 1995. Ductile creep, compaction, and rate and state dependent friction within major fault zones. Journal of Geophysical Research, 100(B7): 13,065-13,080.
Sleep, N.H., 1997. Application of a unified rate and state friction theory to the mechanics of fault zones with strain localization. Journal of Geophysical Research, 102(B2): 2875-2895.
Sleep, N.H. and Blanpied, M.L., 1992. Creep, compaction and the weak rheology of major faults. Nature, 359: 687-692.
Sleep, N.H. and Blanpied, M.L., 1994. Ductile creep and compaction: A mechanism for transiently increasing fluid pressure in mostly sealed fault zones. Pure and Applied Geophysics, 143: 9-40.
Sleep, N.H., Richardson, E. and Marone, C., 2000. Physics of friction and strain rate localization in synthetic fault gouge. Journal of Geophysical Research, 105(B11): 25875-25890.
Spiers, C.J. and Brzesowsky, R.H., 1993. Densification behaviour of wet granular salt: Theory versus experiment, Seventh Symposium on Salt. Elsevier, pp. 83-92.
Spiers, C.J., De Meer, S., Niemeijer, A.R. and Zhang, X., 2004. Kinetics of rock deformation by pressure solution and the role of thin aqueous films. In: S. Nakashima, C.J. Spiers, L. Mercury, P.A. Fenter and J.M.F. Hochella (Editors), Physicochemistry of water in geological and biological systems. Frontiers science series. Univerisal Academy Press, Inc., Tokyo, Japan, pp. 129-158.
Spiers, C.J. and Schutjens, P.M.T.M., 1990. Densification of crystalline aggregates by fluid phase diffusional creep. In: D.J. Barber and P.G. Meredith (Editors), Deformation processes in minerals, ceramics and rocks. Unwin Hyman, London, pp. 334-353.
Spiers, C.J., Schutjens, P.M.T.M., Brzesowsky, R.H., Peach, C.J., Liezenberg, J.L. and Zwart, H.J., 1990. Experimental determination of constitutive parameters governing creep of rocksalt by pressure solution, Deformation mechanisms, rheology and tectonics. Geological society special publication. The Geolocial Society of London, London, pp. 215-227.
Stewart, M., Holdsworth, R.E. and Strachan, R.A., 2000. Deformation processes and weakening mechanisms within the frictional-viscous transition zone of major crustal-scale faults: Insights from the great glen fault zone, scotland. Journal of Structural Geology, 22: 543-560.
Stöckhert, B., Wachmann, M., Küster, M. and Bimmerman, S., 1999. Low effective viscosity during high pressure metamorphism due to dissolution precipitation creep: The record of hp-lt metamorphic carbonates and siliciclastic rocks from crete. Tectonophysics, 303: 299-319.
Stuart, W.D. and Tullis, T.E., 1995. Fault model for preseismic deformation at parkfield, california. Journal of Geophysical Research, 100(B12): 24079-24099.
Sverjensky, D.A., 1994. Zero-point-of-charge prediction from crystal chemistry and solvation theory. Geochimica et Cosmochimica Acta, 58(14): 3123-3129.
Tada, R. and Siever, R., 1989. Pressure solution during diagenesis. Annual Reviews Earth and Planetary Science Letters, 17: 89-118.
Ter Heege, J.H., de Bresser, J.H.P. and Spiers, C.J., 2004. Composite flow laws for crystalline materials with log-normally distributed grain size: Theory and application to olivine. Journal of Structural Geology: in press.

Ter Voorde, M., Van Balen, R.T., Bertotti, G. and Cloetingh, S.A.P.L., 1998. The influence of a stratified rheology on the flexural response of the lithosphere to (un)loading by extensional faulting. Geophysical Journal International, 134: 721-735.

Townend, J. and Zoback, M., 2001. Implications of earth quake focal mechanisms for the frictional strength of the san andreas fault system. In: R.E. Holdsworth, R.A. Strachan, J.F. Magloughlin and R.J. Knipe (Editors), The nature and tectonic significance of fault zone weakening. Geological society special publication. The Geological Society of London, London, pp. 13-22.

Townend, J. and Zoback, M.D., 2000. How faulting keeps the crust strong. Geology, 28: 399-402.

Townend, J. and Zoback, M.D., 2004. Regional tectonic stress near the san andreas fault in central and southern california. Geophysical Research Letters, 31(L15S11): doi:10.1029/2003GL018918.

Tullis, J. and Yund, R.A., 1977. Experimental deformation of dry westerly granite. Journal of Geophysical Research, 82: 5705-5718.

Tullis, T.E., 1994. The effect of pore fluid chemistry on the friction of quartz gouge. In: S. Hickman, R. Sibson and R. Bruhn (Editors), The mechanical involvement of fluids in faulting. USGS Open File reports, Menlo Park, California, pp. 509-513.

Tullis, T.E., 1996. Rock friction and its implications for earthquake prediction examined via models of parkfield earthquakes. Proceedings of the National Academy of Sciences of the United States of America, 93(9): 3803-3810.

Vrolijk, P. and van der Pluijm, B.A., 1999. Clay gouge. Journal of Structural Geology, 21(8-9): 1039-1048.

Wang, Y., Houseman, G.A., Lin, G., Guo, F., Wang, Y.-J., Fan, W.-M. and Chang, X., 2005. Mesozoic lithospheric deformation in the north china block: Numerical simulation of evolution from orogenic belt to extensional basin system. Tectonophysics, 405(1-4): 47-63.

Warr, L.N. and Cox, S., 2001. Clay mineral transformations and weakening mechanism along the alpine fault, new zealand. In: R.E. Holdsworth, R.A. Strachan, J.F. Magloughlin and R.J. Knipe (Editors), The nature and tectonic significance of fault zone weakening. Geological society special publication. The Geological Society of London, London, pp. 85-102.

White, S.H., Bretan, P.G. and Rutter, E.H., 1986. Fault-zone reactivation: Kinematics and mechanisms. Phil. Trans. R. Soc. Lond., A317: 81-97.

Wibberley, C.A.J. and Shimamoto, T., 2003. Internal structure and permeability of major strike-slip fault zones: The median tectonic line in mie prefecture, southwest japan. Journal of Structural Geology, 25: 59-78.

Wintsch, R.P., Christoffersen, R. and Kronenberg, A.K., 1994. Water-rock reaction in fault zones - reaction hardening verses reaction softening. In: S. Hickman, R. Sibson and R. Bruhn (Editors), The mechanical involvement of fluids in faulting. USGS Open File reports, Menlo Park, California, pp. 533-539.

Wintsch, R.P., Christoffersen, R. and Kronenberg, A.K., 1995. Fluid-rock reaction weakening of fault zones. Journal of Geophysical Research, 100: 13,021-13,032.

Wintsch, R.P. and Yi, K., 2002. Dissolution and replacement creep: A significant deformation mechanism in mid-crustal rocks. Journal of Structural Geology, 24(6-7): 1179-1193.

Wu, F.T., Blatter, L. and Roberson, H., 1975. Clay gouges in the san andreas fault system and their possible implications. Pure and Applied Geophysics, 113: 87-95.

Xenaki, V.C. and Athanasopoulos, G.A., 2003. Liquefaction resistance of sand-silt mixtures: An experimental investigation of the effect of fines. Soil Dynamics and Earthquake Engineering, 23(3): 1-12.

Yan, Y., van der Pluijm, B.A. and Peacor, D.R., 2001. Deformation microfabrics of clay gouge, lewis thrust, canada: A case of fault weakening from clay transformation. In: R.E. Holdsworth, R.A. Strachan, J.F. Magloughlin and R.J. Knipe (Editors), The nature and tectonic significance of fault zone weakening. Geological society special publication. The Geological Society of London, London, pp. 103-112.

Yang, Z. and Jeremic, B., 2002. Numerical analysis of pile behaviour under lateral loads in layered elastic-plastic soils. International Journal for numerial and analytical methods in geomechanics, 26: 1385-1406.

Yasuhara, H., Marone, C. and Elsworth, D., 2005. Fault zone restrengthening and frictional healing: The role of pressure solution. Journal of Geophysical Research, 110(B06310): doi:10.1029/2004JB003327.

Zoback, M.D., 2000. Strength of the san andreas. Nature, 405: 31-32.

Zoback, M.D., Apel, R., Baumgaertner, J., Brudy, M., Emmermann, R., Engeser, B., Fuchs, K., Kessels, W., Rischmueller, H., Rummel, F. and Vernik, L., 1993. Upper-crustal strength inferred from stress measurements to 6 km depth in the ktb borehole. Nature, 365: 633-635.

Zoback, M.D. and Healy, J.H., 1992. In situ stress measurements to 3.5 km depth in the cajon pass scientific research borehole: Implications for the mechanics of crustal faulting. Journal of Geophysical Research, 102: 18,477-18,491.

Zoback, M.D., Zoback, M.L., Mount, V.S. and others, 1987. New evidence for the state of stress of the san andreas fault system. Science, 238: 1105-1111.

NEDERLANDSE SAMENVATTING

Natuurrampen hebben in de afgelopen decennia voor veel schade en slachtoffers gezorgd en daarom is er veel interesse in wetenschappenlijk onderzoek om de processen die leiden tot aardbevingen, vulkaanuitbarstingen, overstromingen en modderstromen te leren begrijpen. Dit proefschrift behandelt een experimenteel onderzoek naar de eigenschappen van breukgesteenten. Breukgesteenten onstaan door de beweging van aardplaten over, onder en langs elkaar. De beweging van deze aardplaten veroorzaakt wrijving waardoor het gesteente verpulverd wordt en breukgesteente onstaat. De beweging van de platen kan leiden tot aardbevingen, zoals in het geval van de tsunami van 2004 in Zuid-Oost Azië, waarbij de Indische plaat onder de Burma plaat schoof. Deze beweging leidde tot een aardbeving van magnitude 9.15 en omdat de aardbeving in de Indische oceaan plaatsvond, leidde dit tot de dodelijke tsunami.

Om beter te begrijpen waarom, waar en wanneer een aarbeving plaatsvindt, is het belangrijk om te weten hoe het breukgesteente reageert op de beweging van de platen. Ook is het belangrijk om te weten hoe sterk of zwak het gesteente is om juiste numerieke modellen te kunnen maken voor processes als gebergtevorming en ertsvorming. Wetenschappers hebben vastgesteld met behulp van laboratorium experimenten dat de sterkte van het bovenste deel van de aardkorst bepaald wordt door bros breukgedrag of wrijving langs breukvlakken. De sterkte neemt toe met de diepte omdat door toename van de druk door het bovenliggende gesteente de normaalkracht op het breukvlak toeneemt. Het is voornamelijk in dit door bros gedrag gedomineerde gedeelte van de korst dat aardbevingen voorkomen. Op grotere diepte wordt de sterkte van de korst bepaald door vloeigedrag. Door een toename in temperatuur kunnen intrakristallijne processen optreden, waardoor het gesteente ductiel wordt oftewel kan vloeien. In dit gedeelte neemt de sterkte af met de diepte, omdat het gesteente makkelijker vloeit op hogere temperaturen. De overgang van bros naar ductiel gedrag wordt klassiek gelegd op een diepte van 5-20 km. Hier is de sterkte van het gesteente het hoogst.

Ondanks het feit dat dit soort sterkte profielen al jaren gebruikt worden in numerieke modellen en het feit dat de sterkte overeenkomt met metingen gedaan in diepe boringen (KTB, Duitsland), is er ook al jaren kritiek op, omdat het de zaken veel simpeler voorstelt dan ze zijn. Een berucht voorbeeld is de San Andreas breuk in California waar metingen aangeven dat de sterkte van deze breuk veel lager is dan voorspeld door simpele bros-ductiele sterkte profielen. Mogelijke verklaring kunnen zijn:

1. De aanwezigheid van een hoge vloeistofdruk in de San Andreas breuk zone. Door de hoge vloeistofdruk wordt de normaalkracht op de breuk verlaagd, waardoor de breuk zwakker is. Het is echter onduidelijk, waar deze vloeistof vandaan komt en hoe een hoge vloeistofdruk vastgehouden kan worden voor langere tijd.
2. De sterkteprofielen zijn voor gesteentes die uit slechts 1 mineraal bestaan, terwijl veldobservaties van oude breuken duidelijk laten zien dat de breukgesteentes uit verscheidene mineralen bestaan, waaronder veel phyllosilicaten. Dit zijn platige

mineralen die veel zwakker zijn dan andere gesteentevormende mineralen als quartz en feldspaat.

3. De sterkteprofielen zijn veelal gebaseerd op droge experimenten. Hierdoor worden mogelijke chemische processen, zoals het oplossen en neerslaan van materiaal, genegeerd. Bovendien is al langer bekend dat water gesteentes verzwakt, waardoor ze wellicht op lagere diepte al kunnen vloeien.

Hoewel deze gebreken van de bestaande sterkteprofielen al langere tijd bekend zijn, is er nog weinig experimenteel bewijs voor de sterkte of zwakte van breukgesteentes bestaande uit meer dan 1 mineraal en in de aanwezigheid van water en zijn er ook nog geen fysische modellen voor deze processen.

Het oplossen en neerslaan van materiaal als gevolg van de aanwezigheid van water en een normaalkracht ("drukoplossing") is waarschijnlijk erg belangrijk in gesteentes op een diepte van 5-15 km. Niet alleen kan drukoplossing het gesteente zwakker maken, maar het kan ook leiden tot verdichting van gesteente in de afwezigheid van breukbeweging. De verdichting van gesteente door drukoplossing kan juist leiden tot een sterkere breuk omdat de vrije ruimte (porositeit) verwijderd wordt. Voor de olie- en gas-industrie is deze verdichting ook van belang, omdat de porositeit de mogelijke hoeveelheid olie en gas in het reservoir bepaald. Ook kan drukoplossing in reservoir gesteentes na de productie van gas, leiden tot bodemdaling.

Om drukoplossing in het laboratorium te bestuderen, heb ik een aantal experimenten uitgevoerd op hoge druk en temperatuur in aggregaten van quartz. In deze experimenten, wordt een hoeveelheid quartz zand afgewogen in een koperen capsule die verbonden is aan een vloeistofpomp. De capsule wordt vervolgens dichtgelast en geplaatst in een "tuttle" bom, die verbonden is aan het druknet in het laboratorium. Door de bom onder druk te zetten met Argon gas, wordt de capsule met quartz zand samengedrukt. Vloeistofdruk wordt gegenereerd door handmatig met de pomp vloeistof in het systeem te brengen. Door een oven om de "tuttle" bom wordt de temperatuur verhoogd naar 400-600 ºC. De effectieve druk (het verschil tussen de gasdruk en de vloeistofdruk) is 50-150 MPa (oftwel 1000 keer de atmosferische druk). Het quartz zand in de capsule verdicht doordat het quartz op de contacten oplost in de vloeistof, diffundeert langs het contact en weer neerslaat in de vrije ruimtes. Door deze verdichting stijgt de vloeistofdruk en door deze handmatig weer te verlagen en de volumeverandering te noteren, kan de verdichting als functie van de tijd gemeten worden. In hoofdstuk 2 beschrijf ik de resultaten van deze experimenten. De voornaamste conclusie is dat de snelheid van verdichting voornamelijk afhangt van de snelheid van het oplossen van materiaal op de contacten. Bovendien is de snelheid van verdichting niet linear afhankelijk van de effectieve druk, zoals altijd gedacht, maar eerder exponentieel met een exponent van 2-3. In hoofdstuk 3 beschrijf ik de resultaten van soortgelijke experimenten maar dan op mengsels van quartz en muscoviet (een phyllosilicaat). Een theoretisch model verklaart de resultaten redelijk goed. Wetenschappers hebben lang aangenomen dat de aanwezigheid van muscoviet de verdichting versnelt, maar mijn resultaten laten eerder een langzamere verdichting zien. Dit is waarschijnlijk het

gevolg van een verlaging van de oplossnelheid van quartz op de contacten door de aanwezigheid van aluminium ionen in de vloeistof.
Om de effecten van de aanwezigheid van phyllosilicaten en drukoplossing op de sterkte van breuken te onderzoeken, heb ik een serie experimenten uitgevoerd op een analoog materiaal, namelijk mengsels van muscoviet en zout in de aanwezigheid van een verzadigde zout-oplossing. Ik heb een analoog materiaal gebruikt, waarvan bekend is dat processen als drukoplossing en breukgedrag plaatsvinden op kamer temperatuur met een meetbare snelheid. Deze experimenten zijn uitgevoerd in een rotary shear apparataat. Dit apparaat bestaat uit twee rigide stalen ringen waartussen het monster ingeklemd wordt. Hierdoor onstaat een soort donut die in een Instron apparaat, waarmee normaaldruk gegenereerd kan worden, geplaatst wordt. Door de onderste ring te draaien en de bovenste ring vast te houden, wordt het tussenliggende monster blootgesteld aan beweging. Omdat het ringen zijn, is de hoeveelheid deformatie (dus de totale verplaatsing) die gehaald kan worden in principe oneindig. Dit is belangrijk, omdat natuurlijke breuken vaak een grote hoeveelheid aan deformatie hebben gehad (mede door hun ouderdom). De resultaten van dit onderzoek zijn te vinden in hoofdstukken 4 en 5. In hoofdstuk 4 laat ik zien dat de sterkte van de gesimuleerde breuk met een mengel van zout en muscoviet sterk afhankelijk is van de snelheid van verplaatsing, terwijl de sterkte van de twee pure monsters bijna onafhankelijk is van de snelheid. Bij lage snelheden (<0.3-1 μm/s) wordt de breuk sterker met toenemende snelheid. Op de laagste snelheid is het mengsel zwakker dan de pure muscoviet. De microstructuren van de breuk laten een sterke golvende foliatie van muscovite plaatjes zien met daartussen in verlengde korrels van zout. Dit gedrag kan verklaard worden door het schuiven van de zoutkorrels over de muscoviet foliatie, waarbij geometrische onvolkomenheden weggenomen door het oplossen, diffunderen en neerslaan van het zout. Door de toenemende snelheid van deformatie, wordt het moeilijk om de verplaatsing bij te houden door de drukoplossing en wordt de breuk sterker. Een microfysisch model gebaseerd op een eerder model kan de experimentele resultaten goed verklaren. Extrapolatie van dit model naar natuurlijke breuken gebruikmakend van natuurlijke waardes voor de kinetiek, laat een serieuze verzwakking (faktoor 2-5) van de bovenkorst zien in vergelijking tot klassieke sterkeprofielen.
Op hogere snelheden (> 1 μm/s) is de breuk van zout en muscovite zwak en wordt zwakker met toenemende snelheid. De microstructuren laten een chaotische breuk zien, zonder duidelijke struktuur en met veel gebroken korrels en porositeit. Dit gedrag kan verklaard worden door een toenemende neiging van de breuk om zijn volume te vergroten om de verplaatsing te kunnen accomoderen. Door de volumevergroting wordt de verdichting door drukoplossing versneld, totdat er een evenwichtsvolume is bereikt. Op hogere snelheden is de verdichting door drukoplossing per hoeveelheid verplaatsing minder en is de porositeit van de breuk dus groter. Door de hogere porositeit zijn er minder contacten en is de gemiddelde hoek van de contacten lager en is de breuk dus zwakker. In hoofdstuk 5 bekijk ik hoe een breuk zijn sterkte terugkrijgt gedurende periodes van nul beweging, door de gesimuleerde breuken eerst te bewegen en dan voor een vastgestelde periode niet te

bewegen, waarna de beweging weer gestart wordt. Tijdens de periode van nul beweging, zal de breuk verdichten en dus sterker worden. Het verschil tussen de evenwichtssterkte en de piek sterkte tijdens de herstarte beweging bepaalt de versterkingspotentie van de breuk. Voor breuken gedeformeerd op lage snelheden is deze versterking zo goed als nihil. Dit wordt verklaard doordat er bijna geen porositeit is in deze breuken tijdens evenwichtsbeweging en dus is er ook geen verdichting tijdens periodes van nul beweging. In tegenstelling tot deze breuken, versterken breuken gedeformeerd op hoge snelheid veel meer. Dit komt doordat de breuken een hoge porositeit hebben tijdens evenwicht en dus snel verdichten tijdens periodes van nul beweging. De snelheid van versterken neemt toe met toenemende snelheid door de toenemende porositeit. Als eenzelfde proces plaatsvindt in natuurlijke breuken, betekent dit dat natuurlijke breuken snel zullen versterken als ze snel gedeformeerd zijn, maar niet zullen versterken als ze langzaam gedeformeerd zijn.
Om de invloed van vloeistoffen op de sterkte van natuurlijke breuken te onderzoeken, is in de afgelopen jaren in Utrecht een hydrothermaal rotary shear apparaat ontwikkeld, gebaseerd op het rotary shear apparaat zoals eerder beschreven. In dit apparaat is het mogelijk natuurlijke materialen op hoge druk en temperatuur (tot 300 MPa en 700 ºC) te vervormen tot een hele hoge verplaatsing in de aanwezigheid van water. In hoofdstuk 6 beschrijf ik de eerste resultaten van een serie van experimenten op breuken van quartz zand. Deze experimenten laten zien dat met toenemende verplaatsing de sterkte van de breuken afneemt. In vergelijking met andere experimenten is de afname van sterkte groot en vindt plaats over een grote verplaatsing (meer dan 5 mm). De verzwakking is waarschijnlijk het resultaat van het lokalizeren van de verplaatsing in een zone op de grens van het monster en de deformatiepiston. Door drukoplossing van knelpunten in deze zone, wordt de zone gladder en het monster zwakker. Breuken zijn zwakker bij hogere temperaturen, grotere korrelgroottes en hogere snelheden.
Uiteindelijk kom ik in hoofdstuk 7 terug op de analoge experimenten van hoofdstukken 4 en 5. In hoofdstuk 7 beschrijf ik een microfysisch model voor het gedrag van de breuken van mengsels van zout en muscoviet op hoge snelheden. Dit model is gebaseerd op de competitie tussen volume-vergroting door deformatie en volume-verkleining door drukoplossing. Het model voorspelt de resultaten van de experimenten redelijk goed. Als we aannemen dat hetzelfde proces in natuurlijke breuken plaatsvindt, kan het model geextrapoleerd worden naar natuurlijk situaties. Om dit te doen, neem ik aan dat een natuurlijk breuk deformeert volgens het lage snelheids model en dat er in de breuk een segment niet verplaatst, maar op een zeker moment met een aardbeving “losschiet”. Als de aardbeving zich voortplant tot in het zwakke deel van de breuk, zal dit gedeelte in het regime van de hoge snelheid gaan deformeren. Door de twee modellen van elkaar af te trekken, krijgen we een idee van het spanningsverval dat optreedt tijdens deze aardbeving. Door dit voor verschillende diepte te doen, ontstaat een spanningsverval curve, die de spanningsvervallen, zoals gemeten met behulp van geofysische methoden in natuurlijke aardbevingen, redelijk kan voorspellen.

Concluderend heeft dit proefschrift tot een beter inzicht geleid in de processen die kunnen leiden tot het versterken en verzwakken van breuken en in het proces van drukoplossing. Bovendien is een microfysisch model gepresenteerd dat gebruikt kan worden in numeriek modellen voor gebergtevorming en de seismische cyclus. De ultieme test voor het verifieren van de toepasbaarheid van de resultaten op de analoge materialen (namelijk rotary shear experimenten op mengsels van natuurlijke materialen, bijvoorbeeld quartz en muscovite) zal in de toekomst nog meer interessante resultaten geven, die tot meer inzicht in het breukgedrag van gesteentes zal leiden.

ACKNOWLEDGEMENTS/DANKWOORD

Na vier jaar promoveren ben ik eindelijk aangekomen bij wat wellicht het moeilijkste stuk is om te schrijven, namelijk het dankwoord. Toch is dit ook het leukste stuk om te schrijven, omdat je voor jezelf de afgelopen vier jaar weer nagaat wat je ook alweer allemaal gedaan hebt en wie je er allemaal bij geholpen hebben. De vier jaar zijn eigenlijk omgevlogen, zonder dat ik besef waar ik eigenlijk zo druk mee bezig ben geweest. In de afgelopen jaren zijn er vele mensen geweest die me geholpen en gesteund hebben en ik bied bij voorbaat mijn excuses aan bij de mensen die ik eventueel mocht vergeten in dit dankwoord.

De technici van het hoge druk en temperatuur laboratorium in Utrecht zijn natuurlijk onmisbaar geweest tijdens mijn promotie onderzoek. Peter was de eerste met wie ik in aanraking kwam. Hij was altijd bereid te helpen bij de meest uiteenlopende dingen, waarbij zijn oog voor detail mij veel (overbodig) werk bespaard heeft. Gert was onmisbaar op de momenten dat er dingen kapot gingen en bij het ontwikkelen van nieuwe toepassingen. Bij veel gelegenheden kreeg je te horen dat het aan het eind van de week klaar zou zijn en was het stiekem de volgende dag al gebeurd. Eimert was altijd druk, maar vond toch tijd me te helpen bij de vele elektronische mankementen en aanpassingen. Ik begreep nooit precies wat het mankement inhield, maar toch probeerde hij het elke keer weer uit te leggen. The same can be said of Colin ("Dr Fix-it" as he called himself in Bochum), who provided me with the necessary assistance with the Instron machine. All problems with the Instron machine were eventually fixed, but I cannot say that I can fix them now, if they would occur again. De deur van Hans stond altijd open en bij verschillende microscoop problemen was zijn hulp een belangrijke toegevoegde waarde. Zonder de inzet van Thony was de ontwikkeling van het nieuwe hydrothermale ring shear apparaat nooit geslaagd en ik weet zeker dat in de toekomst dit apparaat nog belangrijke nieuwe resultaten zal genereren.

Op het sociale vlak zijn de volgende mensen (in willekeurige volgorde) belangrijk geweest om de broodnodige afleiding, ontspanning en alcoholconsumptie te verzorgen. Ik zal beginnen met de UGV-besturen van de afgelopen vijf jaar, te weten van Eijndthoven, Wielaard, Faassen, Verheul en Wassmer. Altijd handig zo'n supermarkt/kroeg op de faculteit! Ook nog bedankt voor het organiseren van de nodige excursies, borrels en feesten. Verder is het voetbal (zaal en veld) de afgelopen jaren erg belangrijk geweest voor de nodige lichamelijke oefening en ontspanning (de 3e helft). Heeren van Rivierwijkers 2, bedankt! En dan met name onze onverschrokken aanvoerder Bas Lodder, puik dat je al zo lang alles rond ons team regelt. Het goudpannen is tijdens mijn promotie ook een belangrijke afleiding geweest. De verschillende tripjes binnen Europa en laatst Zuid-Afrika waren super! Bruno en Veronica nog bedankt voor het lezen van hoofdstuk 2. Met name wil ik mijn reisgenoten van Zuid-Afrika noemen, Ruurd en Gonneke, Sam en Esther, en Walter, bedankt voor de leuke tijd en dat geld krijgen jullie echt terug. In Finland wil ik ook een medaille met het nationale team! De (resten van) G7 was altijd goed voor een avondje in de kroeg, dat heeft me zeker een half jaar gekost. Ferry, Rob, Heiko, Jelle, Maarten en Joris,

laten we proberen in ieder geval elkaar zo af en toe eens te zien, of dat nou in Pennsylvania, Nieuw-Zeeland, Angola of Utrecht is, maakt mij niet uit. De laatste 2 jaar was de tweewekelijkse pubquiz in de Florin ook een zeer welkome afleiden, teamgenoten van H, the spot formerly known as G, bedankt en we gaan voor die 1e plek! Jan-Willem (Edje?, Basket?) en Paulien (roken?), bedankt voor de gezelligheid en succes in respectievelijk Utrecht en Noorwegen.

In de dagelijkse gang van zaken op de faculteit zijn er nog een aantal mensen die belangrijk voor me geweest zijn. Het Solid Rock Seminar comité (Saskia, Siska, Reinier), bedankt voor het organiseren van een serie interessante praatjes. Bernard de Jong, bedankt voor je immer kritisch opstelling ten opzichte van welk onderzoek dan ook. Ik ben altijd wel in voor een goede discussie. Verder wil ik Magda bedanken voor hulp bij de meest uiteenlopende vragen en problemen. Ook moet ik Hans Bliek, Reinoud Vissers, Bart Meininger, Herman van Roermond, Emilia, Suzanne, Vincent, Sergio, Reinier, Kim Hein, Hugo de Boorder, Gill Pennock, Dirk Spengler en Martin Drury bedanken voor alle gezellige gesprekken en discussies tijdens lunches, koffiepauzes, borrels en excursies. Otto Stiekema, bedankt voor de snelle preparatie van de slijpplaten.

I would also like to thank the reviewers of the manuscripts of Chapters 2, 3, 4 and 5. These are: E.H. Rutter, A. Hajash, B. den Brok, J.-P. Gratier, D. Moore, A. Kronenberg, T.E. Tullis and C. Marone. The following people have contributed to my general understanding of faults and fault behaviour during discussions at conferences and during visits: Cristiano Colletini, Steve Hickman, Bob Holdsworth, David Lockner, Diane Moore, Brian Evans, Michael Edwards, Chris Marone, James Dieterich, Florian Lehner, Frederic Gueydan and Derek Elsworth. I would also like to thank the people of the dissertation committee, F.M. Chester, C. Marone, B. Holdswordth, T. Shimamoto and R. Wortel for their carefull reading and comments which helped improve the quality of the manuscript.

The most important person during the 4 years of this PhD is of course my promotor, Chris Spiers. Chris, thank you for giving me the chance to do this PhD in the great group of the HPT laboratory. You have inspired me at moments when I was completely unmotivated and slowed me down at times when my enthousiasm made me overlook some important points. I hope we will work together again in the future.

Natuurlijk kan ik mijn paranimfen niet ongenoemd laten. Arthur, bedankt voor de 4 jaar dat je mijn kamergenoot was. Altijd prettig om de frustraties van een promotie te bespreken onder het genot van een biertje. Stefan, bedankt voor je nuchtere kijk op de zaken en je hulp bij de verschillende programmeerproblemen.

Als laatste wil ik mijn directe familie bedanken voor hun steun. Pa, ma, Marco, Willemijn en Paul, bedankt en wees niet ongerust, de V.S. is maar 8 uurtjes vliegen!

"Het probleem met nietsdoen is dat je niet weet wanneer je klaar bent!"

Curriculum vitae

March 27th 1977	Born in Tiel, The Netherlands
1989-1995	Secondary school, Koningin Wilhemina College, Culemborg, The Netherlands
1995-2001	Study of Geochemistry, Utrecht University, The Netherlands
2002-2006	Ph.D. Student in the Experimental Rock Deformation Group, Utrecht University, The Netherlands